UiT
THE ARCTIC UNIVERSITY OF NORWAY

Faculty of Science and Technology

Department of Geosciences

Climate controlled sedimentary processes in the Riiser Larsen Sea offshore Queen Maud Land, Antarctica

Rita Brekken

GEO-3900 Master's thesis in geology
November 2018

(adapted from AZAMARA (2018))

UNIVERSITY OF TROMSØ

Abstract

Multi-proxy analysis of gravity core PS56/029-1 have been performed in order to describe sedimentary processes and dynamics under pelagic, turbiditic and contouritic influences. The purpose is to reconstruct climate-controlled environmental change in the Riiser Larsen Sea, Antarctica, through past glacial/interglacial cycles. The gravity core was retrieved during expedition ANTARKTIS XVII/2 of R/V Polarstern in 2000. Data analysis was carried out in a collaboration between the Alfred Wegner Institute, Helmholtz centre for polar and marine research in Germany and the Department of Geosciences at UiT The Artic University of Tromsø.

The core was retrieved from a levee in the central part of a large channel system in the Riiser Larsen Sea, at c. 4000 m water depth and c. 200 km offshore Princess Ragnhild Coast, Queen Maud Land, Antarctica. A multi-proxy analysis was conducted in order to determine depositional environments through past glacial/interglacial cycles. The analysis included physical properties, e.g. magnetic susceptibility, p-wave velocity and wet-bulk density, interpretation of line-scan images and X-radiographs, qualitative element geochemical analysis using an Avaatech XRF Core Scanner and high resolution grain-size distribution analysis using a CILAS 1180 laser granulometer.

Core PS56/029-1 reveals alternating repetitive intervals of poorly sorted and fine-grained sediment accumulated in lighter brownish and greyish coloured intervals. The deposits have a polymodal signature which is interpreted to reflect a mixed pelagic, turbiditic, and contouritic influence, and the more occasional influence of icebergs. Four lithofacies are defined: Laminated Grey Layer (LGL), Grey Layer Thin (GLT), Massive Lighter Layer (MML) and Red Brown Layer (RBL). The greyish coloured intervals LGL and GLT are interpreted to be deposited during glacial periods, including fine sediments attributed to the advancing ice-sheet, along with a more extensive sea-ice, and smaller coastal polynyas. More frequent turbidity currents are suggested to be the explaining factor. The lighter brownish coloured layers MLL and RBL are interpreted to be deposited during interglacial periods, including slightly coarser sediments attributed to a stable or retreating ice sheet, along with less extensive sea-ice cover, and stronger coastal polynyas. Increased bottom-water velocities and denser water masses created in coastal polynyas are suggested to be the explaining factors.

Acknowledgements

The Master's thesis is ready to be submitted, but I couldn't have done it alone. I want especially give huge thanks to my supervisors Dr. Matthias Forwick and Dr. Christian Hass for excellent supervision and guidance through this past year. I have been privileged to be able to learn from you guys!

Thank you Dr. Matthias Forrwick for always replaying my emails quickly and for always make time for me in your busy schedule. This is very much appreciated. I also want to thank you for the kindness you showed during my sick leaf. For giving me the time I needed in order to complete this thesis, thank you!

Thank you Dr. Christian Hass for helping me through my stay at the Alfred Wegner Institute in Bremen and on Sylt, Germany, and for letting me participate on your cruises, this have truly been an interesting journey for me!

Additionally I want to thank:

- All the kind people at the Alfred Wegner Institute on Sylt, which made my stay there so much better.
- Ingrid for helping me with the Avaatech XRF Core Scanner.
- Karina for helping me at the Geoscience Laboratory.
- My geology friends for five amazing years together! Especially thanks to, Sindre for solving my computer problems and Rebekka for helping me with the final correlations on this thesis.
- My boyfriend Chris Brynjulfsen for supporting me through this thesis. I will always be grateful and could not have done this without you!
- My family for supporting me through these five years.

Rita Brekken

Tromsø 12.11.2018

Contents

Abbreviations:

AABW = Antarctic Bottom Water

AIS = Antarctic Ice Sheet

ACC = Antarctic Circumpolar Current

APIS = Antarctic Peninsula Ice Sheet

CDW = Circumpolar Deep Water

EAIS = East Antarctica Ice Sheet

GL = Grounding line

GZW = Grounding zone wedge

HSSW = High Salinity Shelf Water

LGM = Last Glacial Maximum

LGL = Laminated Grey Layer

LSSW = Low Salinity Shelf Waters

Ma = Million years ago

MLL = Massive Lighter Layer

MS = Magnetic susceptibility

MSCL = Multi-Sensor Core Logger

MSGL = Mega-scale glacial lineation

NH = Northern Hemisphere

RBL = Red Brown Layer

RLS = Riiser Larsen Sea

SH = Southern Hemisphere

Sv = Sverdrup ($10^6 m^3/s$)

TAM = Transantarctic Mountains

UCDW = Upper Circumpolar Deep Water

UTL = Undefined Transition Layer

WAIS = West Antarctic Ice Sheet

WDW = Warm Deep Water

1 Introduction

1.1 Objectives

The main objective of this Master's thesis is to investigate sedimentary processes in the central part of a large channel system in the Riiser Larsen Sea (RLS), Antarctica, at approximately 4000 m water depth and approximately 200 km offshore Princess Ragnhild Coast, Queen Maud Land. The objectives are to:

- Describe sedimentary processes and dynamics under pelagic, turbiditic and contouritic influences, and to;
- Reconstruct climate-controlled environmental change in the Riiser Larsen Sea through the past glacial/interglacial cycles.

1.2 Motivation

The Antarctic Ice Sheet (AIS) is the largest single mass of ice on earth, storing 27 million km^3 of ice at present, equivalent to a global sea level rise of 58 m (Fretwell et al., 2013a). Melting of ice sheets is likely the dominant contributor to sea level rise in the 21st century (Rignot et al., 2011). At present, ice loss contribute c. 1.8 mm per year globally to sea level rise. Thinning of ice shelves and tidewater glaciers removing grounded ice or unstable parts of the ice in a large-scale collapse could further increase the contribution to sea level rise from ice (Pritchard et al., 2009; Rignot et al., 2011; DeConto and Pollard, 2016a).

The Transantarctic Mountains (TAM) divide the Antarctic continent into two distinct regions, with colossal glaciers on both sides known as the East Antarctica Ice Sheet (EAIS) and the West Antarctica Ice Sheet (WAIS). In addition, the Antarctic Peninsula Ice Sheet (APIS) (part of WAIS) makes a 3rd subdivision of the ice masses in Antarctica (Fig. 1.1). The ice sheets contain kilometres of thick ice accumulations that locally drain towards the open ocean through fast flowing outlet glaciers and ice streams (Fig. 1.2). These works as pathways for the moving ice, transporting ice from the interior of the continent towards the ocean, capable of moving several meters of ice per day (Rignot et al., 2011). Ice shelves are formed as the ice sheet flows down to the coastline and flows onto the ocean (Rignot et al., 2011). The boundary between the floating ice shelf and the ice sheet is called the grounding line. Ice shelves are important contributors to the ice sheet dynamics because they give backstress, buttressing the ice by

lowering the velocity and loss of ice through ice streams and outlet glaciers (Van der Veen, 1997; Pritchard et al., 2012; Matsuoka et al., 2015; DeConto and Pollard, 2016b). Between 1992 and 2011 the ice sheets of East Antarctica and West Antarctica changed in mass by +14 ± 43 and -65 ± 26 gigatons per year respectively (Shepherd et al., 2012). It is likely that the EAIS and WAIS will respond differently to increased temperatures globally.

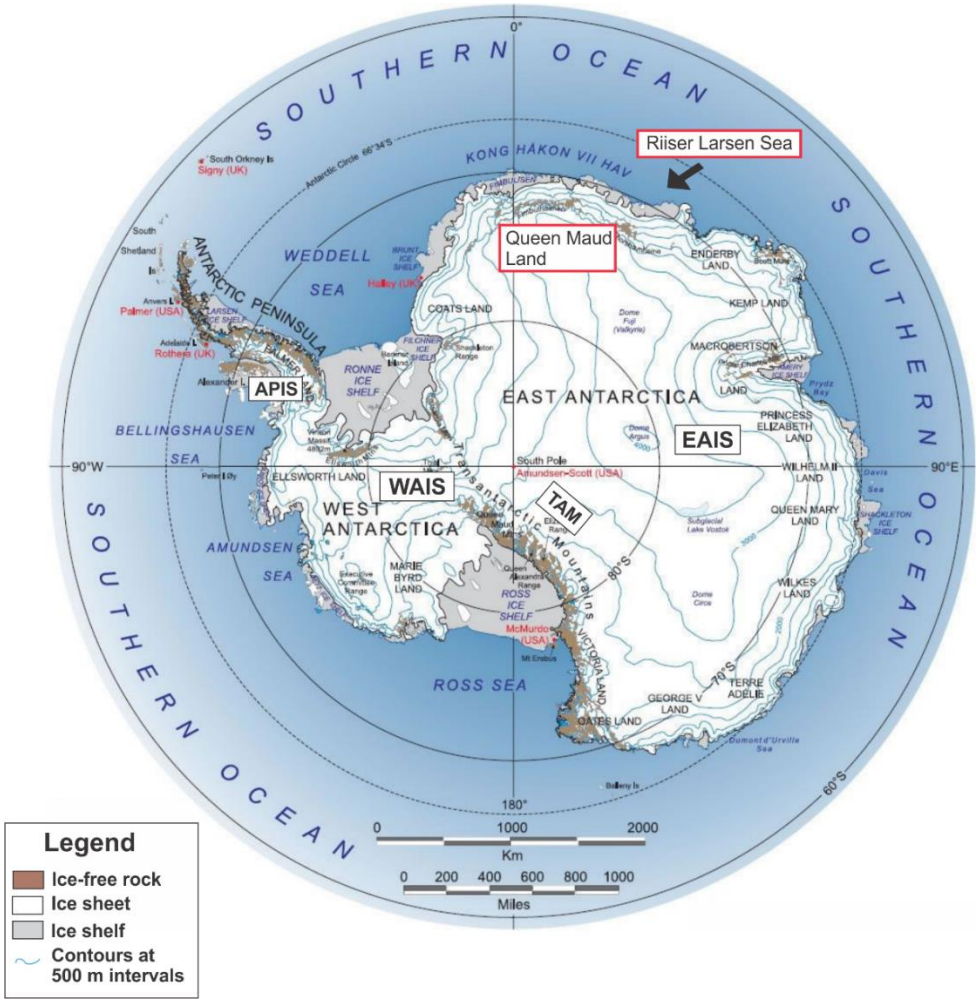

Fig. 1.1: Map of the Antarctic continent and the surrounding Southern Ocean, including the East Antarctic Ice Sheet, the West Antarctic Ice Sheet, the Antarctic Peninsula Ice Sheet and the Transantarctic Mountains (EAIS, WAIS, APIS and TAM) displayed by white rectangles. Queen Maud Land and Riiser Larsen Sea (RLS) are displayed by white rectangles highlighted with a red outline. RLS is the study area of this Master's thesis (modified after Geology.com (2018)).

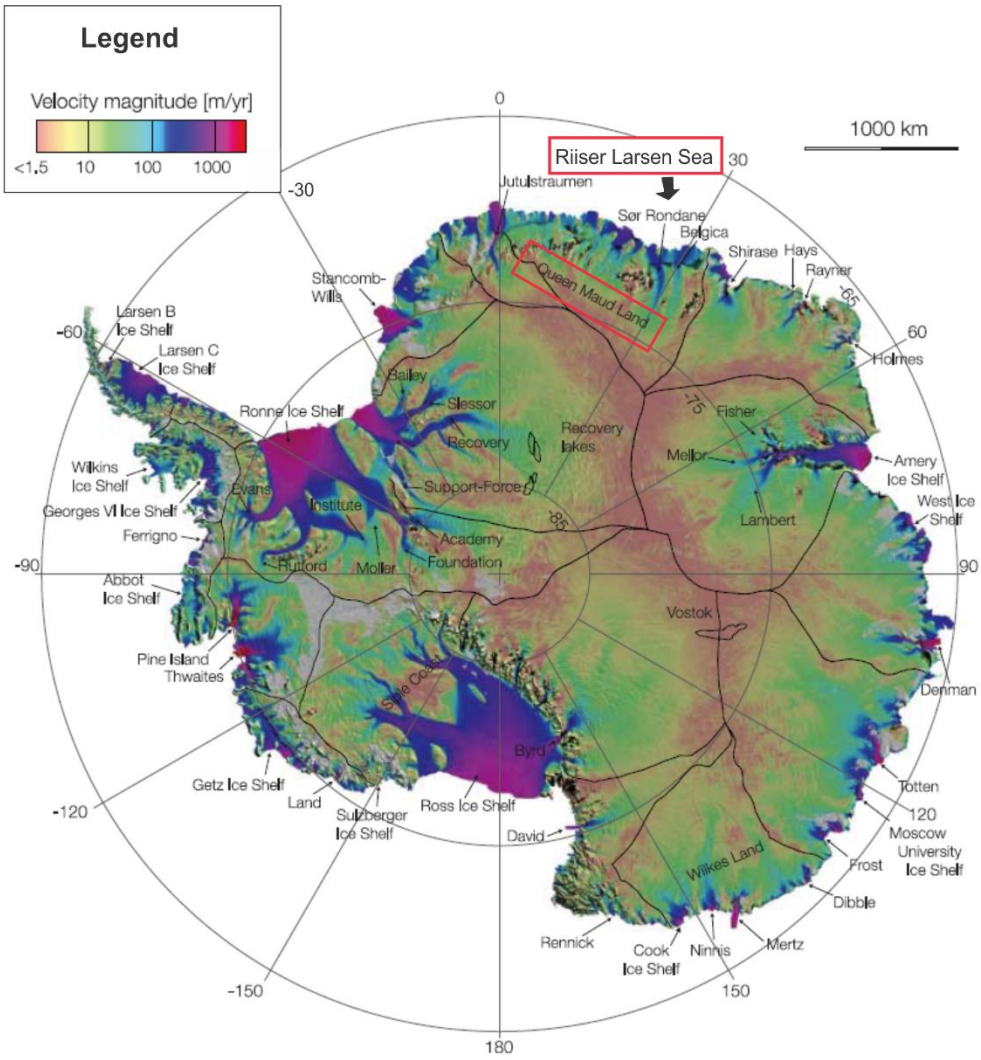

Fig. 1.2: Map of the Antarctic continent, including ice velocities colour-coded to the legend to the left. Thick black lines delineate major ice divides, while thin black lines outline subglacial lakes. Queen Maud Land and Riiser Larsen Sea are displayed by rectangles outlined in red (modified after Rignot (2011)).

A large portion of the latest research has focused on the behaviour and dynamics of the WAIS and the APIS. Both have lost a great amount of ice volume recently, much due to ongoing and past acceleration of outlet glaciers, transporting ice from the interior towards the ocean (Vaughan and Doake, 1996; Oppenheimer, 1998; Vaughan and Spouge, 2002; Scambos et al., 2003; Rignot, 2004; Cook et al., 2005). In contrast, EAIS seems to gain volume, due to an increase in accumulation of snow (Rignot, 2008; Shepherd et al., 2012)

All grounded ice of the WAIS rests on land well below sea level and lies on bedrock that deepens inland and is characterized as a marine-based ice sheet (Fig. 1.3) (Bamber et al., 2009; Fretwell et al., 2013a). At present, floating ice shelves and ice tongues extend over the oceans in West Antarctica and buttress the ice (DeConto and Pollard, 2016b). They impede the seaward flow of ice and stabilize the marine grounding-zones. Higher ocean temperatures can result in

basal melting and eventual thinning of ice shelves and ice tongues. This would reduce the buttressing effect, favouring a seaward movement of the ice and result in grounding-zone thinning. This could accelerate the flow of non-floating ice near the coast and expose the ice sheet interior to floating. Researchers are concerned about the vulnerability and the stability of the WAIS in the future (Joghuhin, 2011; DeConto and Pollard, 2016b). At present, the possibility of a collapse of the ice sheet remains unknown. Estimates suggest that a collapse of the WAIS could rise the global sea level by as much as c. 3.4 m (Bamber et al., 2009; Joghuhin, 2011; Fretwell et al., 2013a). For the APIS, the consequence of global warming is reported through the melting of the floating ice shelves. Temperatures have increased by 2-4°C during the last 50 years. For the last 30 years, ice shelves have retreated equal to an area of more than 13.500 km^2 (Scambos et al., 2004). Especially, the collapse of the Larsen B ice shelf, the Ross Ice Shelf and the Amundsen Sea embayment have been of great concern to scientists (Scambos et al., 2003; Rignot, 2004; Rignot, 2008; Pritchard et al., 2009).

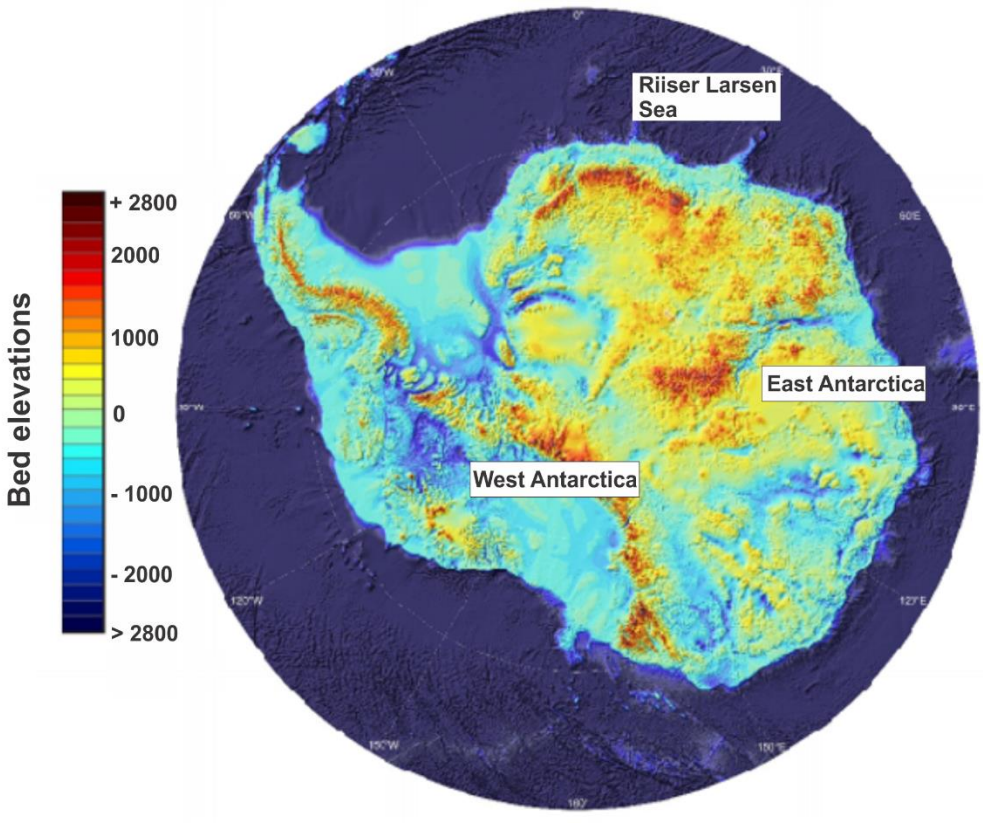

Fig. 1.3: Map of the Antarctic continent, including bed elevations based on Fretwell et al. (2013b). Bed elevations are colour-coded based on the scale to the left, ranging from blue (low elevations) to red (high elevations). West Antarctica, East Antarctica and Riiser Larsen Sea are displayed by white rectangles. Differences in bed elevations between East Antarctica and West Antarctica are clearly visible (modified after Fretwell et al. (2013b).

The EAIS as the largest ice sheet on earth, comprises 77% of the entire continent and spans the continental area between longitudes of c. 45°W and c. 168°E (Rignot, 2011; Mackintosh et al., 2014). Until recently, the EAIS has been assumed to be rather stable, because the ice rests on bed well above sea level and the ice sheet actually gains volume (Fig. 1.3) (Shepherd et al., 2012; Fretwell et al., 2013b). However, in recent years researches have concluded that also the EAIS is affected by thinning, posing a threat to global sea levels (Pritchard et al., 2009).

The Quaternary history of EAIS is important for several reasons, listed below:

1. Recent research has shown that the EAIS rests on bed below sea level and therefore making the ice vulnerable to erosion by ocean currents (Mackintosh et al., 2014).
2. Fast-flowing outlet glaciers (e.g. Phillipi Glacier and Totten Glacier) are currently loosing mass, while more slow-flowing outlet glaciers (e.g. in Enderby Land) are gaining mass (Pritchard et al., 2009; Shepherd et al., 2012).
3. Ice sheets are important parts within the climate system because they change in response to planetary albedo, ice elevation, and atmospheric circulation. Ice sheet are also important for oceanic circulation and temperature, as they affect formation of deep waters (Pollard and DeConto, 2009; Mackintosh et al., 2014).
4. Ice loss from the EAIS during the last interglacial likely contributed to the global sea level rise (Pingree et al., 2011), indicating the vulnerability of the EAIS in regards to climate change/warming.
5. EAIS with its $21.76 * 10^6$ unit of grounded ice, equivalent to c. 53 m of sea level rise can influence global sea level with just small changes in its ice volume (Lythe and Vaughan, 2001; Fretwell et al., 2013a).

Knowledge and understanding of the factors controlling the advance and the subsequent retreat of the AIS in the past might contribute to our comprehension of more recent ice sheet behaviour.

The contribution to sea level rise from Antarctica involves large uncertainties. Global warming may increase accumulation of snow on the continent's interior, while the glaciers in coastal regions may experience a retreat as a result of warmer air and higher ocean temperatures leading to a removal of the buttressing effect from ice shelves (Rignot, 2008). In order to predict and understand collapses or retreats of the ice on Antarctica we need further knowledge about the changing precipitation, atmospheric temperature, oceanographic conditions, and the changes in

glacier dynamics that prevail in the region (Pritchard et al., 2009). Paleoenvironmental reconstruction using proxies from the geologic record allows us to reconstruct past climates and is the main tool to figure out the climate to come.

1.3 Glacial history of Antarctica

The behaviour, extent, and dynamics of the AIS through glacial/interglacial cycles, and the timing and style of the retreat has been the focus of multiple discussions and debates through the last decades, resulting in numerous articles on the topic (Huybrechts, 1990; Bentley, 1999; Denton and Hughes, 2002; Scambos et al., 2004; Rignot et al., 2013).

Antarctica claims a long history of Cenozoic glaciation, which can be traced in the geological record (Anderson, 1999). After the break-up of Gondwana, Antarctica drifted southward resulting in a thermal isolation of the continent, favouring colder conditions (Lawver, 1992). Geological evidence strongly suggests that ice growth in Antarctica began in the earliest Oligocene (c. 34 Ma) or in the Eocene/Oligocene boundary, supported by enrichment in deep-water marine $\delta^{18}O$ values (Zachos et al., 1996; Coxall et al., 2005; Hay et al., 2005). The glacial build-up was asynchronous through the continent, favouring an earlier glaciation in the east (Zachos et al., 1996; Solli et al., 2007). The Drake Passage opened in Early Miocene (c. 24 Ma), separating South America and the Antarctic Peninsula, leading to the development off the circumpolar current and the formation of cold waters in the Southern Hemisphere preventing warm tropical sea currents from flowing south (Pfuhl and McCave, 2005). By the middle Miocene, the alpine glaciers had formed into continental ice sheets of near present day size. This suggests the ice sheet configuration has been more or less the same for the last c. 14 Ma years, however substantial fluctuation occurred during the Quaternary (Ingólfsson, 2004). Through time, the coastal margins surrounding Antarctica have been glaciated several times (Zachos et al., 1996; DeConto and Pollard, 2003; Coxall et al., 2005; Bohaty et al., 2012).

A recent study by Bentley et al. (2014) gathered all geological data available from the last glacial/interglacial cycle in order to make a combined reconstruction of the AIS (Fig. 1.4). The continent was divided into six sectors: East Antarctica (Mackintosh et al., 2014) , Ross Sea (Anderson et al., 2014), Amundsen-Bellingshausen Sea (Larter et al., 2014), Antarctic Peninsula (Cofaigh et al., 2014), Weddell Sea (Hillenbrand et al., 2014) and sub-Antarctic Islands (Hodgson et al., 2014).

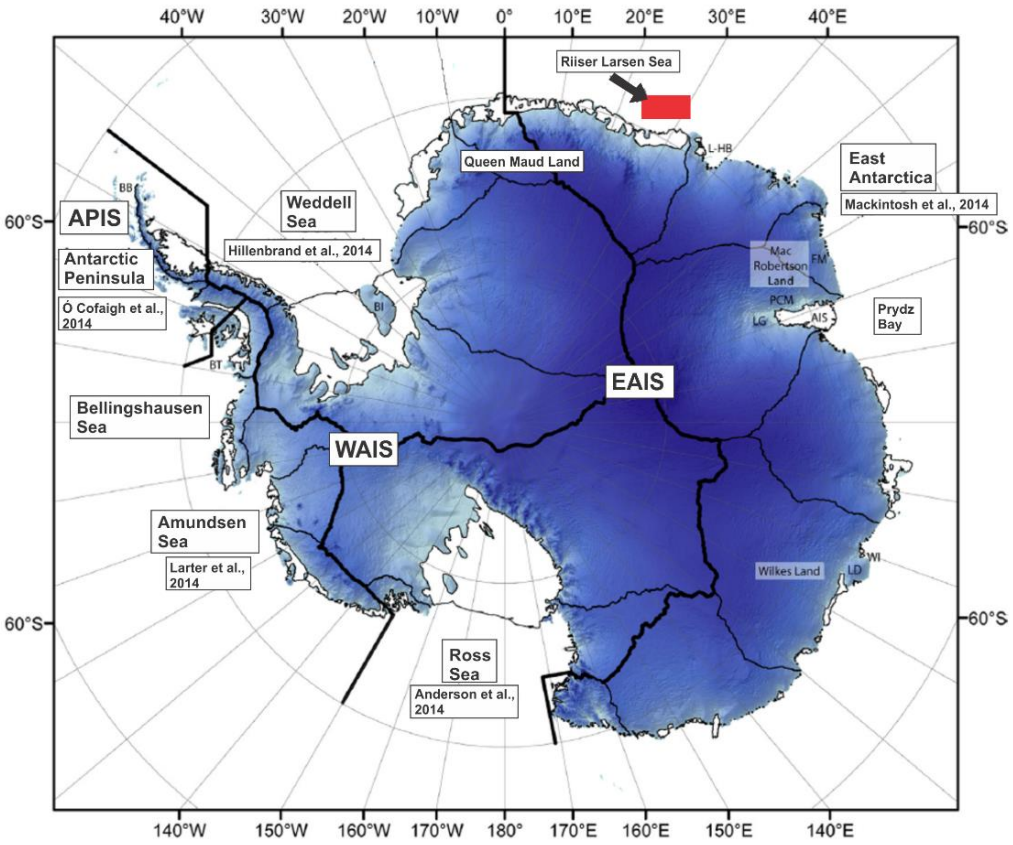

Fig. 1.4: Map of the Antarctic continent, including the EAIS, the WAIS and the APIS. Ice sheet elevation is marked with blue shading, while ice shelves are coloured in white. Names mentioned in the text are displayed by white rectangles and black lines shows their sector boundaries. Riiser Larsen Sea is displayed by a red rectangle (modified after Bentley et al. (2014)).

The global LGM (Last Glacial Maximum) (c. 26-21 ka BP) ice extent was more extensive compared to present levels (Davies, 2017). Reconstructions of the AIS extent during the LGM indicate it did not reach a synchronous maximum extent and the position of LGM varied widely in timing between different sectors of Antarctica (Bentley et al., 2014). By 20 ka BP the grounding line was near or at the continental shelf break around most of the Antarctic continent, except in the Weddell Sea, the Ross Sea and the Prydz Bay regions (Fig. 1.4). Some regions even experienced a maximum ice extent prior to 20 ka BP, and the retreat of the ice had already started by 20 ka BP. In the easternmost part of the APIS the retreat was underway by 18 ka BP (Fig. 1.4), while in Brainsfield Basin (located out of the northern tip of the Antarctic Peninsula) the initial retreat was at 17.5 ka BP. In contrast, only one location on the EAIS shows evidence of ice retreat on the continental shelf before 15 ka BP (Bentley et al., 2014), while the rest of the EAIS was close to its maximum at 15 ka BP (Bentley et al., 2014). In Amundsen Sea (Fig. 1.4) the grounding line had retreated over most of it shelf by 15 ka BP. Along eastern and western side of the APIS the substantial recession occurred between 15 – 10 ka BP. In Ross

Sea (Fig. 1.4) the retreat of the EAIS occurred mostly after 13 ka BP, however the retreat was more rapid during the Holocene epoch. By 10 ka BP the retreat of the WAIS from Weddell Sea and eastern Ross Sea was ongoing. The AIS grounding line was at the innermost shelf around the Antarctic continent by 5 ka BP. The extension of the AIS is still controversial at LGM, involving large uncertainties. More research on the Antarctic continent is needed in order to get a more thorough understanding of the extent and the subsequent retreat of the ice. In the following sub-chapters (*see Chapter 1.3.1 and 1.3.2*) Weddell Sea and East Antarctica are investigated in more detail.

1.3.1 Weddell Sea

The Weddell Sea (Fig. 1.5) sector receives glacial drainage from EAIS, WAIS, and APIS, and is therefore an ideal region to investigate the asynchronous behaviour of the AIS through the last glacial/interglacial cycle (Bentley and Anderson, 1998; Joughin et al., 2006; Hillenbrand et al., 2014). The Weddell Sea is also an important site for the formation of Antarctic Bottom Water, feeding the Southern Ocean with dense, cold water which spreads northwards into the deep-sea basins of the Pacific, Atlantic and Indian Oceans (Nicholls et al., 2009; Fukamachi et al., 2010; Hillenbrand et al., 2014). Reconstructions of AIS dynamics through the last glacial/interglacial cycle in the Weddell Sea sector includes multiple studies (Elverhøi, 1981; Bentley and Anderson, 1998; Hein et al., 2011; Le Brocq et al., 2011; Larter et al., 2012; Bentley et al., 2014). However, conflicting evidence from terrestrial studies (Fogwill et al., 2004; Hein et al., 2011), marine studies (Kuhn et al., 1993; Crawford et al., 1996; Larter et al., 2012) and ice core studies (members et al., 2004; Mulvaney et al., 2007) show different outcomes concerning a consensus of the ice extent and thickness since LGM in the Weddell Sea sector (Hillenbrand et al., 2014).

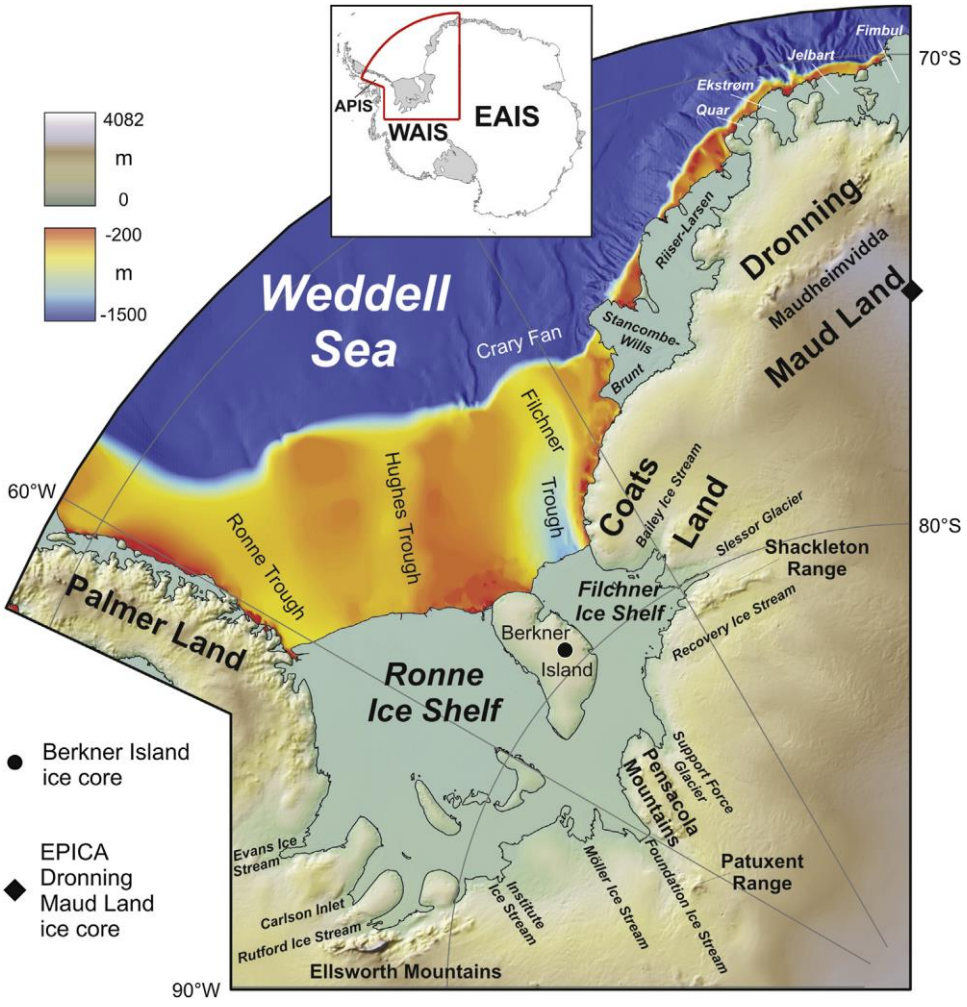

Fig. 1.5: Map of the Weddell Sea sector, including shelf bathymetry and ice-sheet surface elevations (given in meters above sea level) according to Bed Map 2 (Fretwell et al., 2013a). Ice shelves are displayed in grey-green shading. Inset map shows the Weddell Sea sector outlined by a red line, in context with the Antarctic continent, including sub-ice sheets and ice shelves displayed in grey shading (EAIS, WAIS and APIS) (adapted from Hillenbrand et al. (2014)).

Due to the scarcity of data available in the Weddell Sea region, reconstructions of the LGM ice-sheet configuration shows different extents. Some studies argue for a thick ice-sheet covering the entire continental shelf (Bassett et al., 2007; Pollard and DeConto, 2009; Golledge et al., 2012), while others suggest a thinner ice-sheet extension covering only shallower parts of the shelf (Bentley et al., 2010; Whitehouse et al., 2012; Hillenbrand et al., 2014).

Hillenbrand et al. (2014) proposes two alternative scenarios (A and B) of the LGM ice-sheet extent and the following retreat in the Weddell Sea sector, based upon the marine and terrestrial data available at present. Scenario A implies a more restricted advance during LGM compared to scenario B, which proposes a more extensive advance (Fig. 1.6 and Fig. 1.7).

Scenario A

Scenario A (Fig. 1.6) uses terrestrial models to assume ice extent under LGM according to Bentley et al. (2010), Le Brocq et al. (2011) and Whitehouse et al. (2012). Following this scenario, all dates (even the oldest) from marine sediments cores are minimum ages from grounded ice retreat from the continental shelf. Grounding events recorded in sediments and subglacial bedforms were mostly pre-LGM. In this model the advance of the grounded ice-sheet during LGM was restricted to the shelf offshore Ronne Ice Shelf and the grounding line was close to the present day-position or only slightly beyond it (Hillenbrand et al., 2014).

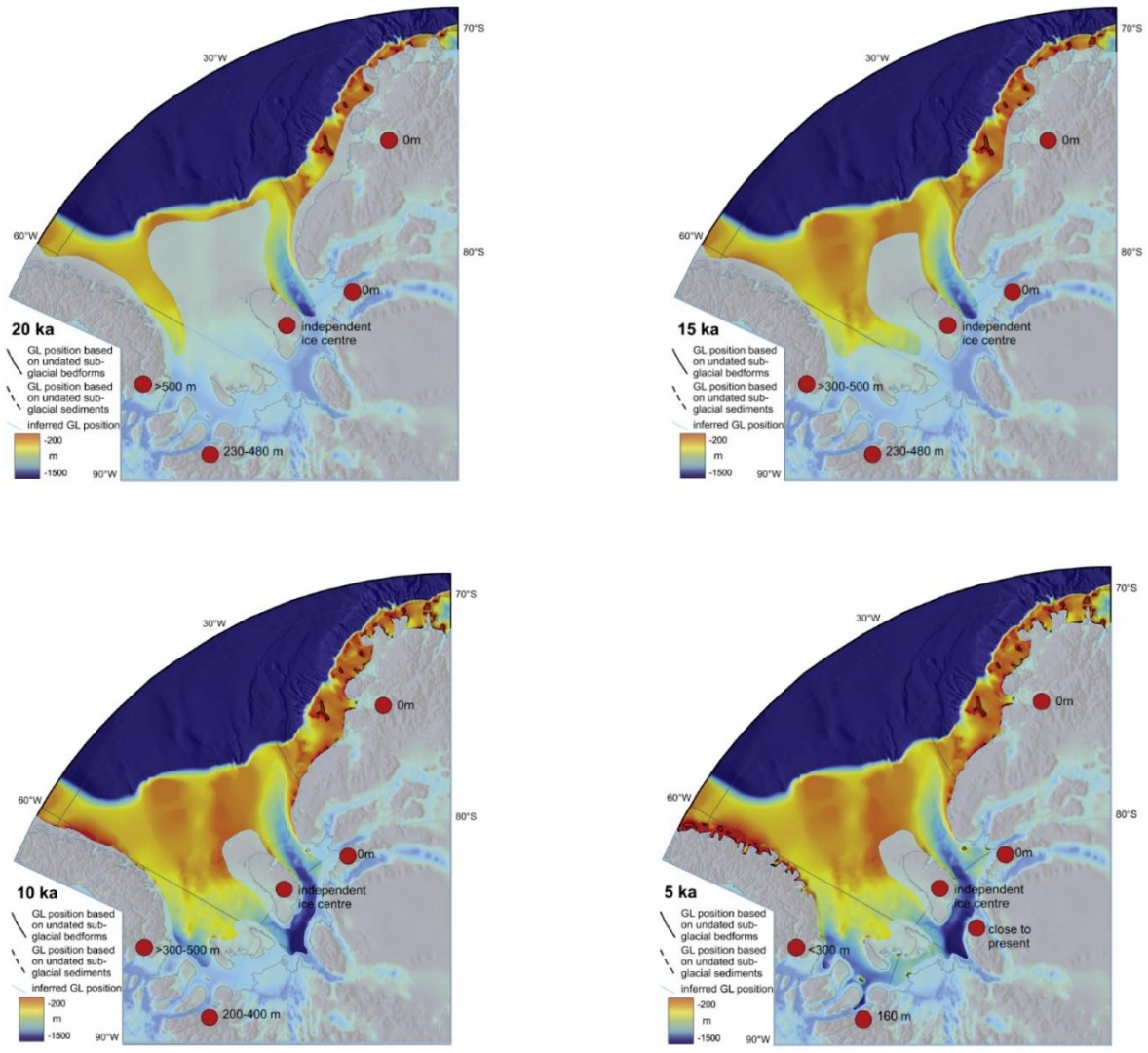

Fig. 1.6: Map showing grounded ice-sheet extent in the Weddell Sea sector according to Scenario A by Hillenbrand et al. (2014), in time intervals of 20 ka BP, 15 ka BP, 10 ka BP and 5 ka BP. Red circles indicates different core locations and the associated ice sheet elevation. Scale displaying depth in meters (from blue to orange shading) (GL: grounding line) (modified after Hillenbrand et al. (2014)).

20 ka BP (Fig. 1.6): The ice-sheet reached its maximum extent at/or close to in the Ellsworth Mountains and maximum extent in the SE Antarctic Peninsula, while the ice-sheet in the Shackleton Range was at present day level or thinner (Fig. 1.5). Berkner Island (Fig. 1.5 and Fig. 1.6) operated as an independent ice dispersal centre, meaning the inland ice did not overrun the island (Hillenbrand et al., 2014).

15 ka BP (Fig. 1.6): In Ellsworth Mountains the lower trimline was abandoned by the thinning ice-sheet, continuing into the Holocene. Ice in the Shackleton Range was close to present day levels or thinner. Whitehouse et al. (2012) propose a landward retreat of the ice along troughs and away from the continental shelf north of Berkner Island.

10 ka BP (Fig. 1.6): The grounding line was at the inner shelf in almost all regions, except north of the Berkner Island. Ice elevations in Shackleton Range were similar to the present day levels, or even lower.

5 ka BP (Fig. 1.6): The grounding line was at or close to present day grounding line. Ice elevation in the Ellsworth Mountains was more than 160 m above present day levels. On the SE Antarctic Peninsula, the ice was c. 300 m thicker compared to present day level and the ice elevations in the Shackleton Range were at present day level or thinner. According to isotopic data from EDML, ice-sheet thinning in Central Queen Maud Land began at c. 5 ka BP.

Scenario B

Scenario B (Fig. 1.7) is based of the interpretation on marine sediment cores. The ages in Scenario B include a mixture of minimum and maximum ages for the previous ice-sheet retreat and the interpretation that the most extended of the apparent hiatuses observed in the Weddell Sea sector were the result of an advancing ice-sheet moving over the core sites. The dates constraining the termination of the hiatus from c. 31.0 and c. 21.5 cal ka BP seen north of the Riiser-Larsen and Filchner-Ronne ice shelves are ages near the previous grounding-line retreat (Hillenbrand et al., 2014). During LGM, grounded ice did extend to the shelf break north of Filchner-Ronne Ice Shelf according to this scenario. To keep consistency with the terrestrial data, this scenario requires only very thin, low profile for the ice on the continental shelf (Bentley et al., 2010).

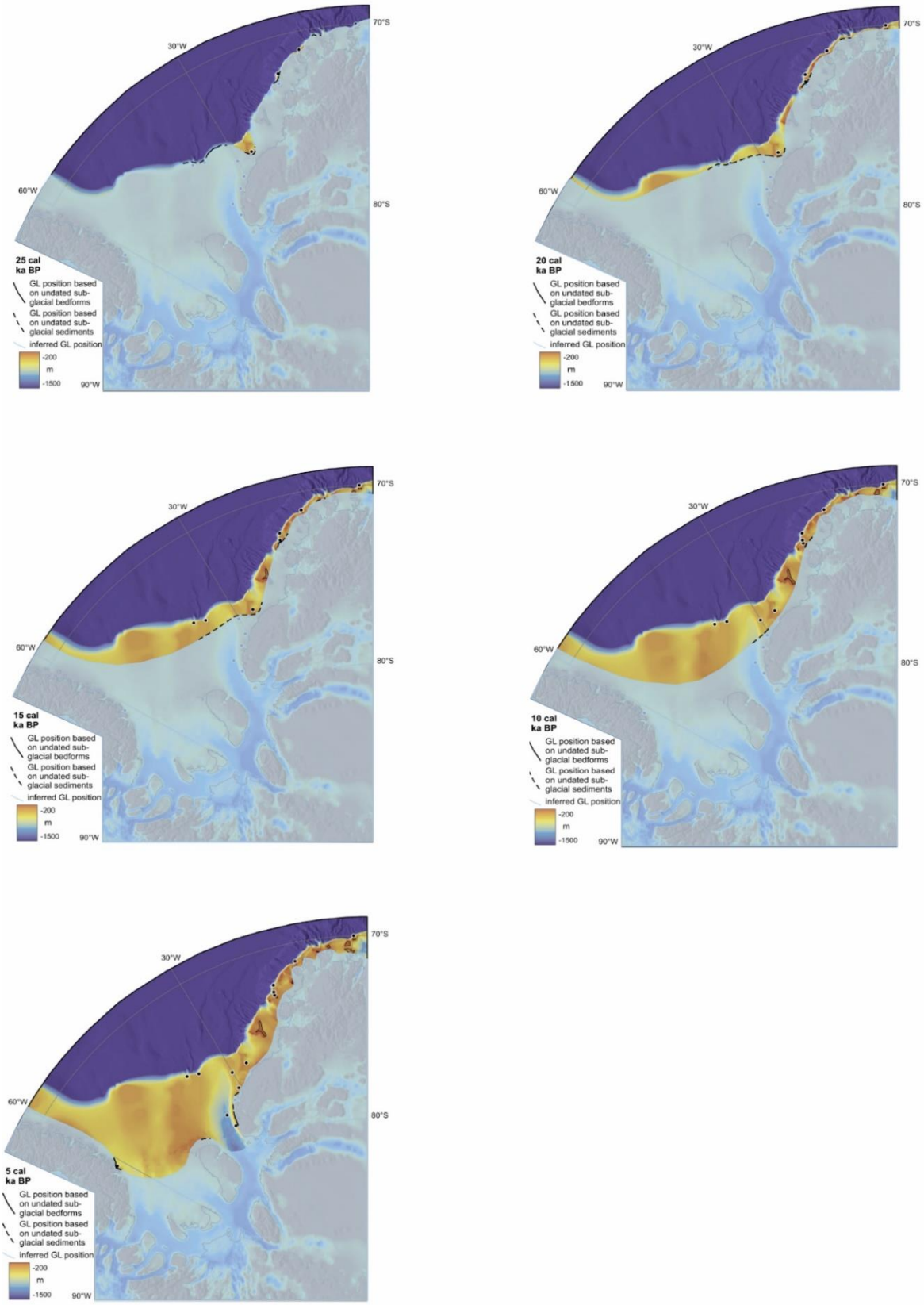

Fig. 1.7: Grounded ice-sheet extent in the Weddell Sea sector in time intervals of 25 cal ka BP, 20 cal ka BP, 15 cal ka BP, 10 cal ka BP and 5 cal ka BP, according to scenario B by Hillenbrand et al. (2014). Scale displaying depth in meters (from blue to orange shading) (modified after Hillenbrand et al. (2014)).

25 cal ka BP (Fig. 1.7): The grounded ice had retreated from the shelf offshore the Brunt Ice Shelf and the Quar Ice Shelf (Fig. 1.5), while the grounding line at the rest of the Weddell Sea sector was at the shelf break or further out. A moraine belt seen north of the Riiser-Larsen Ice Shelf (Fig. 1.5) may mark the outer position of the grounding-line at this time interval.

20 cal ka BP (Fig. 1.7): Based on data from different sites, the grounding line had started to retreat from the shelf break in most parts of the Weddell Sea.

15 cal ka BP (Fig. 1.7): Both the WAIS and EAIS had retreated from their outer shelf locations north of the Filchner-Ronne Ice Shelf by this time. Larter et al. (2012) suggests a stop in the ice-sheet retreat followed by a minor re-advance in this time interval.

10 cal ka BP (Fig. 1.7): The eastern outer shelf of Filchner Trough and the inner shelf north of Riiser Larsen Ice Shelf were ice free. While, the ice retreat continued in the rest of the Weddell Sea.

5 cal ka BP (Fig. 1.7): Only areas close to Coats Land coast were still covered with grounded ice at this time. The grounding line position in the western part of the Weddell Sea sector may have been close to present day calving lines of the Filchner-Ronne Ice Shelf.

The maximum extent and retreat dynamics of the grounded ice in Weddell Sea Sector remain still uncertain (Hillenbrand et al., 2014).

1.3.2 East Antarctica

Since the EAIS is the largest continental ice mass on Earth, mapping and understanding of the ice-sheet evolution since LGM (data spanning back c. 30 000 years) is necessary to understand and model present-day and future ice sheet behaviour (Mackintosh et al., 2014). In comparison to WAIS, the LGM glacial history of EAIS is even more fragmentary and the documentation concerning the LGM expansion and subsequent contraction is still poorly documented (Ingólfsson et al., 1998; Bentley, 1999). Most of the continental margin around East Antarctica has not been investigated yet (Anderson et al., 2002; Livingstone et al., 2012), but there are areas of the margin for which there exist geological data (Fig. 1.8).

For the continental margin, three areas are highly studied in East Antarctica. These are (1) Mac. Robertson Land Shelf, (2) Prydz Bay and (3) the George V Land – Terre Adelie Coast Shelf (Fig. 1.8) (Mackintosh et al., 2014).

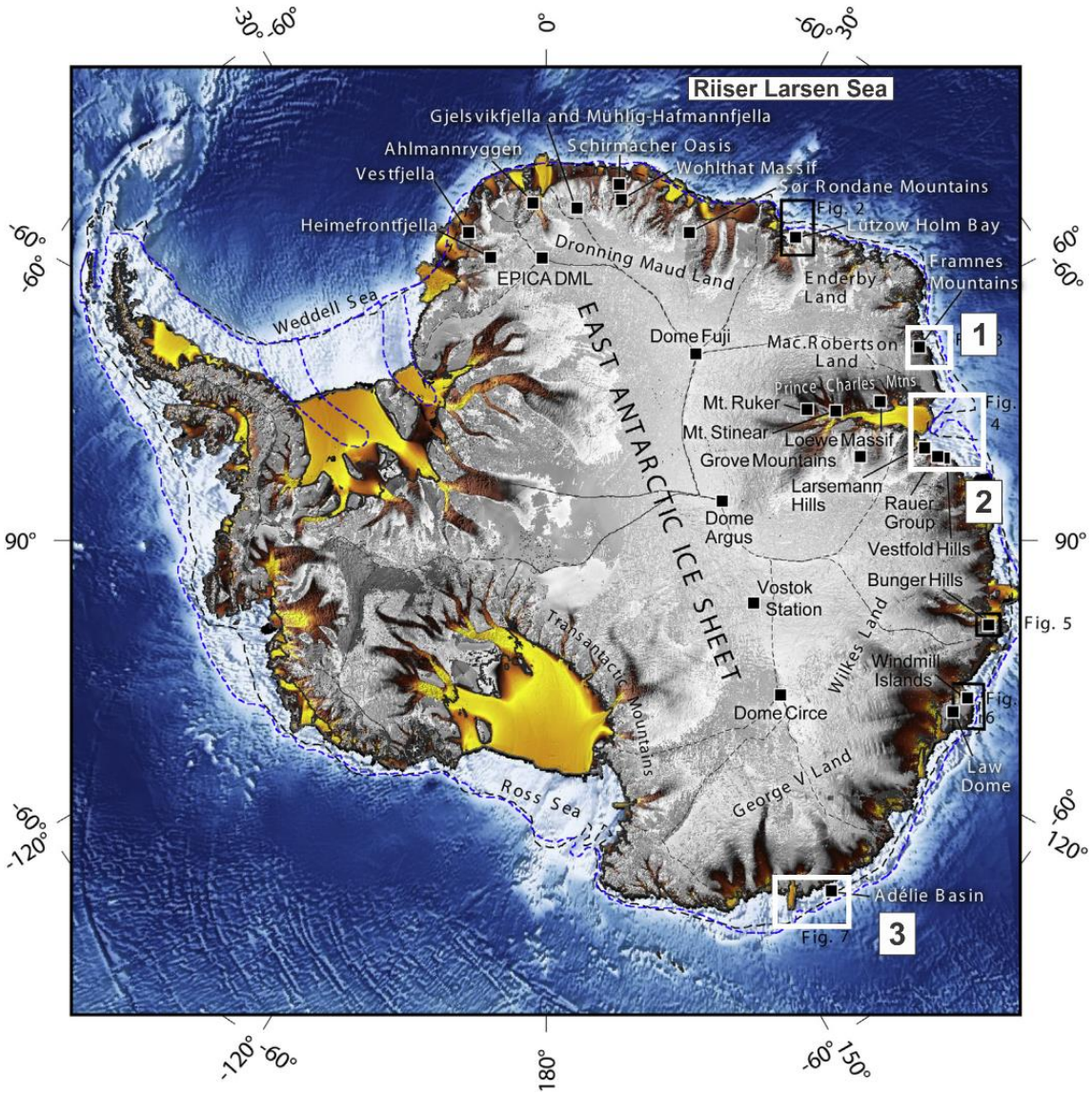

Fig. 1.8: Map of the Antarctic continent displaying areas mentioned in the text, namely (1) Mac. Robertson Land Shelf, (2) Prydz Bay and (3) the George V Land – Terre Adelie Coast Shelf. Ice sheets are displayed in grey shading, including ice divides marked with grey lines. Fast moving ice streams and ice shelves are displayed in orange and yellow. Continental shelves are displayed in white shading and the more distal and deeper ocean is displayed in blue. LGM grounding zones position are taken from Anderson et al. (2002) (black lines) and Livingstone et al. (2012) (blue line) (modified after Mackintosh et al. (2014)).

Ice extent of the EAIS during the LGM (Fig. 1.9a)

Anderson et al. (2002) argue that the EAIS did not expand to the continental shelf edge during the LGM, but rather reached a maximum mid-shelf position in many locations, while Mackintosh et al. (2014) argue that the ice probably advanced close to the continental shelf margin at many locations during the LGM (Mackintosh et al., 2014). Evidence that support Mackintosh et al. (2014) interpretation is seen in Mac. Robertson Land (Fig. 1.8), where the outermost grounding zone wedge lies only c. 10 km from the shelf break and more than 90 km north of present-day ice margin. In addition, in this region, LGM ice was grounded in troughs

on the inner shelf, more than 1 km deep. In Prydz Bay (located outside Larsemann Hills in Fig. 1.8), the expanding EAIS reached the shelf edge on the Four Ladies Bank. Meanwhile, the Lambert/Amery system (located in the bay below Prince Charles Mountains in Fig. 1.8) showed a more restricted advance. In George V Land/ Terre Adelie Coast (Fig. 1.8) the expanding ice sheet occupied the inner to mid shelf during LGM. Geomorphological evidence hints towards past ice-sheet advance to the shelf edge. However, chronological constraints are currently lacking from the outer shelf in order to identify the extent of the ice-sheet. In many regions geological data are lacking, especially for Queen Maud Land, Enderby Land and much of Wilkes Land. Consequently, information about the LGM maximum extents or reconstructions of the LGM maximum extents are missing in these regions (Mackintosh et al., 2014).

Geological evidence preserved in coastal oases and nunatak regions suggest thickening and expansion of EAIS at LGM (e.g. Lutzow-Holm Bay, Framnes Mountains, the Windmill Islands and Prince Charles Mountains) (Mackintosh et al., 2014). Evidence from the Framnes Mountains near the present coast, indicate a thickening of c. 400 m compared to present day (Fig. 1.8). Meanwhile, several inland nunataks located in East Antarctica (e.g. Sør Rondane Mountains, Wohlthat Massif and Grove Mountains) show no or limited evidence of LGM ice-sheet thickening. Moreover, the ice surface elevation may have decreased in some of these locations at this time, this is supported by ice core evidence and numerical models (Mackintosh et al., 2014).

To summarize, evidence concerning the LGM extent and thickening in East Antarctica is poor, and on most of the continental margins evidence is lacking or absent. In an overall perspective, the ice was thinner at its centre, thicker towards the ice margin, and expanding towards the continental shelf during the LGM.

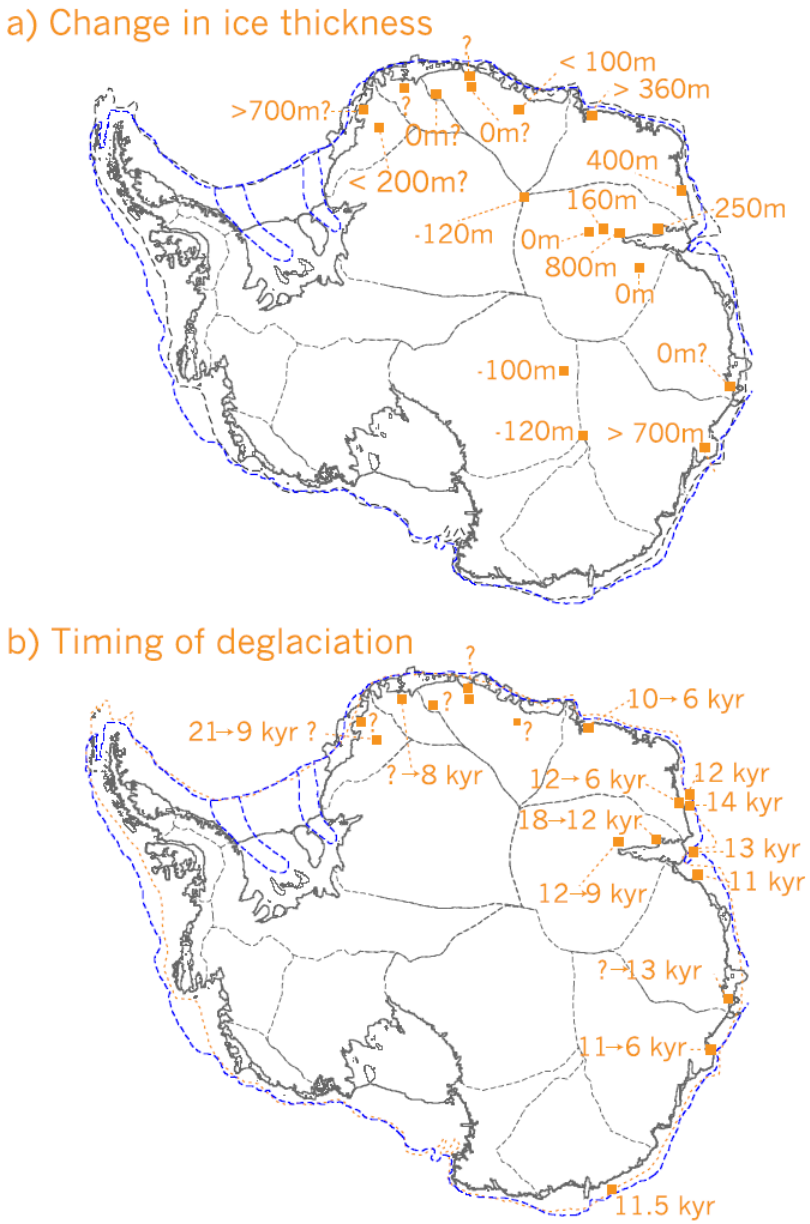

*Fig. 1.9: Map of Antarctica, including **a)** change in ice thickness at LGM compared to present and **b)** timing of deglaciation, rounded to the nearest thousand years (adapted from Mackintosh et al. (2014)).*

Timing of maximum ice extent and subsequent retreat (Fig. 1.9b)

Ages concerning the timing and retreat of the ice extent and subsequent retreat is obtained from these methods: (1) marine ^{14}C ages from sedimentary deposits on the continental shelf, (2) Terrestrial Cosmogenic Nuclide dating of glacial erratic's in ice-free oases and (3) ^{14}C and luminescence dates from terrestrial deposits (Mackintosh et al., 2014). It is not yet possible to time-slice reconstruct the EAIS deglaciation history with the same precision as it is done for WAIS (*see Chapter 1.3.1*). The first sign of early retreat of the EAIS is seen in the Prince

Charles Mountains (Fig. 1.8), which indicates a retreat in the Lambert/Amery system by c. 18 ka BP (White et al., 2011). Golledge et al. (2012) suggest high sensitivity resulting from an abrupt post-glacial sea-level rise as the responsible factor for the retreat in the Lambert/Amery system. Together with Adelie Basin (Fig. 1.8), ice-sheet retreat was almost complete in these regions by c. 12 ka BP. At Nielsen Basin in Mac. Robertson Land (Fig. 1.8), deglaciation began by c. 14 ka BP, while in other regions (e.g. Svenner Channel, Windwell Islands, Lutzow-Holm Bay, Iceberg Alley and Framnes Mountains) deglaciation began at c. 12 ka BP and continued into the Holocene.

With the data currently available, the EAIS respond to the LGM and transition to the Holocene as follows:

- The onset of ice-sheet retreat began as early as c. 18 ka BP in the Lambert/Amery system.
- Other regions did not retreat before c. 14 ka BP (coinciding with melt water plume 1a) (Mackintosh et al., 2011).
- The majority of EAIS started to retreat at c. 12 ka BP (onset of Holocene).
- By the middle Holocene present-day ice extent was reached (Mackintosh et al., 2014).

2 Study area

2.1 Physiographic settings

Antarctica is the Earth's southernmost continent. It is located asymmetrically around the geographic South Pole in the Southern Hemisphere (SH), covering an area of c. 14 million km^2 including a coastline of c. 17.968 km. The Southern Ocean (south of 60° S) encircles the entire continent, connecting the Pacific, the Indian and the Atlantic Oceans (Anderson, 1999). Antarctica is an ice-dominated continent which can be divided into three major areas: East Antarctica, West Antarctica and the Antarctic Peninsula (Anderson, 1999).

Queen Maud Land is a part of the EAIS and located within the territories claimed by Norway (Fig. 2.1). It is located as a triangle between the British Antarctic Territory to the west and the Australian Antarctic Territory to the east. The main offshore areas of Queen Maud Land are the easternmost part of the Weddell Sea, the Lazarev Sea and the Riiser Larsen Sea (RLS) offshore Princess Ragnhild Coast (Solli et al., 2007; Leitchenkov et al., 2008).

Matsuoka et al. (2015) argue for smaller fluctuations in the ice-sheet margin of Queen Maud Land (20°W – 45°E) through glacial/interglacial cycles compared to most other regions in Antarctica. The close location of the ice-sheet to the continental shelf break is proposed as one explaining factor. Currently, Queen Maud Land consist of 1500 km of ice-shelves, which are fed by outlet glaciers and punctuated by ice rises (Matsuoka et al., 2015). Characteristic of these ice shelves are the short distance from the grounding line to the calving front, which is normally less than 100 km (close to or beyond the continental shelf break) (Fig. 1.1) (Arndt et al., 2013; Mackintosh et al., 2014; Matsuoka et al., 2015).

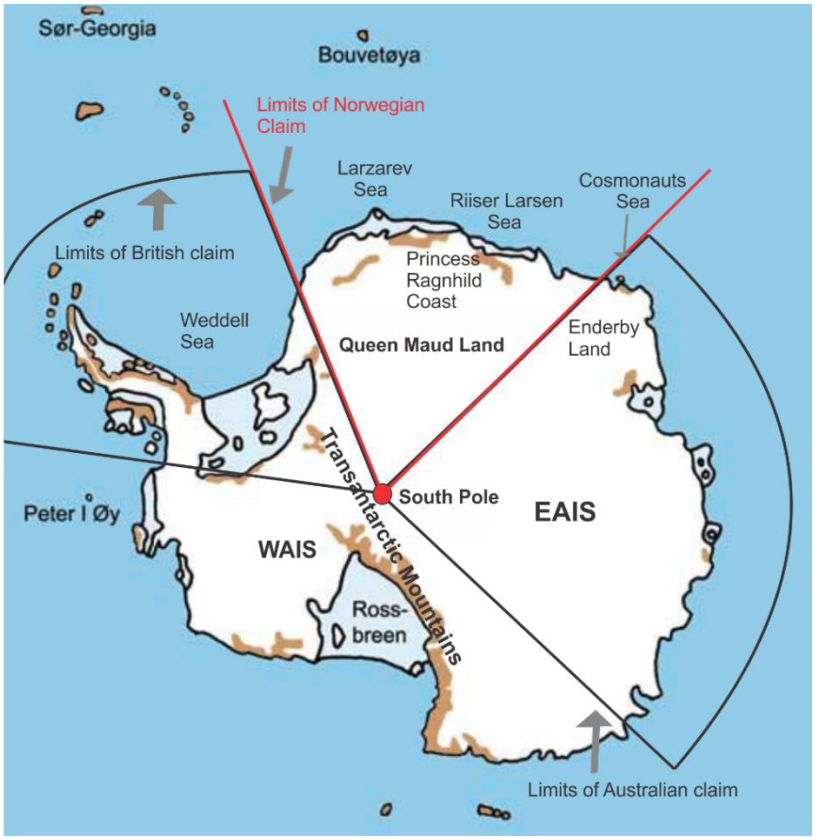

Fig. 2.1: Map of Antarctica, including Queen Maud Land, Princess Raghild Coast, Riiser Larsen Sea, Cosmonauts Sea, Lazarev Sea and Weddell Sea mentioned in the text. Limits of Australian and British claim are displayed with black lines, whereas limits of Norwegian claim is displayed by red lines (modified after Facebook (2018)).

2.1.1 Riiser Larsen Sea (RLS)

2.1.1.1 Geological development

The RLS is located off the East Antarctic coastline facing the Indian Ocean and is one of three main marine basins offshore Queen Maud Land and Enderby Land (Fig. 2.1). The passive continental margin was formed after the breakup of Gondwana (late Jurassic to early Cretaceous), resulting in the formation of the conjugate spreading compartments RLS and the

Mozambique Basin (Fig. 2.2) (Marks and Tikku, 2001). The RLS is suggested to be the oldest of the basins, formed around 155 Ma ago (Solli et al., 2007). The RLS consists of two prominent basement ridges namely the Gunnerus Ridge to the east and the Astrid Ridge to the west (Fig. 2.3). The Gunnerus Ridge is believed to be a former fragment of the continental crust (Kuvaas et al., 2004).

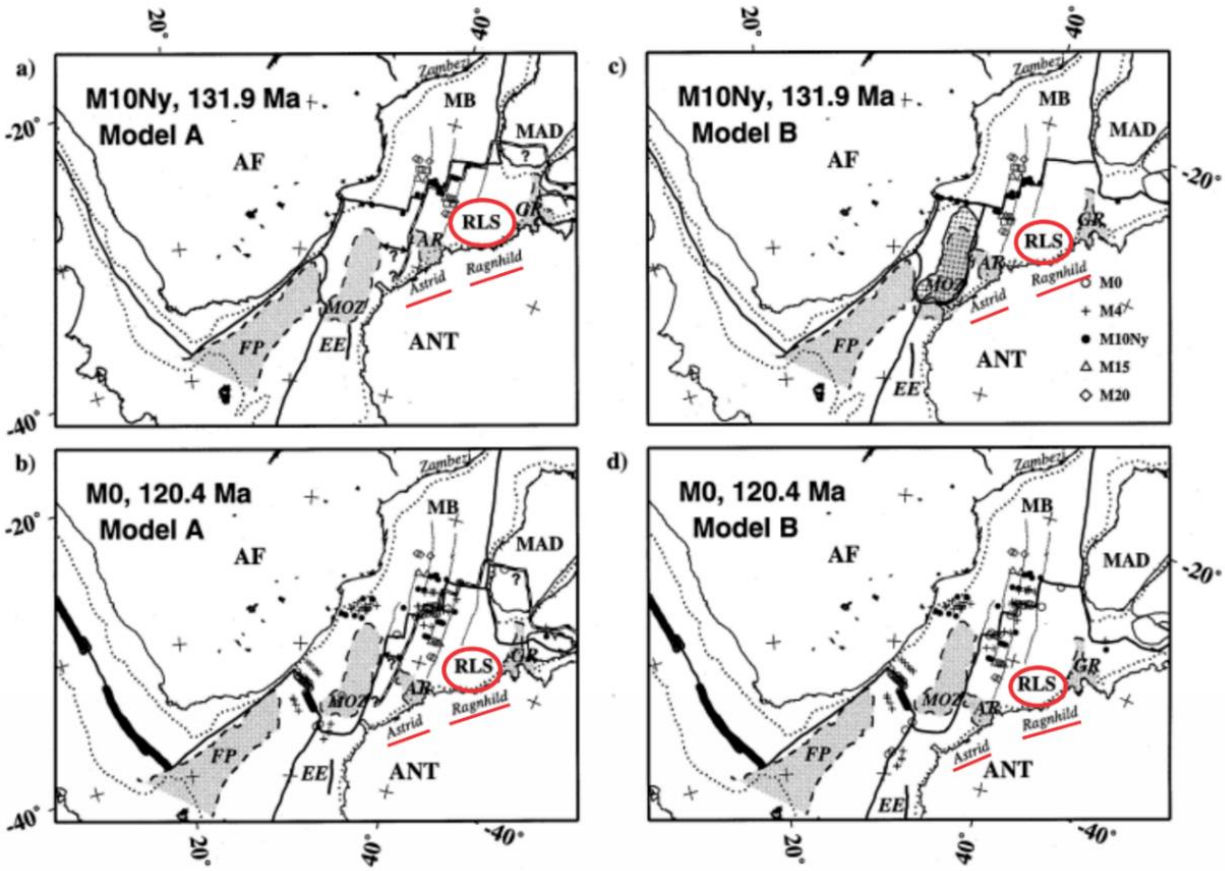

Fig. 2.2: Map showing the paleo-geographic situation of the RLS at 120.4 ka BP, including the position of Princess Astrid and Ragnhild Coast. Model A (a and b) have large fracture zone offset, whereas Model B (c and d) aligns fracture zones and magnetic anomalies. Heavy black lines are isochrones. RLS and Princess Astrid and Ragnhild Coast are outlined in red (ANT – Antarctica, MB - Mozambique basin, AF – Africa and MAD – Madagascar) (modified after Marks and Tikku (2001)).

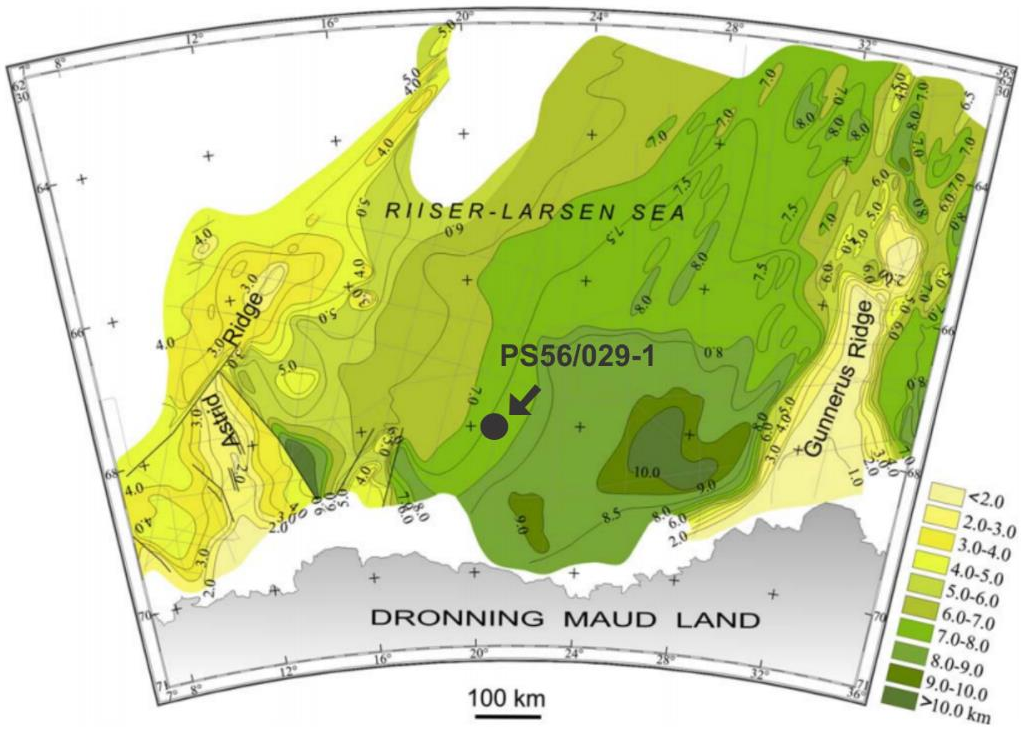

Fig. 2.3: Measured sediment thicknesses in the RLS, including sediment thickness scale on the right. Core location of PS56/029-1 is displayed with a ellipsoid (modified after Leitchenkov et al. (2008)).

2.1.1.2 Physiographic setting

The RLS is bordered by the Cosmonauts Sea to the east and by the Lazarev Sea to the west (between 14 °E and 30 °E) (Fig. 2.1). Located south of RLS is the Princess Ragnhild Coast and the Princess Astrid Coast of Queen Maud Land. The bathymetry of the RLS includes water depths exceeding 3000 meters and a relatively flat seafloor. The Gunnerus Ridge is located at shallow depths (500-1500 m), being 200-2500 m shallower than the adjacent RLS continental rise (Kuvaas et al., 2004). The shelf-ice edge in the RLS is located over 1000 m of water depth and the continental shelf is short or virtually absent (Thiede and Oerter, 2002). The continental slope in the RLS is steep and reaches down to 5000 m water depth where the seafloor of the RLS connects to the Enderby Abyssal Plain. The measured sediment thicknesses in the RLS indicate two areas of higher sediment thicknesses, namely one deposition centre on the western side of the Gunnerus Ridge and a smaller deposition centre located on the eastern side of the Astrid Ridge (Fig 2.3) (Leitchenkov et al., 2008).

Few studies focus on the RLS area (e.g. Kuvaas et al. (2004), Solli et al. (2007), Aoki (2003), Matsuoka et al. (2015) and Leitchenkov et al. (2008)). Thus, the area is regarded as a nearly unexplored sector of Antarctica and information about the region is sparse.

The RLS is believed to be one of the first areas to be affected by the expanding ice sheet as it grew on Antarctica (DeConto and Pollard, 2003). Therefore, the region should be ideal to investigate the EAIS history (DeConto and Pollard, 2003; Solli et al., 2007). Large channel-levee complexes located within RLS demonstrate the interaction between glacial and interglacial deposits, and the RLS should therefore be an ideal location to study climate-controlled processes, e.g. deep-water production and ice-sheet dynamics (Kuvaas et al., 2004).

2.1.1.3 Seismic stratigraphy

Available data from the eastern RLS area shows different seismic facies interpreted as products of downslope and alongslope processes (Kuvaas et al., 2004) (Fig. 2.4). Sedimentation in RLS occur both in glacial and interglacial periods, but the turbiditic activity is higher towards glacial maxima (Kuvaas et al., 2004).

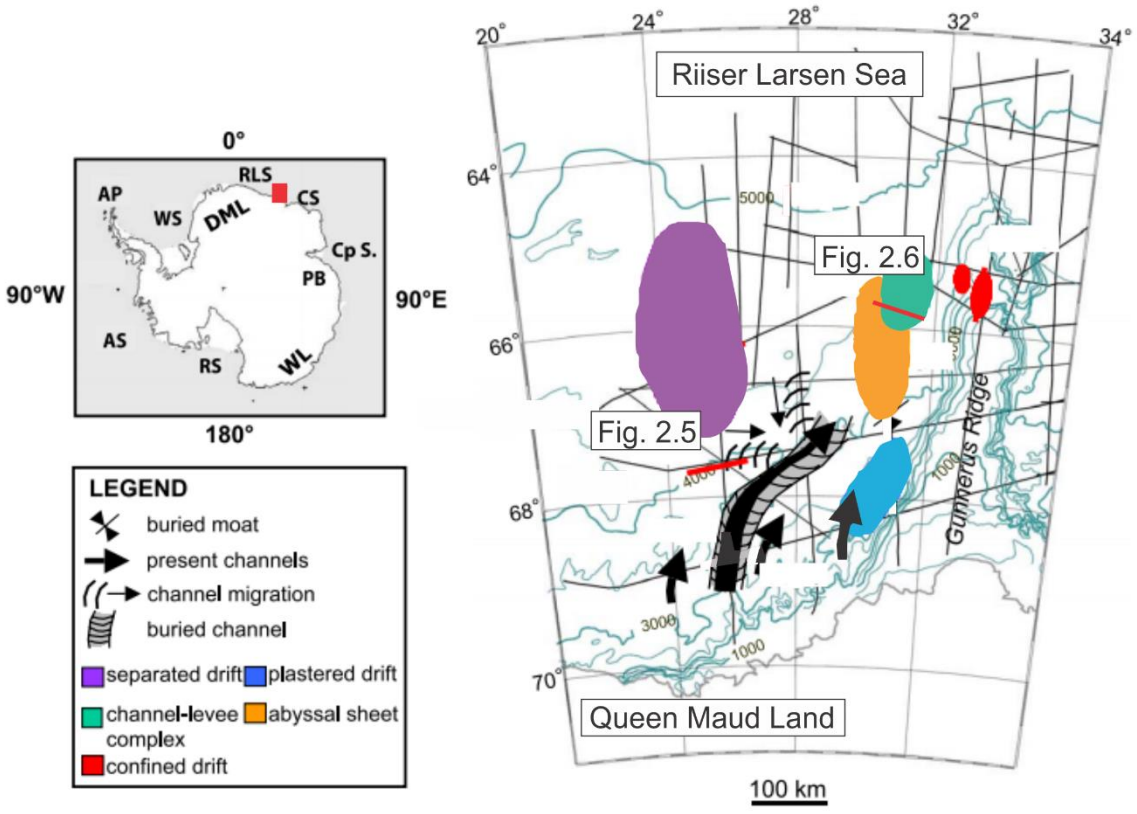

Fig. 2.4: Bathymetric map of the RLS showing main sedimentary units displayed with colours, seismic profiles obtained in the area are displayed with grey straight lines and red lines show the seismic profile used in Fig. 2.5 and Fig. 2.6. The overview map to the left shows the Antarctic continent, where the RLS is displayed with a red rectangle (modified from Kuvaas et al., 2004).

Seismic facies in the RLS include well-stratified facies, chaotic, transparent, and wavy facies (see below for detailed description). A regional unconformity (RLS-4) shows the boundary

from pre-glacial to glacial deposits. Sediments above the unconformity result from a higher energy environment and enhanced terrigenous supply from the continent due to glacial activity, in contrast to pre-glacial deposits below (Kuvaas et al., 2004; Solli et al., 2007). Seismic facies identified by Kuvaas et al. (2004) are listed below (Fig. 2.4):

- **Well-stratified facies** (Fig. 2.5): These facies are the most common facies in the area and are observed in several units only differing in geometry and extent. The units of well-stratified facies are named extensive tabular units, units associated with scour-and-fill features and mounded units unrelated to scour-and-fill features. Extensive tabular units are interpreted as (1) distal sheet-like turbidites alternating with hemipelagic deposits or (2) as sediment sheets emplaced by contour currents. It is not possible to distinguish between these two interpretations. Units associated with scour and fill features suggest that they are a part of a larger channel-levee complex. The mounded units unrelated to scour and fill features are interpreted as (1) a combination of turbidites and contourites or (2) only as contourites.
- **Chaotic and transparent facies** (Fig. 2.5): These facies are often seen together in the seismic profiles, located on the lower slope and continental rise. The chaotic facies are interpreted to represent the uppermost part of debris-flow deposits, while the transparent facies are linked to debris-flow deposits in general. They both represent deposits from the initial phase of the channel activity, as a product of slumps originating higher up on the slope.
- **Wavy facies** (Fig. 2.5): Interpretation of these facies is associated to the present day seafloor, and is only represented on the continental rise. Similar sediment waves are known to originate from both contour currents and turbidity currents.

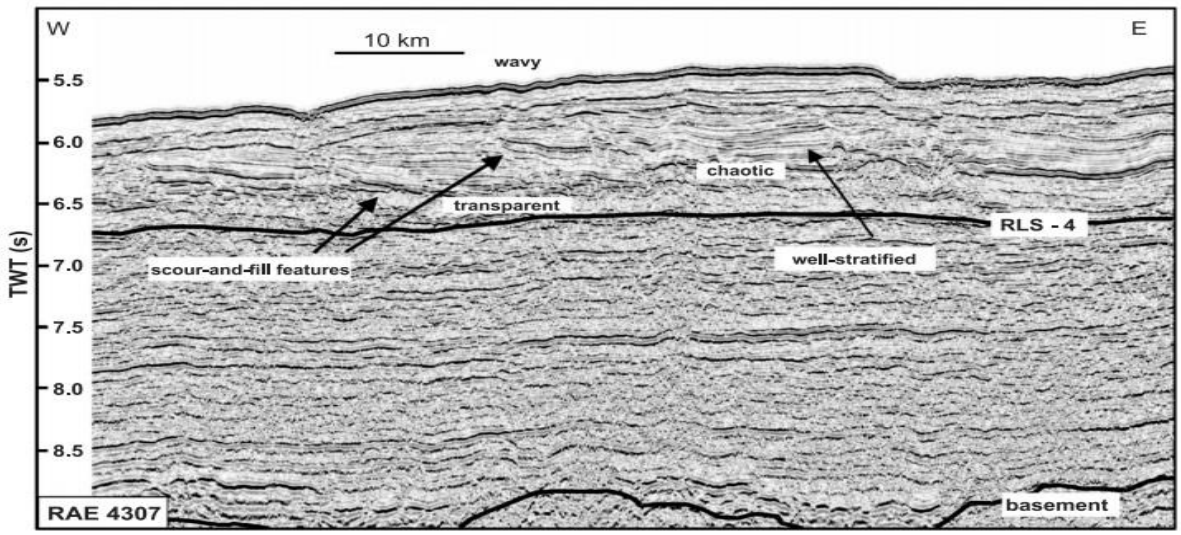

Fig. 2.5: Seismic profile including the RLS-4 reflector and the seismic facies well-stratified, chaotic and transparent and wavy facies mentioned in the text. For location of the profile, see Fig. 2.4 (adapted from Kuvaas et al. (2004)).

Additionally, small channel-levee systems are recognized in the RLS (Fig. 2.4 and Fig. 2.6). Containing well-stratified seismic facies made up of layers that show a thickening trend towards the channel axis. Deposits that are similar to extensive tabular units overlies these small channel-levee systems, suggesting distal turbidites and possible sediments deposited by bottom currents. Channel-levee complexes can reveal important information about the operating sedimentary processes, both downslope and alongslope activity. Downslope activity is observed through the channel margins containing both scour and fill features and flanking sediment ridges. Alongslope activity is observed through the different mounds located in RLS (Fig. 2.4). Channel-levee complexes in the RLS are highly asymmetrical and oblique due to the eastward migration caused by the Coriolis effect (Kuvaas et al., 2004).

Abyssal plain sediment ridges in RLS are associated with glaciomarine sediments and this indicate an environment influenced by an advancing ice sheet.

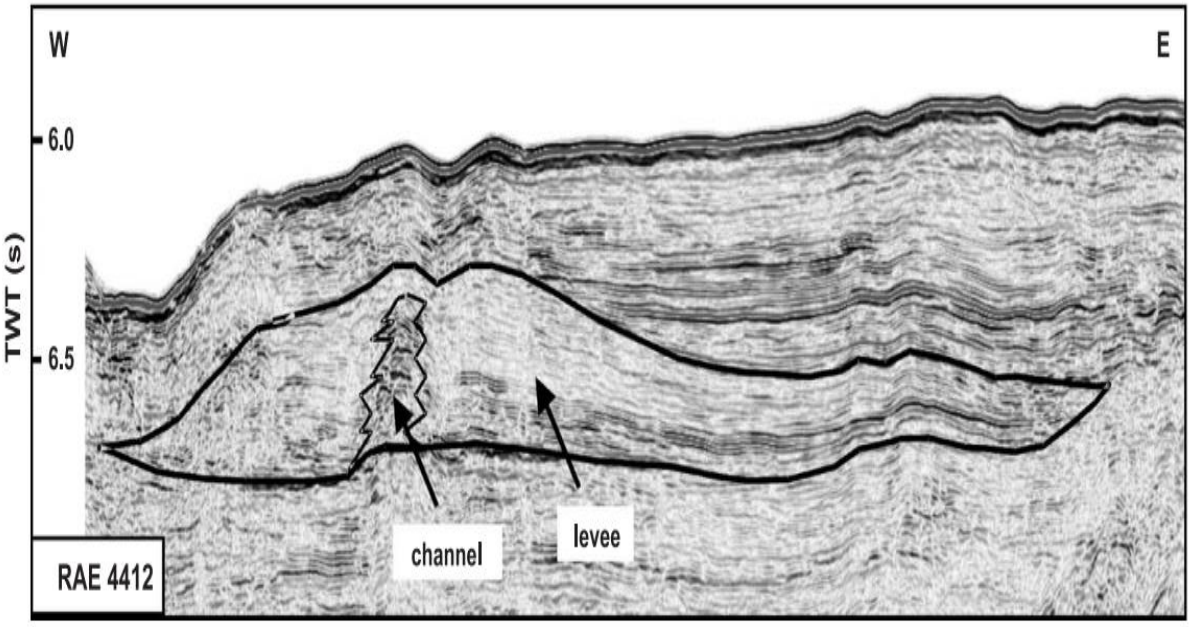

Fig. 2.6: Seismic profile including the presence of channel and levee at the foot of the Gunnerus Ridge in the RLS. For location of profile, see Fig. 2.4 (adapted from Kuvaas et al. (2004)).

Multiple papers have discussed possibilities for distinguishing between sediments deposited by gravity-driven downslope currents and those deposited by alongslope processes (McCave and Tucholke, 1986; Myers and Piper, 1988; Rebesco and Stow, 2001; Stow et al., 2002; Solli et al., 2007). In polar regions this an issue which becomes more complicated as the sediment dispersal through glacial/interglacial cycles differ considerably and the Coriolis effect is so high (Kuvaas et al., 2004).

2.2 Oceanography

2.2.1 The Southern Ocean

The Southern Ocean (Fig. 2.7) encircles the Antarctic continent and forms a link between the major ocean basins in the south, namely the Pacific, the Indian and Atlantic Oceans (Arrigo et al., 1998; Fahrbach, 2013). The area is an important sight for deep and intermediate water ventilation, transporting and mixing the water masses and properties from one basin to the next (Cunningham, 2005). The Southern Ocean with its physical properties is of great importance for the global climate, because it ventilates and regulates the global system through uptake and storing of heat, fresh water, oxygen and atmospheric CO_2 (Böning et al., 2008). The Southern Ocean northern border is set to c. 60° south by the International Hydrographic Organization (Central Intelligence Agency, 2018), however geographers discuss both the boundary and the entire Southern Ocean's existence (Anderson, 1999; Rosenberg, 2018). Some scientists argue

against the existence of the Southern Ocean, suggesting the waters surrounding Antarctica are merely extensions of the Pacific, the Indian and the Atlantic Oceans. While others scientists suggest the water masses surrounding Antarctica are a distinct body of water with its own properties. In this study, the Southern Ocean refers to the water masses surrounding Antarctica.

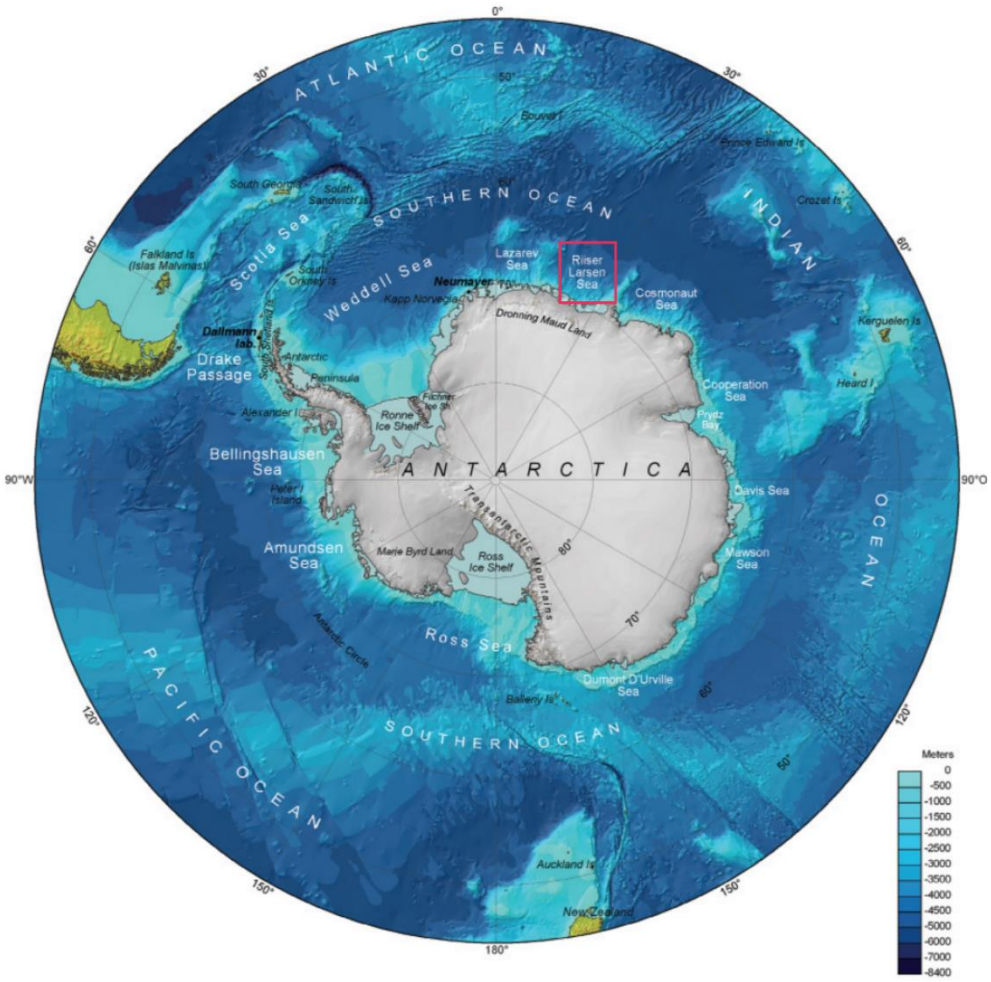

Fig. 2.7: Map of the Southern Ocean and the surrounding Atlantic, Indian and Pacific Oceans. Including the Riiser Larsen Sea outlined by a red rectangle (modified after Fahrbach (2013)).

Different water masses are identified within the Southern Ocean and are distinguished depending on salinity, temperature, and other physical properties. Water masses identified within the Southern Ocean are Antarctic Surface Water (ASW), the Circumpolar Deep Water (CDW) and the Antarctic Bottom water (AABW) (Carter et al., 2008) (Fig. 2.8).

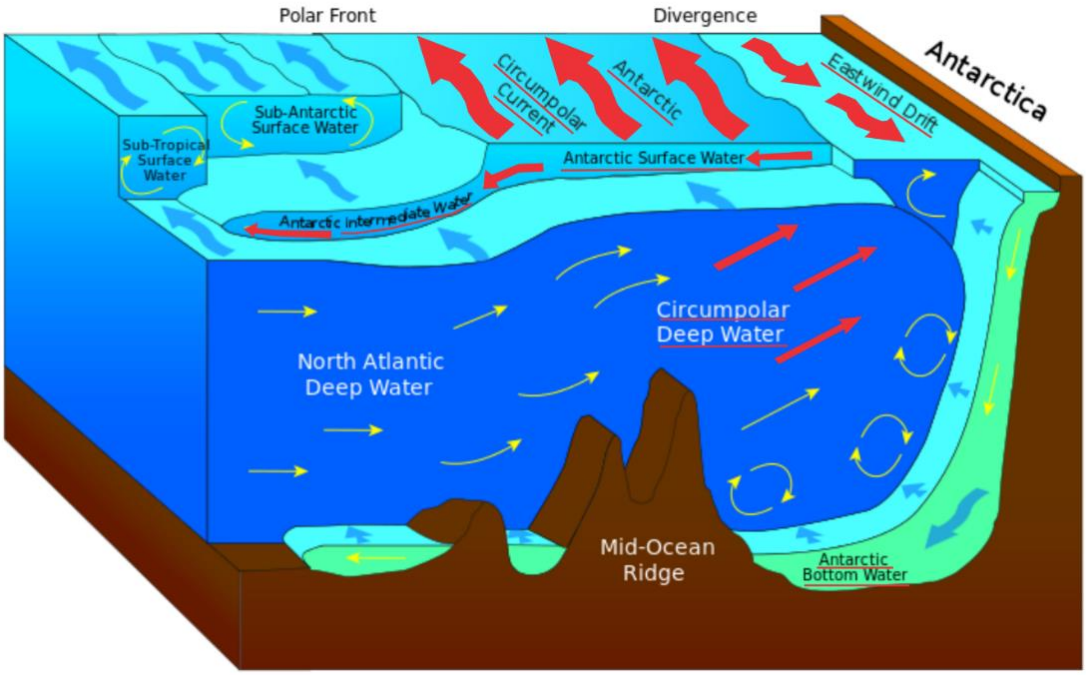

Fig. 2.8: The oceanographic circulation pattern around the Antarctic continent, including the three major water masses the ASW, the CDW and the AABW outlined by red, all are mentioned in the text (modified after Davies (2014)).

The ASW (Fig. 2.8) includes (1) the westward circumpolar flow of the Antarctic Coastal Current and (2) the eastward flow of the more distal Antarctic Circumpolar Current. Locally, ASW influences the entire water column, despite its occurrence within a deep bathymetric zone (Foldvik and Gammelsrød, 1988). The ASW originates from the continental shelf and runs in a northerly direction, mixing with Sub-Antarctic Surface Waters, before sinking and mixing with intermediate water masses (Fig. 2.8). The shelf waters around Antarctica can be divided into two groups, High Salinity Shelf Water (HSSW) or Low Salinity Shelf Water (LSSW). The salinity difference of these two waters is largely a result of the time the waters stay on the continental shelf, annual brine production by freezing of sea-ice, dilution from melting sea-ice, glacial ice and precipitation. The salinity of shelf waters controls whether Warm Deep Water (WDW) flows onto the shelf or not (Anderson, 1999).

The CDW (Fig. 2.8 and Fig. 2.9) is the core of the Antarctic Circumpolar Current (ACC) and is composed of deep waters from all the World's oceans (Orsi et al., 1995). It is a relatively warm and salty (T >0°C and >34.6, respectively) current flowing in a counter clockwise direction around the continent affecting the water column from c. 250 m to 4000 m (Fig. 2.8) (Orsi et al., 1995; Dinniman et al., 2011; Davies, 2014). The CDW can be further subdivided into the Upper Circumpolar Deep Water (UCDW) and Lower Circumpolar Deep Water

(LCDW) (Orsi et al., 1995). Low oxygen levels and high nutrition concentrations characterize the UCDW, whereas the LCDW is characterized by higher salinities. The differences between these two water masses are due to the different source regions, where UCDW originate from the Pacific and Indian Oceans and the LCDW derives from North Atlantic Deep Water (Fig. 2.9) (Orsi et al., 1995; Whitworth et al., 1998; Dinniman et al., 2011).

The AABW (Fig. 2.8 and Fig. 2.9) consists of dense water masses which are produced on the continental shelf. It runs over the continental shelf-edge before flowing into the ocean basins (Orsi et al., 1999). It is derived from interactions between the AIS and the water masses within the ACC. Most of the AABW production occurs in the Weddell Sea, some in the Ross Sea and off Wikes Land in association with subpolar gyres (e.g. the Weddell Sea Gyre, the Ross Sea Gyre and off Wikes Land) (Anderson, 1999; Orsi et al., 1999; Schröder and Fahrbach, 1999). High production rates of dense water masses are still not discovered in the RLS (Solli et al., 2007).

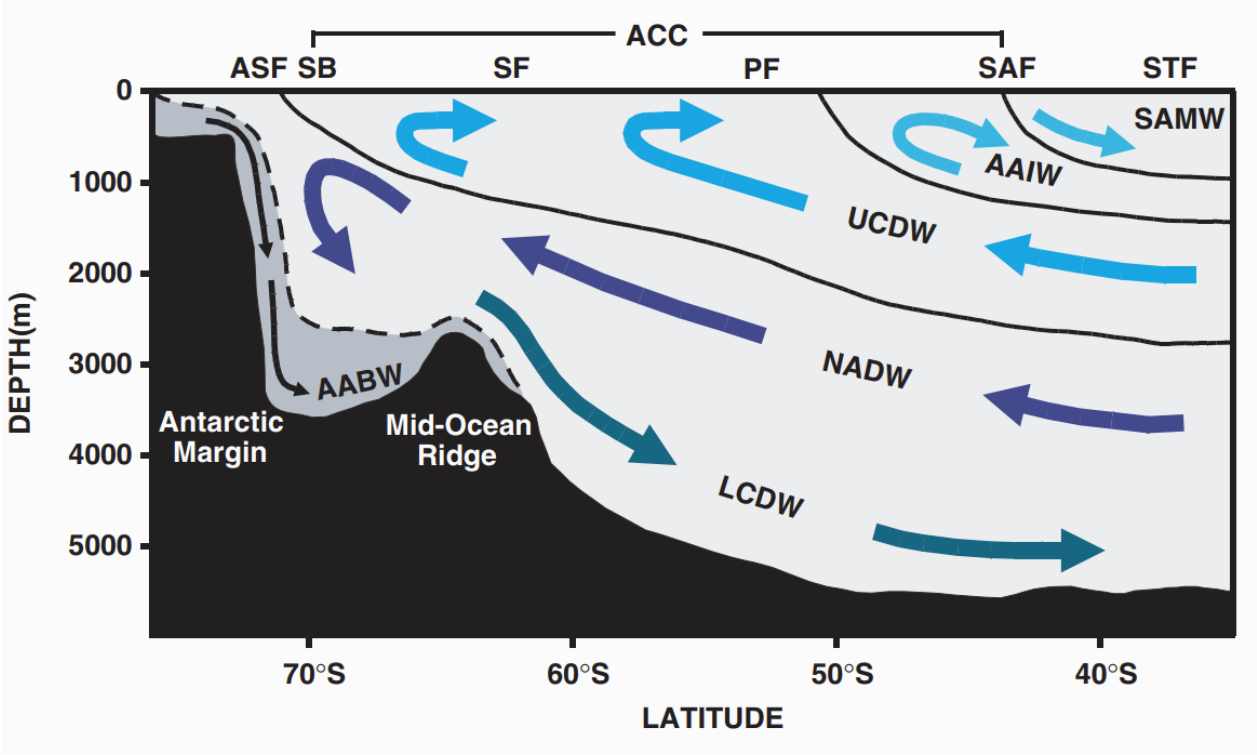

Fig. 2.9: Schematic section of the main water masses and frontal systems associated with the Antarctic continental margin. The ACC is towards the reader (including water masses: SAMW – Sub-Antarctic mode water, AAIW – Antarctic Intermediate Water, UCDW, LCDW, NADW – North Atlantic Deep Water and AABW and frontal systems ASF –Antarctic Slope Front, SB – Southern boundary of the ACC, SF – Southern Front, PF – Polar Front, SAF – Sub-Antarctic Front and STF – Subtropical Front) (adapted from Carter et al. (2008)).

2.2.2 The Antarctic Circumpolar Current (ACC)

Absence of land barriers in the Southern Ocean creates an ocean circulation pattern that flows undisturbed around the entire continent, namely the Antarctic circumpolar current (ACC) (Fig. 2.8 and Fig. 2.9). In terms of circulation in the Southern Ocean the ACC is by far the main feature, transporting $137\pm8*10^6$ m^3s^{-1} of water through the Drake Passage. The age of the ACC is still debated. Lawver (1992) argues that the ACC was formed after the opening and deepening of the Drake Passage, and the Tasman-Antarctic gateway, located south of Tasmania around Eocene-Oligocene boundary, c. 34 Ma. However, others propose that the ACC was formed long after the Eocene-Oligocene boundary (Barker and Thomas, 2004; Pfuhl and McCave, 2005).

The ACC is a wind driven current, flowing in a clockwise direction around the Antarctic Continent, powered by the westerly winds at c. 45-55° (Orsi, 1994). The current operates as a barrier in the Southern Ocean, separating the Southern Ocean from the warmer oceans further north, thus, helps maintain the ice sheet on Antarctica. The ACC connects the Atlantic, the Pacific, the Indian, and the Southern Ocean together through interaction in the interbasins (Rintoul, 2010) and affect the entire water column (Barker and Thomas, 2004).

The ACC is associated with several fronts, which are transition zones between water masses (Fig. 2.9). From south to north these are the Antarctic Southern Front, the Subtropical Front, the Polar Front and the Subantarctic Front (Carter et al., 2008). The Subtropical Front is located north of the ACC and defines the northern boundary of the Southern Ocean. It separates warm, salty and subtropical waters from the colder sub-Antarctic waters in the south (Orsi et al., 1995) (Fig. 2.8). The fronts are characterized by sharp horizontal gradients (e.g. salinity, temperature, nutrients, oxygen and density), which marks the different boundaries between the water masses. These boundaries between the water masses slops down and away from the Antarctic continent (Fig. 2.9) (Orsi et al., 1995; Carter et al., 2008).

The ACC has a profound implication for the global ocean circulation pattern and climate (Rintoul, 2010). Oceanographers have concluded that the ACC reflects the interplay between wind and the buoyancy exchange with the atmosphere, eddy fluxes and momentum, water mass modification and strong interactions between the flow and the bathymetry (Rintoul, 2010). Another important part of the ACC is the air-to-sea exchange of heat, fresh water and atmospheric gases (Böning et al., 2008). In addition, the ACC regime accounts for a large fraction of global ocean warming and c. 40 % of the global oceanic uptake of anthropogenic CO_2 over the last two centuries (Böning et al., 2008).

2.3 Geomorphology of glaciated continental shelves

The morphology of continental shelves at high latitudes have a distinct shape due to successive modification by repetitive glaciations through time (Fig. 2.10). This includes both large-scale morphological features such as banks and troughs, and smaller scale features such as mega-scale glacial lineations, moraines and iceberg ploughmarks. These features provide evidence for the presence of grounded glaciers and icebergs in the past and at present (Vorren, 2003). During glaciations, ice works as an active agent of erosion, eroding troughs into the underlying strata. These troughs have acted as pathways for fast-flowing ice (so-called ice streams), draining the interior of the continental ice sheet (Vorren and Laberg, 1997; Anderson, 1999; Cofaigh et al., 2003; Livingstone et al., 2012). Mega-scale glacial lineations (MSGL) provide additional evidence of fast-flowing grounded ice streams (Clark, 1993). Marginal moraines and grounding zone wedges (GZW) show where the ice margin and/or grounding line has been temporarily (O'Brien et al., 1999; Dowdeswell et al., 2008; Batchelor and Dowdeswell, 2015). Iceberg ploughmarks and marginal moraines are more common on shallower banks where evidence of fast-flowing ice is lacking (Belderson et al., 1973; Lien et al., 1989).

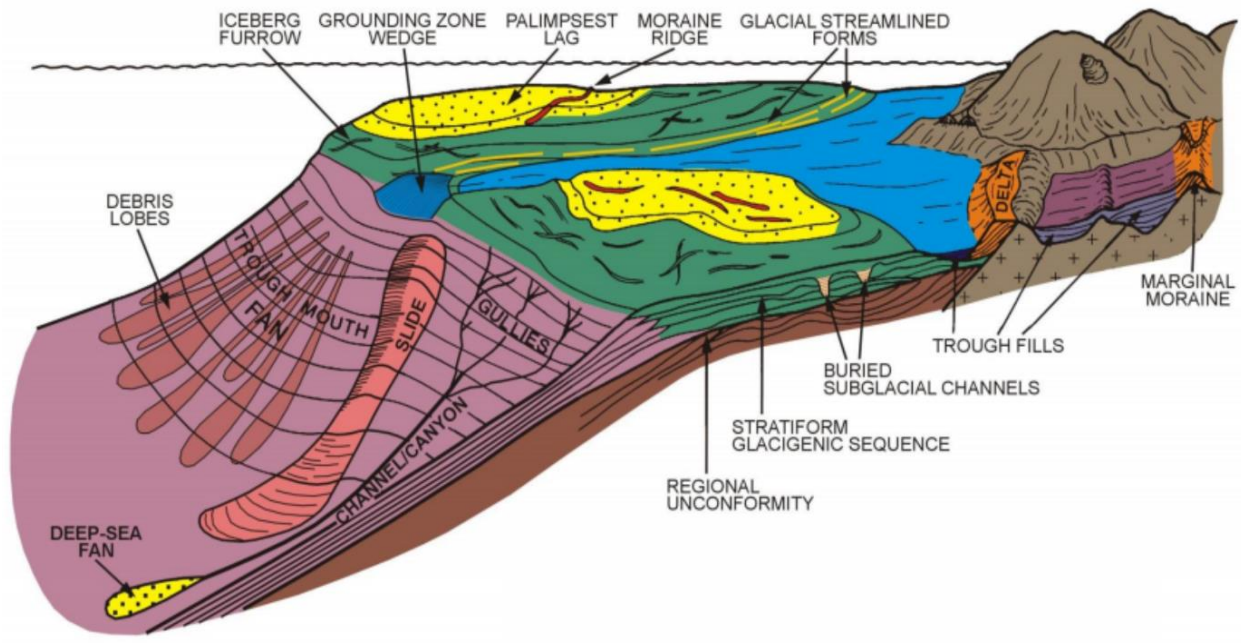

Fig. 2.10: Glaciated continental shelf with associated sedimentary features (adapted from Vorren (2003)).

The Antarctic continental shelf contains evidence of glacial erosion. This is evident through the great depth surrounding the Antarctic continent, its landward-sloping profile and the geomorphological features observed on the continental margin (Anderson, 1999; Wellner et al., 2006). The East Antarctic continental shelf is narrow in comparison to the West Antarctic continental shelf, which is generally broad and mostly covered with ice (Anderson, 1999).

2.3.1 Sea-ice

Sea-ice growth and decay around the Antarctic continent influences both climate and ocean circulation in the Southern Hemisphere (SH), and differs greatly from sea-ice conditions in the Northern Hemisphere (NH) (Fig. 2.11) (Turner and Overland, 2009). Geographically, the Arctic is semi-enclosed by the surrounding landmasses, trapping sea-ice within the borders of the landmasses. In contrast, the Antarctic is open, favouring a northward movement of the sea-ice towards warmer oceans. Antarctica therefore experience large seasonal variations in sea-ice extent, where winter maximum sea-ice cover (September) equals an area of c. 18.5 million km^2 on average, whereas the summer minimum sea-ice cover (February) decreases to an extent of c. 3.1 million km^2 on average (Parkinson and Cavalieri, 2012).

The Arctic and the Antarctic have experienced different climatic changes through the last decades resulting in uneven sea-ice development (National Snow & Ice Data Center, 2018c; National Snow & Ice Data Center, 2018a). Whereas the sea-ice extent in the Arctic has decreased dramatically, the sea-ice extent in the Antarctic has slightly increased (Turner and Overland, 2009; Sigmond and Fyfe, 2010). Topographic factors together with land-to-sea distribution can be one explanation for the dissimilar development, although an exact reason for the increase in the SH remains unknown. Basal melt of the ice shelves and a freshening of the oceans (Zhang, 2007) in addition to an increasingly higher level of ozone in the atmosphere, leading to stratospheric cooling and stronger winds (Gillett and Thompson, 2003; Shindell and Schmidt, 2004), are pointed out as some of the explaining factors.

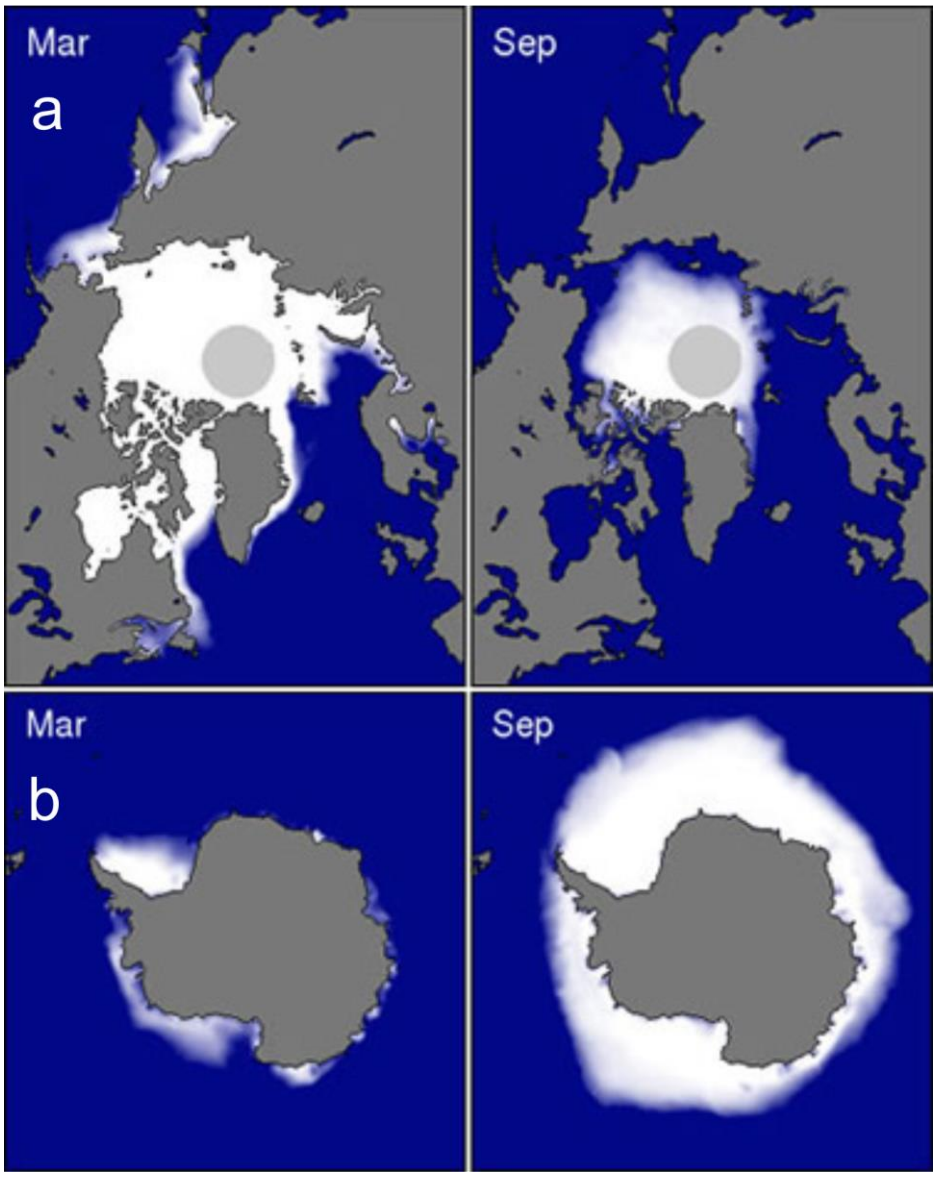

*Fig. 2.11: Satellite images showing sea-ice concentration of minimum and maximum coverage during March and September for **a)** Arctic and **b)** Antarctic between 1981 and 2010. Seasons are opposite between the SH and NH (SH – summer minimum in February. NH – summer minimum in September) (modified after National Snow & Ice Data Center (2018c)).*

2.3.2 Polynyas

Polynyas are ice-free areas in ice-covered ocean (Zhang, 2007). Polynyas are kept ice-free by different processes that either prevent ice formation or remove newly formed ice. Two types of polynyas exists, namely open-water and coastal polynyas (Fig. 2.12) (Massom et al., 1998; Smith et al., 2010). Polynyas are areas of massive heat and gas exchange between the ocean and the atmosphere (Ishikawa et al., 1996). They can be important sites for bottom water production and often include nutrient rich water masses (Ohshima et al., 2013; National Snow & Ice Data Center, 2018b).

Open ocean polynyas form due to the temperature difference of two inferring bodies of water. They form where water is located above freezing upwells, or when water originating from lower depths moves towards the surface. Heat-transfer from water to the ice will melt the ice and prevent formation of new ice (National Snow & Ice Data Center, 2018b).

Coastal polynyas form due to the constant removal of newly formed ice by strong winds (Massom et al., 1998). The polynyas are kept ice-free due to the strong katabatic winds blowing in a persistent direction from the Antarctic continent. Water masses observed in coastal polynyas have high salt concentrations and the water will sink as it becomes dense and salty, process known as brine formation. The high density surface waters can then mix with the bottom currents (National Snow & Ice Data Center, 2018b). Smaller coastal polynyas can alter the freshwater flux by reducing the downward movement of high-density waters. The coastal polynyas in Antarctica are reported to form in the western side of the capes and/or along the eastern part of protected bays (Ishikawa et al., 1996). Two coastal polynyas are identified in eastern part of Queen Maud Land, namely Breid Bay and one along the shelf break (Ishikawa et al., 1996).

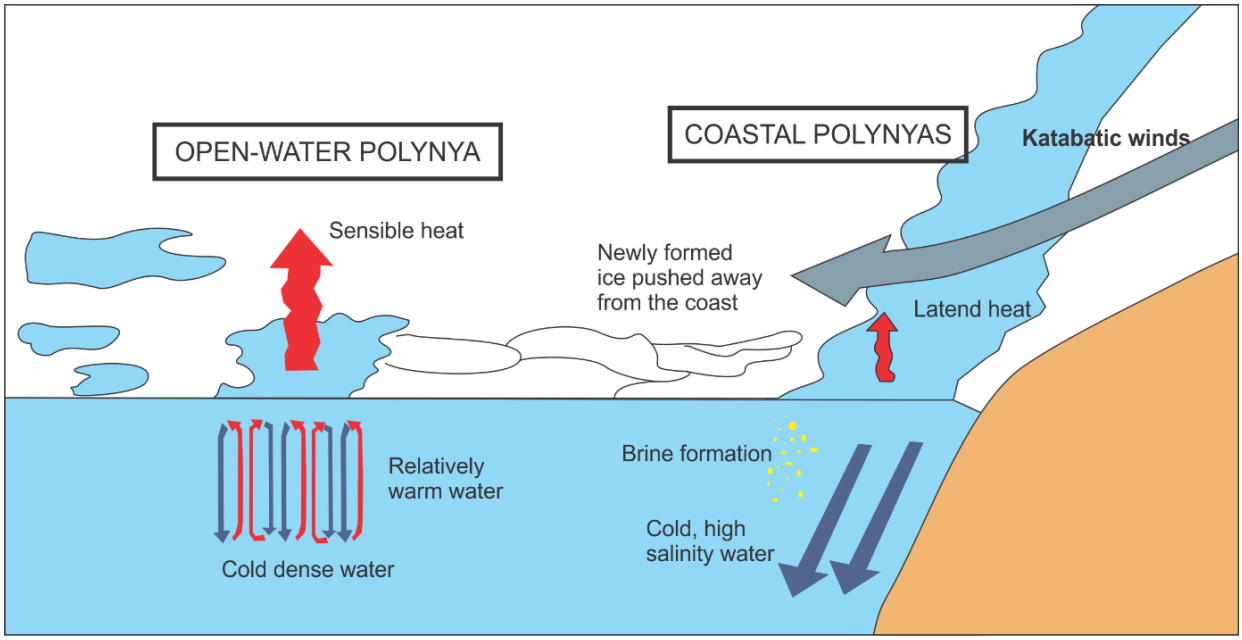

Fig. 2.12: Figure showing open-ocean and coastal polynya formation (modified after National Snow & Ice Data Center (2018b)).

2.3.3 Icebergs

Icebergs are observed offshore the Antarctic continent (Swithinbank et al., 1977; Barnes and Lien, 1988). They originate from calving glaciers and ice shelfs, or decay into smaller icebergs and float with the operating atmospheric and oceanographic currents. Icebergs affect freshwater

flux in the ocean, and the formation and distribution of sea-ice and polynyas (Matsuoka et al., 2015). Additionally, icebergs have the ability to scour the seafloor and/or mix sediments on the seafloor.

Icebergs have the ability to (1) act as a barrier preventing the pack ice to move in its usual path and (2) to reduce the size of costal polynyas by preventing newly formed ice to move (Massom et al., 2001). An iceberg calving off the Ross Ice Shelf (WAIS) in 2000 restricted the normal drift of pack ice and led to a heavier spring/summer pack ice cover than recorded earlier (Arrigo et al., 2002).

Aoki (2003) reported the iceberg drift speed in Queen Maud Land to increase westward. The icebergs investigated used on average c. 500 days to move from 70 °E to 10 °E, resulting in average iceberg drift speeds from 0.06 m/s in the Mawson regions to 0.14 m/s in the Greenwich Median region (Fig. 2.13). Seasonal variation in drift speed is high from autumn to early winter and low during spring (0.18 m/s in June-July and 0.02 m/s in October in the middle region and 0.14 m/s in May and 0.003 m/s in November in the Suowa region, see figure 2.13). The magnitude of drift speed also increased westward (Aoki, 2003).

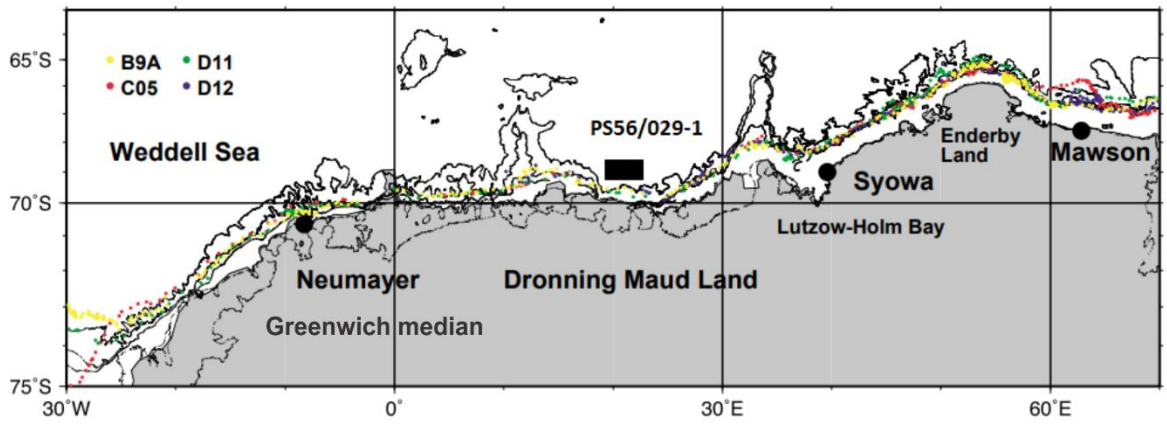

Fig. 2.13: Iceberg drift off Queen Maud Land where B9A, C05, D11 and D12 represent icebergs under investigation and their drift along the continental coast. Core location of PS56/029-1 is displayed with a black square (modified after Aoki (2003)).

2.4 Sedimentary processes and deposition

The deep-marine environment consists of several different sedimentary processes, which in turn leads to sediments with unequal characteristics (Fig. 2.14). By studying marine sediments the different sedimentary processes can be revealed, giving crucial information about the time of deposition. In the following sub-chapters the downslope and alongslope processes active in

the RLS are explained, namely turbidites, contourites and pelagic settling (e.g. Kuvaas et al. (2004) and Solli et al. (2007)).

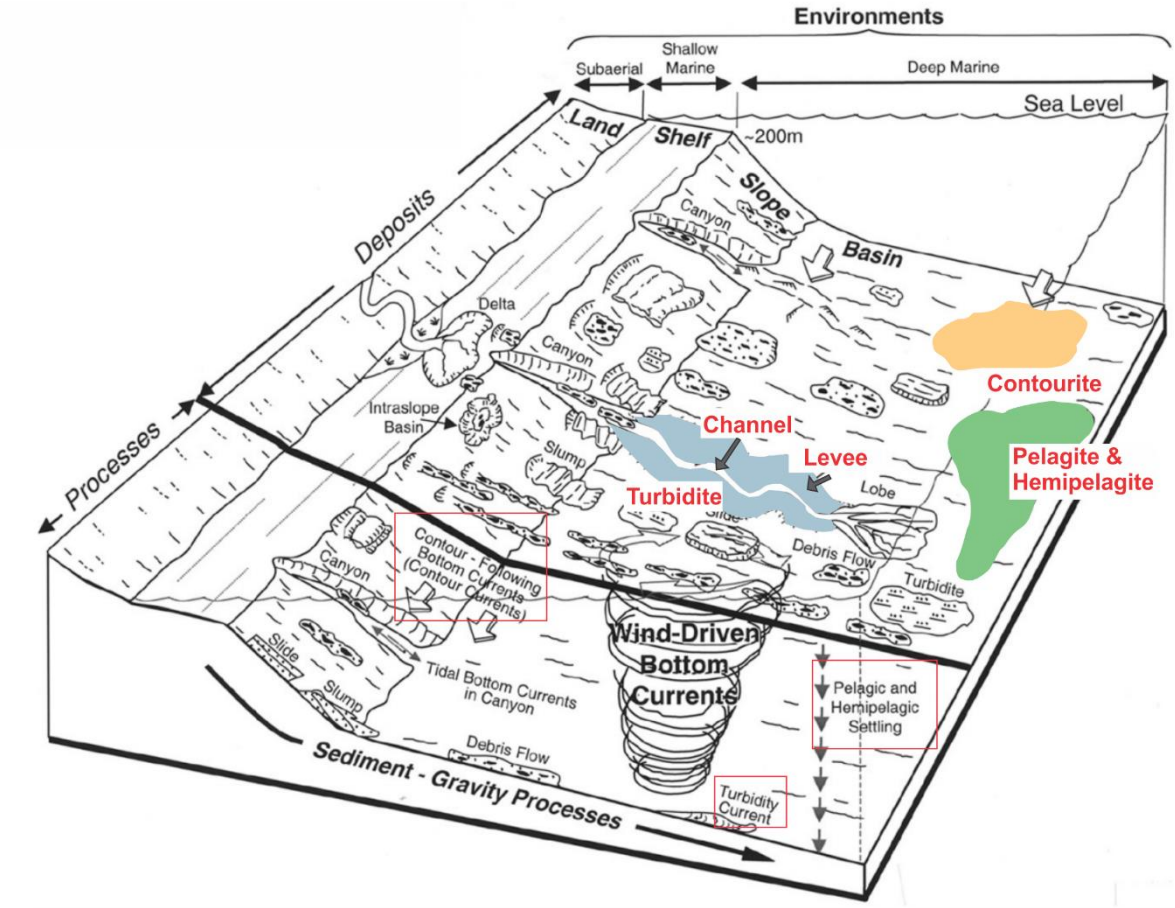

Fig. 2.14: Deep-marine sedimentary environments and associated deposits and processes. Turbidite, channel and levee are marked with blue, pelagite & hemipelagite is marked with green and contourite is marked with orange. Red squares indicate sedimentary processes mentioned in the text (modified after Shanmugam (2006)).

2.4.1 Turbidites

A turbidity current (Fig. 2.14) is a turbulent moving, high velocity, gravity-driven current consisting of sediments temporarily suspended in water (Nichols, 2009). These currents are responsible for incising submarine canyons, the formation of fans and the layering on the abyssal plain. These currents have the ability to carry sediments up to 1000 km from the source region, travelling at speeds up to 90 kmh^{-1} ($25ms^{-1}$) and carry sediment loads of 300 kgm^{-3} ($300gl^{-1}$) (Friedman et al., 1992; Stow and Mayall, 2000; EC, 2009; Nichols, 2009).

Movement of the turbidity current is maintained by the density contrast between the sediment-laden water and the surrounding undisturbed water. Particles fall out of suspension (starting with the coarsest particles first) due to decreasing slope angle and/or declining energy within the current, in which case the velocity of the current that does not allow grains to remain in

suspension. Sediments deposited by turbidity currents are characterized as normally graded deposits. A turbidity current can be subdivided into a head, body and tail (Nichols, 2009). Where the head is the steep leading edge of the current, roughly twice as thick as the body. It contains the coarsest grains within the current and is responsible for erosion of underlying, finer strata. Grains from the head are transported forward and upward to mix with the surrounding waters and are re-integrated through the body and tail. The body of the current has uniform thickness where the grains are kept in suspension by friction between the overlying water and bed. The body and tail are regions for deposition. The tail will decrease in thickness rapidly and become more diluted. The remaining sediments in suspension will deposit as the flow fades away (Stow and Mayall, 2000). Deposition by a turbidity current is called a turbidite, which is characterized as well sorted sediments containing rarely any mixtures of sediments. A turbidite will ideally form a succession called Bouma sequence, containing five units (T_a – T_e) (Fig. 2.15) (Bouma, 1964).

- T_a: Consists of poorly sorted and structureless sand. Material falls out of suspension with reduced turbulence inhibiting the formation of bedforms.
- T_b: Laminated sand, normally containing finer particles than 'T_a' and is better sorted. The laminae is a product of the separation of grains in the upper flow regime transport.
- T_c: Cross-laminated medium to fine sand, can also contain climbing ripple lamination. This middle division characterize high sedimentation rates and moderate flow velocities in the ripple bedform stability field. Convolute lamination can also occur in this division.
- T_d: Consist of fine sand and silt, a result of the waning flow within the turbidity current. Horizontal laminae may occur, but is less defined than in 'T_b'.
- T_e: Fine-grained sediments such as silt and clay dominate this uppermost part of the Bouma sequence. They fall out of suspension as the turbidity current has come to rest and is therefore a hemipelagic deposit.

In nature, it is rare to find the complete Bouma sequence. Turbidites either lack bottom intervals, top intervals or bottom and top intervals of the sequence (Bouma, 1964; Stow and Shanmugam, 1980).

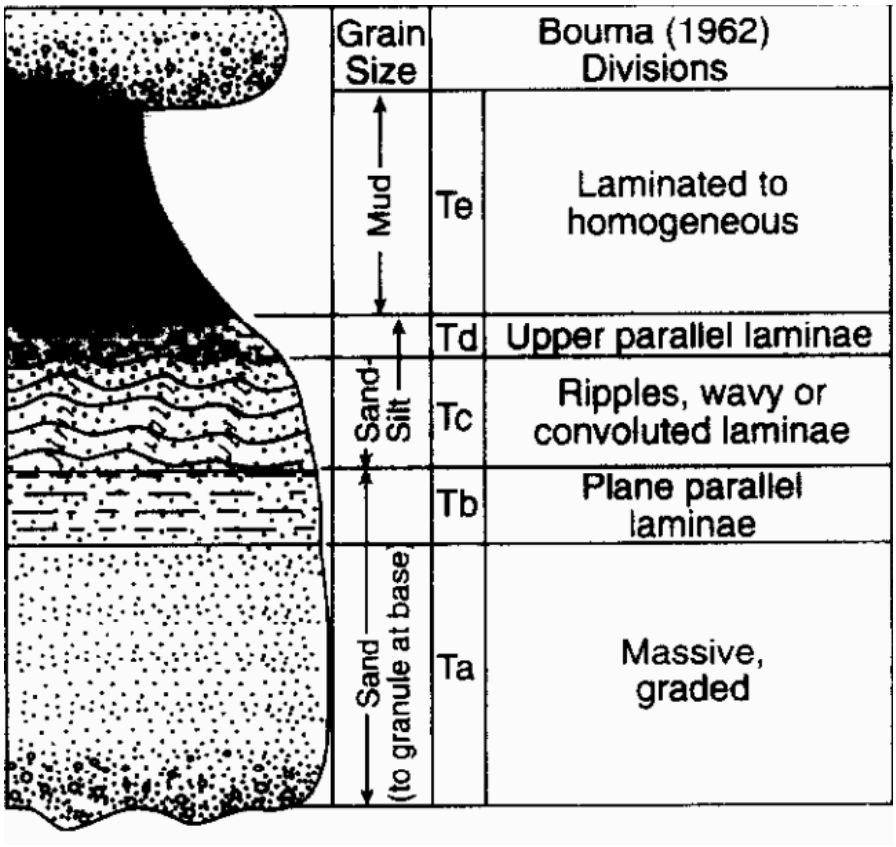

Fig. 2.15: The ideal Bouma sequence (T_a – T_e), including the grain-size involved and the associated sedimentary features(adapted from Shanmugam (1997)).

In the sedimentary record a turbidite is recognized as a deposit from a rapid and short-lasting event interrupting the "normal sedimentation". Affecting the area with more energy compared to e.g. contourites. By studying the grain-size distribution obtained from analysis of marine sediments the signature of a turbidite might be coarse particles - less coarse particles - fine particles, thus showing the characteristic normal grading of sediments. Turbidites include well sorted sediments with an erosive lower boundary, whereas the occurrences of foraminifera are a minor component. Turbidites often cut wormholes and other bioturbation marks. Turbidites around the Antarctic continental margin consists of sediments with a high input of terrigenous sediments from the Antarctic continent (Rebesco et al., 2014). Additionally, a sediment core retrieved in the distal end of these turbidity currents, where turbidites are reduced to a fine-grained sediment, could include characteristics that are less clear than the mentioned characteristics above.

2.4.2 Contourites

Contourites (Fig. 2.14) are defined as "sediments deposited or substantially reworked by the persistent action of bottom currents" (Stow, 2002; Stow et al., 2002; Rebesco et al., 2014). Contourites are significant in deep marine environments, but minor in continental shelf areas.

They consist of whatever particles that are within the bottom currents and the size depends upon the flow velocity, but the sediment size is normally within the range from mud to sand. Contourites are normally a product of a continuous flow, creating sheets or elongated bodies parallel to the basin margin on the seafloor. The characteristics of a contourite depends upon the flow velocity, the sediment supply, and degree of modification (e.g. bioturbation). In the sedimentary record contourites can be hard to recognize (e.g. they can be both normal and reverse graded) (Nichols, 2009). Bottom currents affect various type of sediments, both during and after deposition, which can make them difficult to identify in the sedimentary record. Additionally, the action of bottom currents does not exclude other sedimentary processes, e.g. turbidites. Contourites are generally hard to recognize in the sedimentary record because they lack a simple unambiguous diagnostic criteria (Rebesco et al., 2014). However, the sortable silt fraction (10-63 μm) is shown to be a highly useful current strength indicator (McCave et al., 1995; Pfuhl and McCave, 2005). Particles below 10 μm are considered as "cohesive", while particles above 10 μm are considered as "non-cohesive". The "non-cohesive" fraction from 10 to 63 μm has shown to be sortable by deep-marine currents. It is independent from sediment supply and varies only according to current speed, nevertheless, a constant sediment supply and a grain transport that only is affected by deep-marine currents are required for the creation of contourites (McCave et al., 1995).

In the sedimentary record contourites are recognized as well sorted deposits including fine sediments, often clay to silt in size. Contouritic sediments often show indication of bioturbation. Normally, these currents initiate slowly before increasing gradually and decreasing again. Seen in the grain size distribution in the sedimentary record as finer – coarser – finer.

2.4.3 Pelagic settling

Pelagic sedimentation (Fig. 2.14) is the result of slow vertical settling of particles through the water column under the influence of gravity and in the absence of bottom and turbidity currents (Stoker et al., 1998). Pelagic muds are considered as the most common sediments in the deep-sea. Pelagic mud deposits consist of biogenic (siliceous and calcareous oozes) and terrigenous components. The pelagic sediments in high latitude regions often contain high amounts of illite and chlorite (Kennish, 2000).

There are three factors controlling the composition of the pelagic sediments: (1) The distance from major landmasses, which controls the dissolution of terrigenous or land-derived sediments. (2) The water depth affecting the preservation of calcareous and siliceous biogenic

particles as they settle through the water column. (3) The ocean fertility, which control the amount of biogenic particles produced in the uppermost part of the water column (e.g. Von Bodungen et al. (1995), Jones et al. (1998) and Navarrete et al. (2005)).

In the sedimentary record pelagites are recognized as poorly sorted, including fine sediments with a relative constant lithological composition compared to turbidites. These sediments often show indications of bioturbation and the biogenic input is high compared to e.g. turbidites.

2.5 Channel-levee complexes

Channel-levee complexes consist of deep channels and higher levees (levees – ridges who frequently flank the channels). These complicated systems are found on the continental slope and are believed to be a result of climate-controlled processes, e.g. ice sheet dynamics and deep-water production (Kuhn et al., 1993; Presti et al., 2003; Hass et al., in prep). Channel-levee complexes are morphodynamic structures with a long build-up phase, making them ideal to investigate climatically and related hydrographic fluctuation and changes through glacial/interglacial cycles. The associated sediments therefore allow us to interpret recent environmental conditions and paleoenvironment (Kuvaas and Kristoffersen, 1991).

Channels are normally a product of erosion (Mosher et al., 2004). They may also form in a depositional environment as a product of lowered sediment accumulation in close proximity to gravity driven bottom currents (Gervais et al., 2001, McHugh and Ryan, 2000). Levees are higher areas flanking the channels normally not affected by erosion. However, the levees can move laterally if the associated channel moves its bed. Levees form as the channel gets over-flooded, transporting sediment out of the channel and onto the levees as overbank deposits. In addition to overbank deposits, hemipelagic sediments accumulated through the water column, which build up the rest of the sediments on the levee (McHugh and Ryan, 2000). Hass et al. (in prep) suggest that the levee sediments can be an interesting tool for paleoceanographic and paleoclimatic investigations. This is because they are at the end of a chain of processes associated with climate-triggered oceanographic changes and contain sediments of high resolution.

2.6 Sedimentation through a glacial/interglacial cycle

Sediments deposited in glacial periods differ from sediments deposited in interglacial periods. Therefore, by studying marine sediments glacial and interglacial periods can be distinguished. A case study from the Antarctic Peninsula by Rebesco et al. (2002) suggest distinct sedimentary

processes connected to specific climatic conditions through a glacial/interglacial cycle (Fig. 2.16).

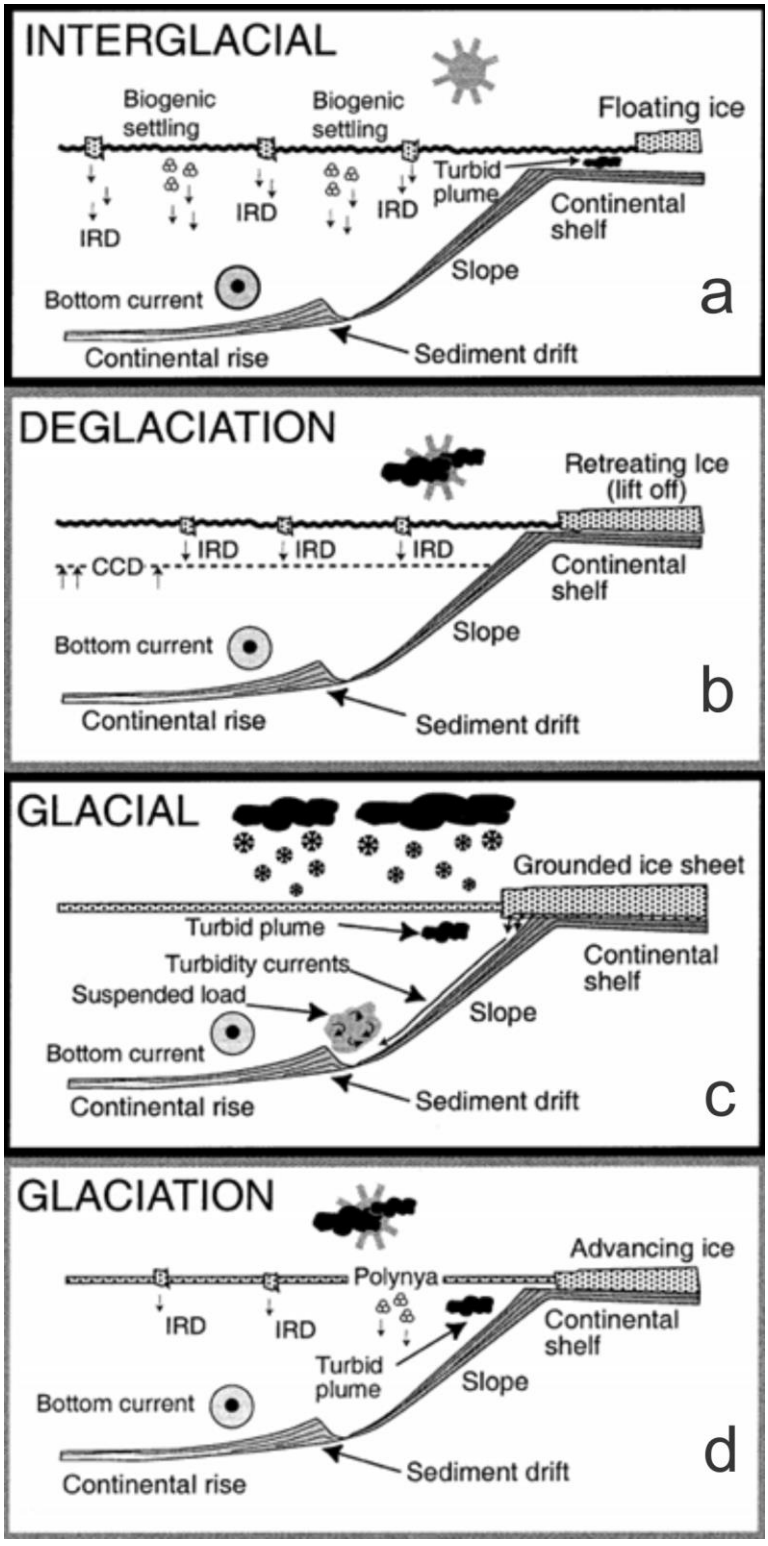

*Fig. 2.16: Sedimentary processes prevailing through glacial/interglacial cycle, including **a)** interglacial, **b)** deglaciation, **c)** glacial and **d)** glaciation (modified after Rebesco et al. (2002)).*

Transition from interglacial to glacial period.

This stage is characteristic with deposition of structureless mud, with sparse IRD content. The sediments are of terrigenous origin, containing few or none planktonic foraminifera or diatoms. The clay mineral assemblage is close to smectite and free of kaolinite. Climatic setting associated with the transition from interglacial to glacial period is the advancing grounded ice sheet towards the edge of the continental shelf. Sediment laden plumes bring fine sediments to the upper rise, meanwhile diluting the smectite signal from the southwest flowing bottom currents. The attribution of sediments from turbidity currents is still not important. The existing sea-ice cover reduces the planktonic foraminifera signal, but in regions with polynyas the planktonic foraminifera signal can be present.

Glaciation

Interacting sedimentary processes in this climatic setting give rise to sub-facies of laminated, terrigenous sediments. Sedimentary features expected to be incorporated in this setting are: 1) laminated mud with silty laminae 2) laminated mud with IRD layers 3) layers and lenses 4) cross-stratified mud and 5) slumps and sand/gravelly-grained turbidites. Bulk sediment is terrigenous mud dominated by chlorite and illite, while smectite and kaolinite concentrations are low. Transportation of sediments towards the continental rise is by different downslope processes together with meltwater plumes (enhanced by the position of the grounded ice sheet).

Deglaciation – transition from glacial to interglacial conditions

The transition from glacial to interglacial conditions includes structureless mud with IRD layers. The sediment texture is characterized as hemipelagic mud, with a mineral clay assemblage of smectite with some kaolinitt. Foraminifera and diatom content is normally low.

Interglacial

Interglacial are characterized by bioturbated mud with sparse IRD content and with few IRD layers. The sediment composition is hemipelagic mud, with siliceous and calcareous microfossils. The clay assemblage contains high smectite values with less kaolinite. Pelagic settling of biogenic and terrigenous material through the water column predominantly makes up interglacial sediments.

3 Materials and methods

This study is based on multi-proxy analysis of gravity core PS59/029-1. The analysis includes measurement of physical properties using a Multi Sensor Core Logger (MSCL), grains size distribution, visual core description, analysis of X-radiographs, line scan images, and qualitative element-geochemical analysis using a XRF core scanner.

3.1 Sediment cores

The sediment core was collected with a gravity corer on the 11th and 12th of February 2000 (Table 3.1). The sediments were retrieved during expedition ANTARKTIS XVII/2 aboard the research vessel Polarstern (Thiede and Oerter, 2002). Details of the sediment core is provided in Table 3.1 below.

Table 3.1*: Core station, date, time, location and information on the core used in this study (Thiede and Oerter, 2002).*

Station	**Date**	**Time (UTC)**	**Lat. (S)**	**Long. (E)**	**Water depth (m)**	**Penetration (m)**	**Recovery (m)**
PS59/029-1	11.02.00	11:14	68°00,03’	20°45,13’	3850	16	12,67

The gravity corer onboard Polarstern consisted of a long steel barrel with a heavy weight (c. 1.5 tonnes) attached to its top (Fig. 3.1). The steel barrel contains a long plastic liner with a core cutter and core catcher securing it at the bottom. As the gravity corer penetrates through the seafloor sediments, the core cutter cuts into the sediments like a knife, making room for the sediments to be filled within the steel barrel and the plastic liner. The core catcher at the bottom makes sure that the sediments are kept at place when the gravity corer is pulled up again. After bringing the gravity corer up, the plastic liner is removed from the steel barrel and cut into up to one meter long sections. Each section is labelled with station and depth below seafloor.

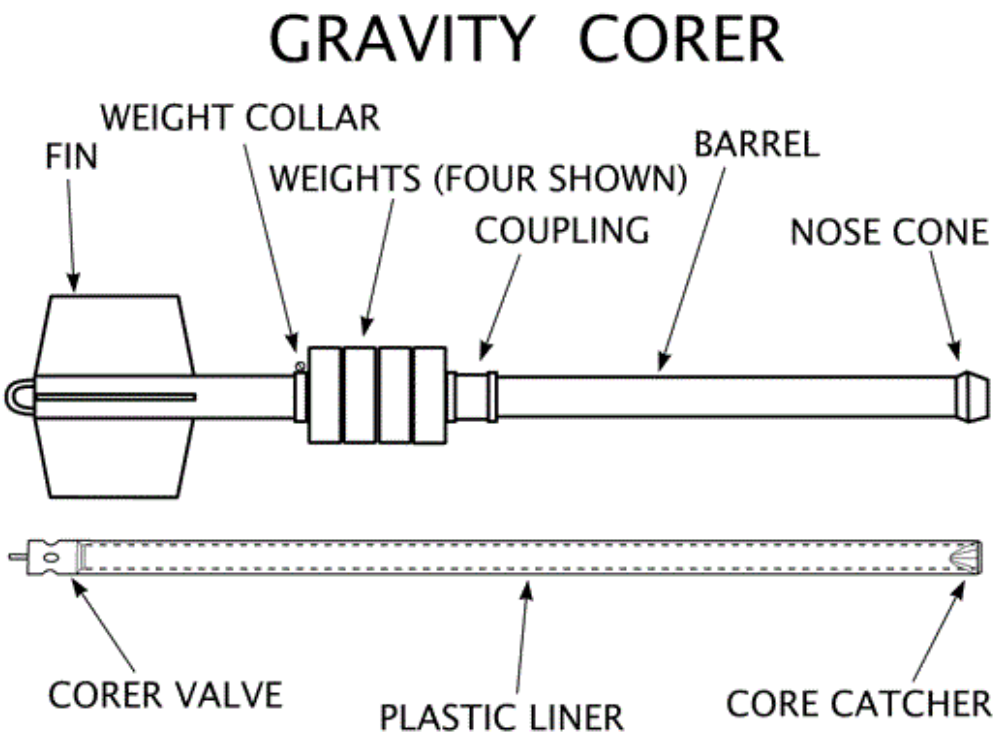

Fig. 3.1: Schematic figure of a gravity corer (adapted from USGS science for a changing world (2017)).

Aboard the research vessel each one meter long core section was cut into two halves, creating a working and an archive half. Whereas the archive half was stored away in 4° C conditions, the working half was used for further investigations. The 12.67 m long gravity core PS56/029-1 consists of 13 sections.

In the next sections, the methods performed on the gravity core PS56/029-1 are presented.

3.2 Laboratory work

The laboratory work started in March 2017 and completed by September 2017. The main laboratory work (grain-size distribution analysis) was carried out at the geology laboratory of the Alfred Wegner Institute (AWI) on List, Sylt, Germany and AWI in Bremerhaven, Germany. The X-radiographs, visual core description, XRF core scanning and line-scan imaging was carried out at the laboratory of the Department of Geosciences, UiT The Arctic University of Norway in Tromsø (UiT).

3.2.1 Visual core description

A visual core description of the core surface is important in order to collect detailed observations and to distinguish characteristics throughout the core. A visual core description

provides a good initial impression of the sediment depositional history and of the sedimentary processes involved.

Already aboard Polarstern in 2000, the core PS56/029-1 was logged (p. 227 in Thiede and Oerter (2002)). Still, I concluded to include my own visual core description into this study. For the visual core description done in year 2000, go to www.pangea.de and/or Thiede and Oerter (2002).

The surface of the working half was cleaned and investigated. Special visible features/changes such as lithological transitions or boundaries, sedimentary structures or textures, grain-size changes, ice rafted debris (IRD), colour variation, occurrence or absence of foraminifera, and organic matter content were noted down. In this study the Munsell Soil Colour Chart was used to define sediment colours. *MUNSELL* is a colour chart with up to 199 different colour standard chips, which provide an exact description of the colours by direct comparison and numerical designation.

3.2.2 X-radiographs

GEOTEK X-ray core imaging provides information about the sediments internal structures by using electromagnetic radiation (Fig. 3.2). The X-radiographs enable detection of features not visible from the surface (e.g. bioturbation, lithological variations, shells and IRD). X-rays are sent through the core, after which the X-rays are attenuated by the sediments. The degree of attenuation depends on the sediment. In general, sediments with high-density features attenuate more X-rays (e.g. compact and coarse sediments, gravel rich sediments and small stones), whereas low-density deposits attenuate less X-rays (e.g. soft bioturbated sediments). The core image is given in greyscale, where the density differences are proportional to the grey values.

The X-radiographs were taking on the working half of the core. The exposure time was 10 ms, the aperture was 11, the X-ray voltage was 119.99 kV and X-ray current strength was 224.2 W.

Fig. 3.2: Photos of the GEOTEK MSCL-XCT X-ray used in this study (adapted from UiT the Arctic University of Norway (2018a)).

3.2.3 Line-scan image

A Jai L-107CC 3 CCD RGB Line Scan Camera installed on the Avaatech XRF Core Scanner was used for the acquisition of colour line-scan images. The camera has RGB channels at 630 nm, 535 nm, and 450 nm in order to get an exquisite channel separation.

Fig. 3.3: Photos of the Avaatech XRF Core Scanner used in this study, which is placed in a container at UiT, The Artic University of Norway (adapted from Uit the Arctic University of Norway (2018b)).

In order to get a line-scan image of good quality the core surfaces were cleaned and smoothened prior to image acquisition to provide the best possible conditions for a good image. The core section is then placed into the Avaatech XRF Core Scanner (Fig. 3.3). A ruler was placed next to the section to keep track of the depth (mm). The Avaatech XRF Core Scanner acquire an image with a resolution of 70 µm.

3.2.4 XRF core scanning data

XRF-scanning or "X-ray fluorescence scanning" is a tool for rapid, continuous and non-destructive determination of the qualitative element-geochemical composition of the sediments, frequently used on marine bottom sediments. It is successfully used for high-resolution time series, detailed sedimentary and climatic reconstructions on various timescales and for stratigraphic correlations (Haug et al., 2001; Bahr et al., 2005; Hepp et al., 2006; Tjallingii et al., 2007). The XRF core-scanning measurements were obtained directly from the working half surface with the Avaatech XRF core scanner at the Department of Geosciences, UiT The Arctic University of Norway in Tromsø.

The Avaatech XRF core scanner is a core-scanning tool that analyse the chemical composition of the sediments at its uppermost micrometres, normally from Aluminium (Al, atomic number 13) to Uranium (U, atomic number 92) (Tjallingii et al., 2007). The XRF-scanning principle is based on X-rays colliding with matter, which generates secondary radiation, i.e. fluorescence (Forwick, 2013). Making it possible to determine the qualitative element composition of powders and solid. The source of the X-rays is an X-ray tube, including a cathode (C) and an anode (A) (Fig. 3.4). The C is headed, emitting electrons in the direction of the A. The amounts of electrons emitted is linked to the electric current (I) (e.g. higher current equals larger amounts of emitted electrons). The emitted electrons are accelerated due to the voltage (U) between C and A (e.g. higher voltage equals stronger acceleration). In the end, the emitted electrons will collide with A resulting in X-ray emission. The A consist of rhodium (Rh), meaning Rh-radiation is applied for the measurements (Forwick, 2013).

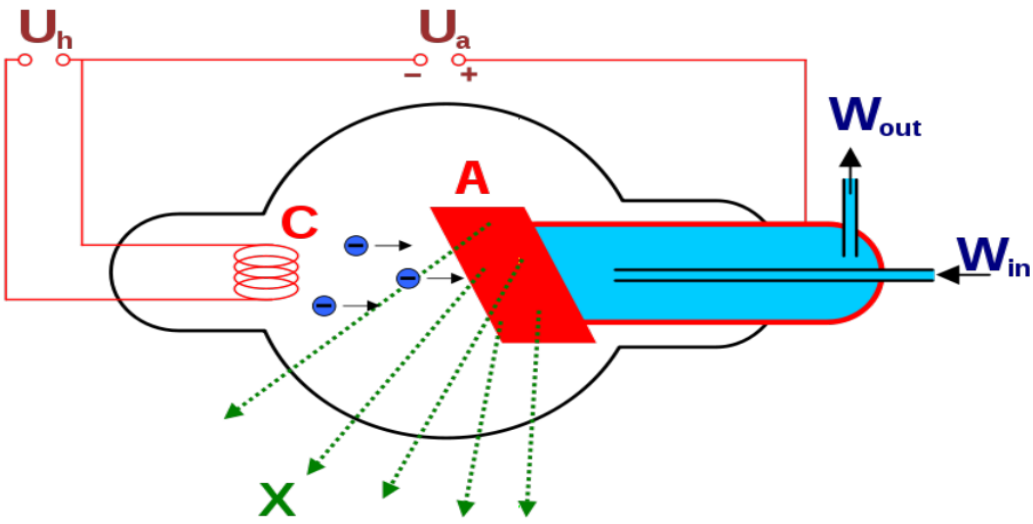

Fig. 3.4: Illustration figure of a water-cooled X-ray tube (Forwick, 2013).

The Avaatech XRF core-scanner includes both a X-ray source, a helium chamber/measuring triangle, and a detector (Fig. 3.5). The measuring triangle "lands" on the sediment surface during data acquisition. The helium chamber is added to the measuring unit, because helium exposes smaller friction on the secondary radiation than air, making it easier to detect lighter elements (e.g. Al and Si). The split core surface is cleaned and covered with a 4 µm thin special foil to avoid desiccation of the sediment and contamination of the XRF measurements unit or the landing triangle (Forwick, 2013).

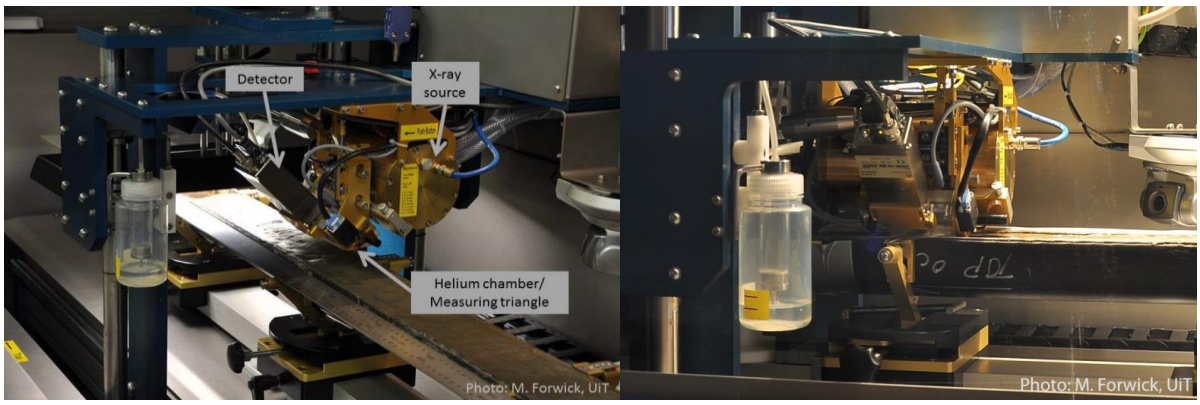

Fig. 3.5: Photos of the Avaatech XRF Core Scanner used in this study. ***Left)*** *detector, X-ray source and helium chamber/measuring triangle mentioned in the text.* ***Right)*** *triangle as it lands on the sediments during measurements (adapted from Forwick (2013)).*

The measurements were performed in two runs, because lighter elements require lower energy, whereas heavier elements require higher energy. In order to measure as many elements as possible, it is usual to perform several runs with different currents, voltages and filters. During scanning of core PS56/029-1, the following parameters were used:

1. 10 kV, 1000 µA, 10 sec, to measure light elements from Mg to Co.
2. 30 kV, 2000 µA, 10 sec, to measure medium-heavy elements from Ni to Mo.

The down-core distance between the measurements was set to 5 mm. The cross-core slit size was set to 12 mm, whereas the down-core slit size was 10 mm.

When all measurements are completed the results are presented in an excel sheet for further work, which include general core information and the respective element-geochemical compositions. The element-geochemical compositions in this study are presented, described, and discussed as trends relative to a calculated "Sum" or through element/element ratios. The "Sum" consists of the 10 most abundant elements for core PS56/029-1. Further work was done through software Grapher 8 and CorelDRAW 2017. Elements measured in core PS56/029-1 include: aluminium (Al), silicon (Si), iron (Fe), sulphur (S), potassium (K), calcium (Ca),

titanium (Ti), chromium (Cr), copper (Cu), zinc (Zn), rubidium (Rb), bromine (Br), zirconium (Zr), strontium (Sr) and manganese (Mn).

3.2.5 Multi-Sensor Core Logger (MSCL)

The core was logged prior to opening with a GEOTEK MSCL (Fig. 3.6), aboard the research vessel Polarstern in 2000 (Thiede and Oerter, 2002). This is a non-destructive core logging method, revealing the physical properties of the sediments in a micro macro perspective (Weber et al., 1997). Parameters includes both actual values (e.g. p-wave velocity and gamma density) and proxies (e.g. magnetic susceptibility, natural gamma) (GEOTEK, 2016; GEOTEK, 2018).

All sensors are calibrated prior to logging in order to avoid erroneous measurements. The cores are logged in room temperature in order to avoid any changes in the physical parameters during logging (Weber et al., 1997). The core sections are placed on the MSCL belt and pushed past the different sensors, which collect data during transportation on the belt (Fig. 3.6) (GEOTEK, 2018).

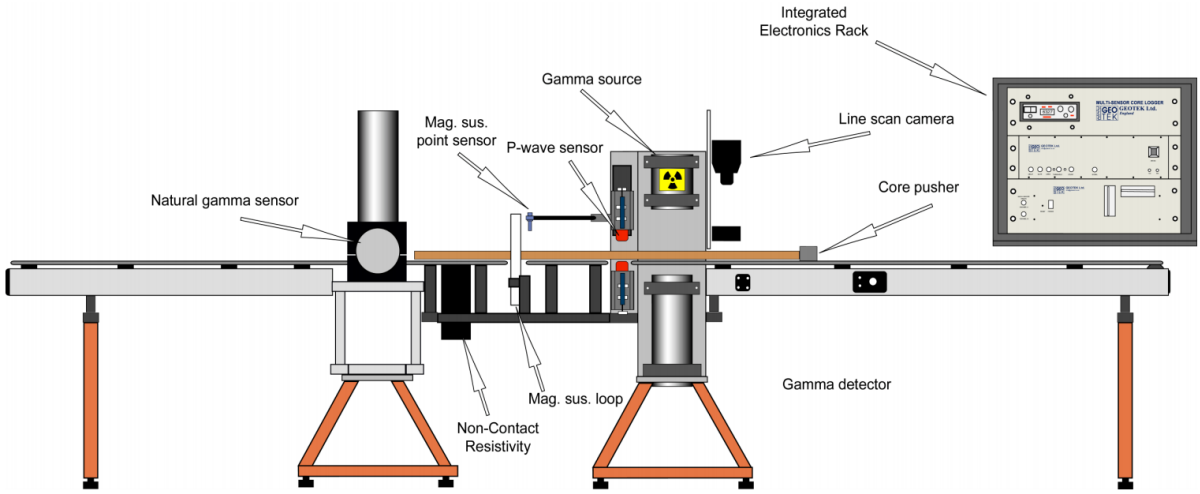

Fig. 3.6: The GEOTEK MSCL, including the main sensors (adapted from GEOTEK (2000)).

3.2.5.1 Temperature measurements

A standard platinum resistance thermometer probe is used to measure temperature and is necessary because changing temperature influence the physical parameters (e.g. p-wave velocity, wet-bulk density and MS are affected by the temperature) (Weber et al., 1997; GEOTEK, 2000). Therefore, all core sections were adjusted to room temperature prior to measurements in order to avoid the influence of temperature changes.

3.2.5.2 Thickness measurements

With the help of two rectilinear displacement transducers attached on the p-wave transducers the thickness can be measured (Gunn and Best, 1998; GEOTEK, 2000). Core thickness is measured relative to a known reference thickness, thus any deviation from this reference thickness is measured. The thickness is then used to calculate p-wave velocity and wet-bulk density (GEOTEK, 2000).

3.2.5.3 Wet-bulk density

Wet-bulk density is a function of wet weight of the material (material plus liquid) divided by wet volume (total volume as a whole).

$$Wet - bulk\ densitiy = \frac{mass}{volume}$$

The operating principle include narrow beams of collimated gamma rays emitted from a ^{137}Cs source and sent through the sediment core within the energy range of 0.662 MeV. The photons penetrating through the core are detected on the opposite side of the core (Gunn and Best, 1998; GEOTEK, 2000). A collimated beam of gamma-rays will be attenuated by Compton scattering as the gamma-rays pass through the sediment core (Evans, 1965). Photons are scattered as they react with electrons, involving a partial energy loss (Weber et al., 1997). Finally, measurement of photons passing through the core unattenuated provide information about the core density. The sensor only measures gamma rays within the same energy range as the source, namely around 0.662 MeV. Logically, a dense medium or a sediment will contain a dense composition of electrons and less photons will be emitted to the receiver (GEOTEK, 2000). In order to calculate the wet-bulk density, the thickness is necessary, described in section 3.2.5.2: Thickness measurements.

3.2.5.4 P-wave amplitude

P-wave amplitude is a measurement of the p-wave intensity when it arrives at the receiver. In order to measure the p-wave velocity, a p-wave pulse is sent through the core from a transducer acting as a transmitter to a receiver transducer on the other side of the core. The p-wave amplitude is normally used to obtain information about the contact between sediments and core liner. This contact will in turn affect both the p-wave amplitude and the p-wave velocity. A low p-wave amplitude reflect a bad contact, and may result in an incorrect p-wave velocity (Forwick, 2001). P-wave amplitude can also reveal porosity, e.g. high values may reflect lower porosity of the sediments (GEOTEK, 2000).

Through this study the p-wave amplitude was used to correct for anomalous p-wave velocities. At depths when the p-wave amplitude was below 80 the p-wave velocity was excluded.

3.2.5.5 P-wave velocity

A p-wave (primary wave) is an elastic body wave, or a seismic wave, also known as a compressional wave. The motion of the particles in the material is the same direction as the wave propagation. The speed of propagation depends on both the density of the medium, the modulus of incompressibility, and modulus of rigidity. The wave can be transmitted through all mediums (GPG, 2017). The p-wave velocity and/or rather changes in p-wave velocities can give important information about the characteristics of the sediments (e.g. Klages (2010)).

The travelling time and traveling distance is recorded before the p-wave velocities are calculated by the equation:

$$Vp = \frac{d}{t}$$

Where Vp is velocity of the wave (m/s), d is distance travelled (m) and t is the time it take to travel distance d (s).

3.2.5.6 Acoustic impedance

When wet bulk density of the core is known the acoustic impedance can be calculated (GEOTEK, 2000). The acoustic impedance is the product of the wet bulk density and the p-wave velocity. The acoustic impedance is calculated by the equation:

$$Z = Vp * \rho$$

Where Z = impedance, V_p = p-wave velocity and ρ = wet bulk density.

3.2.5.7 Magnetic susceptibility (MS)

Magnetic susceptibility (MS) is a dimensionless parameter that measures the degree of a material to be magnetized in response to an applied magnetic field (Mosher, 2007). The MS can have positive values (paramagnetic, ferromagnetic or antiferromagnetic) or negative values (diamagnetic), all depending on whether the magnetic field is strengthened or weakened by the presence of the material. The operating principle in the MS sensor is that an oscillator circuit produces a low intensity, non-saturating, alternating magnetic field. If the material under measuring has a magnetic susceptibility it will change the oscillator frequency (GEOTEK, 2000). These data of pulsed frequency information is converted by the GEOTEK MSCL into

magnetic susceptibilities, as International System of Units (SI) or Centimetre-gram-second system of units (CGS) values (GEOTEK, 2000). In this study SI are used.

Changes observed in the MS are excellent tool for core to core correlation (Jessen et al., 2010). Furthermore, the MS in marine sediments are highly dependent on glacial activity and oceanography (Jessen et al., 2010). Studies of the North Atlantic and Southern Norwegian Sea suggests that the MS are linked to bottom water activity, hence it can indicate deep-water production in the Nordic seas (Rasmussen et al., 1996; Rasmussen et al., 1998; Moros et al., 2002). Occasionally overprinted by alternations concerning the sediment provenance, e.g. dilution with non-magnetic material or input of ice rafted particles with high magnetic material response (Pirrung et al., 2002; Jessen et al., 2010). Additionally, meltwater plumes and mass transportation are reported to alter and influence the MS on glaciated continental margins (Robinson et al., 2000; Rasmussen et al., 2007). Sediments densities linked to local glacial activity also affects MS (e.g. Hillenbrand et al. (2009)). Due to the close correlation to environmental changes the MS can be used as a correlative tool in deep sea sediments on local to global scales (Robinson et al., 1995; Jessen et al., 2010).

3.2.6 Granulometry

Granulometry or a size distribution of grains is a good tool for classifying sedimentary environments (e.g. Sun et al. (2002) and Hass et al. (2010)). Grain size is a fundamental property of a sediment particle, affecting how they are carried from their original position, through transport and deposition (Hass et al., 2010). The following analysis can reveal the sediment provenances, transport history, and depositional conditions (Blott and Pye, 2001). Core PS56/029-1 was sampled with 1 cm interval using a CILAS 1180 laser granulometer in order to obtain a high resolution grain-size distribution.

3.2.6.1 Laser-diffractometry

The CILAS 1180 laser-granulometer (Fig. 3.7) uses a laser diffraction and CCD (charge-coupled device) camera to measure grain-sizes in the sample. The laser-granulometer is able to measure particles in the range of 0.04-2500 µm. Grains larger than > 2500 µm needs to be removed prior to measurements.

When using the CILAS 1180 laser-granulometer a cup containing a mixture of sediments and water is brought directly from the shaker table to the machine, this prevents formation of aggregates. The mixture is gently poured into the machine using a plastic water bottle to gently

flush the material out of the cup. The mixture is mixed in the closed water circle driven by two peristatic pumps. The particles are kept in suspension by an ultrasound, whereas a self-contained water circulation is transporting the particles through the CILAS 1180. The particles are transported through two sequenced measuring cells where laser beams are emitting monochromatic light. As the particles are passing the measuring cells will cause a diffraction angle. This diffraction pattern, characterized by concentric cells, is dependent on the particle grain-size diameter. Larger grain-sizes yield smaller diffraction angles and vice versa. Hence, particles with grain-sizes 0.04 to 500 µm (fine particles) are recorded in the first measuring cell on a photodiode-detection device and particles with grain-sizes 300 to 2500 µm (coarser particles) are recorded in the second measuring cell, where a CCD camera including a digital signal processing unit is located. The signal processing unit displays photo of every grain with the help of a laser beam. The photos are converted with the help of Relatime-Fast-Fourier-Transformation into light spectrum. Lastly, the two spectra (laser diffraction and converted photos) are put together mathematically. The final stage is provided by Fraunhofer approximation or Mie-theory. Raw data is stored on the computer after measuring is done.

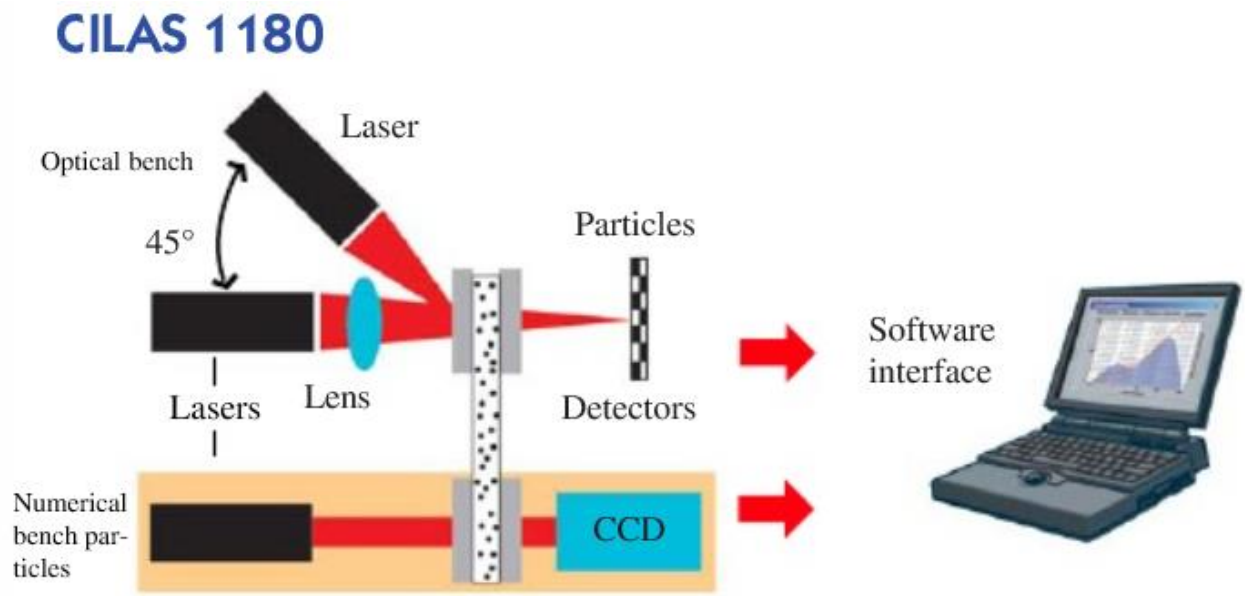

Fig. 3.7: Illustration figure of the CILAS 1180 (adapted from SCRIBD (2018).

After analysis using the CILAS 1180 laser granulometer, the grain size data need to be processed. The CILAS 1180 laser granulometer gives the raw data in a logarithmic scale (ϕ-scale). The equation to convert metric to phi values is based on:

$$\phi = - \log_2 d/d_0$$

Where d (mm) is grain-size and d_0 (mm) is consistent diameter = 1 mm.

This information is further used for calculation in Matlab 7.6, to bring the measurements in order into one single file. Finally, the data are inserted into the program GRADISTAT 4.0 (Blott and Pye, 2001), converting 200 samples each time, because the program only can covert 200 samples in one arithmetic procedure.

The data is further processed using Excel. Grain-size statistics using GRADISTAT can include e.g. the mean, mode, skewness and sorting (Blott and Pye, 2001). These statistics can yield valuable information about the depositional environment of the sediment. The four grain-size parameters are explained below.

Mean size (M_G) (Table 3.2): Mean size indicates the average size of the sediment, which explain the kinetics energy involved when sediments are deposited. High velocity of the depositional process will result in an average size of coarser particles, and vice versa (Sahu, 1964). The mean is calculated by using the formula below:

$$M_G = \exp\frac{lnP_{16} + lnP_{50} + lnP_{84}}{3}$$

Where P_{16}, P_{50} and P_{84} are the exact grain-size value of the cumulative curve at 16, 50 and 84 percent, respectively (Folk and Ward, 1957).

Sorting (σ_G) (Table 3.3): The sorting (standard deviation) reflects how the different grain sizes are spread out compared to the average and indicates changes in the kinetic energy of depositional process compared to the average (Blott and Pye, 2001). Good sorting reflects relatively stable conditions, meaning small variations in the sedimentary processes. Unstable conditions mean different processes are involved in order to deposit these sediments, and will result in poor sorting (Sahu, 1964). The standard deviation is expressed by the formula:

$$\sigma_G = \exp(\frac{lnP_{16} - lnP_{84}}{4} + \frac{lnP_5 - lnP_{95}}{6.6})$$

Where P_5, P_{16}, P_{84} and P_{95} are the exact grain-size value of the cumulative curve at 5, 16, 84 and 95, respectively (Folk and Ward, 1957).

Skewness (Sk_G) (Table 3.3): Skewness measures the shape of the grain-size distribution curve. It explains if it is a symmetrical curve or if the grain sizes are deflected to one or the other side away from the average. For example if the curve leans towards the coarser side from the average, it is considered as coarsely-skewed, meaning a lower energy process of deposition than the mean is involved. Finely-skewed has a curve that bends towards the finer side from the average, indicating that the process of deposition has a higher energy than the average (Sahu, 1964). Skewness is expressed by the formula:

$$Sk_G = \frac{lnP_{16} + lnP_{84} - 2(lnP_{50})}{2(lnP_{84} - lnP_{16})} + \frac{lnP_5 + lnP_{95} - 2(lnP_{50})}{2(lnP_{25} - lnP_5)}$$

Where P_5, P_{16}, P_{25}, P_{50}, P_{84} and P_{95} are the exact grain-size value of the cumulative curve at 5, 16, 25, 50, 84 and 95, respectively (Folk and Ward, 1957).

Kurtosis (K_G) (Table 3.3): Kurtosis measures the degree of concentration of the grains compared to the average. It shows if the shape of the grain-size distribution curve is flat or peaked. It is the measure of the ratio of the sorting, in the interval of central 90% to the central 50% of the distribution (Sahu, 1964). For example if the K_G is 1.00 (normal Gaussian curve), it means that the sorting in the tails of the curve equals that of the central parts (Folk and Ward, 1957). High numbers of kurtosis increase the likelihood that the distribution is well sorted, and visa versa (Cadigan, 1961). Kurtosis is expressed by the formula:

$$K_G = \frac{lnP_5 - lnP_{95}}{2.44\,(lnP_{25} - lnP_{75})}$$

Where P_5, P_{25}, P_{75} and P_{95} are the exact grain-size value of the cumulative curve at 5, 25, 75 and 95, respectively (Folk and Ward, 1957).

The descriptive terminology used in this thesis is adapted from the terminology used in GRADISTAT taken from Blott and Pye (2001) (Table 3.2).

Table 3.2: Descriptive terminology adapted in the GRADISTAT program, modified from Udden (1914) and Wentworth (1922), Friedman and Sanders (1978) (Blott and Pye, 2001).

Grain size		Descriptive terminology			
phi	mm/μm	Udden (1914) and Wentworth (1922)	Friedman and Sanders (1978)	GRADISTAT program	
			Very large boulders		
−11	2048 mm				
			Large boulders	Very large	
−10	1024				
			Medium boulders	Large	
−9	512	Cobbles			
			Small boulders	Medium	Boulders
−8	256				
			Large cobbles	Small	
−7	128				
			Small cobbles	Very small	
−6	64				
			Very coarse pebbles	Very coarse	
−5	32				
			Coarse pebbles	Coarse	
−4	16	Pebbles			
			Medium pebbles	Medium	Gravel
−3	8				
			Fine pebbles	Fine	
−2	4				
		Granules	Very fine pebbles	Very fine	
−1	2				
		Very coarse sand	Very coarse sand	Very coarse	
0	1				
		Coarse sand	Coarse sand	Coarse	
1	500 μm				
		Medium sand	Medium sand	Medium	Sand
2	250				
		Fine sand	Fine sand	Fine	
3	125				
		Very fine sand	Very fine sand	Very fine	
4	63				
			Very coarse silt	Very coarse	
5	31				
			Coarse silt	Coarse	
6	16	Silt			
			Medium silt	Medium	Silt
7	8				
			Fine silt	Fine	
8	4				
			Very fine silt	Very fine	
9	2	Clay			
			Clay	Clay	

Table 3.3: Classification of sediments according to sorting (σ_G), skewness (SK_G) and kurtosis (K_G). A classification modified from Folk and Ward (1957) (Blott and Pye, 2001).

Sorting (σ_G)		Skewness (Sk_G)		Kurtosis (K_G)	
Very well sorted	<1·27	Very fine skewed	$^{-}$0·3 to $^{-}$1·0	Very platykurtic	<0·67
Well sorted	1·27–1·41	Fine skewed	$^{-}$0·1 to $^{-}$0·3	Platykurtic	0·67–0·90
Moderately well sorted	1·41–1·62	Symmetrical	$^{-}$0·1 to $^{+}$0·1	Mesokurtic	0·90–1·11
Moderately sorted	1·62–2·00	Coarse skewed	$^{+}$0·1 to $^{+}$0·3	Leptokurtic	1·11–1·50
Poorly sorted	2·00–4·00	Very coarse skewed	$^{+}$0·3 to $^{+}$1·0	Very leptokurtic	1·50–3·00
Very poorly sorted	4·00–16·00			Extremely leptokurtic	>3·00
Extremely poorly sorted	>16·00				

3.2.6.2 Sub-sampling

In order to obtain the grain-size distribution on gravity core PS56/029-1 some preparations needed to be carried out. The working half of gravity core PS56/029-1 was sub-sampled with one cm intervals, from the top (1= 0 – 1 cm) to the bottom (1267 =1266 – 1267 cm). The sampling was performed at AWI, Bremerhaven, Germany. For each centimetre, a small sediment amount was sampled and placed in a box with just enough water to cover the sediment. The water was added to prevent the sediments to dry out during transportation to AWI on List, Sylt, Germany, for the actual measurements.

3.2.6.3 Preparations

To achieve a grain-size distribution of good quality throughout the core, the particle size analyser CILAS 1180 laser-granulometer was used (Fig. 3.7).

Before the samples could be measured in the CILAS 1180 laser-granulometer, they were chemically treated in order to avoid erroneous measurements. Both organic and calcareous components need to be removed in order to get a clear pristine siliclastic signal. Additionally, it is important that all samples are free of aggregates before being measured. The first step of the chemical treatment was to add 96%-acetic acid (CH_3COOH), in a proportion 1:3 with water in order to remove calcareous components. The samples were left over night in order to dissolve all calcareous contents. The acid was removed through suction before treated with water in a two-step process. The two-step water process was performed to be sure all acid was removed from the sediments. Water was added and left until the sediments had settled to the bottom of the cup, the water could then be removed through suction. This process was performed two times to be sure all acid was removed. Organic components in the samples were removed with hydrogen peroxide (H_2O_2) in a proportion 1:3 with water. The two-step rinsing process performed after the acid treatment was repeated after the hydrogen peroxide treatment. Afterwards, sodium polyphosphate [$(NaPO_3)n$] was added to avoid any aggregates from

forming. After the chemical treatment, the samples were left on the shaker for 24 hours (with 110 rotations per minute) before placing them into the ultrasonic bath for 10 minutes in order to dissolve all aggregates. Due to the relatively fine particles in core PS56/029-1 (high amounts of clay that are cohesive) the aggregates were not completely dissolved and could therefore not be measured directly through the CILAS 1180. To eliminate this issue, each sample was freeze dried in order to dissolve them completely, which successfully removed the last aggregates. The samples were then put on the shaker before placed in the ultrasonic bath in preparation for the measurements.

4 Lithostratigraphy

In the following chapter, the results obtained with methods presented in Chapter 3: Materials and Methods are presented.

4.1 Introduction

The 12.67 m long gravity core PS56/029-1 was retrieved from a levee in the central part of a large channel system in the RLS at c. 4000 m water depth and c. 200 km offshore Princess Ragnhild Coast (Fig. 4.1). The core site was chosen with the goal of retrieving sediments from mass-transported (turbidites) and pelagic deposits (pelagites and contourites), deposits which can yield useful information about the paleoenvironment of the area (*see Chapter 2*).

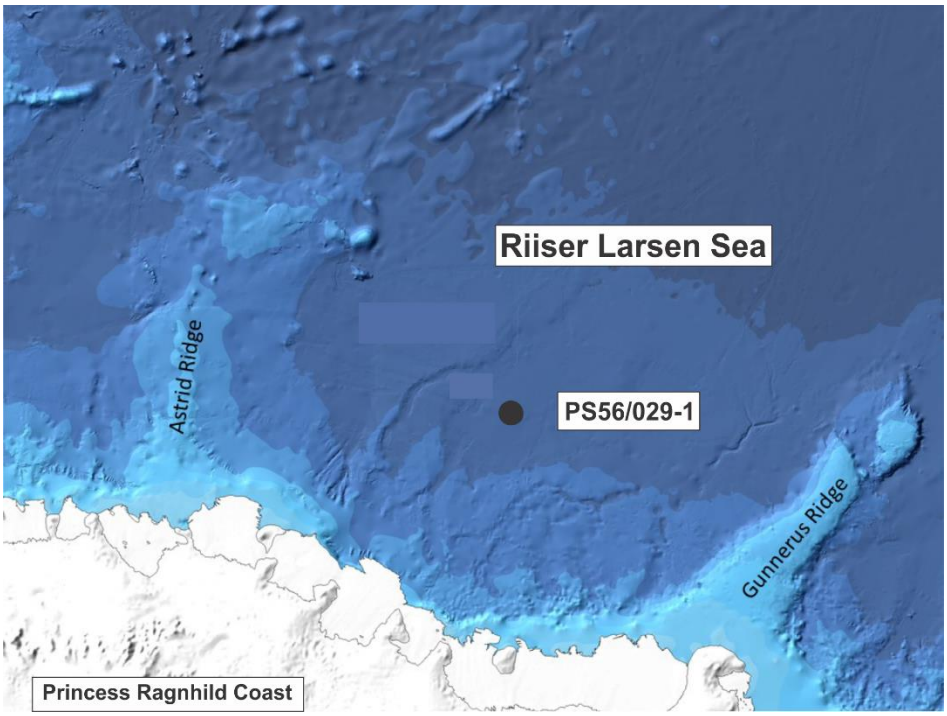

Fig. 4.1: Map of the RLS, including core location of PS56/029-1 (68°00.03' S and 020°45.13' E) displayed with a black circle.

By compiling results from visual core description, X-radiographs, line-scan images, element geochemical, physical properties, and granulometry of core PS56/029-1 five lithofacies were distinguished. Description and presentation of the five lithofacies are further used to distinguish glacial/interglacial cycles. Due to the repetitive alternation of layers it was deemed more appropriate to described the core through lithofacies instead of dividing the core into units.

4.1.1 Lithological logs / visual core description

The lithological log is based on interpretation of the sediment surface (e.g. colour variations, sedimentary structures, lithological transitions, presence and absence of foraminifera…). It is also supported by X-radiographs (e.g. lamination, changes in lithology and ice-rafted debris (IRD)) and line-scan images (e.g. bioturbation, changes in lithology and sharp lower boundaries) together with results obtained from grain-size analysis. The lithological log is presented together with line-scan images in figure 4.2. Colours are based on MUNSELLs colour chart and due to the frequent changes in colour, only the most prominent colours are displayed in the lithological log (Fig. 4.2). Alternating coloured intervals of olive greyish (5Y 5/2), dark greyish brown (2.5 Y 4/2) and dark greyish (5Y 4/1) are observed throughout the core.

The lithological log also contains multiple lithofacies, which are distinguished and described below (*see Chapter 4.1.11*). Foraminifera and stones are marked as individual features in the log. The sediment core's matrix is presented by its widths and consists mostly of mud. Hence, the legend in figure 4.2 only shows the description of mud, due to the lack of coarser sediments.

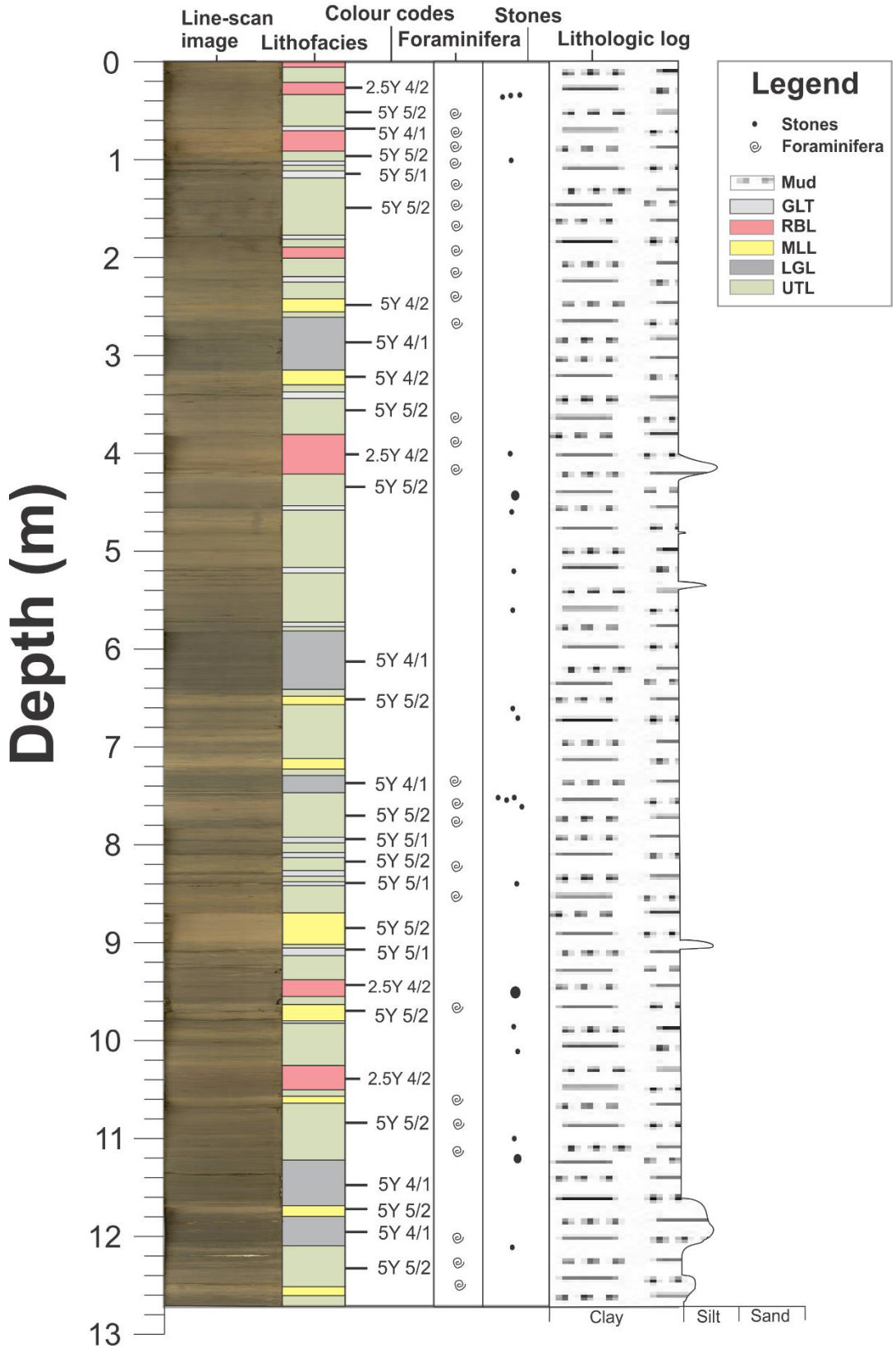

Fig 4.2: Lithological log of core PS56/029-1, including line-scan image, lithofacies (GLT – Grey Layer Thin, RBL – Red Brown Layer, MLL – Massive Lighter Layer, LGL – Laminated Grey Layer and UTL – Undefined Transition Layer), Munsell colour codes (2.5 Y 4/2 – dark greyish brown, 5Y 5/1 – grey, 5Y 5/2 – olive grey, 5Y 4/2 – olive grey and 5Y 4/1 – dark grey) and the occurrences of foraminifera and stones.

4.1.2 Grain-size analysis

Volume percentages of clay, silt, sand and sortable silt (10-63µm) are presented vs. depth in figure 4.3. Grain-size parameters (mean, sorting, skewness and kurtosis) and mode(s) are presented vs. depth in figure 4.4. Mean (0-8 µm) and sortable silt (10-63 µm) are presented vs. depth in figure 4.5. Sortable silt (10-63 µm) including the five lithofacies, which are Laminated Grey Layer (LGL), Grey Layer Thin (GLT), Massive Lighter Layer (MLL), Red Brown Layer (RBL) and Undefined Transition Layer (UTL), are presented vs. depth in figure 4.6. Mean (0-8 µm) with depths of coarser grain-sizes presented vs. depth in figure 4.7. Volume percentages of silt and silt 5 point running mean together with the five lithofacies LGL, GLT, MLL, RBL and UTL are presented vs. depth in figure 4.8.

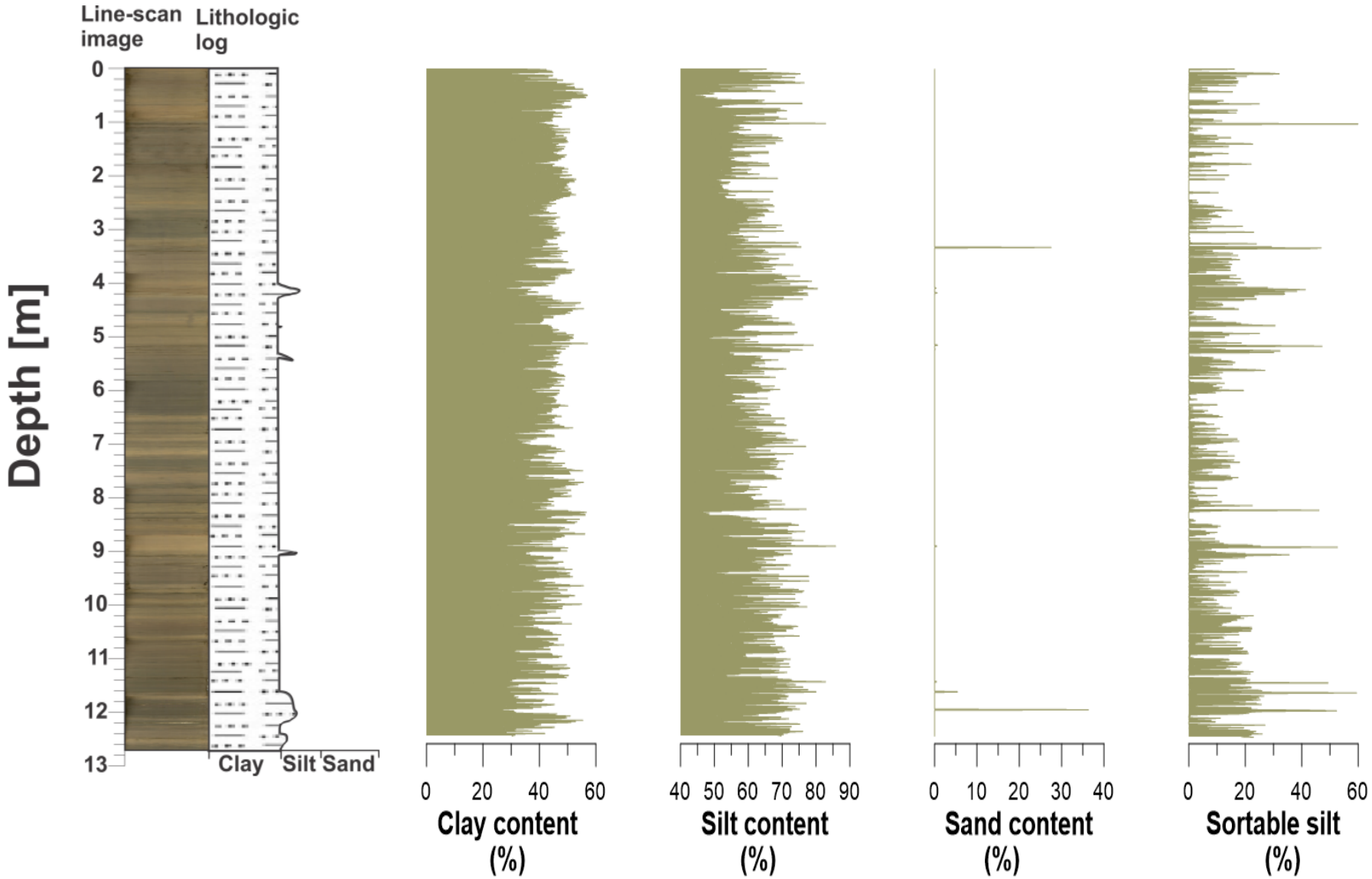

Fig. 4.3: Line-scan image, lithological log and volume percentages of clay, silt, sand and sortable silt plotted vs. depth.

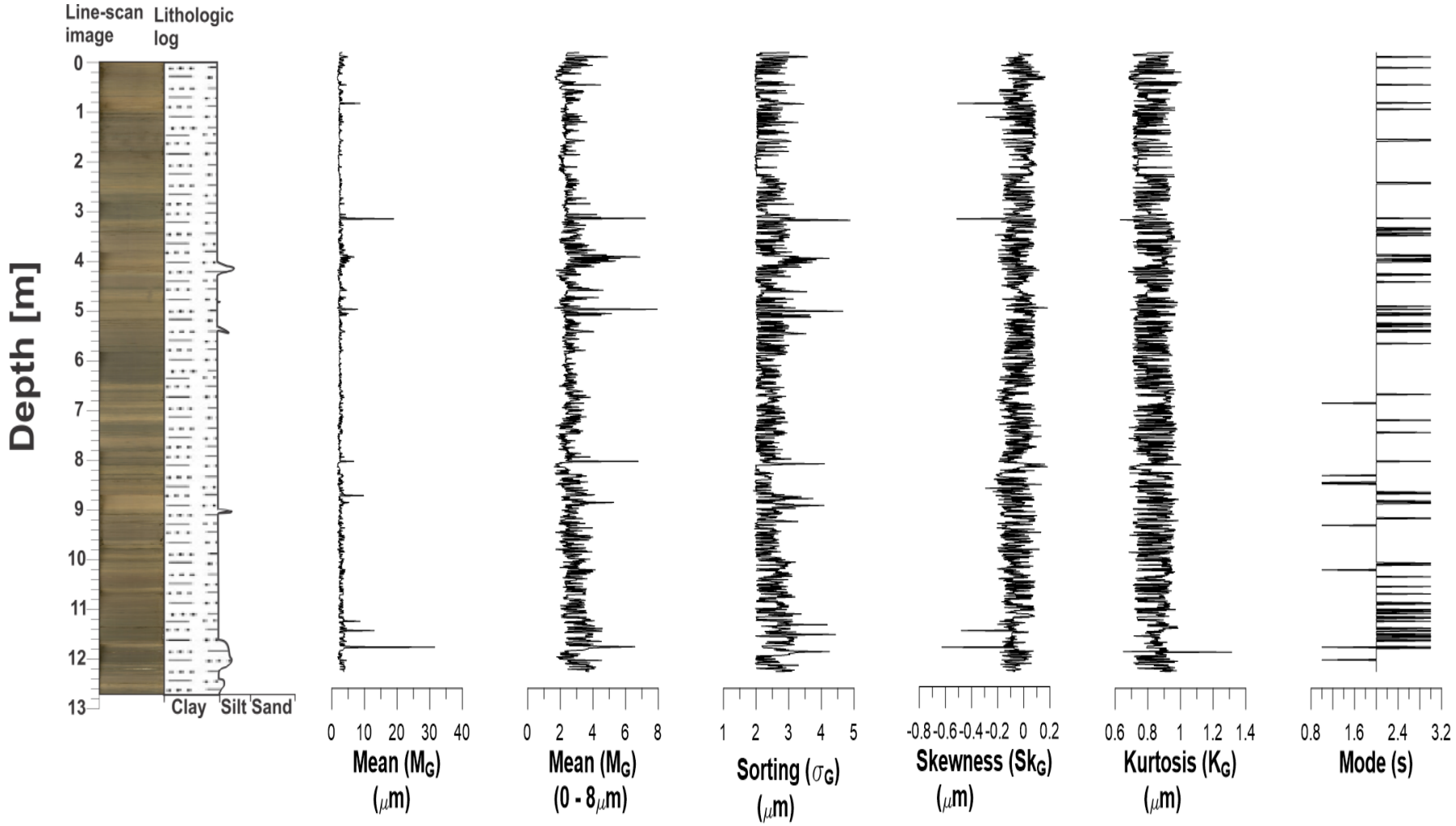

Fig. 4.4: Line-scan image, lithological log, mean (μm), mean (0-8 μm), sorting (μm), skewness (μm), kurtosis (μm) and mode(s) plotted vs. depth.

Volume percentages of clay, silt, sand and sortable silt (Fig. 4.3): Core PS56/029-1 consists mostly of clay and silt, with volume percentages 14.53-57.09 and 43.2-85.8, respectively. Sand is a minor component throughout the core, only present at three individual depths. These are 1216 cm, 1182 cm and 340 cm, with volume percentages 36.35, 5.42 and 27.53, respectively. Volume percentages of sortable silt (10-63μm) fluctuate between 0 and 59.97, where the calculated average volume percentage of sortable silt (10-63 μm) is 5.63. The sortable silt (10-63 μm) fraction increases at depths between 1219-1146 cm, 926-902 cm, 836 cm, 537-525 cm, 436-414 cm, 339-337 cm, 104 cm and 27-8 cm, with volume percentages between 0-59.44, 0-52.7, 46.15, 0-47.3, 0-41.3, 2-46.9, 59.97 and 0-32.05, respectively.

Mean (M_G) (Fig. 4.4): The average geometrical mean (μm) calculated by GRADISTAT varies between 2 and 8 μm, with lower exceptions of 1.5 μm and higher exceptions of 31.5 μm, where the average grain-size is 2.7 μm. Values indicating clay (< 2 μm) to silt (2 – 63 μm) in size. Grain-size fluctuations are detected throughout the 12.67 m long core, fluctuating from clay to very coarse silt. A coarser grain-size distribution is detected at depths between 1217-1214 cm, 1183-1182 cm, 1163-1162 cm, 906 cm, 836 cm, 525-524 cm, 427-417 cm, 340-337 cm and 104 cm, with grain-sizes between 4.22-31.56, 4.55-13, 4.1-8.7, 9.77, 6.78, 4.1-7.94, 2.4-6.89, 2.4-19 and 8.7 (μm), respectively.

Mean (0-8 μm) (Fig. 4.4) shows the fluctuations of the bulk of the cores sediments, with values between 0 and 8 μm, excluding higher exceptions in order to present the fluctuations within the core better.

Sorting (σ_G) (Fig. 4.4): The average geometrical sorting (μm) calculated by GRADISTAT varies between 2 and 5 μm (moderately to poorly sorted). Most samples are poorly sorted, while only a few are very poorly sorted and moderately sorted. The sorting signal fluctuate throughout the core, with increased level of sorting detected at depths between 1222-1212 cm, 1187-1181 cm, 1165-1163 cm, 923-917 cm, 836 cm, 530-524 cm, 437-414, 345-337 cm and 20-0 cm, including values between 2-4.3, 2-4.4, 2.2-4.2, 2.6-4.1, 4.1, 2-4.7, 2.2-4.2, 2-4.9 and 2-3.5 (μm), respectively.

Skewness (SK_G) (Fig. 4.4): The average geometrical skewness (μm) calculated by GRADISTAT varies between -0.2 and +0.1 (μm), with lower exceptions of -0.628 (μm) and higher exceptions of +0.182 (μm). Values indicating very fine skewed (-0.3 to -1.00), fine skewed (-0.3 to -0.1), symmetrical (-0.1 to +0.1) and coarse skewed (+0.1 to +0.3) sediments.

The skewness signal changes from very fine skewed to symmetrical skewed throughout the core. Coarse skewed sediments are present, but is a minor component. The core consists of sediments that are positively (very fine skewed and fine skewed) to symmetrically skewed.

Kurtosis (K_G) (Fig. 4.4): The average geometrical kurtosis (µm) calculated by GRADISTAT varies between 0.7 and 1.0 (µm), with lower exceptions of 0.63 and higher exceptions of 1.32. The core consists of sediments that are very platykurtic (<0.67), platykurtic (0.67-0.90), mesokurtic (0.90-1.11) and leptokurtic (1.11-1.5).

Mode(s) (Fig. 4.4): The mode(s) calculated by GRADISTAT varies between unimodal and trimodal, where the dominate mode(s) signal is bimodal. The unimodal signal is absent between 716 cm and up, while present from 717 cm and down. The unimodal signal include nine individual depths, where the average grain-size is 11.3 µm (minimum: 3.3 µm, maximum: 70.4 µm). The bimodal signal include 1172 individual depths, where the average grain-size is 4.9 µm (minimum: 1.5 µm, maximum: 14.3 µm). The trimodal signal is present throughout the core, but increases from 1000 cm and down. The trimodal signal include 83 individual depths, where the average grain-size is 9.6 µm (minimum: 1 µm, maximum: 37.7 µm).

To summarize, core PS56/029-1 consists of poorly-sorted clay to fine silt sediments and include sediments that are positively to symmetrical skewed and platykurtic to mesokurtic. The polymodal signal include unimodal to trimodal signals, where bimodal predominates.

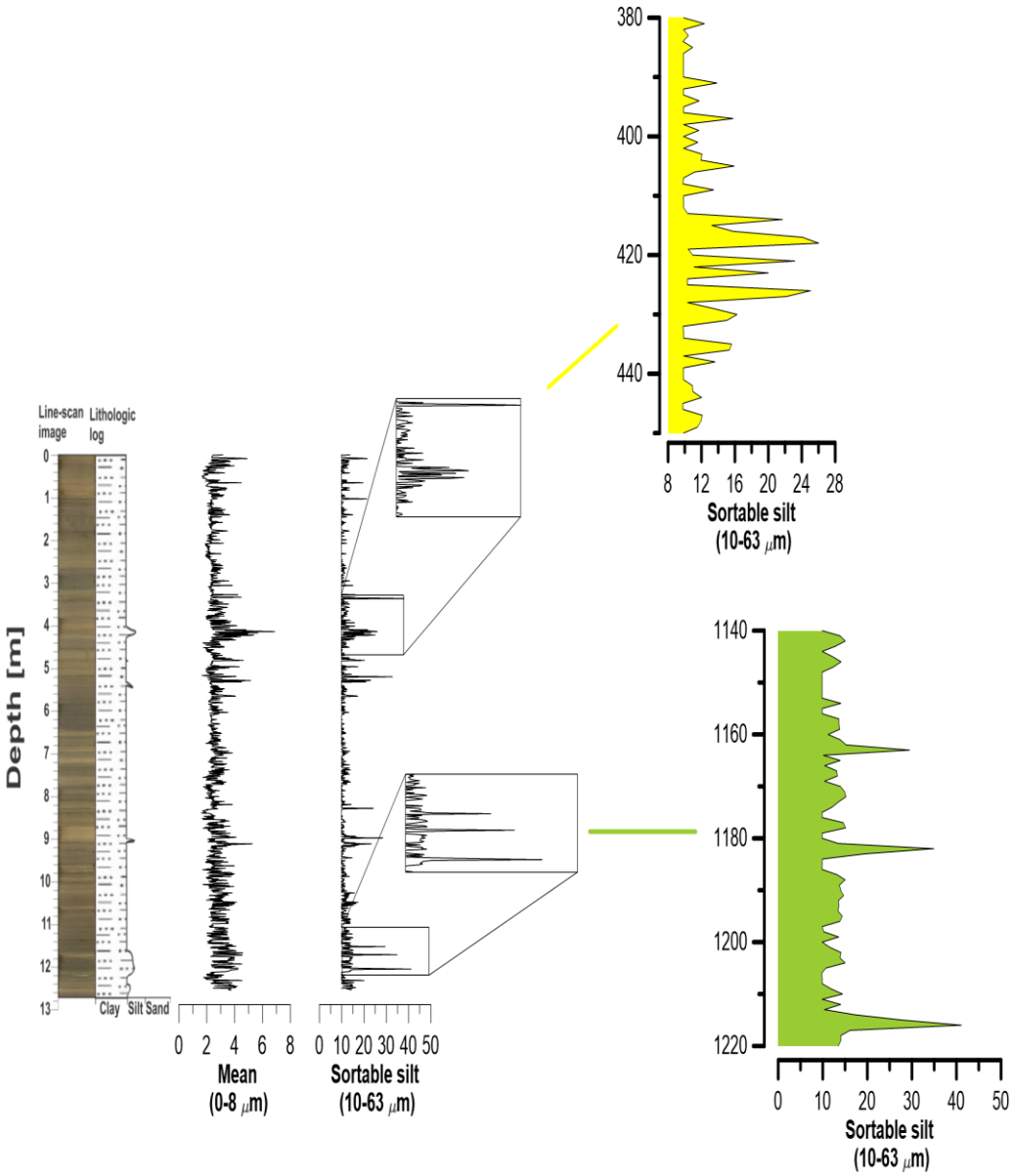

Fig. 4.5: Line-scan image and lithological log together with mean (0-8 μm) and sortable silt (10-63μm) plotted against depth.

The sortable silt fraction include grain-sizes between 10 and 63 µm. Two individual depths of increased sortable silt are detected at 1220-1140 cm and 450-380 cm, highlighted in figure 4.5. The average grain-size for sortable silt (10-63 µm) throughout the core is 11.07 µm. The sortable silt at 1220-1140 cm (highlighted in green in figure 4.4) fluctuate between 10 and 40 µm with three higher peaks. Where depths between 1220-1210 cm, 1190-1180 cm and 1175-1160 include grain-sizes up to 40 µm, 35 µm and 30 µm, respectively. The sortable silt at 450-350 cm (highlighted in yellow in figure 4.4) fluctuate between 10 and 26 µm.

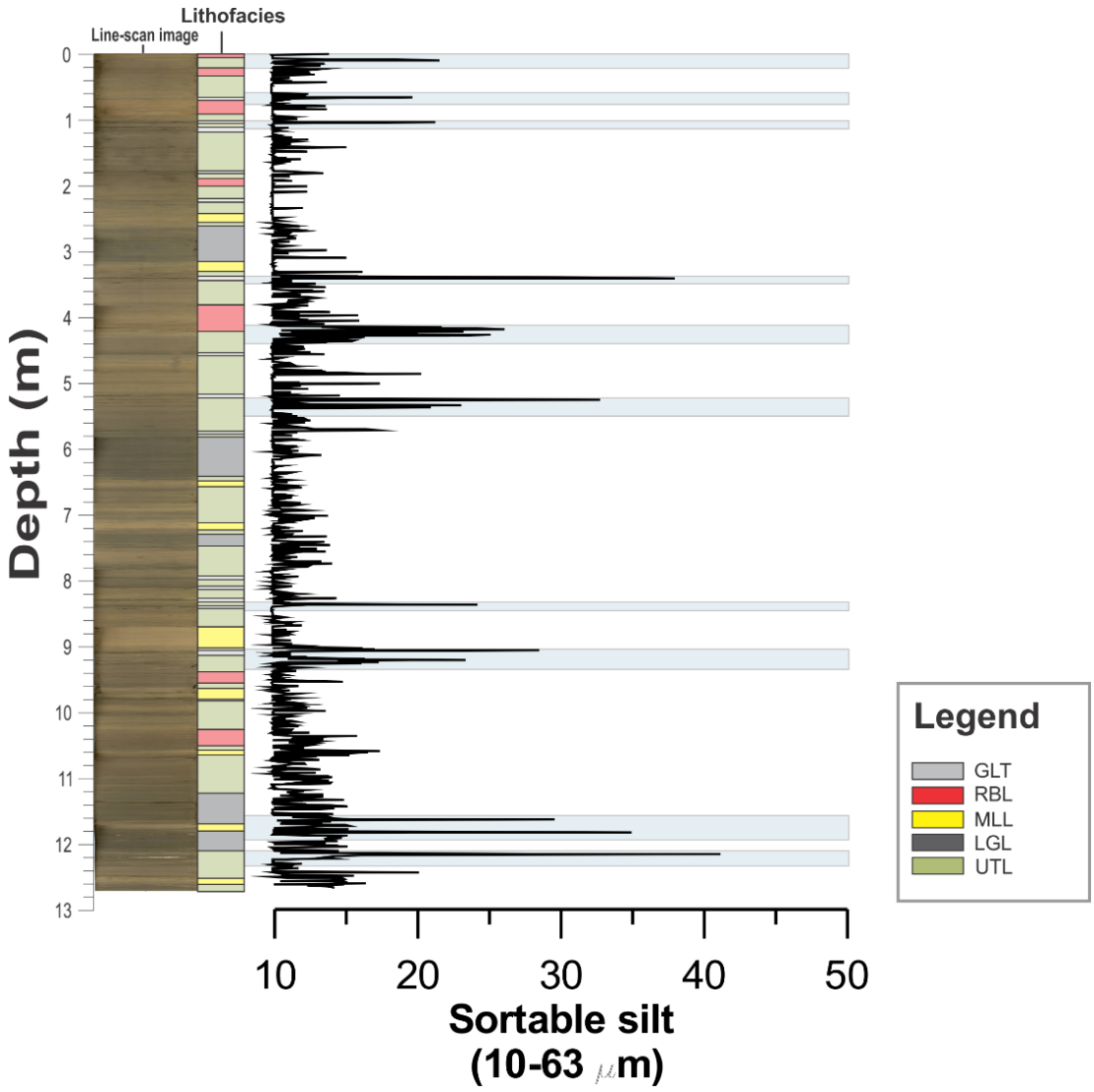

Fig. 4.6: Line-scan image, lithofacies and sortable silt (μm) plotted against depth. Depth of increased sortable silt are highlighted with blue rectangles.

The sortable silt (10-63 μm) signal is present in all lithofacies distinguished for core PS56/029-1 (Fig. 4.6), but increases to higher values for lithofacies GLT.

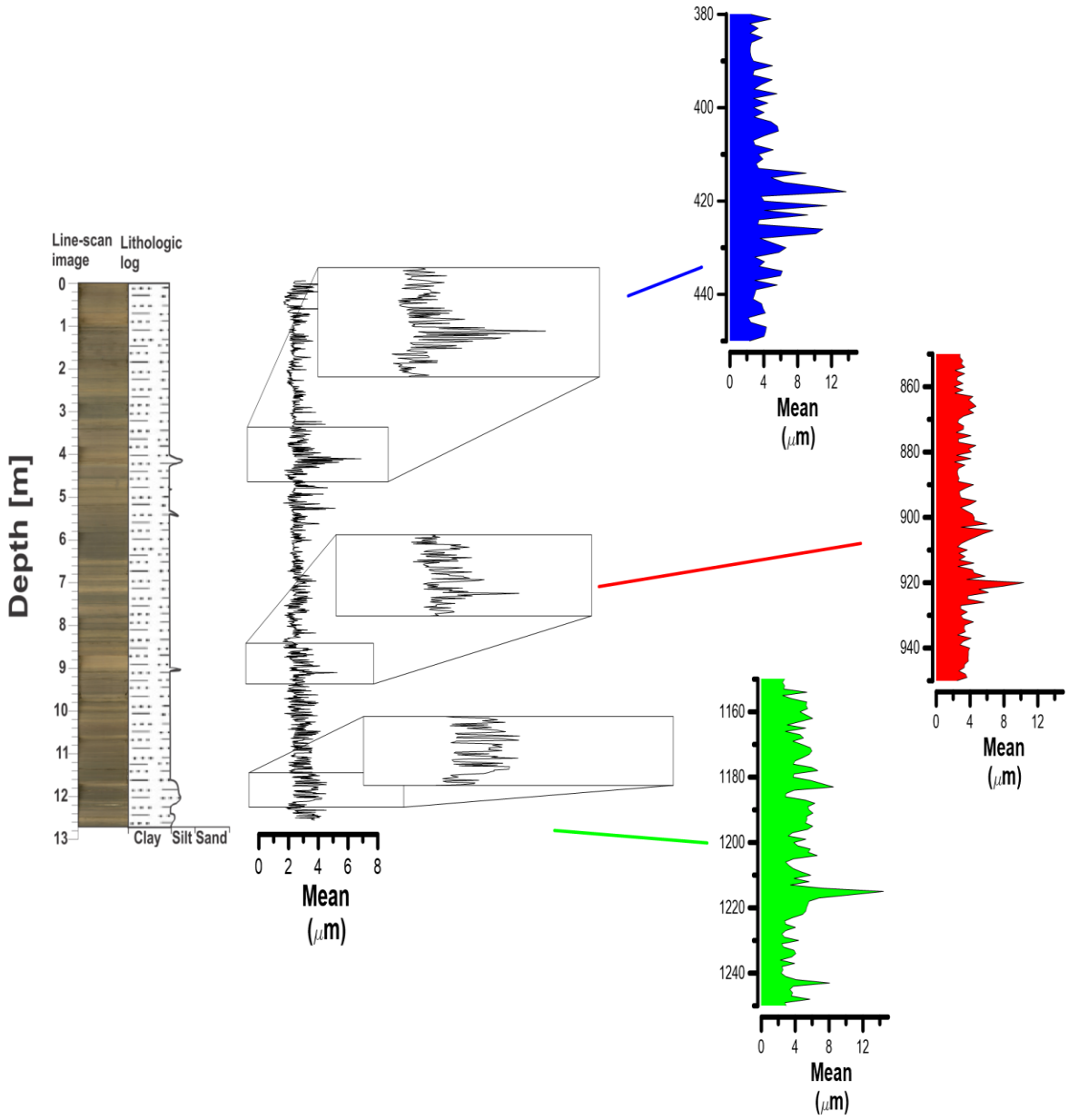

Fig. 4.7: Line-scan image, lithological log and mean (μm) plotted against depth. Including three individual depths with a coarser grain-size distribution.

A coarser grain-size distribution is detected at three individual intervals, located at depths between 1240-1160 cm, 940-860 cm and 440-380 cm (Fig. 4.7). The coarser grain-size distribution include grain-sizes up to 13 µm, 10 µm and 13 µm, respectively.

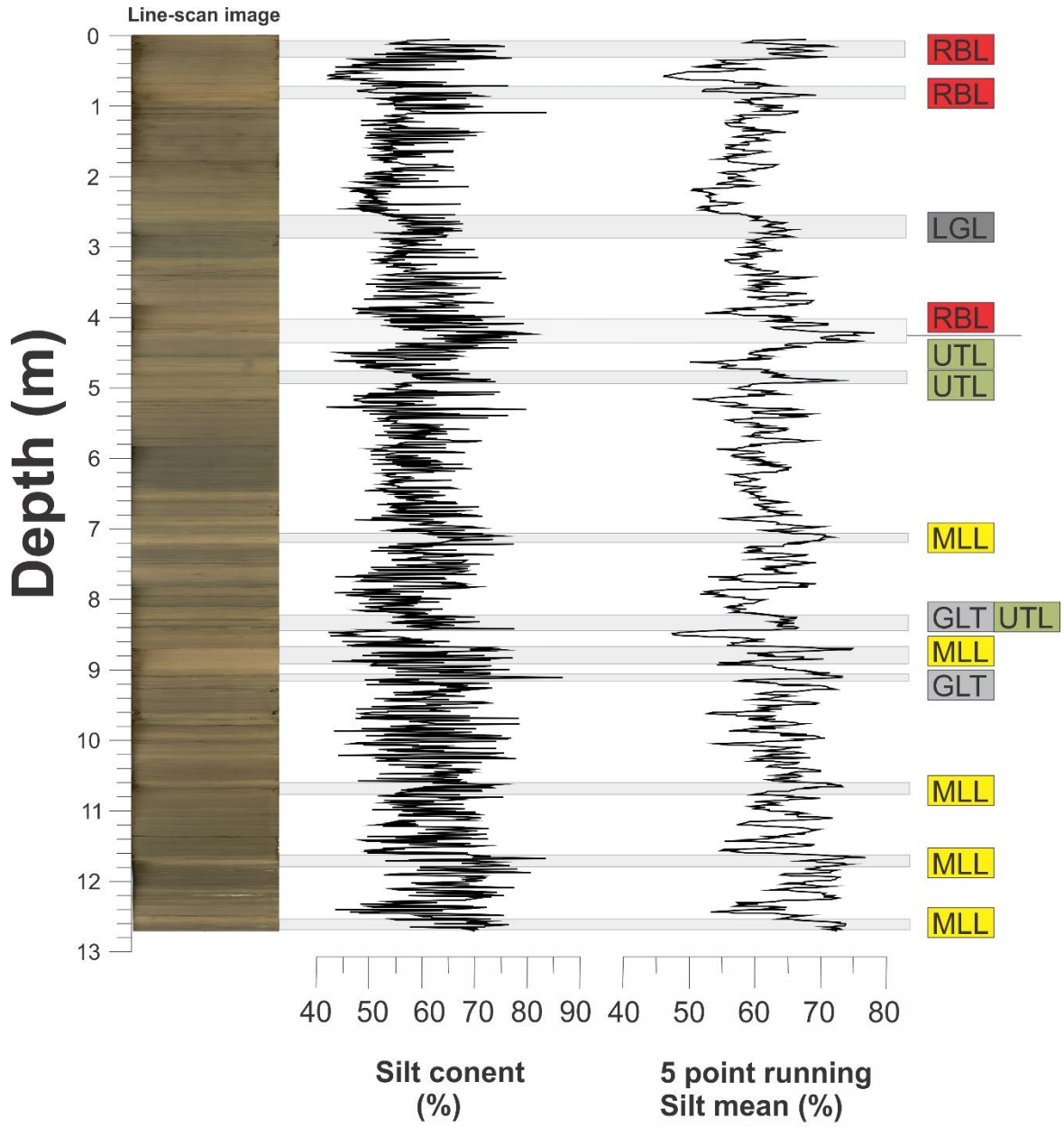

Fig. 4.8: Line-scan image, volume percentages of silt and silt 5 point running silt mean plotted vs. depth. Including the five lithofacies Red Brown Layer (RBL), Massive Lighter Layer (MLL), Grey Layer Thin (GLT, Laminated Grey Layer (LGL) and Undefined Transition Layer (UTL).

Volume percentages of silt as the dominate grain-size in core PS56/029-1 (Fig. 4.3) are plotted against volume percentages of 5 point running silt mean, including lithofacies RBL, MLL, GLT, LGL and UTL (Fig. 4.8). Volume percentages of 5 point running silt mean increases at depths between 413-400 cm, 85-70 cm and 30-5 cm associated with lithofacies RBL, including volume percentages between 62 and 78. Volume percentages of 5 point running silt mean increases at depths 1264-1250 cm, 1180-1160 cm, 1080-160 cm and 720-705 cm associated with lithofacies MLL, including volume percentages between 55 and 75. Volume percentages

of 5 point running silt mean increases at depths 287-250 cm associated with lithofacies LGL, including volume percentages between 60 and 67. Volume percentages of 5 point running silt mean increases at depths 915-905 cm and 845-823 cm associated with lithofacies GLT, including volume percentages between 60 and 66. Volume percentages of 5 point running silt mean increases at depths 845-823, 495-478 cm and 418-413 cm associated with lithofacies UTL, including volume percentages between 58 and 73. Volume percentages of 5 point running silt mean increases to higher percentages more frequently in association with MLL and RBL compared to GLT, LGL and UTL (Fig. 4.8).

4.1.3 Physical properties

Magnetic susceptibility (10^{-8} SI (m^3/kg)), p-wave amplitude, p-wave velocity (m/s), wet-bulk density (g/cm^3) and acoustic impedance (g*m*cm^{-3}*s^{-1}) are presented vs. depth in figure 4.9. Changes in physical properties are used to desbribe and distinquish the five lithofacies distiguished in core PS56/029-1.

4.1.4 Element geochemical properties

The element geochemistry is presented in element/sum and element/element ratios plotted vs. depth in figure 4.10 and 4.11 *(see chapter 3.2.4*). Chlorine, phosphor and rhodium are not included because these signals would be misleading (e.g. Tjallingii et al. (2007) and Forwick (2013)). Chlorine is present in seawater, whereas phosphor and rhodium are present in the XRF core scanner, hence the measured amount of these elements will not exclusively represent the geochemical composition of the sediment. Changes in the element ratios (element/sum and element/element) are used to described and distinguish the five lithofacies in core PS56/029-1.

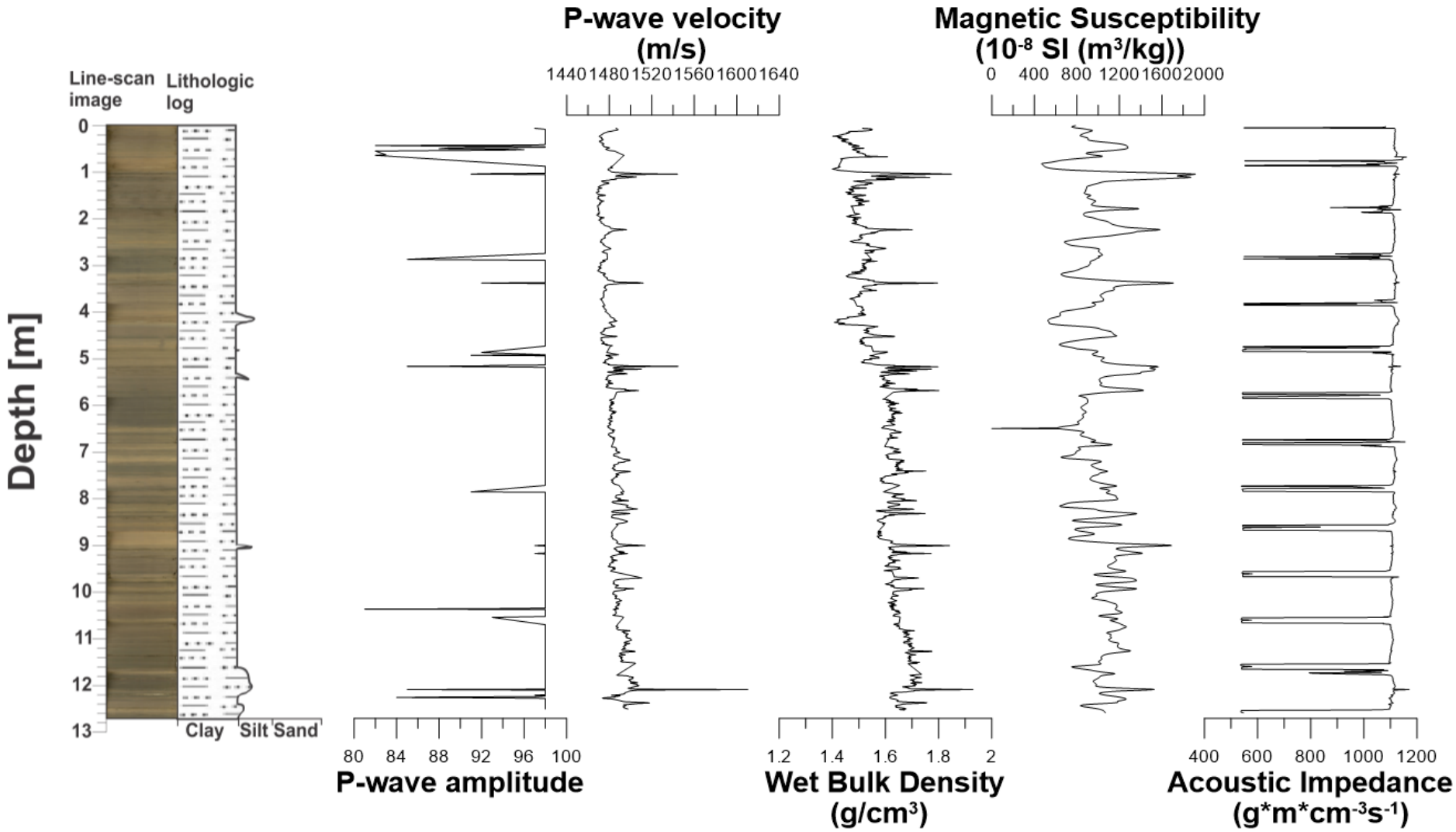

Fig. 4.9: Line-scan image, lithological log and physical properties (p-wave amplitude, p-wave velocity, magnetic susceptibility and acoustic impedance) plotted vs. depth.

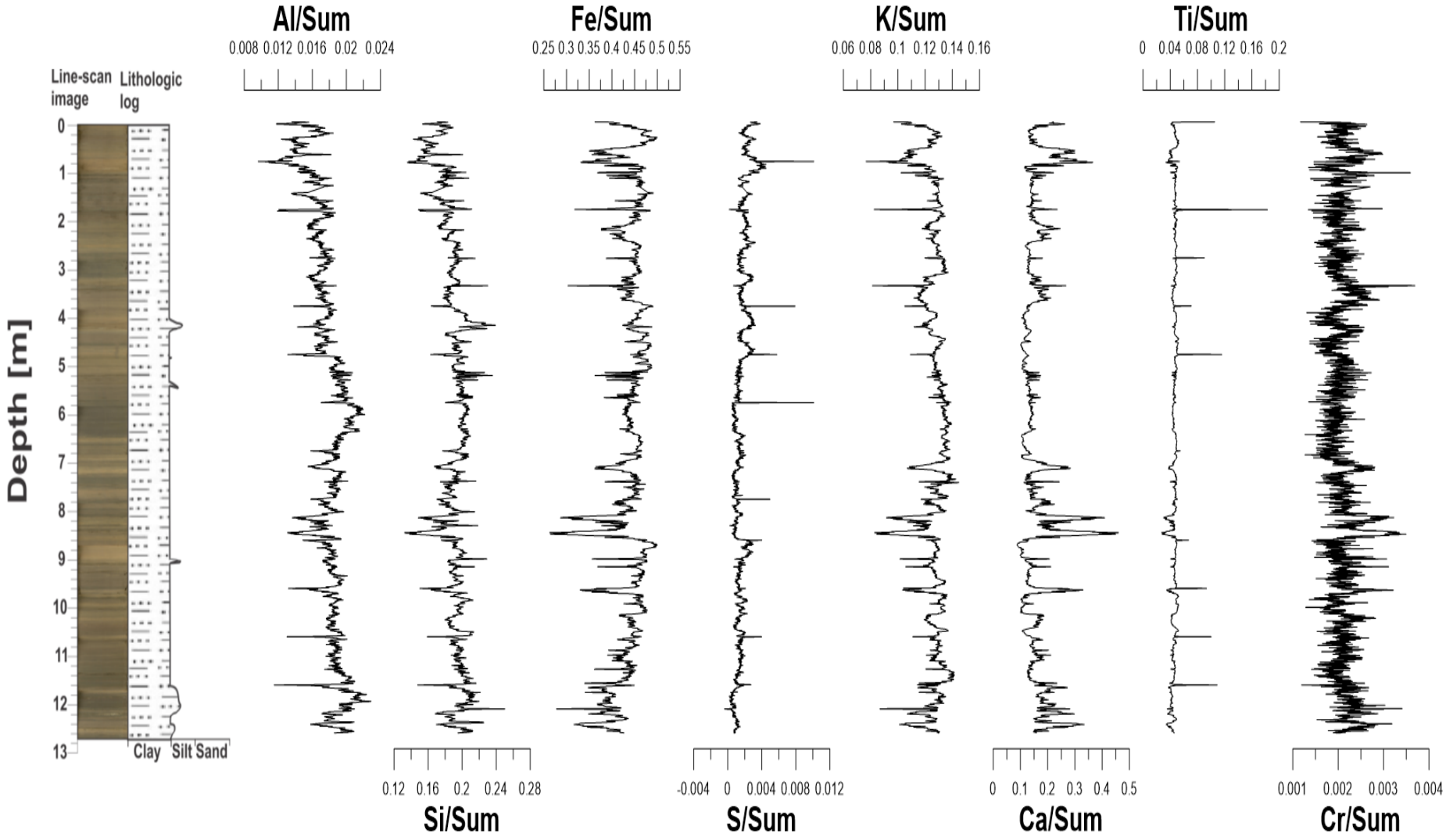

Fig. 4.10: Line-scan image, lithological log and element geochemistry of core PS56/029-1 plotted vs. depth (including Al/Sum, Si/Sum, S/Sum, K/Sum, Ca/Sum, Ti/Sum and Cr/Sum).

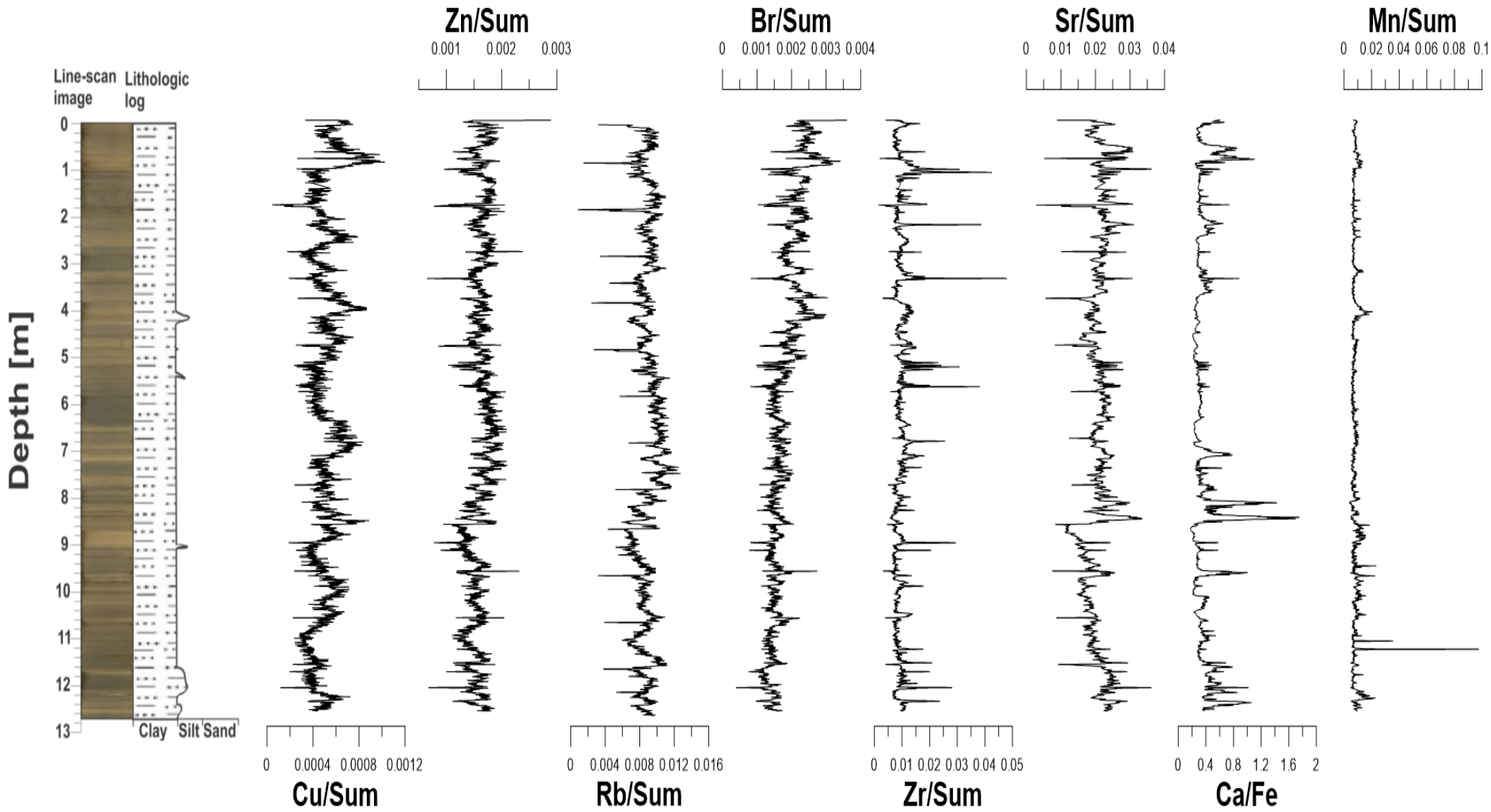

Fig. 4.11: Line-scan image, lithological log and element geochemistry of core PS56/029-1 plotted vs. depth (including Cu/Sum, Zn/Sum, Rb/Sum, Br/Sum, Zr/Sum, Sr/Sum, Ca/Fe and Mn/Sum).

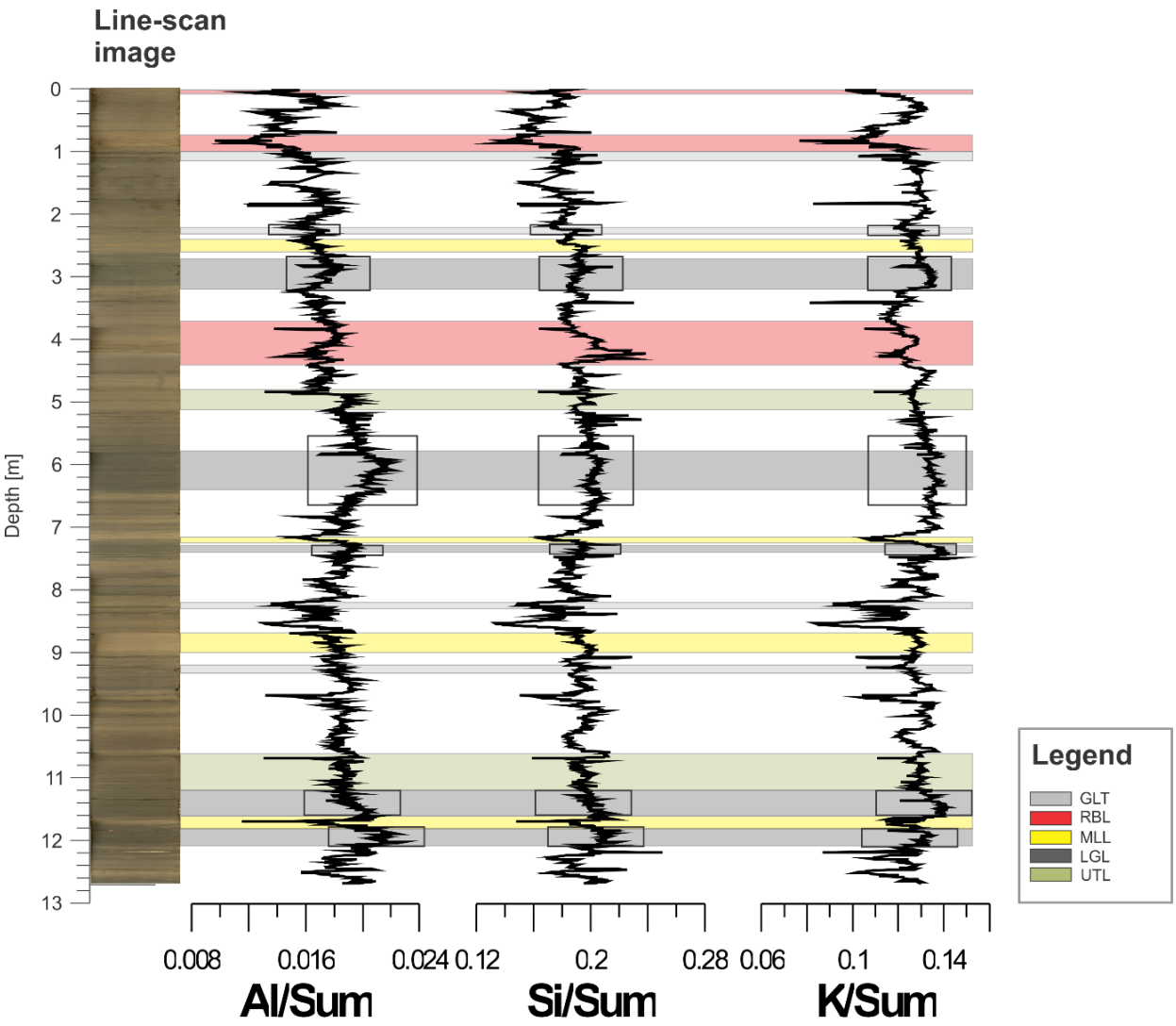

Fig. 4.12: Element geochemical ratios of Al/Sum, Si/Sum and K/Sum together with the five lithofacies GLT, RBL, MLL, LGL and UTL plotted against depth. Depths with increased geochemical ratios of Al/Sum. Si/Sum and K/Sum are highlighted with black rectangles.

4.1.5 Presence/absence of foraminifera

White circled features that resemble the shape of foraminifera and appear as interruptions or "wholes" on the sediment surface are interpreted as foraminifera. Foraminifera in core PS56/029-1 are visible with the naked eye, either present at the sediment surface and/or on line-scan images (Fig. 4.2 and Fig. 4.13). In core PS56/029-1 repetitive intervals of foraminifera bearing zones are observed. Additionally, foraminifera bearing zones are supplemented by an increase in the element geochemical ratio of Ca/Sum (Fig. 4.14). Foraminifera bearing zones are detected at depths between 1267-1200 cm, 1180-1170 cm, 1123-1067 cm, 978-967 cm, 867-817 cm, 790-708 cm, 424-337 cm, 282-106 cm, 102-43 cm and 10-0 cm (Fig. 4.2).

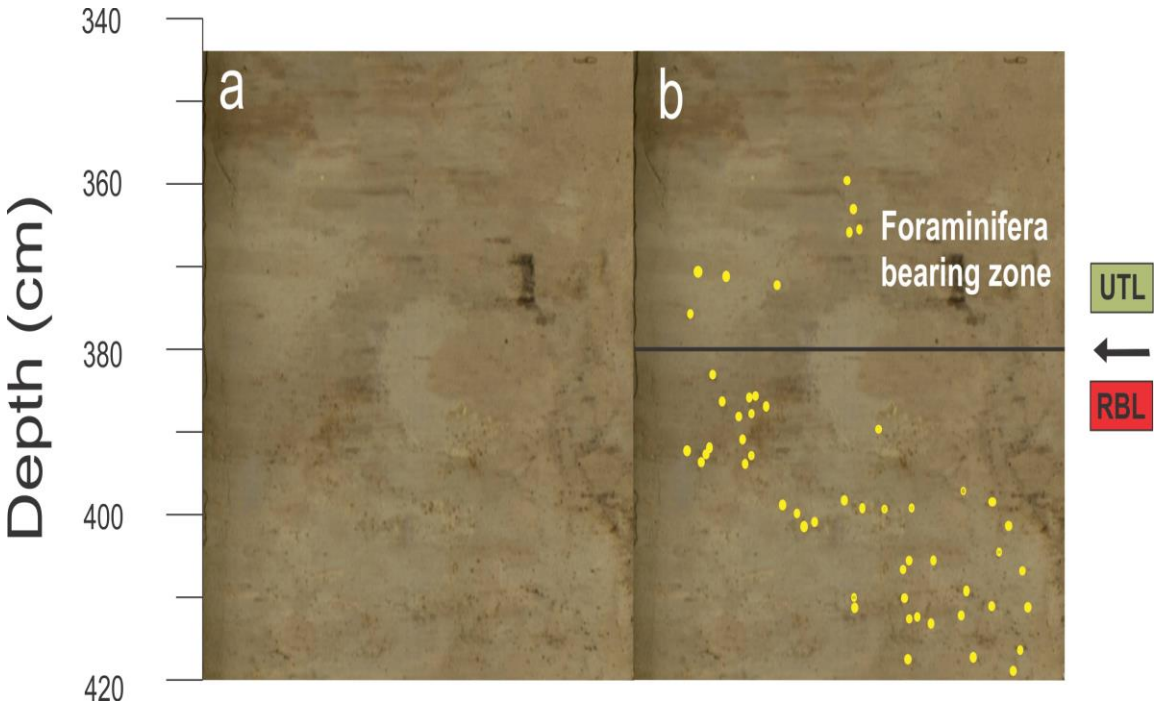

Fig. 4.13: ***a)*** *Line-scan image of foraminifera bearing zone at depth 420-345 cm* ***b)*** *interpretation* ***a*** *(UTL – Undefined Transition Layer and RBL – Red-Brown Layer).*

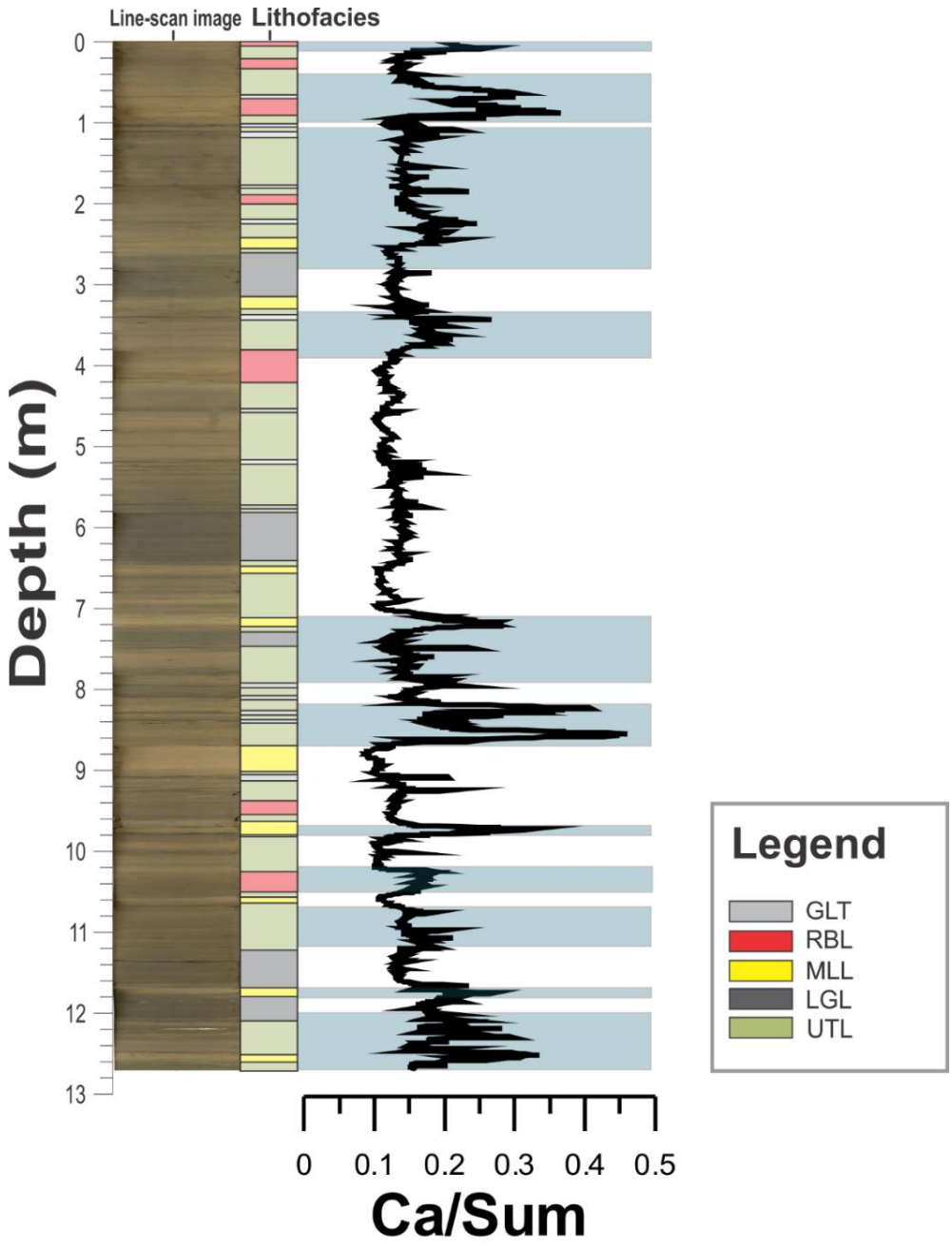

Fig. 4.14: Line-scan, lithofacies GLT, RBL, MLL, LGL and UTL and element geochemical ratio of Ca/Sum plotted against depth. Including depths with increased element geochemical ratio of Ca/Sum displayed by blue rectangles.

Varying concentrations of calcium are detected throughout the core. Intervals of higher calcium concentration are detected at depths between 1267-1200 cm, 1123-1067 cm, 1080-1070 cm, 1050-1018 cm, 978-967 cm, 867-817 cm, 790-708 cm, 390-337 cm, 282-106 cm, 102-43 cm and 10-0 cm. Intervals of increased calcium content occur more frequently and have higher concentrations within lithofacies RBL and MML compared to lithofacies LGL, GLT and UTL. Additionally, the intervals of increased calcium concentration in lithofacies RBL and MLL coincide with foraminifer bearing zones.

4.1.6 Lamination

Laminations are observed in X-ray photos of the core (Fig. 4.15), and they are also detected by grain size analysis as repetitive intervals of coarser grain-sizes (Fig. 4.16). Lamination is repetitive intervals of higher density layers than the surrounding matrix and are detected as thin lighter and "whiter" layers trough density variations. Intervals containing lamination include depths between 1212-1187 cm, 1152-1141 cm, 745-730 cm, 645-582 cm, 318-282 cm and 174-129 cm.

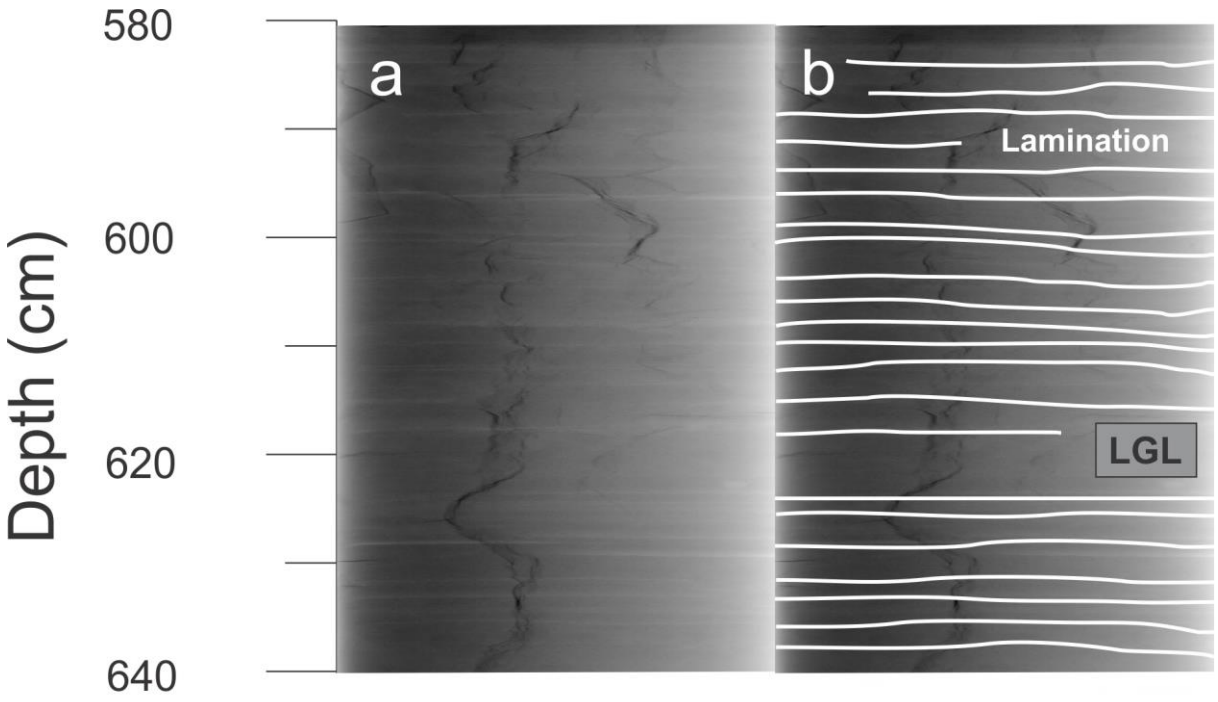

Fig. 4.15: ***a)*** *X-ray photo of lamination at depth 645-580 cm* ***b)*** *interpretation of* ***a*** *(LGL – Laminated Grey Layer). Lightness increases with density.*

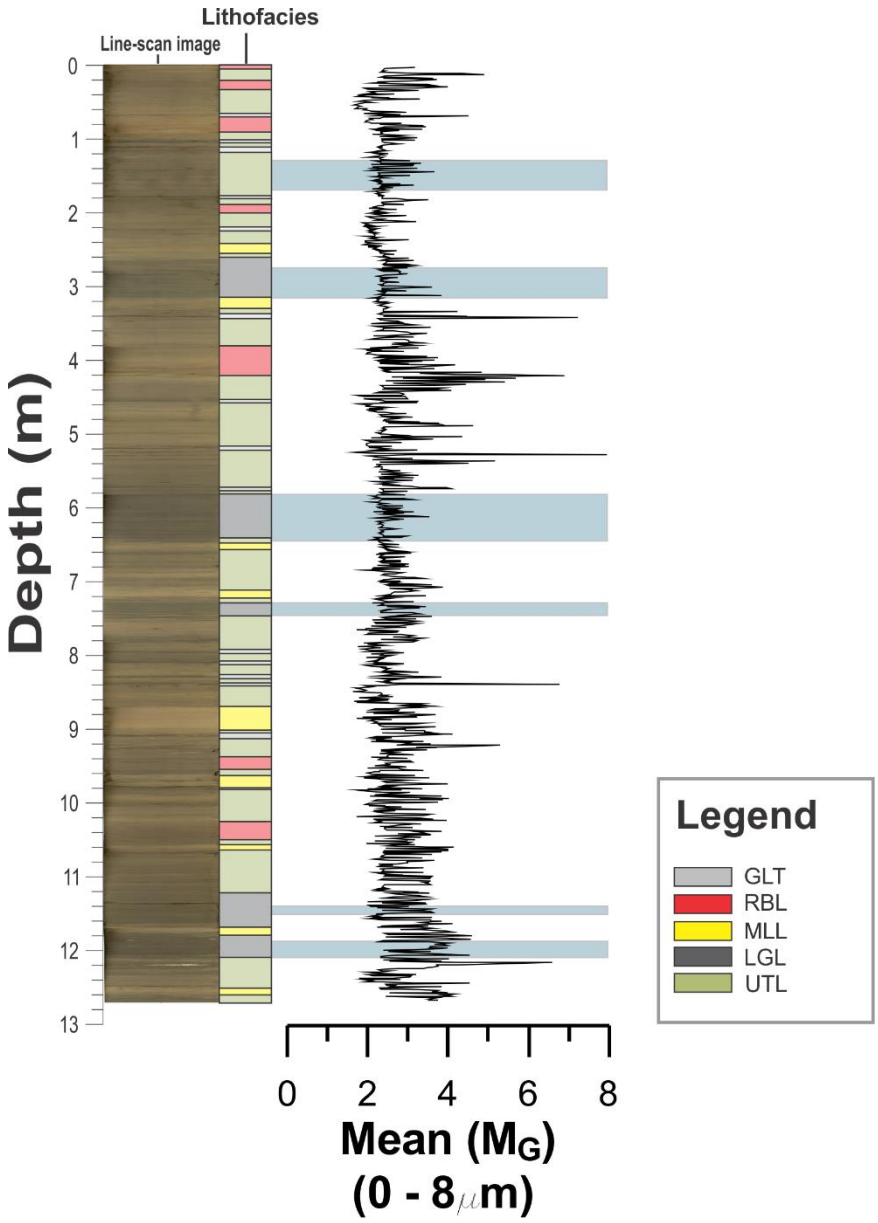

Fig. 4.16: Line-scan image, lithofacies GLT, RBL, MLL, LGL and UTL and mean (0-8μm) plotted against depth. Intervals containing lamination are displayed by blue rectangles.

Intervals containing laminations include fluctuating grain-sizes (Fig. 4.16). The grain-sizes vary between 2 and 4.5 µm throughout the intervals containing lamination. Intervals with lamination in core PS56/029-1 occur in lithofacies LGL, whereas only one interval of lamination occur in UTL.

4.1.7 Ice-rafted debris (IRD)

IRD content in core PS56/029-1 is based on the interpretation of X-ray photos supplemented by visual core description (Fig. 4.2 and Fig. 4.17). Visual inspection of the core only reveals IRD visible on the sediment surface, and potential IRD in the underlying sediments cannot be detected without X-ray imaging. Therefore, in this study "white" higher density circles detected

on X-ray photos are interpreted as IRD (Fig. 4.17). Higher density features with a rounded shape are suggested to be IRD because there is no other likely explanation for the deposition of such features at core site PS56/029-1.

The IRD concentration varies throughout the core, with certain intervals of particularly high coarser sediment concentrations. Higher IRD concentrations are detected at depth 30 cm and between 760 to 745 cm, whereas the IRD signal is absent between 400 and 100 cm (Fig. 4.2).

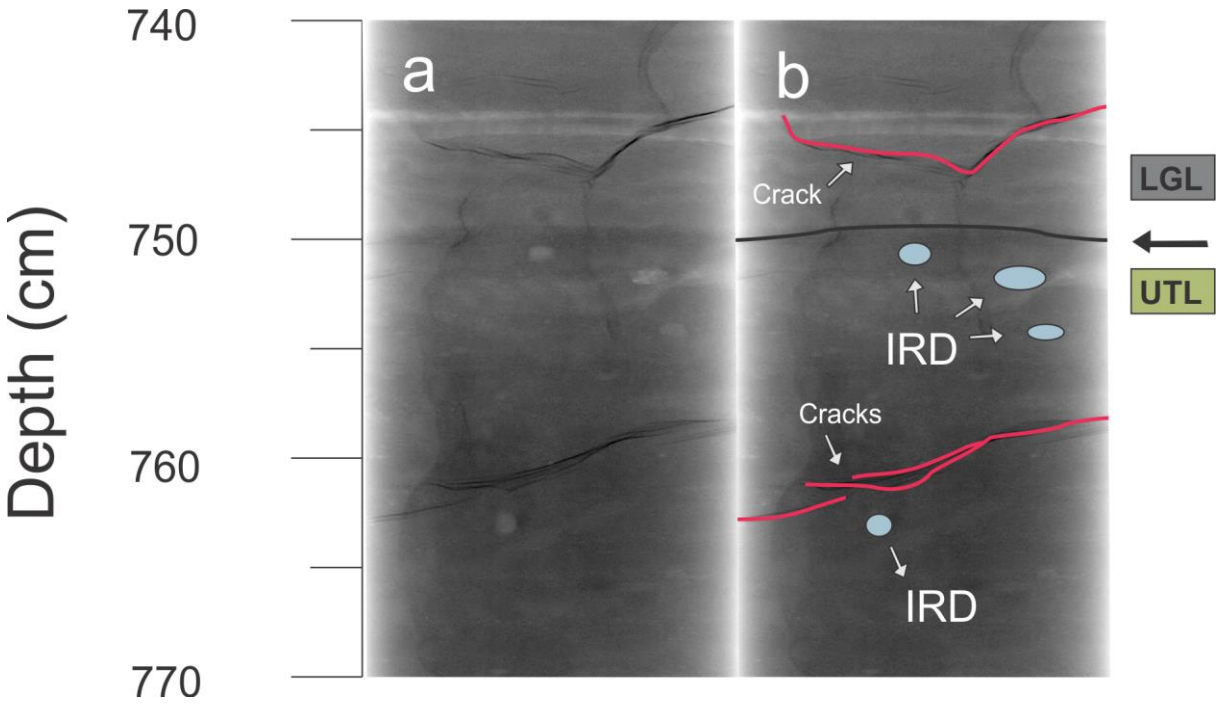

Fig. 4.17: ***a)*** *X-ray photo of IRD at depth 770-740 cm* ***b)*** *interpretation of* ***a*** *(LGL – Laminated Grey Layer and UTL – Undefined Transition Layer). Lightness increases with density.*

4.1.8 Massive mud

The interpretation of massive mud is based on X-ray photos, supplemented by line-scan images (Fig. 4.18). Massive layers lacking structures are normally found in core PS56/029-1 in association with lithofacies MLL and RBL.

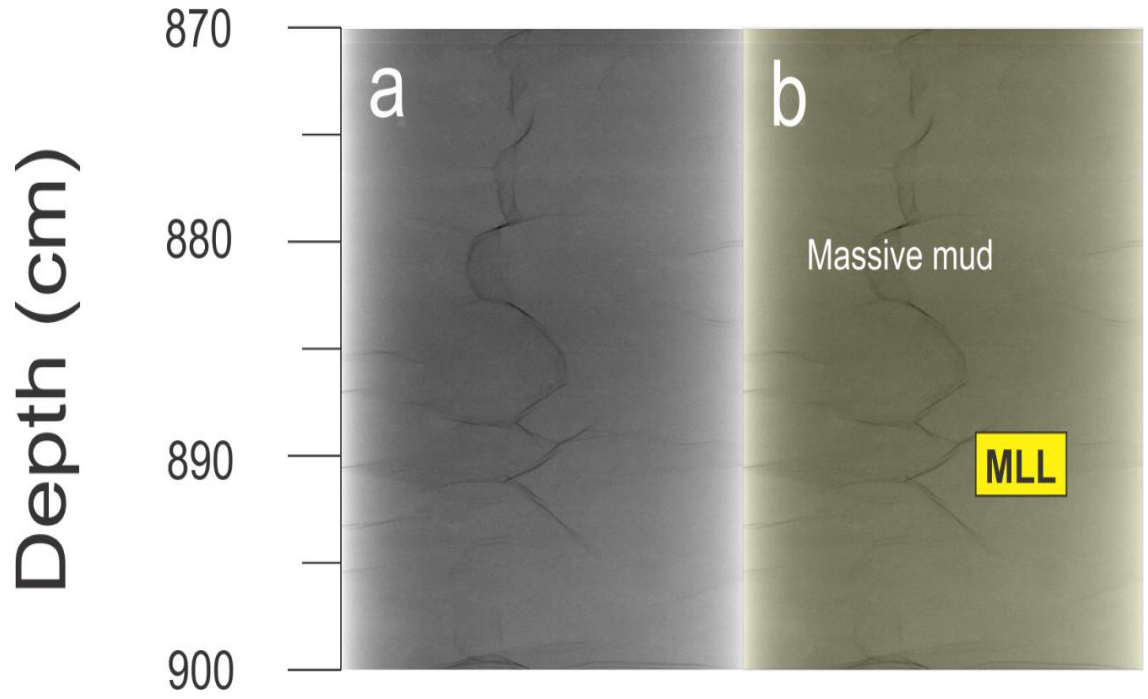

Fig. 4.18: ***a)*** *X-ray photo of massive mud at depth 900-870 cm* ***b)*** *interpretation of* ***a*** *(MLL – Massive Lighter Layer). Lightness increases with density.*

4.1.9 Sharp lower boundaries

Interpretation of sharp lower boundaries are based on line-scan images and X-ray photos (Fig. 4.19). Marked changes in physical properties and grain-size coincide with sharp lower boundaries in core PS56/029-1. Additionally, the element geochemical compositions are changed. A sharp lower boundary is recognized in association with lithofacies LGL, GLT, UTL and MLL (*see Chapter 4.1.11*).

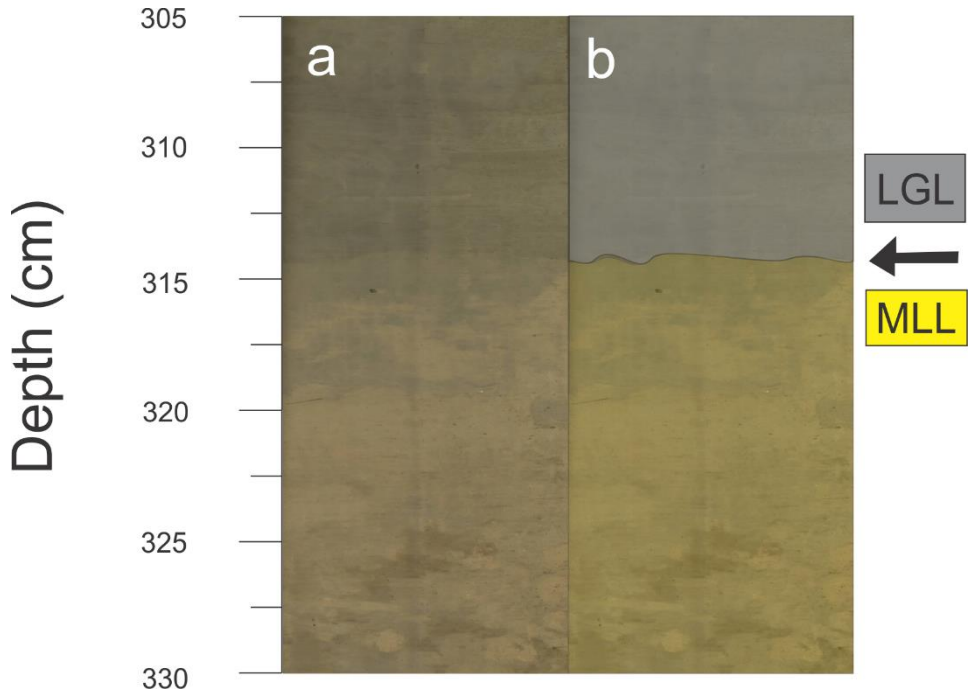

Fig. 4.19: ***a)*** *Line-scan image of a sharp lower boundary at depth 313 cm in core PS56/029-1* ***b)*** *interpretation of* ***a*** *(LGL – Laminated Grey Layer and MLL – Massive Lighter Layers).*

4.1.10 Bioturbation

Bioturbation occurs when benthic organisms rework deposited sediment by burrowing, ingestion and defacation, and therefore disturbs the sediment stratigraphy. Bioturbation of the sediment is indicated by colour changes observed in the line-scan images of the core. Bioturbation is present in core PS56/029-1 in association with lithofacies MLL, RBL and UTL (*see Chapter 4.1.11*). Bioturbation is frequently occurring on the boundaries between lighter coloured layers to darker coloured layers.

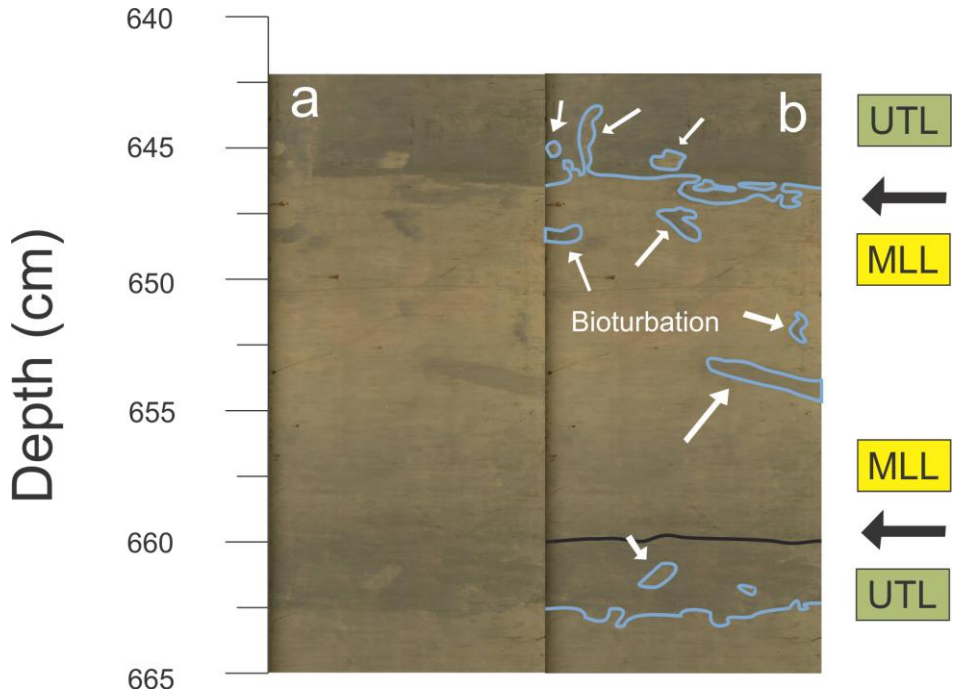

Fig. 4.20: ***a)*** *Line-scan image indicating bioturbation at depth 640 – 665 cm* ***b)*** *interpretation of* ***a*** *(UTL – Undefined Transition Layer and MLL – Massive Lighter Layers).*

4.1.11 Lithofacies

Five lithofacies have been distinguished through visual core description, line-scan images, X-ray photos and grain-size analysis, supplemented by marked changes in physical and geochemical properties (Fig. 4.2, Fig. 4.6, Fig. 4.8 and Fig. 4.12 – 4.21). In order to present the core as clearly as possible, the facies have been given names suitable for their characteristics, these are:

1. *Laminated Grey Layer (LGL).*
2. *Grey Layer Thin (GLT).*
3. *Massive Light Layer (MLL).*
4. *Red Brown Layer (RBL).*
5. *Undefined Transition Layer (UTL).*

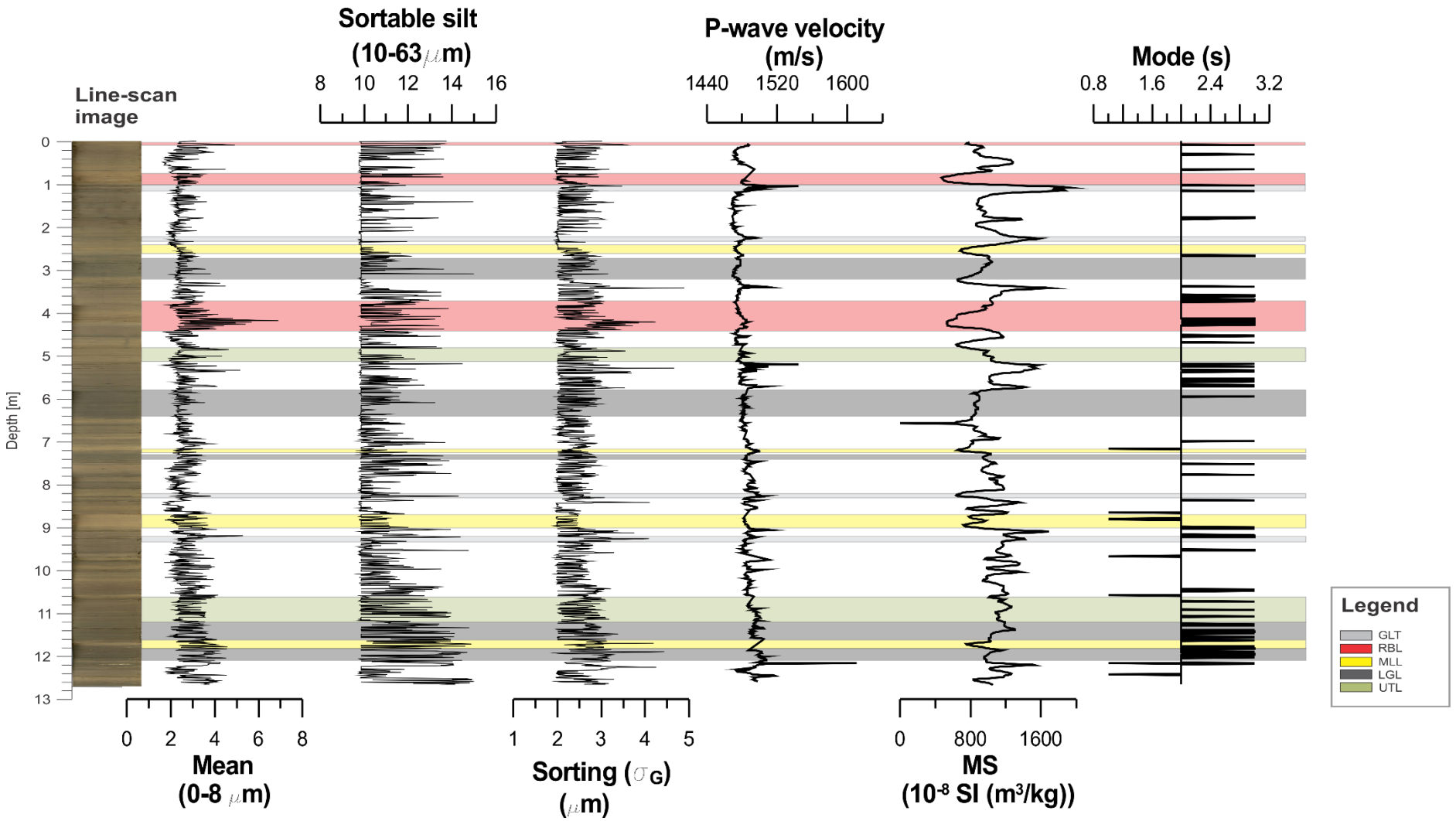

Fig. 4.21: Examples of lithofacies recognized in core PS56/029-1, including parameters mean (0-8 μm), sortable silt (10-63 μm), sorting (μm), p-wave velocity (m/s), magnetic susceptibility (MS) (10^{-8} SI) and mode (s) (GLT – Grey Layer thin, RBL – Red-Brown Layer, MLL – Massive Lighter Layers, LGL – Laminated Grey Layer and UTL – Undefined Transition Layer).

4.1.11.1 Laminated Grey Layer (LGL)

Lithofacies "Laminated Grey Layer" (LGL) (Fig. 4.2, Fig. 4.6, Fig. 4.8, Fig. 4.12, Fig. 4.14-4.17, Fig. 4.19 and Fig. 4.21) represent five dominate layers. LGL comprises predominantly of olive grey (5Y 5/2) to dark grey (5Y 4/1) silty clays. Interval thicknesses varies between 15 and 66 cm. Volume percentages of clay varies between 14.5 and 50.8, whereas volume percentages of silt varies between 49.2 and 77.1. Sand and gravel are absent in these layers. Intervals comprised of these layers include lamination and a sharp lower boundary. Foraminifera are abundant. These five layers are detected at depths between 1210-1180 cm, 1170-1120 cm, 745-730 cm, 646-580 cm and 320-260 cm.

Lithofacies LGL shows constant and average MS values that vary between 800 and 1000 $*10^{-8}$ SI. The physical properties of p-wave velocity, wet-bulk density, acoustic impedance and grain-size varies between 1480 and 1490 m/s, 1.5 and 1.6 g/cm^3, 1100 and 1200 gmcm^{-3}s^{-1} and 2 and 4 µm (very fine silt), respectively. Volume percentages of silt increases and decreases within these layers, corresponding to a coarser grain-size distribution and a finer grain-size distribution. Sorting values vary between 2 and 3 µm (poorly sorted). The sorting signal fluctuate throughout this lithofacies, corresponding to higher and lower values in the range of 2-3 µm. Sorting values of 2-3 µm are some of the poorest-sorted values throughout the core. Geochemical properties of LGL include high element ratios of Al/Sum, Si/Sum, K/Sum and Rb/Sum and low element ratios of Ca/Sum, Cu/Sum and Ca/Fe. X-ray photos reveal clear signs of lamination within these intervals and line-scan images reveal a sharp lower boundary. IRD is absent, with one exception at depth 1202 cm. Lithofacies LGL consists of sediments that show a bimodal to trimodal trend, where the trimodal signal occur more frequent at depths between 1210-1180 cm and 1170-1120 cm compared to 745-730 cm, 646-580 cm and 320-260 cm. The mode(s) signal resemble each other, but with a small detectable change from depths between 1210-180 cm and 1170-1120 cm compared to 745-730 cm, 646-580 cm and 320-260 cm (Fig. 4.22). The bimodal and trimodal signal detected in LGL show two sharp higher peaks, in addition to a more rounded chaotic signal. The bimodal signal at depth 1170-1120 cm include grain-sizes up to 5.8 µm, while depth 640-580 cm include grain-sizes up to 5 µm.

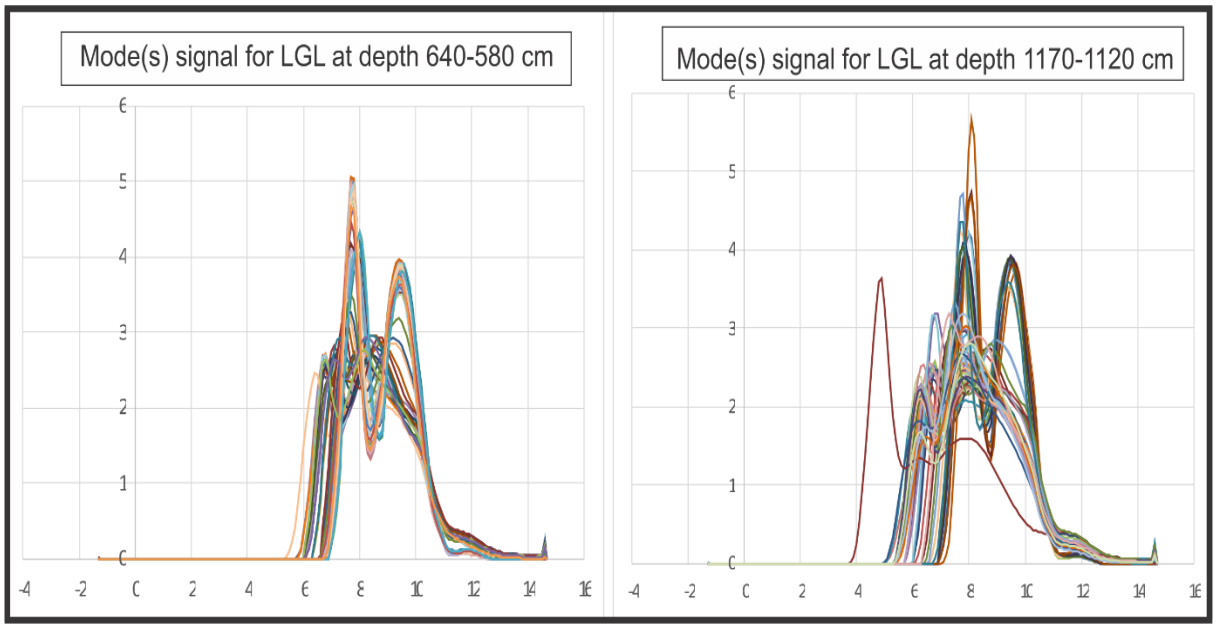

Fig. 4.22: Mode(s) signal for lithofacies LGL at depth 640-580 cm and 1170-1120 cm.

4.1.11.2 Grey Layer Thin (GLT)

Lithofacies "Grey Layer Thin" (GLT) (Fig. 4.2, Fig. 4.6, Fig. 4.8, Fig. 4.12, Fig. 4.14, Fig. 4.16 and Fig. 4.21) consists of olive grey (5Y 5/2) to dark grey (5Y 4/1) silty clays. These intervals occur frequently throughout the core with relatively thin interval thicknesses between 3 and 15 cm, with an average interval thickness of 10 cm. Volume percentages of clay vary between 17.1 and 50.9, whereas volume percentages of silt vary between 44.3 and 82.9. Characteristics of these intervals are a coarser grain-size distribution and a sharp lower boundary. Foraminifera are abundant.

Lithofacies GLT include physical properties of high values (e.g. MS, p-wave velocity and wet-bulk density). The MS, p-wave velocity and wet-bulk density varies between 865 and 1916 $*10^{-8}$ SI, 1500 to 1560 m/s and 1.6 to 1.9 g/cm^3, respectively. The grain-size distribution shows grain-sizes between 2 and 5 µm, where some intervals of this lithofacies are coarser than other intervals. The sorting signal varies between 2.5 and 5 µm, a sorting value of 5 µm belongs to some of the highest sorting values detected throughout the core. Geochemical properties of GLT include high element ratios of Al/Sum and Si/Sum and low element ratios of Cu/Sum, Fe/Sum, Zn/Sum and Rb/Sum. X-ray photos reveal a high density layer cutting the sediments from below at the beginning of GLT and high density layers occur more or less always in association with GLT. The internal structure at depths between 977-974 cm and 838-835 cm reveal higher-density layers with lower-density layers in between, whereas the rest of GLT shows no internal structure. Line-scan images reveal a sharp lower boundary. IRD is

recognized, but occurrences are scattered, with grain diameters varying between 80 to 90 mm. Lithofacies GLT consists of sediments commonly showing a bimodal signal, with trimodal signal only present within a few intervals. The bimodal signal detected in GLT shows in general two sharp higher peaks and two more rounded lower peaks. The bimodal signal at depth 910-903 cm include grain-sizes up to 4.4 µm, while depth 120-110 cm include grain-sizes up to 4.9 µm.

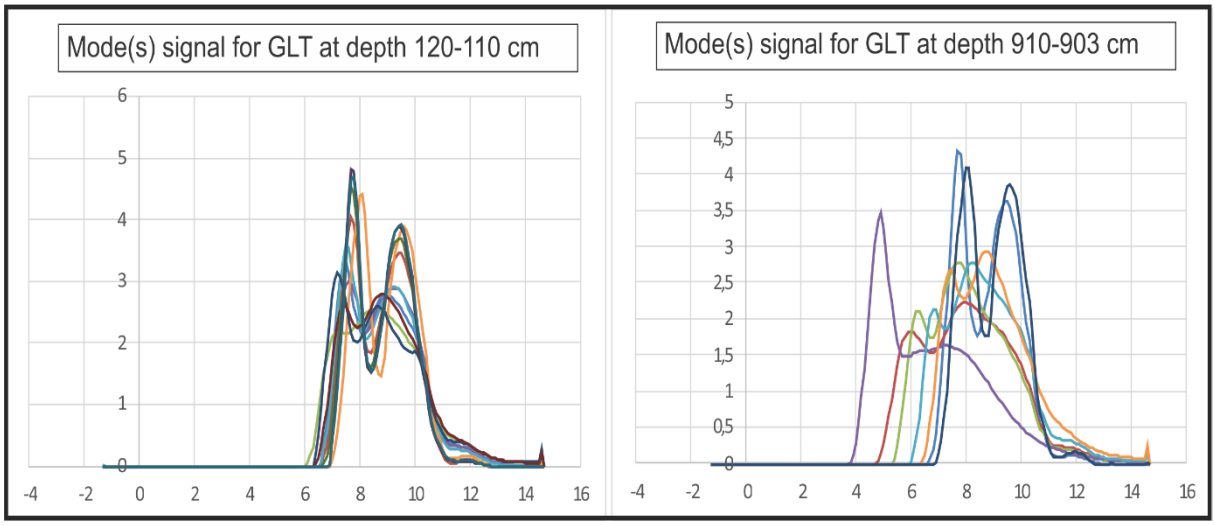

Fig. 4.23: Mode(s) signal at depth 910-903 cm and 120-110 cm for GLT.

4.1.11.3 Massive Light Layers (MLL)

Lithofacies "Massive Light Layers" (MLL) (Fig. 4.2, Fig. 4.6, Fig. 4.8, Fig. 4.12, Fig. 4.14, Fig. 4.16 and Fig. 4.18-4.21) comprises predominantly of olive grey (5Y 4/2) silty clays and silt. Interval thicknesses vary between 10 and 30 cm. Volume percentages of clay vary between 22.2 and 56.1, whereas volume percentages of silt vary between 43.9 and 77.9. Intervals comprising MLL are considered as massive. Characteristics of this lithofacies are the occurrences of foraminifera and bioturbation. The lower boundary is strongly bioturbated, occurring with or without a sharp lower boundary. IRD occurs occasionally with grain diameters of 80 to 90 mm. This lithofacies occur frequently throughout the core, but increases towards the bottom of the core.

Physical properties of lithofacies MLL include p-wave velocity, wet-bulk density and MS values between 1470 and 1480 m/s, 1.5 and 1.6 g/cm^3 and 700 and 1000 *10^{-8} SI, respectively. The grain-size distribution include grain-sizes between 2 and 5 µm, with some layers containing more silt and others more clay. Lithofacies MLL consists of poorly sorted sediments, with values between 2 and 4 µm. Geochemical properties of MLL includes high element ratios of

Sr/Sum, Ca/Sum and Ca/Fe and low element ratios of Al/Sum, Si/Sum, K/Sum, Fe/Sum and Rb/Sum. In contrast, different geochemical properties are detected at one individual depth between 900-870 cm, including high element ratios of S/Sum, Fe/Sum and Cu/Sum and low element ratios of Ca/Sum, Sr/Sum and Ca/Fe. Line-scan images reveal a strongly bioturbated lower boundary, occurring with or without a sharp lower boundary. X-ray photos reveal massive sediments without internal structures. Lithofacies MLL include unimodal to trimodal sediments. Grain-size measurements reveal a slight change concerning the mode(s) signal from the uppermost MLL intervals to the lowermost MLL intervals, but the changes are minor (Fig. 4.24). The unimodal to trimodal signal detected in MLL show in general two sharp higher peaks and a lower more chaotic signal. The mode(s) signal at depth 900-870 cm include grain-sizes up to 6 µm, while depth 655-645 cm include grain-sizes up to 5 µm.

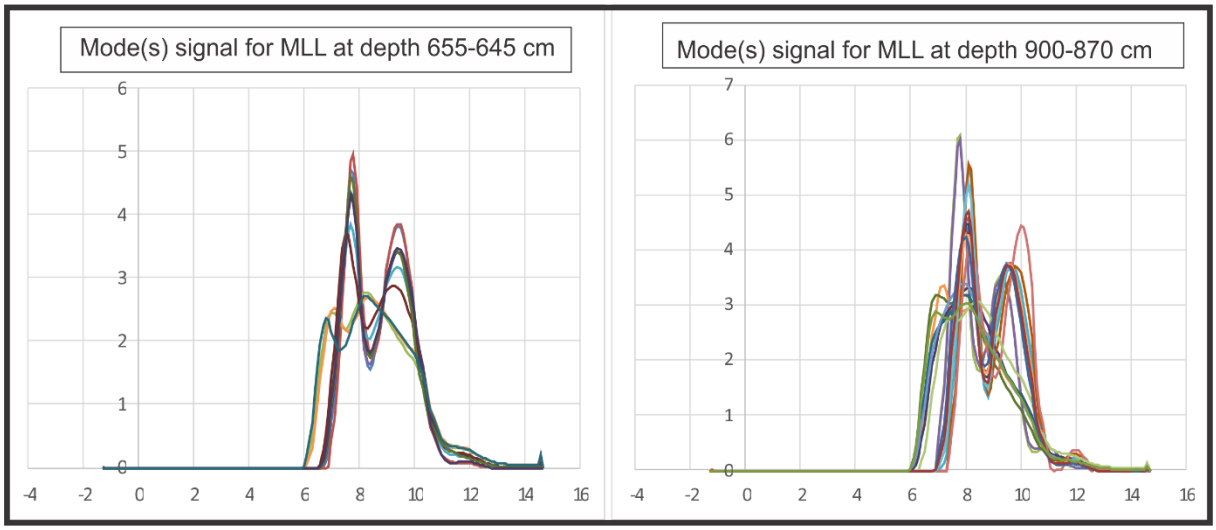

Fig. 4.24: Mode(s) signal for lithofacies MLL at depth 655-645 cm and 900-870 cm.

4.1.11.4 Red Brown Layer (RBL)

Lithofacies "Red Brown Layer" (RBL) (Fig 4.2, Fig. 4.7, Fig. 4.12-4.13, Fig. 4.15 and Fig. 4.20) comprises of reddish to brownish coloured (2.5 Y 4/2 – dark greyish brown) silty clays. Interval thicknesses vary between 10 and 40 cm, located at depths between 1040-1030 cm, 953-937 cm, 421-380 cm, 201-190 cm, 95-72 cm, 32-21 cm and 5-0 cm. Volume percentages of clay vary between 19.5 and 49.7, whereas volume percentages of silt vary between 48.6 and 80.4. Characteristics of this lithofacies are the occurrences of foraminifera, bioturbation and IRD. The diameter of the IRD varies between 20 mm and 90 mm.

Physical properties of RBL include p-wave velocity, wet-bulk density and MS between 1480 m/s and 1500 m/s, 1.4 and 1.6 g/cm^3 and 500 and 900 *10^{-8} SI, respectively. The lowest MS

value measured throughout the core is at depth 100-70 cm and include MS value of 500 $*10^{-8}$ SI. Lithofacies RBL has a coarser grain-distribution compared to the rest of the core, with grain-sizes varying between 2 and 7 µm. The sorting signal varies between 2 and 4.2 µm. The most profound peak throughout the core is detected at depths between 420-380 cm, with sorting values up to 4.2 µm and grain-sizes up to 7 µm. Geochemical properties include high element ratios of S/Sum, Cu/Sum, Ca/Sum and Ca/Fe and low element ratios of Rb/Sum, Al/Sum, K/Sum and Fe/Sum. X-ray photos reveal sediments containing IRD (Fig. 4.23) and line-scan images show bioturbation. Lithofacies RBL at depth 420-380 cm also reveal a lower boundary going from a high-density layer to a low-density layer (Fig. 4.23). Lithofacies RBL include sediments that are bimodal to trimodal (Fig. 4.24). The bimodal to trimodal signal detected in RBL show in general a more chaotic signal compared to LGL, GLT and MLL. The mode(s) signal at depth 1040-1030 cm include grain-sizes up to 4.4 µm, while depth 95-72 cm include grain-sizes up to 6 µm.

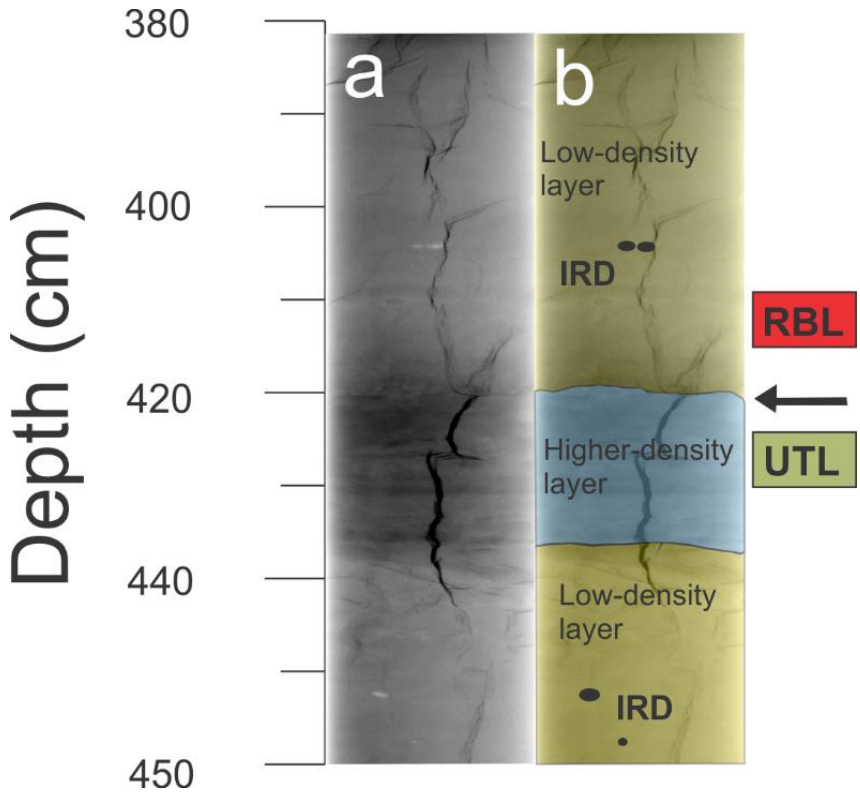

Fig. 4.25: ***a)*** *X-ray photo of IRD in lithofacies RBL at the boundary between UTL and RBL at depth 420 cm* ***b)*** *interpretation of* ***a****. Lightness increases with density.*

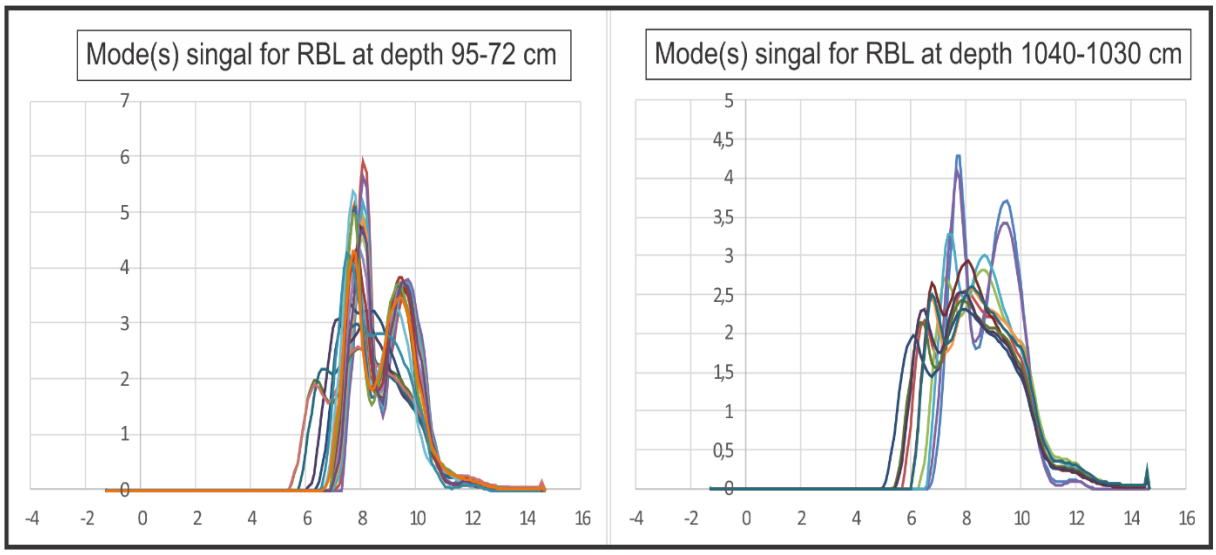

Fig. 4.26: Mode(s) signal for lithofacies RBL at depth 95-72 cm and 1040-1030 cm.

4.1.11.5 Undefined Transition Layers (UTL)

Lithofacies "Undefined Transition Layers" (UTL*)* (Fig. 4.2, Fig. 4.6, Fig. 4.8, Fig. 4.12, Fig. 4.14, Fig 4.16, Fig. 4.18-4.21 and Fig. 4.23) represent transition zones between one lithofacies to the next. This lithofacies consist of a mixture of the previously described lithofacies (*see Chapter 4.1.11.1 – 4.1.11.4*) and contain physical and geochemical properties that grade from one lithofacies to the next.

A summary of the characteristics of the different lithofacies distinguished in core PS56/029-1 are given in Table 4.1.

Table 4.1: Characteristics of lithofacies distinguished in core PS56/029-1.

	LGL	**GLT**	**MLL**	**RBL**
Colour	Olive grey to dark grey	Olive grey to dark grey	Olive grey	Dark greyish brown
Bed thickness (cm)	15-66	3-15	10-30	10-40
Volume percentages Clay Sill	 14.5-50.8 49.2-77.1	 17.1-50.9 44.3-82.9	 22.2-56.1 43.9-77.9	 19.5-49.7 48.6-80.4
Laminations	Yes	Yes and No	No	No
Massive	No	No	Yes	No

Sharp lower boundary	Yes	Yes	Yes and No	No
Bioturbation	No	No	Yes	Yes
IRD	Yes	Yes	Yes	Yes
Foraminifera	Low	Occasionally	High	High
MS (10^{-8}SI)	800-1000	865-1916	700-1000	500-900
P-wave velocity (m/s)	1480-1490	1500-1560	1470-1480	1480-1500
Wet-bulk density (g/cm^3)	1.5-1.6	1.6-1.9	1.5-1.6	1.4-1.6
Acoustic impedance ($gmcm^{-3}s^{-1}$)	1100-1200	1100-1200	1100-1200	1100-1200
Mean (µm)	2-4	2-5	2-5	2-7
Sorting (µm)	2-3	2.5-5	2-4.2	2-4.2
Skewness	-0.2-0.08	-0,5-0.09	-0.3-0.14	-0.2-0.05
Kurtosis	0.7-0.95	0.5-1	0.7-1	0.7-1
Mode (s)	Bimodal and trimodal	Bimodal and trimodal	Unimodal to trimodal	Bimodal and trimodal
Geochemical ratios High Low	 Al, Si, K, Rb Ca, Cu, Ca/Fe	 Al, Si Cu, Fe, Zn, Rb	 Sr, Ca, Ca/Fe Al, Si, K, Fe, Rb	 S, Cu, Ca, Ca/Fe Rb, Al, K, Fe

5 Discussion

Previous studies on the continental margin surrounding Antarctica have concluded that sediments on the continental slope and rise are typically deposited by alongslope currents and downslope gravitational processes (Kuvaas and Kristoffersen, 1991; Michels et al., 2001; Escutia et al., 2002; Rebesco et al., 2002; De Santis et al., 2003). Alongslope currents and gravitational processes are controlled by several factors, such as the continental margin morphology, variability and velocity of bottom and gravitational currents, the length of time the bottom and gravitational currents have operated, and the type and amount of sediments available (Rebesco et al., 2002; Kuvaas et al., 2004; Solli et al., 2008). Due to the sedimentary units (e.g. channel-levee structures, channels and different drifts) provided by Kuvaas et al. (2004) in the RLS, it is likely to assume that alongslope and downslope processes work simultaneously in order to deposit the sediments in the RLS and at core site PS56/029-1 (Fig. 5.1) (e.g. Mienert et al. (1993), Mcginnis and Hayes (1995), Howe et al. (2004) and Solli et al. (2007)).

Grain-size analysis, together with physical and element geochemical properties supplemented with line-scan images and X-radiographs, can provide essential information about marine sediments and their sedimentary environments (e.g. Weber et al. (1997), Blott and Pye (2001), Hepp et al. (2006) and Rothwell and Rack (2006)). Results from core PS56/029-1 reveal various trends provided in Chapter 4: Lithostratigraphy, which are discussed and explained in the following sub-chapters.

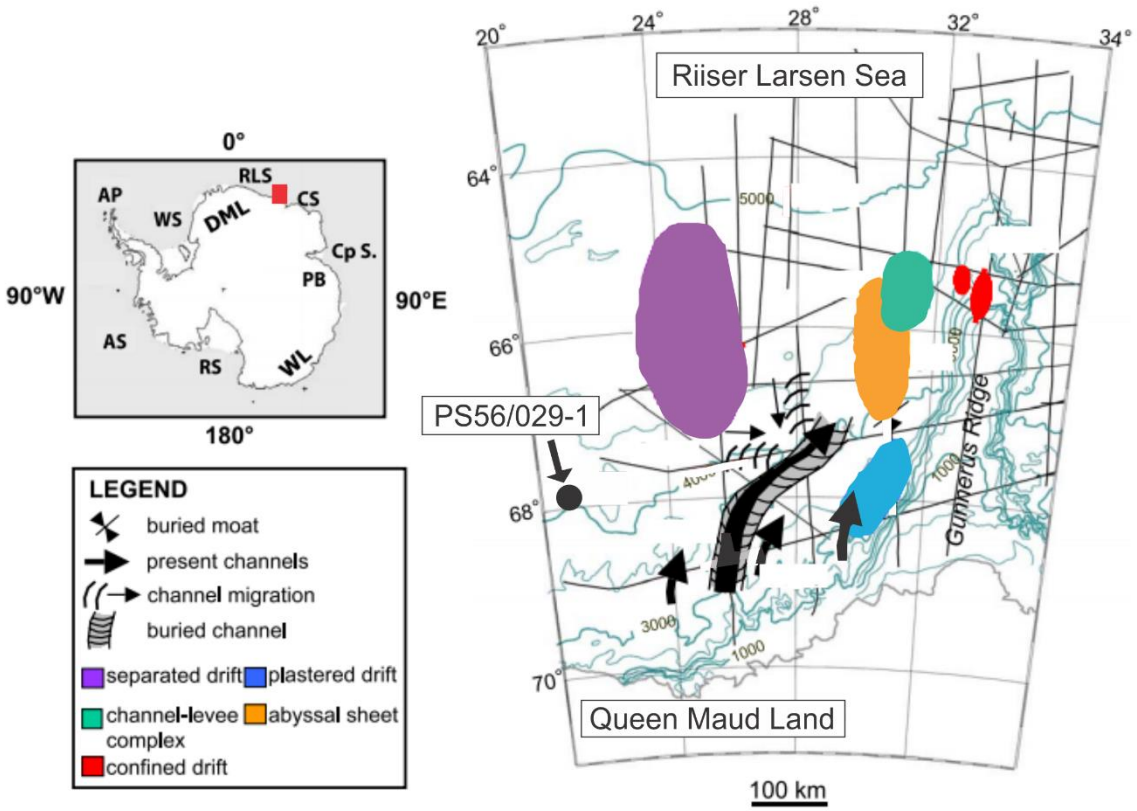

Fig. 5.1: Bathymetric map of the RLS, including main sedimentary units displayed with colours and seismic profiles obtained in the area are displayed with grey straight lines. Core location of PS56/029-1 is displayed with a black circle. Overview map to the left include area under investigation displayed with a red rectangle (modified after Kuvaas et al. (2004)).

The lithological log (Fig 4.2) reveals evidence of changing depositional environments due to alternating repetitive intervals of lithofacies distinguished throughout the core. Sediment colour variation is considered to be diagnostic of changes in soil and marine sediment composition through several decades (e.g. Mix et al. (1992) and Rothwell and Rack (2006)). The colour of marine sediments has shown to be reliable indicators of important sedimentological components, e.g. free and bound iron, carbonate, different iron minerals (e.g. pyrite and hematite) and clay through geochemical investigations (Rothwell and Rack, 2006). The alternating colour change detected in core PS56/029-1 could reveal important information of the paleoenvironment and the sedimentary processes responsible for depositing the sediments. A previous study by Pudsey and Camerlenghi (1998) on sediment drifts on the Pacific margin of the Antarctic Peninsula showed a cyclicity between brown, bioturbated, diatom-bearing mud with foraminifera and radiolarians to grey, laminated, barren mud. The brown layers are interpreted as sediments deposited during interglacial periods, whereas the grey layers are interpreted to be deposited during glacial periods, an interpretation that is later supported by Rebesco et al. (2002) and Lucchi et al. (2002). The 12.67 m long core consists of repetitive

alternating lighter brownish (2.5 Y 4/2 – dark greyish brown and 5Y 5/2 – olive grey) and greyish (5Y 4/1 – dark grey and 5Y 5/1 – grey) coloured layers. The lighter brownish coloured layers include increased IRD content, occurrences of foraminifera and bioturbation, and occasionally a sharp lower boundary, whereas the grey coloured layers include sparse IRD, reduced foraminifera content, a sharp lower boundary and lamination. Physical and geochemical properties observed in the lighter brownish and greyish coloured layers correspond well to the observed colour changes. The MS increases for the greyish coloured layers, whereas the p-wave velocity and the wet-bulk density only increases for the greyish coloured layers with bed thicknesses between 3 and 15 cm. Element geochemical ratios of Al/Sum, Si/Sum, K/Sum and Rb/Sum are higher, whereas the element geochemical ratios of Ca/Sum and Cu/Sum are lower in the greyish coloured layers compared to the lighter brownish coloured layers. The lighter brownish coloured layers include slightly coarser grain-sizes and lower MS values compared to the greyish coloured layers. Element geochemical properties of the lighter brownish coloured layers show different results. Element geochemical ratios of S/Sum, Cu/Sum and Ca/Sum are higher, whereas the element geochemical ratios of Al/Sum, K/Sum and Cr/Sum are lower in the brownish coloured layers compared to the greyish and lighter coloured layers. Element geochemical ratios of the lighter coloured layers show no clear correlation. Based on the physical and geochemical properties, in addition to repetitive alternating colour variations, core PS56/029-1 possibly reveals cyclicity concerning sediments deposited during glacial/interglacial periods.

The influence of glaciological, oceanic and atmospheric processes varies through glacial/interglacial cycles in the RLS (e.g. Schröder and Fahrbach (1999), Böning et al. (2008), Parkinson and Cavalieri (2012) and Mackintosh et al. (2014)). These processes create variations in the sediment supply to core site PS56/029-1, which can be observed through the sedimentary record (Fig. 4.2). Glaciological, oceanic and atmospheric processes in the RLS are as follows:

1. Katabatic winds originating from the Antarctic continent, creating coastal polynyas, which are areas of brine formation (Fig. 5.2) (Ishikawa et al., 1996; Smith et al., 2010).
2. Westward flowing coastal currents and the eastward flowing Antarctic Circumpolar Current (ACC), powered by the East Wind Drift and the West Wind Drift, respectively (Fig. 5.2) (Böning et al., 2008; Rintoul, 2010; Fahrbach, 2013).
3. Decadal and seasonal changing sea-ice cover (Fig. 5.2) (Parkinson and Cavalieri, 2012).
4. Icebergs drifting over the RLS, depositing ice-rafted debris (IRD) (Fig. 5.2) (Arrigo et al., 2002; Aoki, 2003).

5. The advance and subsequent retreat of the EAIS (Fig. 5.2) (Mackintosh et al., 2014).
6. The impact of the easternmost part of the Weddell Gyre (Fig. 5.2 and Fig. 5.3) (Schröder and Fahrbach, 1999; Pudsey, 2000).

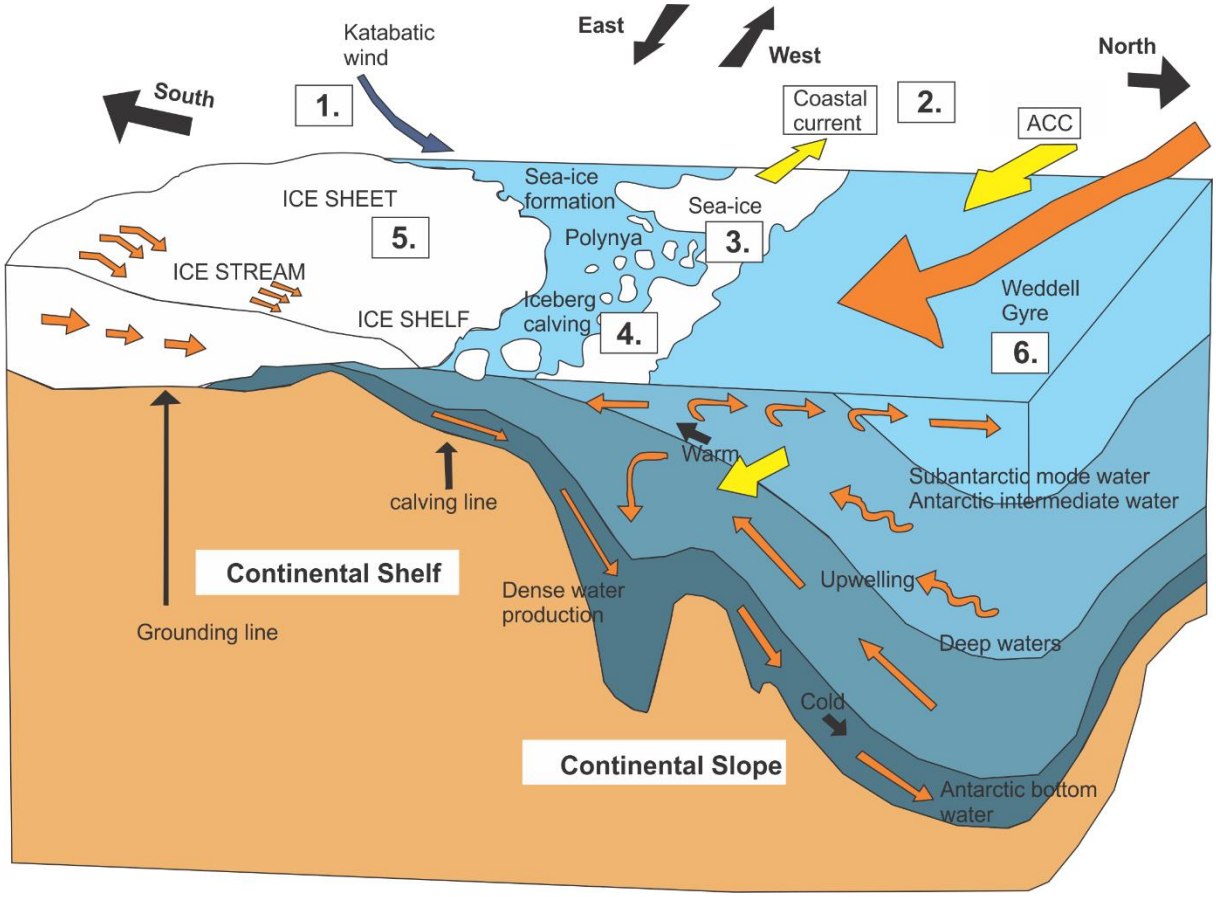

Fig. 5.2: Schematic figure of glaciological, oceanic and atmospheric processes operating through glacial/interglacial cycles in the RLS. Including katabatic winds (1), coastal currents and the ACC (2), sea-ice and sea-ice formation (3), icebergs (4), the position of the EAIS (5) and the easternmost part of the Weddell Gyre (6) (modified after National Research Council (2011)).

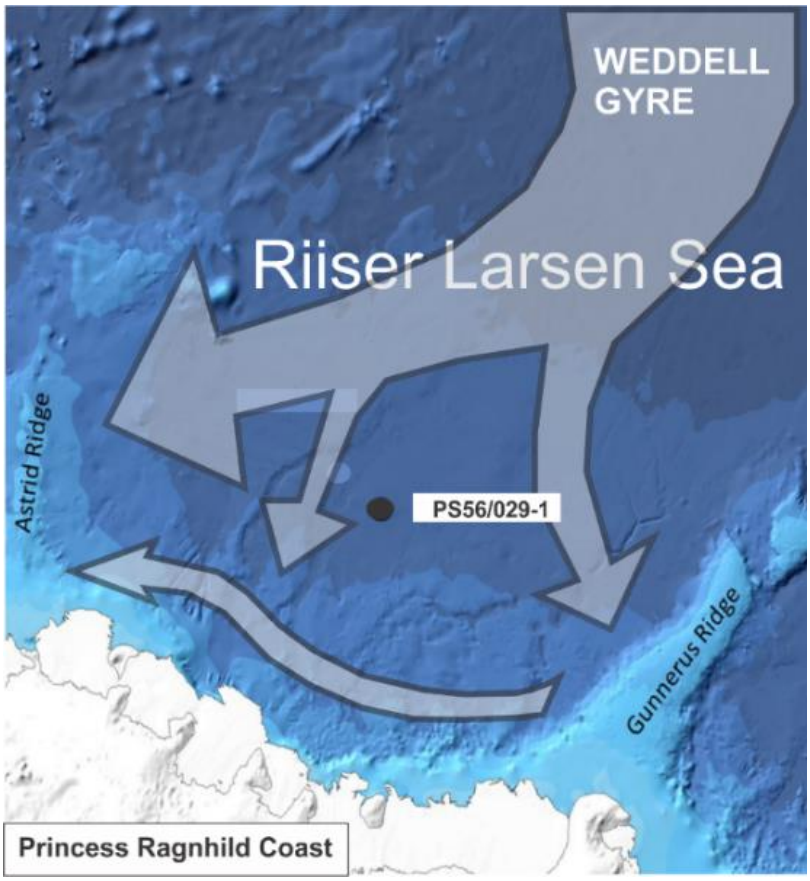

Fig. 5.3: Schematic figure of the impact of the easternmost part of the Weddell Gyre between Astrid and Gunnerus Ridge outside Princess Ragnhild Coast and the westward flowing coastal current including core location of PS56/029-1 displayed by a ellipsoid (modified after Hass et al. (2016) after Schröder and Fahrbach (1999)).

5.1 Location of core PS56/029-1

Core PS56/029-1 was retrieved in a channel-levee complex on top of a levee on the western side of a channel (Fig. 5.4). These channel-levee structures are important, as they have shown to be suitable for paleoenvironmental reconstructions (e.g. Kuvaas and Kristoffersen (1991), Melles and Kuhn (1993), Harris (2000), Presti et al. (2003) and Hass et al. (2016)). The seafloor morphology of the RLS consists of channels up to hundreds of meters deep and several kilometres wide with levees located beside the channels (Hass et al., 2016; Hass et al., in prep). Channels act as active pathways for turbidity currents and dense water masses originating from the continental slope. Seasonal open-water conditions and polynyas are often associated with increased biogenic activity (Ishikawa et al., 1996; Arrigo and Van Dijken, 2003). Brine formation is associated with polynyas (Massom et al., 1998), which is recognized in the RLS (Hass et al., 2016). Icebergs are reported to drift over the RLS (Aoki, 2003), while bottom currents are reported to flow along the western slope of the Gunnerus Ridge (Neelov et al., 1998; Kuvaas et al., 2004).

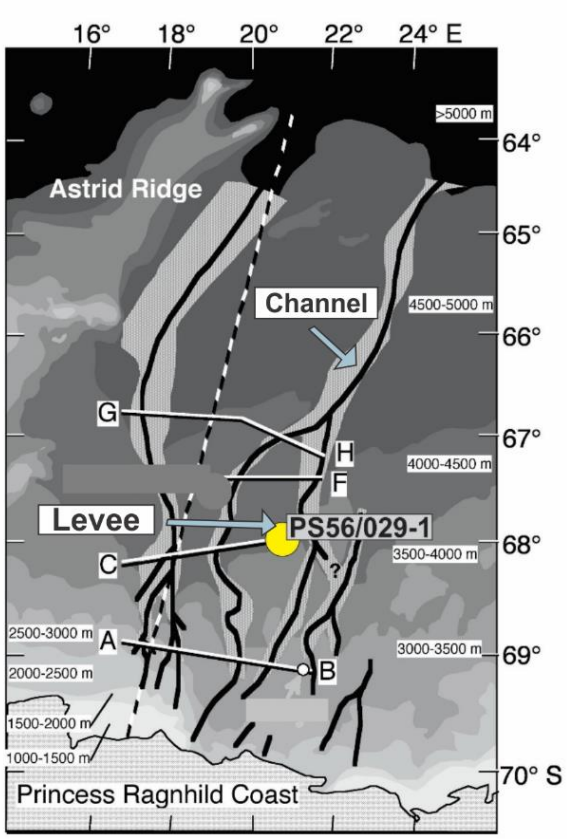

Fig. 5.4: Large-scale bathymetry of the western RLS, including core site PS56/029-1 (yellow circle). Channels are indicated by black lines and the outer position of the EAIS is displayed by light-grey colour (modified after Hass et al. (in prep)).

The forward movement of the EAIS in the RLS is constantly brining terrigenous material onto the continental margin (Fig. 1.2), where it is distributed towards the Enderby Abyssal Plain. Excluding IRD, a successive sorting of the sediments heading towards the Enderby Abyssal Plain will lead to the coarsest particles settling out nearest the coast. Icebergs and sea-ice can deposit IRD and have the ability to carry coarse-grained material far away from the sediment source (Gilbert, 1990). Icebergs may travel up to several thousand kilometres from the glacial source before they are completely melted, while sea-ice melts from below as it drift into warmer oceans and from above due to increased radiative energy in summer (Dowdeswell, 2009). The grain-size distribution for core PS56/029-1 reveals fine-grained sediments, including grain-sizes between 1.5 and 31.5 µm (clay and silt) (Fig. 4.4). The gravity core was retrieved c. 200 km offshore the Princess Ragnhild Coast at c. 4000 m water depth and the fine-grained sediments could therefore be the result of the successive sorting from the continental shelf towards the core site (Fig. 5.4). Additionally, denser water masses and turbidity currents originating from the continental slope would only deposit sediments onto the levee if the current was strong and big enough to flood the levee. The coarsest material of the current are

concentrated in the channel, thus only the fine-grained material of the current will be deposited onto the levee (Nichols, 2009). The factors discussed in this sub-chapter could partly explain the fine-grained sediments for core PS56/029-1 detected in the sedimentary record (Fig. 4.2) and by the high volume percentages of clay and silt (Fig. 4.3).

5.1.1 Bottom currents at core site PS56/029-1

The influence of bottom currents on the glaciated continental margin surrounding Antarctica is evident through multiple studies (e.g. Lucchi et al. (2002), Rebesco et al. (2002), Kuvaas et al. (2004), Maldonado et al. (2005) and Hass et al. (2016)). Bottom currents are capable of affecting the seafloor by transporting, re-suspending, and/or controlling the deposition of the sediments in the area. The speed and direction of these bottom currents are controlled by the acting environmental forces, i.e. oceanic and glaciological processes (e.g. Pudsey and Camerlenghi (1998) and Rebesco et al. (2002)). Furthermore, the intensity and strength of these bottom currents will change according to the acting environmental forces through glacial/interglacial cycles (e.g. Rebesco et al. (2002), Kuvaas et al. (2004) and Hass et al. (2016)).

Bottom currents in the RLS are reported to be present both in glacial and interglacial periods (e.g. Solli et al. (2007) and Kuvaas et al. (2004)), but with substantial variations in their strength. Weaker bottom currents predominate during glacials as a result of the ice-sheet growth, a more extensive sea-ice cover and smaller coastal polynyas (e.g. Pudsey (1992), McCave et al. (1995) and Ohshima et al. (2013)). The presence of an extensive sea-ice cover would reduce the strength of the bottom currents beneath the ice by preventing brine formation and oceanic circulation. Weaker katabatic winds would result in smaller coastal polynyas, which would reduce the heat exchange between the ocean and the atmosphere, leading to reduced brine formation. Hass et al. (2016) suggested that the position of the coastal polynyas in the study area was further north during colder times, since the study area was covered with sea-ice, hence preventing bottom-water formation is prevented during colder times. Stronger bottom currents predominate during interglacials as a result of the retreating ice-sheet, a less extensive sea-ice cover (sea-ice free conditions during austral summer and more sea-ice during austral winter), stronger coastal polynyas and a more active Weddell Gyre (Pudsey, 2000; Kuhn and Diekmann, 2002). Enhanced katabatic winds will encourage formation of coastal polynyas, thus increasing brine formation and consequently bottom water production in the study area. Stronger bottom currents in warmer/interglacial periods could lead to enhanced winnowing, i.e. removal of fine-grained material or longer suspension of fine-grained material, carrying

sediments over larger distances, thus, leaving behind coarser material. Grain-sizes of marine sediments are considered as a good proxy for bottom water strength, where stronger bottom currents lead to a coarsening of the sediments and weaker bottom currents lead to a fining of the sediments (e.g. McCave et al. (1995), McCave (2008) and Jessen and Rasmussen (2015)). Bottom current transported sediments deposited on channel levees during warmer/interglacial periods is expected to be coarser than those deposited during colder/glacial periods.

Bottom currents can rework marine sediments and/or deposit contourites or contourite drifts (Stow et al., 2002). In the sedimentary record for core PS56/029-1 contourites are recognized as better sorted fine-grained sediments, including sortable silt (SS) (10-63 µm), bioturbation and foraminifera with occasionally IRD (*see Chapter 5.2).*

The SS (10-63µm) fraction is a parameter frequently used in previous studies as a proxy for bottom water strength (e.g. Pfuhl and McCave (2005), McCave and Hall (2006) and McCave (2008)). Grain-sizes below 10 µm are considered as "cohesive", while grain-sizes between 10 and 63 µm are considered as "non-cohesive". This "non-cohesive" fraction shows signs of size sorting by bottom currents, thus, an increase in SS (10-63µm) is interpreted as an increase in the strength of the bottom currents (e.g. McCave et al. (1995)). PS56/029-1 is a fine-grained sediment core, where the bulk composition of the sediments varies between 1.5 and 31.5 µm (Fig. 4.4), containing an average grain size of 2.7 µm. This suggests a substantial portion of the sediment is smaller than the boundary for SS analysis (10 µm) and is therefore excluded from the SS results. Signals of bottom current variations from the SS analysis should therefore be interpreted carefully and not exclusively be based on the SS parameter.

The SS signal varies throughout the core, with certain intervals of particularly higher SS values (Fig. 4.6). Particularly increased SS signal is detected at two intervals, between 1220-1140 cm and 450-400 cm (Fig. 4.5). At these two intervals grains sizes up to 41.1 and 41.3 µm are observed. They might reflect two periods in time with stronger bottom currents in the RLS. The SS signal is also present in the five lithofacies distinguished in core PS56/029-1, which could imply that bottom currents of varying strength were present through glacial/interglacial cycles in the RLS.

5.1.2 Pelagic settling at core site PS56/029-1

Multiple studies on the glaciated continent margin surrounding Antarctica have shown that pelagic settling contribute to deposit sediments to the seafloor (e.g. Pudsey (2000), Lucchi et al. (2002) Solli et al. (2007)). Pelagic settling is associated with relatively calm oceanic

conditions in order for the particles to settle through the water column, including biogenic and terrigenous components (Kennish, 2000).

Pelagic settling through the water column occur both in glacial and interglacial periods (e.g. Droxler and Schlager (1985)). Particles accumulate through the water column, including a high ratio of biogenic material (e.g. foraminifera and diatoms) contributing to the abundance of biogenic components in seafloor sediments. Open-water conditions, stronger coastal polynyas and sea-ice free regions are settings associated with increased biogenic activity (Jones et al., 1998; Navarrete et al., 2005; Hass et al., 2016). Increased biogenic activity in near surface waters will lead to enhanced settling of material through the water column (Honjo et al., 1982). Open-water conditions, stronger coastal polynyas and sea-ice free regions are settings associated with warmer/interglacial periods (Ishikawa et al., 1996; Arrigo and Van Dijken, 2003). It is therefore reasonable to assume that pelagic settling occur more frequent in warmer/interglacial periods compared to colder/glacial periods.

Pelagic settling leads to the deposition of pelagic sediments or pelagite. In core PS56/029-1 pelagic sediments are recognized as unsorted fine-grained sediments, including foraminifera and bioturbation. Visual core description and line-scan images show repetitive foraminifera bearing zones throughout the core (Fig. 4.2). Element geochemical ratios reveal repetitive intervals with higher and lower calcium ratios (Ca/Sum and Ca/Fe) (Fig. 4.10 and 4.11). Rothwell and Rack (2006) argue that the calcium content in marine sediments is a good indicator to distinguish sediments of glacial/interglacial origin in the Atlantic Ocean. Where sediments of interglacial periods have higher carbonate concentrations compared to sediments of glacial periods. Additionally, fluctuations in the element geochemical ratios of calcium and iron can reveal the relative abundance of biogenic carbonate and terrigenous material, respectively (Rothwell and Rack, 2006). Assuming that the same applies for sediments in the Southern Ocean. Element geochemical ratios reveal repetitive intervals with higher and lower calcium ratios (Ca/Sum and Ca/Fe). The results can be interpreted as changes in biogenic carbonate and terrigenous material, as well as carbonate source rock. The Ca/Sum and Ca/Fe ratios could derive from carbonate in the source rock that the glaciers erode into, which could lead to higher calcium amounts during glacials (Rüther et al., 2017). Alternatively, the high Ca/Sum and Ca/Fe can be related to increased foraminifera content in interglacial sediments. Where the calcium content is mainly from the calcium carbonate ($CaCO_3$) tied up in the shells of the foraminifera. The latest interpretation is more likely for core PS56/029-1, because

increased calcium content is associated with intervals of increased foraminifera content (Fig. 4.14).

Core PS56/029-1 is a poorly-sorted fine-grained sediment core, including biogenic material. This, together with the long distance from the continent (c. 200 km offshore Princess Raghild Coast) it can be believed that pelagic settling through the water column are present through glacial/interglacial cycles. It is also reasonable to assume that pelagic settling can be one of several sedimentary processes operating simultaneously depositing sediments onto the levee, due to the polymodal signal in core PS56/029-1 (Fig. 4.4). A polymodal signal indicate that different depositional processes occur simultaneously (Hass et al., 2010). The polymodal signature in core PS56/029-1 include a unimodal, bimodal and trimodal signal, indicating sediments deposited by up to three different sedimentary processes. The unimodal signal occur only at nine individual depths (average grain-size 11.3 µm), the bimodal signal occur at 1172 individual depths (average grain-size 4.9 µm), and the trimodal signal occur at 85 individual depths (average grain-size 9.5 µm). It is therefore reasonable to assume that core PS56/029-1 consists of sediments deposited from several sedimentary processes. Furthermore, it is reasonable to believe that pelagic settling could have been one of the sedimentary processes that deposited sediments onto the core site. Additionally, the foraminifera bearing zones show a bimodal to trimodal signal. Pelagic settling is assumed high in biogenic material and it therefore support the interpretation that pelagic settling could have been one of the sedimentary processes that deposited sediments onto the core site.

5.1.3 Turbidity currents at core site PS56/029-1

Multiple studies on deep-water depositional systems on the glaciated continental margin surrounding Antarctica have concluded that turbidite systems are a common component on the Antarctic continental rise (e.g. Anderson et al. (1986), Kuvaas and Kristoffersen (1991), Kuvaas and Leitchenkov (1992), Rebesco et al. (1996) and Pudsey (2000)). Kuvaas et al. (2004) proposes intensified turbidity activity during glacial periods, which is attributed to the advancing ice sheet bringing oversteepend and unstable sediments to the shelf edge and upper slope. These sediments could move downslope as a turbidity current. Turbiditic activity is recognized in the RLS (e.g. Kuvaas et al. (2004), Solli et al. (2007) and Hass et al. (2016)).

The Coriolis force in Antarctica deflect objects to the left, resulting in oceanic currents and winds bending in a westward direction if the moving direction is from south to north (Fig. 5.5). This effect is evident in well-developed levee systems that show asymmetry between the levee

bank heights. In the Northern Hemisphere the right-hand-side channel levee is higher, while the left-hand-side channel levee is higher in the Southern Hemisphere (Cossu et al., 2010). Core PS56/029-1 was retrieved on the west side of the channel and turbidity currents deflecting westward would deflect towards the core location (Fig. 5.4). Thus, higher sedimentation rates are expected on the west side of the channel compared to the east side.

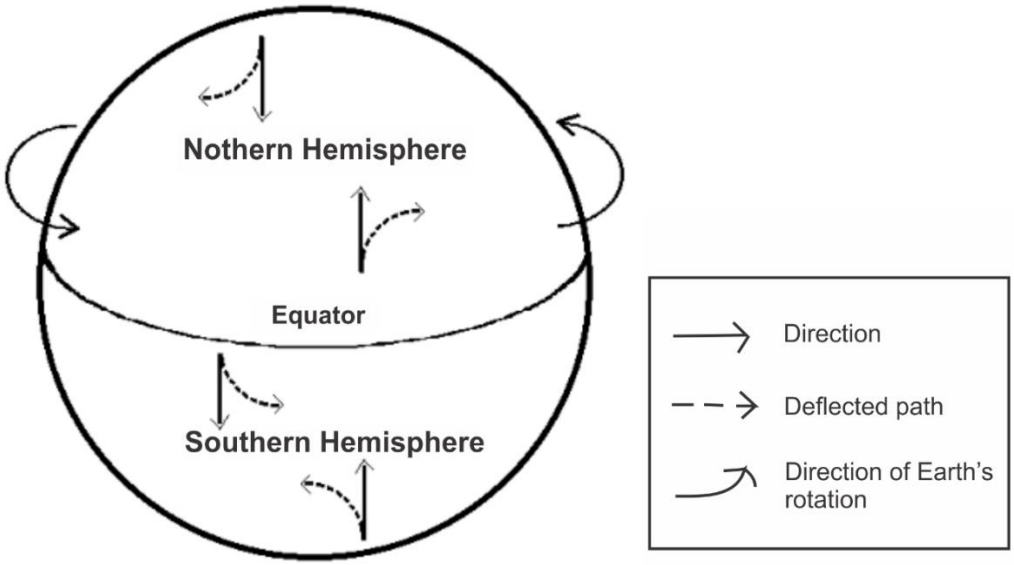

Fig. 5.5: Schematic figure illustrating the effect of the Coriolis force in the Southern and Northern Hemisphere (modified after Segers (2014)).

Turbidity currents in the RLS are reported to be present both in glacial and interglacial periods (e.g. Kuvaas et al. (2004) and Hass et al. (2016)). Turbidity currents occur in glacials due to an advancing ice-sheet or in interglacials due to higher meltwater discharge from the ice-sheet and/or in association with coastal polynyas due to brine formation (e.g. Harris (2000), Shanmugam (2000) Kuvaas et al. (2004) and Shanmugam (2006)). Deposition by a turbidity current onto the levee occur only if the current is strong and big enough to flood onto the levee, as an overbank deposit (Fig. 5.6). Deposition by a turbidity current is called a turbidite. In core PS56/029-1 turbidites are recognized as better sorted fine-grained sediments, including a sharp lower boundary, occurring with or without lamination, as well as having a sparse or absent foraminifera and IRD signal (*see Chapter 5.2*). Turbidites include sediments of terrestrial origin brought to the shelf edge by the advancing ice-sheet. Terrigenous sediments often include quartz high in silicon (Si), feldspar high in aluminium (Al) and potassium (K) and mica high in potassium, aluminium and silicon. Gneiss, granite, migmatite and gabbro include in the bedrock geology in Queen Maud Land, rocks high in Si, K and Si (e.g. Ohta et al. (1990)). It is, therefore, reasonable to assume that the geochemical composition of a turbidite include high element

ratios of Si/Sum, Al/Sum and K/Sum. High element ratios of Si/Sum, Al/Sum and K/Sum occur in association with lithofacies LGL and GLT (Fig. 4.12). However, the high silicon content could also be a result of reworked biogenic material since diatom tests are made up of opal, i.e. they contain a lot of silicon.

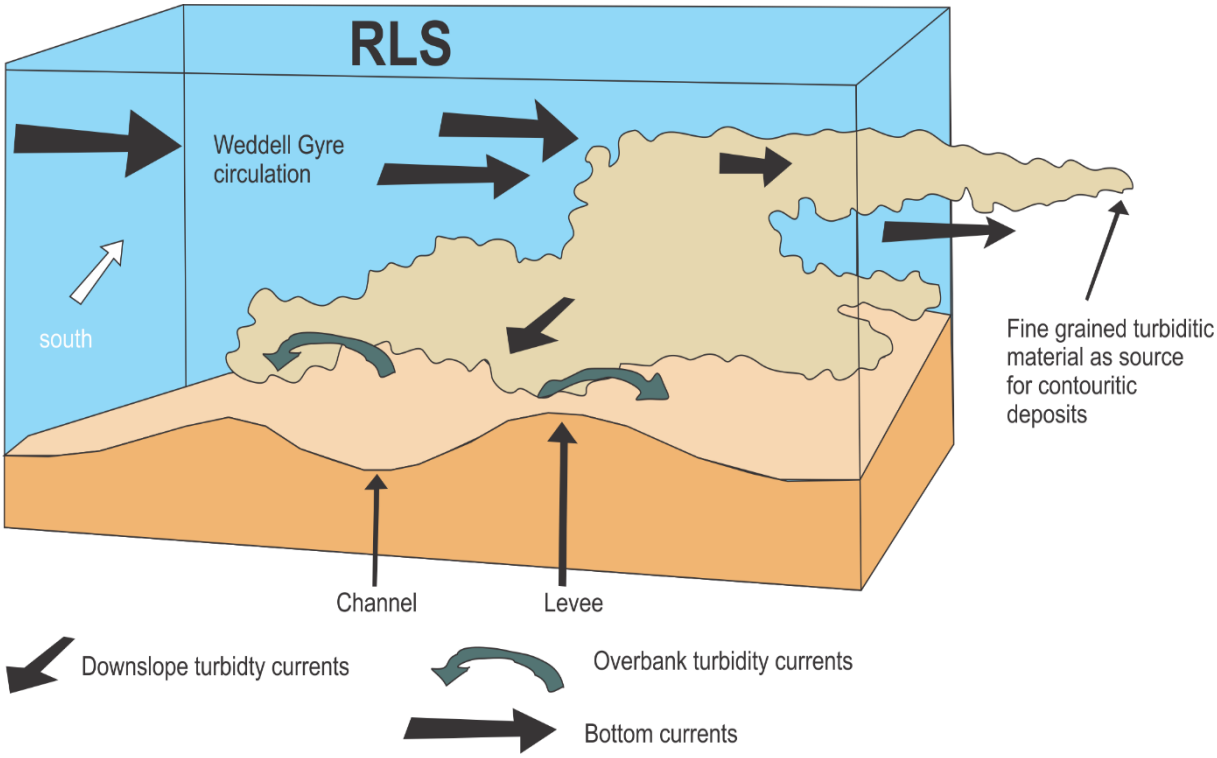

Fig. 5.6: Schematic representation of the interaction between alongslope and downslope driven processes operating in the RLS (modified after Shanmugam (2000)).

The turbidites recognized in core PS56/029-1 most likely represent the uppermost part of the Bouma sequence T_d and T_e (*see Chapter 2.4.1: Turbidites*), indicated by the fine-grained clay and silt sediments involved.

5.1.4 Ice-rafted debris (IRD)

Ice-rafted debris (IRD) is a common phenomenon in seafloor sediments on continental margins surrounding Antarctica (e.g. Keany et al. (1976) Alley and MacAyeal (1994) and Passchier (2011)). Both icebergs and sea-ice can transport and release IRD to the seafloor and both are present in the RLS (Fig. 2.12) (Gilbert, 1990; Aoki, 2003). However, due to the ice-covered coastline in the RLS a scenario where grains could be incorporated into the sea-ice seems unlikely. It is therefore more likely that an iceberg deposit the IRD to core site PS56/029-1.

IRD is reported to be present in both glacial and interglacial periods (e.g. Keany et al. (1976), Lien et al. (1989) and Rebesco et al. (2002)). However, it is reasonable to assume that icebergs occur more frequent in warmer/interglacial periods. Higher calving rates can occur when the ice streams are established and "pump" out icebergs and during deglaciation, and the drift of the icebergs is heavily influenced by the sea-ice cover (Gilbert, 1990; Aoki, 2003). The presence of sea-ice could prevent the icebergs from drifting around in the study area. Cofaigh et al. (2001) investigated the IRD content in sediment cores from the continental rise west of the Antarctic Peninsula and in the northern Weddell and Scotia Seas. Sediment cores from the Antarctic Peninsula contain maximum IRD concentrations in interglacials, whereas IRD concentrations are low deposits from glacials. However, the high IRD concentration in interglacials were suggested to be due to low sedimentation rates and current winnowing, rather than increased iceberg rafting. In contrast, sediment cores from the Weddell and Scotia Seas include low IRD concentration throughout the cores, where the signal is suggested to be of limited regional significance (Cofaigh et al., 2001).

Core PS56/029-1 include scattered IRD throughout the core. At some intervals the grain-size measurements reveal coarser sediments, while other intervals include a larger number of IRD. The coarser sediments are detected at depths 1216 cm, 1182 cm and 340 cm (Fig. 4.3), while a larger number of IRD is detected at depths 758 cm, 673 cm and 38 cm (Fig. 4.2). In the sedimentary record for PS56/029-1 IRD is recognized as unsorted, coarse-grained sediments. IRD can occur as a result of the icebergs dumping material over the core site, which can be detected through the grain-size measurements. Additionally, IRD can occur as individual features detected through X-ray photos, sometimes mixing with the pelagic sediments. Deposition of material from icebergs could explain the sudden rise in coarser grains to core site detected at depths 1216 cm, 1182 cm and 340 cm, containing 36.3, 5.4 and 27.5 volume percentages of sand respectively (Fig. 4.3). The sudden rise in coarser grain-sizes at depth 1216 cm include an unimodal signal of 65.7 µm. Depth 1182 cm include a trimodal signal, where mode 1 is 65.7 µm, mode 2 is 3.1 µm and mode 3 is 7.6 µm. Depth 340 cm include a bimodal signal, where mode 1 is 70.4 µm and mode 2 is 4.1 µm. The IRD signal is interpreted to occur in mode 1 for all these three individual depths, due to the high grain-sizes in mode 1. The IRD is also accompanied by a change in the geochemical composition, due to the new input of sediments. IRD at depth 1216 cm shows an increase of Si, Ca and Cr, while S, K, Fe and Cu decreases. IRD at depth 1182 cm shows an increase of Si and Ca, while K, Fe, Cu, Zn and Br decreases. IRD at depth 340 cm shows an increase of Al, Si, Ca and Cr, while K, Fe, Cu, Zn

and Br decreases. The change in geochemistry between 1216 cm, 1182 cm and 340 cm could imply different source area, i.e. that the icebergs came from different areas. Intervals containing a larger number of IRD at 758 cm, 673 cm and 38 cm could imply increased calving rates from the ice streams pumping out icebergs or represent a deglaciation.

In an overall perspective, the sediments brought to core site PS56/029-1 are deposited by: (1) sediment transport from the Princess Ragnhild Glacier System (PRGS) through the channel and onto the levee as an overbank deposit, either by turbidity currents or density currents. Occurring in glacials due to the advancing ice-sheet or in interglacial due to higher meltwater discharge from the ice-sheet and/or in association with polynyas. (2) Bottom currents responsible for winnowing the sediments, deposition of contourites or related to deep-water formation, i.e. that they are downslope currents. (3) Pelagic settling directly through the water column. (4) Deposition by icebergs drifting over the RLS (Fig. 5.5). The sedimentary record reveals often a combination of multiple processes. Due to the polymodal signal in core PS56/029-1, it is reasonable to believe that these processes have operated simultaneously through glacial/interglacial cycles.

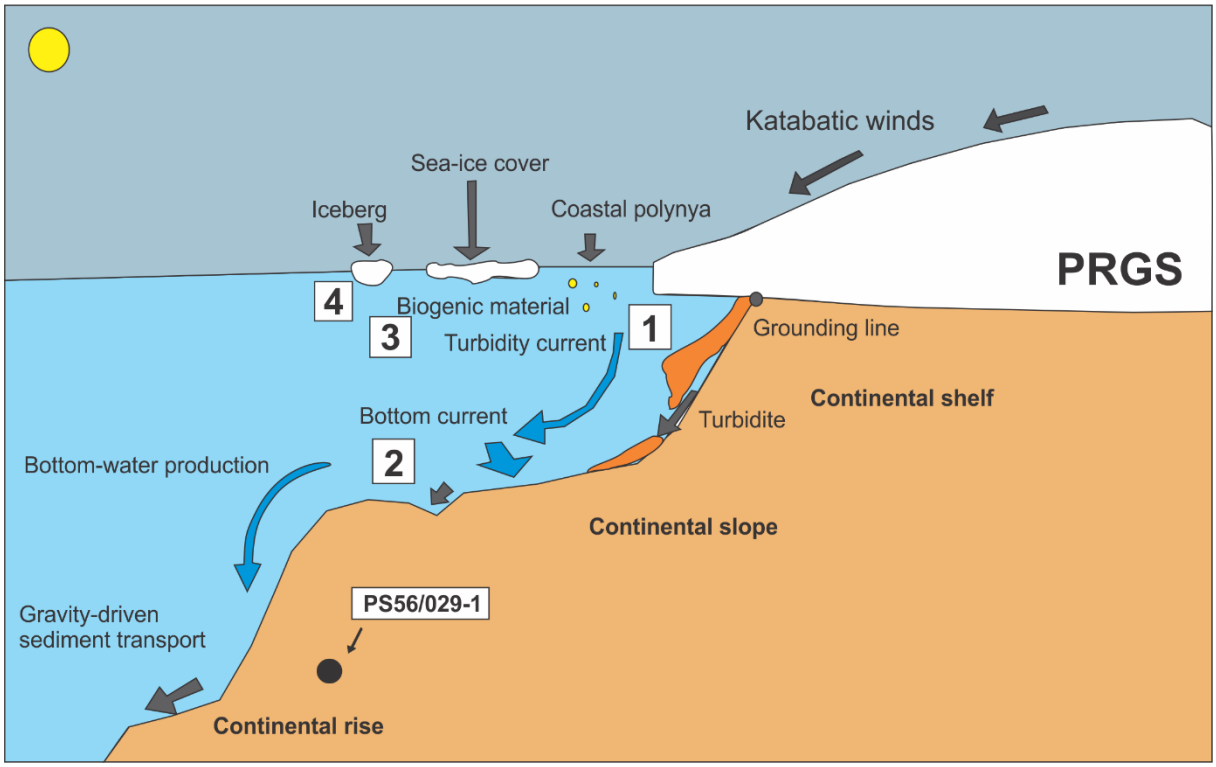

Fig. 5.7: Schematic representation showing the sedimentary processes responsible for the sedimentary record at core site PS56/029-1. Including the downslope sediment transport from the RAG (1), alongslope processes (2), pelagic settling through the water column (3) and the presence of icebergs and sea-ice (4) (modified after Grobe and Mackensen (1992) and Klages (2010)).

5.2 Interpretation of lithofacies

In the following sub-chapters are the lithofacies Laminated Grey Layer (LGL), Grey Layer Thin (GLT), Massive Lighter Layers (MLL) and Red Brown Layer (RBL) interpreted and discussed, and put into context in the glacial/interglacial cycle (Table 4.1).

5.2.1 Interpretation of LGL

Main characteristics of LGL are the greyish colour, presence of lamination, a sharp lower boundary, reduced foraminifer and absent IRD signal. Interval thicknesses varies between 15 and 66 cm. Physical properties include average MS values, average grain-sizes around 3 µm and sorting values between 2 and 3 µm. Geochemical properties include high element ratios of Al/Sum, Si/Sum, K/Sum and Rb/Sum, as well as low element ratios of Ca/Sum, Cu/Sum and Ca/Fe. Lithofacies LGL shows a bimodal trend (Table 4.1).

MS measurements are good indicators of glacial/interglacial cycles and are widely used in paleoenvironmental reconstructions (e.g. Verosub et al. (1993), Vanderaveroet et al. (1999) and Grutzner et al. (2003)). The basic principle is that high values reflect deposition during glacials and low values reflect deposition during interglacials. The enhanced terrigenous delivery from the continent to the ocean in glacial periods include terrestrial sediments that are magnetic, leading to higher MS. Enhanced terrigenous delivery occurs as a combination of lowered sea levels (increases proportion of exposed continent) and the presence of ice (eroding and transporting terrigenous sediments towards and into the oceans). Biogenic material (e.g. foraminifera and diatoms) has a low magnetic response, leading to reduced MS values. High productivity waters with increased biogenic material are associated with warmer/interglacial periods, which could raise the biogenic signal in the seafloor sediments, thus, resulting in lower MS (e.g. Lucchi et al. (2002)). Colder periods or glacials include reduced solar radiation and a more extensive sea-ice cover, conditions that reduce the productivity in the ocean and the biogenic input to the sediments. Lithofacies LGL include constant average MS values varying from 800 to 1000 $*10^{-8}$ SI (Table 4.1). These values could represent a time interval when the climate was relatively cold, with enhanced terrigenous delivery to the core site due to an advancing ice-sheet. It is also reasonable to assume that the input of biogenic material to the seafloor sediments was reduced, which could be explained by an extensive sea-ice cover, weaker coastal polynyas and lower productivity oceans in colder periods or glacials. The relatively constant MS values together with bed thicknesses up to 66 cm can imply a longer lasting and stable period in time. Unfortunately, this is an undated sediment core and this signal could just reflect high sedimentation rates during this time interval. Constant physical

properties (e.g. p-wave velocity, wet-bulk density and acoustic impedance) lead to the impression that the sediment delivery to core site PS56/029-1 was relatively stable. Lithofacies LGL consists of unsorted fine-grained sediments with average sorting values between 2 and 3 µm and grain-sizes between 3 and 5 µm (very fine silt to fine silt), respectively. These unsorted fine-grained sediments where therefore not deposited in a high-energy environment. X-ray photos, supplemented by the grain-size distribution for LGL reveal lamination (Fig. 4.14 and Fig. 4.15), while line-scan images reveal a sharp lower boundary (Fig. 4.18). Based on the mentioned properties of LGL above is it likely that these sediments were deposited by a turbidity current as a turbidite (Fig. 5.5). Due to the fine-grained sediments involved the turbidite sequence most likely represent T_d or T_e in the Bouma sequence (*see Chapter 2.4)*. High element geochemical ratios of Al/Sum, Si/Sum and K/Sum support the interpretation that the sediments within these layers are of terrigenous origin. Rothwell and Rack (2006) suggest that turbidites are richer in Fe and poorer in Ca compared to pelagic interbeds. Hence, the low geochemical ratio of Ca/Fe detected in LGL could further support the interpretation that the sediments are deposited by a turbidity current.

Polymodality is indicative of different depositional processes that occur simultaneously (Hass et al., 2010). Used to reconstruct conditions and energy of depositional environment (e.g. Beierle et al. (2002) and Sun et al. (2002)). The polymodal signature of lithofacies LGL is bimodal (Fig. 4.21), indicating two sedimentary processes responsible for depositing the sediments. The mode (s) signal presented in figure 4.21 indicate two pronounced pointed higher peaks and two lower peaks. The pointed higher peaks including grain-sizes up to 5.5 µm, while the lower peaks include grain-sizes up to 3 µm. The higher peaks are most likely the signal of a turbidite, while the lower peaks could be the signal of suspension settling through the water column. Lithofacies LGL include sortable silt (Fig. 4.16), which indicate sediments deposited by bottom currents. However, it might seem more likely that the polymodal signature is the product of a turbidity current and suspension settling.

Lithofacies LGL is suggested to represent a period in time that turned progressively colder, with turbidity currents present both in glacial summer, autumn, winter and spring, whereas the reduced foraminifera signal was deposited in glacial summer (Fig. 5.8). Reduced solar radiation would lead to lower productivity oceans, reducing the biogenic signal in the seafloor sediments. The advancing ice-sheet would erode and deliver unconsolidated sediment prone to failure to the shelf edge, which could move downslope as a turbidity current in the channel next to core site PS56/029-1. The material in suspension from the turbidity current could result in overbank

deposits on the levee if the current was strong and big enough (Fig. 5.6). The bimodal composition is most likely the result of deposition from suspension settling, but the bottom currents cannot be excluded due to the presence of sortable silt. Sparse IRD and foraminifera signal through lithofacies LGL could be due to a more extensive sea-ice cover in the RLS.

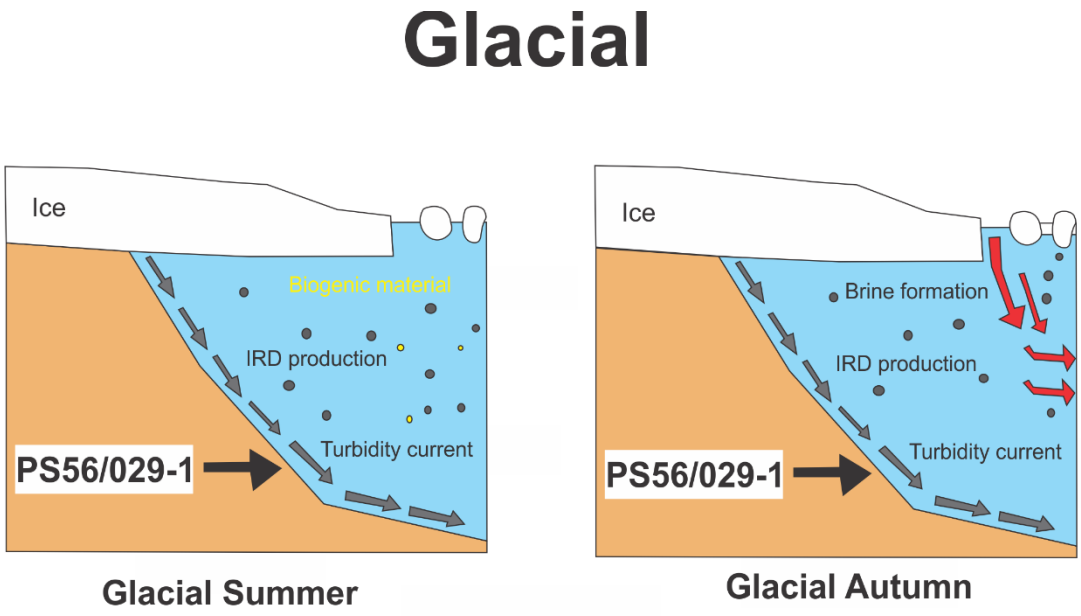

Fig. 5.8: Schematic figure showing the glacial summer and autumn, including sparse IRD and biogenic material (modified after Hass et al. (2016)).

5.2.2 Interpretation of GLT

Main characteristics of lithofacies GLT are the olive grey to dark grey colour and the presence of a sharp lower boundary. Physical properties include high MS values, p-wave velocities and wet-bulk densities, with average grain-sizes between 2 and 5 µm and sorting values between 2.5 and 5µm. Interval thicknesses varies between 3 and 15 cm. Geochemical properties include high element ratios of Al/Sum and Si/Sum, while low element ratios of Cu/Sum, Fe/Sum, Zn/Sum and Rb/Sum. Lithofacies GLT shows a bimodal to trimodal signal (Table 4.1).

Lithofacies GLT shows a clear abrupt increase of the measured physical properties (e.g. p-wave velocity, density and MS). The MS varies between 865 and 1916 $*10^{-8}$ SI, which are the highest measured values throughout the core. Values that can indicate material of terrestrial origin, where the occurrences of terrestrial sediments reflects enhanced glacial activity (compared with Robinson et al. (1995) Jessen et al. (2010)). The abrupt increase in p-wave velocity and wet-bulk density correlate with coarser grain sizes, including grain-sizes up to 5 µm. Gunn and Best (1998) described a characteristic p-wave pattern observed in turbidites, with high velocities at the base and decreasingly lower velocities towards the end of a turbidite sequence. Turbidity

currents are rapid short-lived events that influence the area with more energy, interrupting the "normal" sedimentation, including higher grain-sizes at the base due to higher velocities in the beginning of the current, as the velocity decreases the sediments becomes finer. Physical properties can therefore reveal turbidites in the sedimentary record. The abrupt increase of p-wave velocity and wet-bulk density, together with coarser grain-sizes could reflect one strong turbidite current event. The sorting signal include values between 2.5 and 5 µm, which indicate poorly to very poorly sorted sediments. However, GLT include the highest measured sorting value throughout the core. Relatively thin bed thicknesses and the presence of a sharp lower boundary could indicate a rapid, short-lived turbidity current interrupting the "normal" sedimentation. The ice-sheet advancing towards the shelf-edge in RLS could be responsible for increased turbidity activity, depositing sediments onto the levee as overbank deposits. The geochemical composition could reflect sediments of terrigenous origin, high in Al and Si. The geochemical composition of GLT differ from the geochemical composition of LGL, which could imply a shift in the sediment source between these two lithofacies. This change might partly be explained by the changing ice-sheet position, eroding into different bedrock towards the shelf edge.

The bimodal signal resembles the bimodal signal for lithofacies LGL. The bimodal signal include two sharp higher peaks with grain-sizes up 5.3 µm (Fig. 4.22) interpreted to be the work of a turbidity current depositing sediment onto the levee as an overbank deposit. The bimodal signal is the same through all intervals of GLT. The sortable silt (10-63 µm) fraction increases within these intervals (Fig. 4.6), implying that these sediments could have been deposited by bottom currents.

Lithofacies GLT in core PS56/029-1 is interpreted to include sediments deposited in glacial periods. Glacials represents cold periods in time where the ice-sheet was responsible for bringing unconsolidated sediments towards the shelf edge prone to failure downslope under the influence of gravity (Fig. 5.8). The head and main body of the turbidity current was located in the channel and the sediments in suspension would be deposited on the levee as overbank deposit. The deposited sediments include most likely the T_d and T_e of the Bouma sequence due to the fine-grained sediments involved. The sortable silt signal implies the presence of bottom currents at these intervals.

5.2.3 Interpretation of MLL

Lithofacies MLL consists of massive bioturbated olive grey coloured sediments with IRD and foraminifera. The lower boundary of MLL is highly bioturbated, occasionally including a sharp lower boundary. Interval thicknesses varies between 10 and 30 cm. Physical properties include low p-wave velocity, wet-bulk density and MS values, grain-sizes between 2 and 5 µm and sorting values between 2 and 4.2 µm. Geochemical properties include high element ratios of Sr/Sum, Ca/Sum and Ca/Fe, while low element ratios of Al/Sum, Si/Sum, K/Sum, Fe/Sum and Rb/Sum. Lithofacies MLL shows a unimodal to trimodal signal (Table 4.1).

Measured physical properties of MLL differ greatly from the physical properties detected for lithofacies LGL and GLT. Low MS values (700-1000 $*10^{-8}$ SI) detected in MLL occur after lithofacies LGL and GLT interpreted to be deposited during glacial periods. It is therefore reasonable to assume that MLL represent another time interval in the glacial/interglacial cycle. As discussed above low MS values indicate sediments with increased biogenic material and are attributed to interglacial sediments. Interglacial periods include a retreating ice-sheet, a less extensive sea-ice cover and stronger coastal polynyas. Increased solar radiation in warmer/interglacial periods would additionally contribute to oceans of increased productivity. MLL consists of poorly sorted fine-grained sediments. The presence of foraminifera (Fig. 4.12) and bioturbation (Fig. 4.19) within lithofacies MLL indicate oceans of higher productivity. Foraminiferal tests consisting of calcium carbonate contribute to the increased calcium content in seafloor sediments. The higher element geochemical ratio of Ca/Sum detected in some of the MLL can lead to the interpretation that these time intervals contained a higher portion of foraminifera compared to the rest of the core. The presence of IRD within some of these layers can be evidence for the retreating ice-sheet, which releases icebergs that drift of the core location. The strongly bioturbated lower boundaries of this lithofacies provide evidence that organisms have been active, while the sharp lower boundaries indicate the sudden deposition from a faster moving current. During interglacials, turbidity activity is contributed to higher melt-water discharge from the ice-sheet and/or in association with coastal polynyas. This will be explained in more detail in Chapter 5.3 (p. 114).

The unimodal to trimodal signal reflects the different sedimentary processes. From figure 4.22 the mode signal between 655 cm and 645 cm indicate two higher pointed peaks and two lower flatter peaks. The polymodal signature resemble the polymodal signature in LGL (Fig. 4.21) interpreted as the signal of a turbidite. The higher peaks include grain-sizes up to 6 µm for the MLL, which are slightly coarser than the higher peaks detected at LGL. Based on the mode

signal for MLL it is hard to distinguish the sedimentary processes responsible for depositing the sediments. Since the polymodal signature of LGL is interpreted to be the result of a turbidity current and the polymodal signatures of LGL and RBL resembles each other, it could imply that RBL is also deposited by a turbidity current. This leads to the interpretation that turbidites are present during interglacial cycles, in addition to glacial cycles (Fig. 5.8 and Fig. 5.9). The second signal consists of finer grain-sizes up to 3 µm and could be the attributed to suspension settling or bottom. However, some of MLL intervals include sortable silt, while in other interval the signal is almost absent. Sortable silt indicate bottom currents and the changing presence of sortable silt within MLL could imply that some of these intervals are deposited by bottom currents. When the sortable silt signal is reduced it could imply weaker bottom currents. Based on the polymodal signature resembles the layers suggested to deposited by a turbidity current it seems more likely that the second signal could the sign of suspension settling. The latest interpretation seem more likely for the MML layers that include a sharp lower boundary. Deposition of turbidites might interrupt the normal sedimentation of the area during warmer/interglacial periods due to enhanced brine formation. It is fair to assume that enhanced brine formation occur in interglacial autumns attributed to stronger coastal polynyas and a more extensive sea-ice cover compared to interglacial summers with less or absent sea-ice cover. Interglacial summers would likely include settling of biogenic material through the water column.

Lithofacies MML in core PS56/029-1 is interpreted to include sediments deposited in interglacial periods. Interglacial periods are characterized by a retreating ice-sheet with less extensive sea-ice cover and stronger coastal polynyas with increased brine formation (Fig. 5.8). The strength of the bottom currents were most likely stronger compared to LGL and GLT interpreted to be deposited during glacial periods. Enhanced turbidity currents in interglacial autumn were most likely due to stronger costal polynyas, because stronger coastal polynyas include increased brine formation. The biogenic settling trough the water column was most likely more present in interglacial summers with little or absent sea-ice. The high foraminifera signal is most likely due to high productivity oceans.

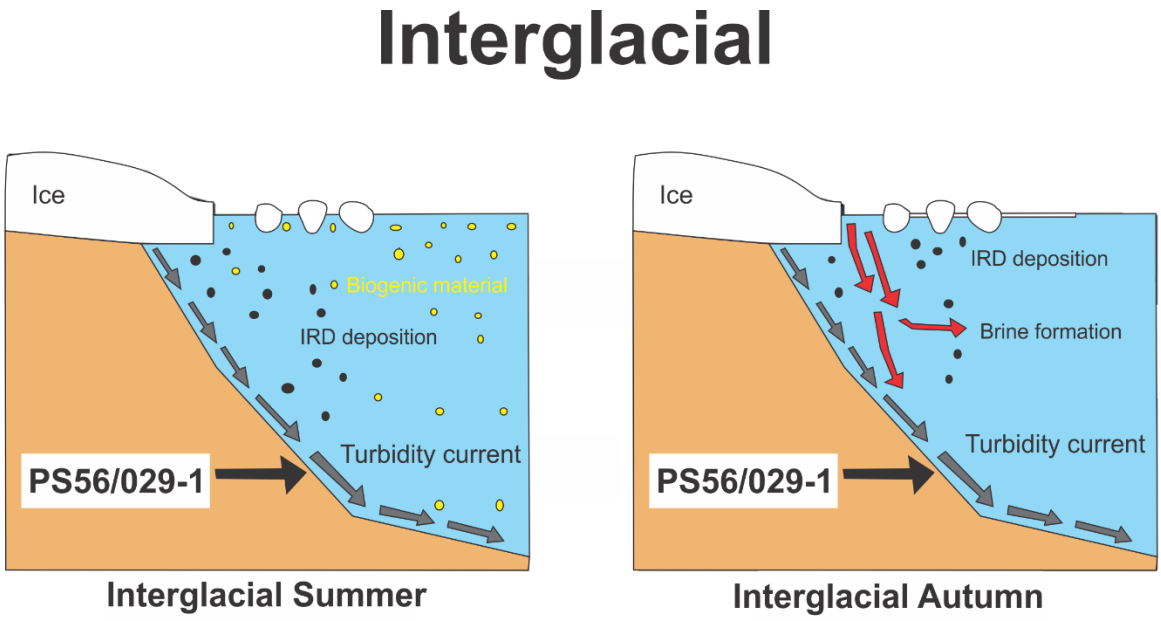

Fig. 5.8: Schematic figure showing the interglacial summer and autumn, including IRD, biogenic material, turbidity currents and brine formation (modified after Hass et al. (2016)).

5.2.4 Interpretation of RBL

The main characteristics of lithofacies RBL are dark greyish brown colour, occurrences of bioturbation, IRD and the presence of foraminifera. Interval thicknesses varies between 10 and 40 cm. RBL has grain-sizes between 2 and 7 µm, and sorting values between 2 and 4.2 µm. Geochemical properties include high element ratios of S/Sum, Cu/Sum, Ca/Sum and Ca/Fe, while low element ratios of Rb/Sum, Al/Sum, K/sum and Fe/Sum. Lithofacies RBL includes a bimodal to trimodal signal.

Measured physical properties of RBL reveal low p-wave velocity, wet-bulk density and MS. Physical properties are similar to MLL. Low MS values (500-900 $*10^{-8}$ SI) detected in RBL indicate sediments of interglacial periods, as discussed above (*see Chapter 5.3.1*). RBL occurs in the core top, thus, reflecting present environmental conditions. Increased marine biologic productivity waters, a reduced sea-ice cover, a stable or retreating ice-sheet and stronger coastal polynyas are conditions associated with warmer periods. The lowest MS values throughout the core occur at depths around 400 cm. It could be due to higher productivity in the ocean. The presence of foraminifera (Fig. 4.2) and bioturbation (Fig. 4.20) contribute to the interpretation of increased marine productivity during these time intervals. Enhanced marine productivity is also, supported by high Ca/Sum ratios (except at depth around 420 cm) (Fig. 4.14). Warmer conditions might also be indicated by the occurrence of IRD in the sediment, suggesting

icebergs were calving from a retreating ice sheet. The grain-size distribution of RBL is slightly coarser in comparison to the grains-size distribution of LGL, GLT and MLL. The increased 5 point running silt fraction supports that RBL consists of slightly coarser sediment grain-sizes (Fig. 4.8). Coarser grain-sizes in warmer periods could be due to intensification of the Weddell Gyre, stronger bottom currents and/or increased meltwater in the RLS (*Chapter 5.3*). The grain-sizes involved in these intervals include low geochemical ratios of Al/Sum and K/Sum (Fig. 4.12). The elements Al and K are suggested to be of terrestrial origin (*see Chapter 5.1.1*), and the low ratios of Al/Sum and K/Sum could possibly indicate a further inland position of the ice-sheet, or alternatively, that there was higher biological productivity "diluting" the terrestrial signal. In general the geochemical ratio of Si/Sum is low, except at 420 cm, where relatively high Si/Sum values are observed (Fig. 4.8). This signal could be explained by an increased abundance of diatoms (siliceous algae). The same interval include sediments with reduced calcium content (Fig. 4.14). As calcium content in core PS56/029-1 is attributed to arrive mainly from foraminifera, this time interval could represent an increase of diatoms relative to foraminifera.

Based on the results of the sortable silt fraction, which increases in intervals of RBL (Fig. 4.6), it is likely to believe that stronger bottom currents were present at depths between 1040-1030 cm, 953-937 cm, 421-380 cm, 201-190 cm, 95-72 cm, 32-21 cm and 5-0 cm. Bottom currents are responsible for depositing contourites or to winnowing of the sediments. Warmer/interglacial periods include stronger bottom currents compared to colder/glacial periods (*see Chapter: 5.1.2*), it is therefore reasonable to assume that warmer/interglacial periods include sediments deposited by bottom currents. Lithofacies RBL is suggested to include interglacial sediments, hence it is likely to assume that grain-sizes deposited by bottom currents are coarser compared to sediments deposited by bottom currents in glacials due to stronger bottom currents in interglacial periods. The detected increase in sortable silt in lithofacies RBL could therefore be due to enhanced bottom currents in warmer/interglacial periods. The increase in sortable silt in RBL is reflected by the coarser grain-size distribution for intervals interpreted as RBL.

The bimodal and trimodal signal detected in RBL indicate two or three sedimentary processes at the time of deposition (Fig. 4.24). The bimodal signal occur more frequently compared to the trimodal signal in RBL. The mode(s) signal observed at depths between 1040-1030 cm shows a more chaotic signature including finer grain-sizes compared to the mode(s) signal at depths between 95-72 cm. Coarser grain-sizes indicate higher velocity within the sedimentary process

depositing the sediments, hence the interval between 95-72 cm include sedimentary processes with higher velocities compared to the interval between 1040-1030 cm. The mode(s) signal at depths between 95-72 cm shows two higher peaks including coarser grain-sizes up to 6 µm, while the mode(s) signal at depths between 1040-1050 cm is more chaotic with grain-sizes up to 4.3 µm. The detectable change in the polymodal signature of these two depths could imply sediments deposited by different sedimentary processes. The polymodal signature at depths between 1040-1030 cm could be explained by different processes. It could be the signal of bottom currents picking up grains from a current located in the channel next to core site PS56/029-1 (Fig. 5.6), or, alternatively be the signal of winnowing removing the fine-grained material or keep it longer in suspension leading to the fine-grained material to be transported away. The latest interpretation is more likely due to the absent of a sharp lower boundary. The flatter lower peaks could be attributed to pelagic settling. Due to the detectable increase in sortable silt at 1040-1030 cm this interpretation seems likely. The polymodal signature detected at depths between 95-72 cm include two pointed higher peaks that resembles the signature interpreted to be the work of turbidity currents in lithofacies LGL and GLT. However, no sharp lower boundary is detected at 95 cm, which is expected since a turbidity current is a fast moving current. The coarser grain-sizes between 95-72 cm is therefore suggested to be due to winnowing, which removes the finer material or keep the fine-grained material longer in suspension, either way leaving behind coarser grain-sizes.

5.3 Coarser sediments in warmer/interglacial periods

The coarsening trend seen in lithofacies MLL and RBL associated with warmer/interglacial periods can be partly explained based on three mechanisms operating in the RLS. These mechanisms are 1) the intensity variations of the Weddell Gyre, 2) stronger coastal polynyas as a site for intensified bottom-water production and 3) turbidity currents triggered by debris-rich meltwater.

5.3.1 Intensity variations of the Weddell Gyre

The Weddell Gyre originate in the Weddell Sea sector and is a major site for dense and cold bottom water production in the Southern Ocean. Deep water formation in the Southern Ocean is an important contributor to the global thermohaline circulation system (e.g. Orsi et al. (1995)). The RLS is affected by the easternmost part of the Weddell Gyre (Fig. 5.3) (Schröder and Fahrbach, 1999).

The intensity of the Weddell Gyre is reported to increase in interglacial periods compared to glacial periods (Pudsey, 2000; Kuhn and Diekmann, 2002). An intensification of the rotation in the Weddell Gyre will affect the water masses near the seafloor resulting in an intensification of the bottom currents operating at these depths. Stronger bottom currents will lead to winnowing of the fine-grained sediments and their re-deposition as contourites. The sediments involved originate either from turbiditic activity on the continental shelf or upper continental slope, or include biogenic components settling through the water column (Maldonado et al., 2005). The presence of a presumable clockwise sub-gyre in the RLS between Astrid and Gunnerus Ridge could further lead to enhanced bottom current activity on the lower continental slope and rise in interglacial periods (Kuvaas et al., 2004). An amplified Weddell Gyre could therefore explain the increase in sortable silt and the slightly coarser grain-sizes detected for lithofacies RBL and MLL.

In the sedimentary record it is challenging to distinguish between alongslope winnowed contouritic material and those sediments deposited by downslope turbiditic activity. Interpretations of physical properties, grain-size distribution, and sortable silt (10-63 µm) fraction suggests contouritic material is deposited from alongslope processes at core site PS56/029-1. However, the sediments consist of the same grain-sizes as those sediments originating from a turbidite, containing grain-sizes also between 1.5 and 31.5 µm. Throughout the core, sortable silt is present and it indicates that grains larger than 10 µm carried in suspension is picked up from the turbidity current and winnowed away with bottom currents before being deposited as a contourite (Fig. 5.6). An amplified Weddell Gyre could therefore partly explain the coarsening trend seen in lithofacies MML and RBL due to the raised ability to pick up coarser particles from the turbidity current and re-deposit them on the levee.

5.3.2 Coastal polynyas: a site for intensified bottom-water production

Coastal polynyas located around the coast of Antarctica, especially in the RLS, is a source for bottom-water production (National Snow & Ice Data Center, 2018b). Enhanced katabatic winds in interglacial periods results in stronger coastal polynyas compared to glacial periods (Ishikawa et al., 1996). Stronger coastal polynyas would intensify formation of cold and dense-water through brine formation. Increased sea-ice formation in interglacial autumns compared to interglacial summers, would likely increase brine formation, and the formation of cold and dense-water (Fig. 5.8 and Fig. 5.9) (e.g. Gordon and Comiso (1988)). Hence, the continental margin in front of the coastal polynya could work as an active pathway for the bottom waters on their way to the Enderby Abbysal Plain. Moreover, the cold and dense-water could influence

the sediments at the continental slope making them unstable, which could result in downward moving turbidity currents (Harris, 2000; Caburlotto et al., 2010).

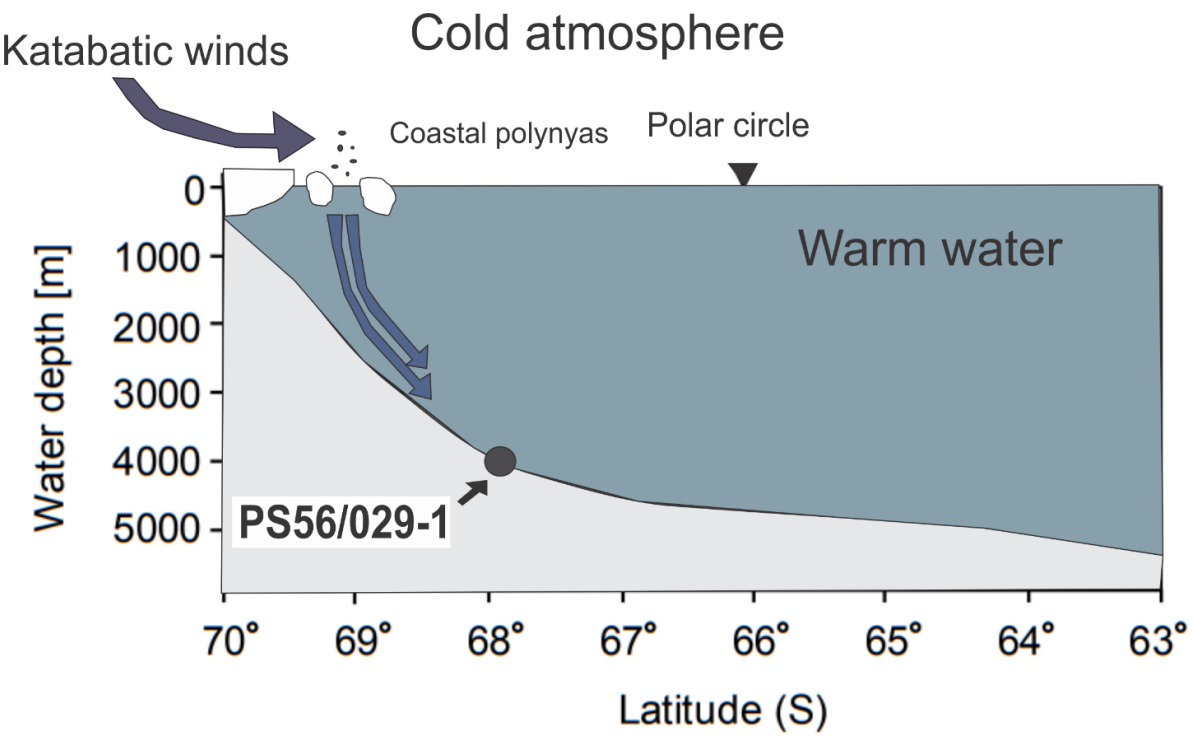

Fig. 5.9: Schematic figure of coastal polynyas, including katabatic winds displayed with a dark blue arrow, denser water masses displayed by lighter blue arrows and core location is displayed by a black circle (modified after Hass et al unpublished)

The sea-ice cover in interglacial periods in Antarctica includes sea-ice free conditions in austral summer, while a more extensive sea-ice cover exists during austral autumns (National Snow & Ice Data Center, 2018a). Sea-ice during interglacial periods is both more brittle and thinner compared to glacial sea-ice. The extensive sea-ice cover in glacial periods, in addition to reduced katabatic winds would prevent coastal polynyas to form. In interglacial periods would enhanced katabatic winds result in coastal polynyas. The interglacial summer include sea-ice free conditions, without sea-ice formation, there would not be coastal polynyas or brine formation. The interglacial autumn would include increased sea-ice formation, and coastal polynyas would therefore be a site for dense water masses. These ice-free areas stay in constant contact with the cold overlying atmosphere, where exchange of heat result in high evaporation rates, sea-ice production and brine formation. The raised salt content in the water results in the downward movement of colder and denser waters resulting in High Saline Shelf Waters (HSSW) (Foldvik et al., 2004). Due to the close proximity of the coast and coastal polynyas in the RLS these denser water masses could reach the continental slope, possibly, triggering

turbidity currents and/or erode channels on their way to the Enderby Abyssal Plain (e.g. Forwick et al. (2015) and references therein). The resulting sediment deposited on the levees could contain coarser particles, from suspension of the fine-grained component of the turbidity currents.

Open water conditions favour increased biologic marine productivity rates, which results in increased biogenic content of seafloor sediments. Coastal polynyas are ice-free regions associated with high biogenic production (National Snow & Ice Data Center, 2018b). Lithofacies RBL and MLL are characterized by high element geochemical ratios of Ca/Sum and Ca/Fe, which could derive from increased biogenic production rates associated with coastal polynyas.

5.3.3 Turbidity currents triggered by debris-rich meltwater

The third process that could be responsible for slightly coarser sediments observed in lithofacies MLL and RBL is the discharge of debris-rich meltwater plumes originating from subglacial meltwater tunnels below the Princess Ragnhild Glacier System draining into the RLS (Fig. 5.10). These debris-rich meltwaters could be responsible for eroding the channels and/or triggered turbidity currents, increasing the grain-sizes deposited on the levee at the core site. The Princess Ragnhild Glacier System is constantly bringing new sediments to the continental shelf and slope, and thus, coarse-grained glacial detritus is deposited close to the outlets of these subglacial tunnels (Hesse et al., 1999). These sediments can become unstable and move downslope as a slump and/or a slide, and are prominent triggers for turbidity currents (Shanmugam, 2006). During interglacial periods were the meltwater discharge is enhanced, turbidity currents triggered by debris-rich meltwater could be intensified. Therefore, the increased grain-size observed in interglacial periods could partly be a result of increased debris-rich meltwater through the Princess Ragnhild Glacier System.

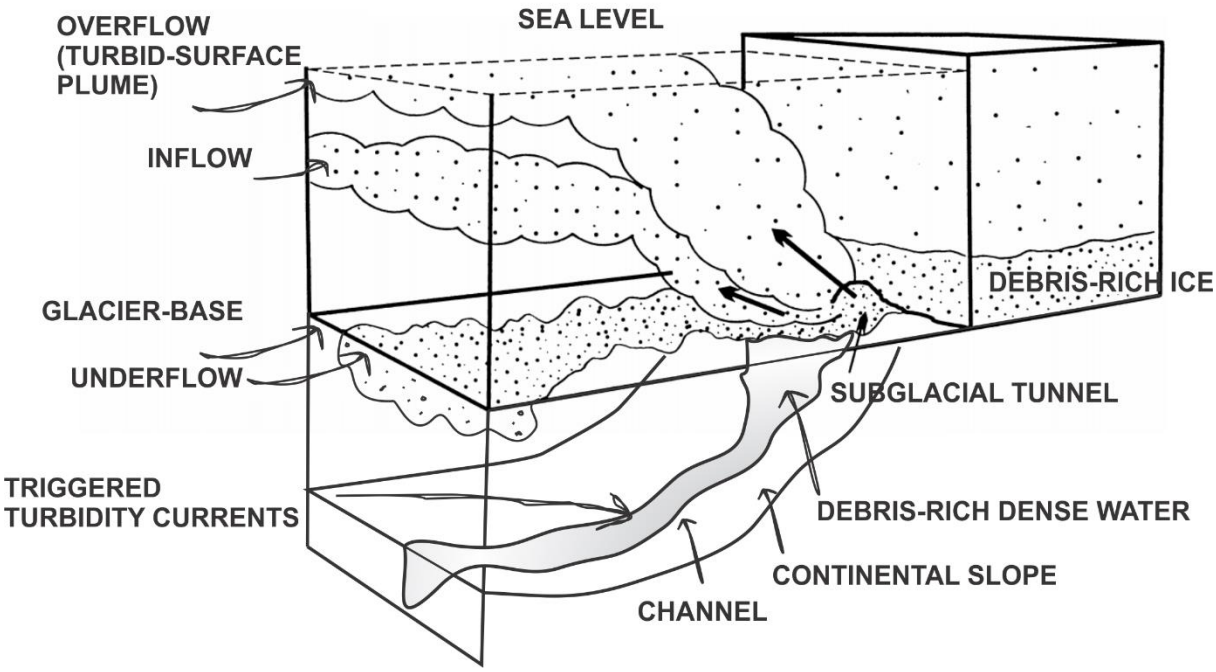

Fig. 5.10: Schematic representation of debris-rich meltwater plumes originating from the Princess Ragnhild Glacier System in the RLS as a trigger for channel erosion and levee accumulation (modified after Hesse et al. (1999)).

5.4 Sediments in colder/glacial periods

Sediments originating from colder/glacial periods are different from sediments originating from warmer/interglacial periods. For core PS56/029-1 lithofacies LGL and GLT are interpreted to include sediments deposited during glacial periods. Sediments in colder/glacial periods generally contain less biogenic material, bioturbation and IRD, as well as lower Ca/Sum and Ca/Fe ratios, in comparison to sediments deposited during warmer/interglacial periods. In contrast, sediment deposited during glacial periods includes increased Si/Sum, Al/Sum and K/Sum ratios, sharp lower boundaries and lamination.

The processes responsible for depositing sediments of glacial origin differ from the processes responsible for depositing sediments of interglacial origin (e.g. Kuvaas and Leitchenkov (1992), Rebesco et al. (2002) and Kuvaas et al. (2004)). Multiple ice streams drain into the RLS between the Astrid Ridge and Gunnerus Ridge (Rignot et al., 2011). These ice-streams reaches the coast and enters into the RLS. The Princess Ragnhild Glacier System constantly drain meltwater into the RLS. Because of these constantly flowing ice-streams in the RLS the continental shelf break is constantly overrun (Fig. 5.2). The seafloor morphology of the RLS include a very short or absent continental shelf, where the shelf-ice edge is located over water depths of 1000 m (Thiede and Oerter, 2002). The continental slope is steep, reaches down to c. 5000 m water depth where the RLS connects to the Enderby Abyssal Plain. Sediments brought to the shelf-ice edge would therefore quickly demobilize and move downslope, which could

lead to enhanced turbidity activity. This would further lead to enhanced turbidity activity in the channel next to core site PS56/029-1. Consequently, resulting in overbank deposits on the levee if the current was strong and big enough to flood the levee.

Turbidity currents are believed to be more frequent and active during glacials and enhanced towards glacial maxima (Kuvaas et al., 2004). More frequent and active turbidity currents in colder/glacial periods could however be smaller than turbidity currents in warmer/interglacial periods. Smaller turbidity currents would result in finer particles deposited onto the levee, due to finer particles in the turbidity current. The result would be finer particles deposited onto the levee during colder/glacial periods compared to warmer/interglacial periods. During colder/glacial periods the activity regarding turbidity flows could have been higher compared to warmer/interglacial periods. Turbidity currents in colder/glacial periods could occur so often that it was not possible to accumulate large volumes of sediment that could fail. Therefore, the turbidity currents were relatively small and they could not deposit coarser grains on the levee. It can be believed that this occurred at core site PS56/029-1 due to the slightly coarser interglacial sediments.

Lithofacies LGL and GLT interpreted as sediments deposited during glacial periods that consists mostly of turbidites interpreted to be the T_d and T_e units of the Bouma sequence are likely from weaker or smaller turbidity currents. The reason for this are explained and discussed below:

5.4.1 A weakened Weddell Gyre

The Weddell Gyre has been less active during glacial times and more active during interglacial periods (Schröder and Fahrbach, 1999; Pudsey, 2000; Kuhn and Diekmann, 2002). The Weddell Gyre is powered by vertical fluxes of heat and moisture in association with a changing sea-ice cover in the Weddell Sea Sector (Schröder and Fahrbach, 1999). With a more extensive sea-ice cover during cold periods, the exchange between ocean water and the cold atmosphere will be lowered, possibly reducing the intensity of the Weddell Gyre, and consequently maybe slowing the formation of AABW in the Weddell Sea Sector. A less active Weddell Gyre in the RLS during colder periods with extensive sea-ice cover would have been imprinted on the sediments at the core site. A less active Weddell Gyre will likely be observed as finer particles at the core site.

5.4.2 Weaker coastal polynyas

Coastal polynyas located in the RLS as mentioned above are reported to be more extensive during interglacials. If the coastal polynyas were smaller it could prevent brine formation, preventing high salinity waters to flow down the continental slope and rise. If the brine formation was prevented it would not trigger turbidity currents to move down the channel next to core site PS56/029-1. Deposition onto the levee as a result of denser water masses created in association with coastal polynyas would be absent.

5.5 Summary of lithostratigraphy

It is suggested that core PS56/029-1 includes sediments deposited during glacial and interglacial periods. The polymodal signature is interpreted to reflect mixed contouritic, pelagic and turbiditic influence, as well as occasionally IRD. The alternating repetitive intervals of lithofacies distinguished throughout the core are believed to reflect changing depositional environments in the RLS, accumulated in lighter brownish and greyish coloured intervals.

The lighter brownish intervals make up lithofacies MML and RBL, suggested to be deposited during interglacial periods. Sediments deposited during interglacial periode include increased IRD content, occurrences of foraminifera and bioturbation, occasionally a sharp lower boundary, low MS and slightly coarser grain-sizes. The geochemical composition include in general high ratios of Ca/Sum and Ca/Fe, and low ratios of Al/Sum and K/Sum. The slightly coarser sediments are suggested to be the result of enhanced contouritic and turbiditic activity. The stable or retreating ice-sheet, larger coastal polynyas and a less extensive sea-ice cover are suggested as the controlling factors. Turbidity currents in interglacial periods are likely triggered by denser water masses created in coastal polynyas or a result of increased debris-rich meltwater from the Princess Ragnhild Glacier System. Stronger contour currents and an increased strength of the Weddell Gyre in interglacial periods result in winnowing or deposition of slightly coarser contourites compared to contourites deposited during glacials. It is suggested that the finer fraction in suspension is carried away with bottom-currents, thus leaving behind coarser sediments at the core site.

The greyish intervals make up lithofacies LGL and GLT, suggested to be deposited during glacial periods. Sediments deposited during glacial periods include sparse IRD, reduced foraminifera content, a sharp lower boundary, lamination, average to high MS and slightly finer grain-sizes. The geochemical composition include high ratios of Al/Sum, Si/Sum, K/Sum and Rb/Sum, and low ratios of Ca/Sum and Cu/Sum. The slightly finer sediments are suggested to

be the result mainly of turbiditic activity, with reduced contouritic activity. The advancing ice-sheet would bring huge amounts of sediments towards the shelf edge, where it would demobilize and move downslope, resulting in turbidity currents. More frequent turbidity currents in glacial periods are suggested, but the turbidity currents were likely smaller and weaker resulting in finer particles deposited onto the levee. Weaker bottom currents in glacial periods would reduce the currents ability to carry the finer fraction in suspension and, thus, result in finer sediments at the core site.

The repetitive alternating layers observed reveal that the depositional environment in RLS changed through glacial/interglacial cycles and sediment deposition occurred mainly from turbiditic and contouritic activity. The strong turbiditic signal in core PS56/029-1 suggests that turbidity currents occurred repeatedly. However, grain-size measurements suggest stronger and bigger turbidity currents in interglacials and weaker and smaller turbidity currents in glacials. Where turbidity currents in glacials occurred more repeatedly compared to turbidity currents in interglacials. More repeatedly occurring turbidity currents in glacials could have prevented large volumes of sediments to build-up on the shelf edge, resulting in weaker and smaller turbidity currents that would have deposited finer sediments onto the levee compared to stronger and bigger turbidity currents. The turbidity currents in interglacials were likely stronger and bigger, but occurred less frequently, resulting in coarser grain-sizes deposited onto the levee. Due to the strong turbidity signal throughout the core it is reasonable to believe that this was the dominant contributor to deposit sediments at core site PS56/029-1. The contouritic signal varies throughout the core and reflect bottom currents of varying strength. Bottom currents in interglacials are believed to be stronger compared to bottom currents in glacials. Stronger bottom currents at core site PS56/029-1 are believed to result in coarser sediments due to the currents ability to carry the fine fraction in suspension away from the core site. Pelagic sediments are interpreted to occur more frequent in interglacials compared to glacials. The absent foraminifera signal between 740 cm to 420 cm could reflect deteriorated environmental conditions where the living conditions were not that good, or alternatively reflect dissolution of the calcium composing the foraminifera. The scattered IRD signal implies that icebergs drift over the RLS, and increased IRD concentration in interglacial sediments implies that icebergs were more present in interglacials compared to glacials. Higher calving rates in interglacials are most likely due to a retreating ice-sheet.

5.6 Marine isotope stages (MIS)

Marine isotope stages (MIS) are alternating warmer and colder periods through Earths paleoclimate, widely used to create a global stratigraphic framework for marine sediment (Shackleton et al., 2003). By using the $\delta^{18}O$ record, which reflect the oxygen isotopic composition of the global ocean, it is possible to distinguish sediments deposited in either glacial or interglacial periods (Shackleton, 1967). Sediments deposited in glacial periods have a high content of ^{18}O and include even MIS numbers (e.g. 2, 4, 6…). Sediments deposited in interglacial periods have a low content of ^{18}O and include odd MIS number (e.g. 1, 3, 5…) (Bradley, 2014).

By using the MS for core PS56/029-1 number of MIS can be interpreted. High MS values reflect sediments deposited in glacials, while low MS values reflect sediments deposited in interglacial periods (*see Chapter 5.2*). It is suggested that core PS56/029-1 consists of 39 MIS (Fig. 5.11). 20 glacial periods and 19 interglacial periods.

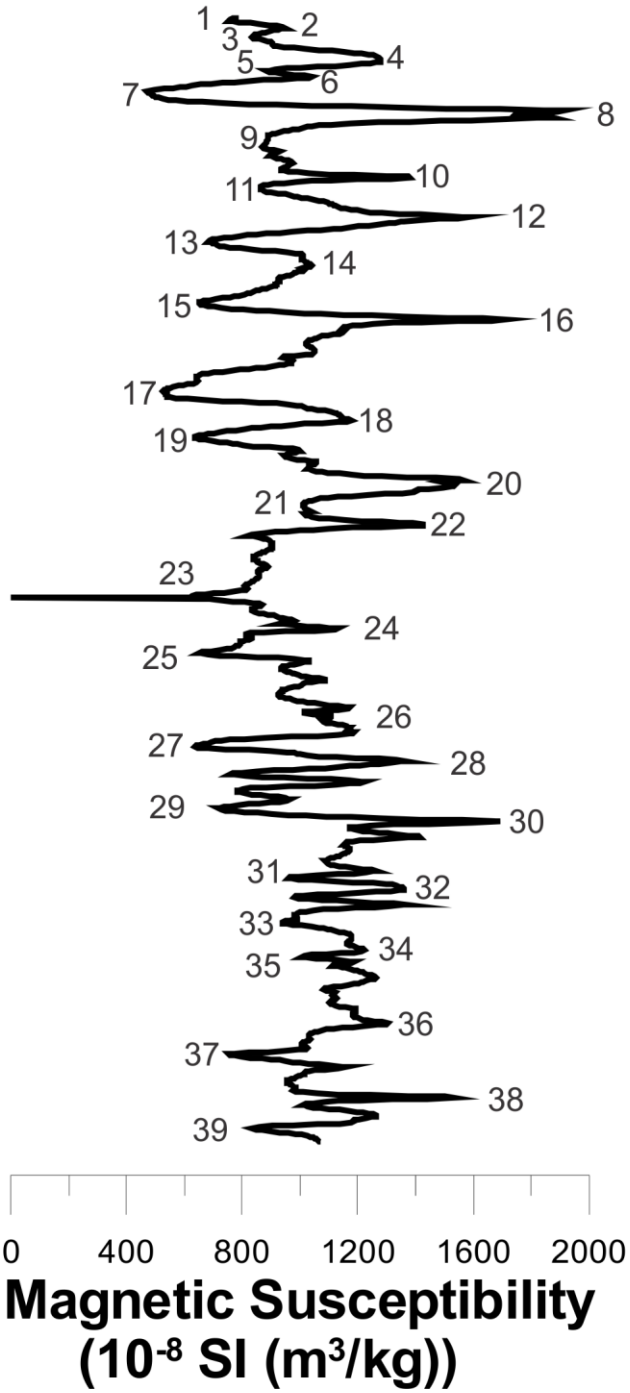

Fig. 5.11: MIS stages for core PS56/029-1.

6 Conclusion

The main objectives of this thesis were to describe sedimentary processes and dynamics under pelagic, turbiditic and contouritic influences, and to possibly reconstruct climate-controlled environmental change in the RLS through the past glacial/interglacial cycles. To address these objectives, multi-proxy analysis of a 12.67 m long gravity core retrieved on a levee within a large channel system in the RLS, Antarctica, were performed. The analysed proxies include physical and geochemical properties, as well as sedimentological parameters.

The main conclusions of this study are:

- Core PS56/029-1 reveals alternating repetitive intervals of poorly sorted and fine-grained sediment accumulated in lighter brownish and greyish coloured intervals. The lighter brownish intervals are characterized by increased IRD content, bioturbation and foraminifera. They are suggested to be deposited during interglacial periods. Sparse IRD, reduced foraminifer content, a sharp lower boundary and lamination characterize the greyish coloured intervals. These intervals are interpreted to be deposited during glacial periods. Physical and geochemical properties observed in the lighter brownish and greyish coloured layers correspond as well to the observed colour changes. Low MS and slightly coarser grain-sizes, as well as high ratios of Ca/Sum and Ca/Fe, and low ratios of Al/Sum and K/Sum correspond to the lighter brownish coloured intervals. Increased MS and finer grain-sizes, as well as high ratios of Al/Sum and Si/Sum, and low ratio of Cu/Sum correspond to the greyish coloured intervals.
- The deposits have a polymodal signature which is interpreted to be the result of pelagic, turbiditic, and contouritic activity, with occasional influence of icebergs.
- Four lithofacies are defined in core PS56/029-1 based on colour, physical properties, geochemical composition and grain-sizes. Facies LGL is characterized by the greyish colour, presence of lamination, a sharp lower boundary, reduced foraminifer and absent IRD signal, average MS and grain-sizes of 3 µm, as well as high ratios of Al/Sum, Si/Sum and K/Sum, and low ratios of Ca/Sum, Cu/Sum and Ca/Fe. It is interpreted to reflect deposition mainly from turbidity currents. Facies GLT is characterized by greyish colour, sharp lower boundary, high MS, p-wave velocity and wet-bulk density, and grain-sizes between 2 and 5 µm, as well as high ratios of Al/Sum and Si/Sum, and low ratios of Cu/Sum, Fe/Sum, Zn/Sum and Rb/Sum. It is interpreted to reflect deposition of turbidity currents and contour currents. Facies MML is characterized by

the olive greyish colour, bioturbation, IRD and foraminifera, occasionally including a sharp lower boundary, low MS, p-wave velocity and wet-bulk density, and grain-sizes between 2 and 5 µm, as well as high ratios of Sr/Sum, Ca/Sum and Ca/Fe, and low ratios of Al/Sum, Si/Sum, K/Sum, Fe/Sum and Rb/Sum. Interpreted to reflect the deposition from turbidity currents, contour currents and pelagic settling. Facies RBL is characterized by brownish colour, bioturbation, IRD, foraminifera, low MS, grain-sizes between 2 and 7 µm, as well as high ratios of S/Sum, Cu/Sum, Ca/Sum and Ca/Fe, and low ratios of Rb/Sum, Al/Sum, K/sum and Fe/Sum. Interpreted to reflect the deposition from turbidity currents, contour currents and pelagic settling.

- Results from grain-size analysis reveal occurrences of slightly coarser grain-size distribution, which are interpreted as interglacial sediments, clearly distinguishable from finer glacial sediments. Coarser sediments are expected to be deposited during interglacials from a stable or retreating ice sheet, along with less extensive sea-ice cover, and stronger coastal polynyas. Three main mechanisms likely affects the coarsening of seafloor sediments during interglacials, namely higher intensity of the Wedell Gyre, intensified bottom-water production, and debris-rich meltwater which can cause raised turbidity activity.
- Intervals of finer sediments are interpreted as sediments deposited during glacials. During glacials the advancing ice-sheet, along with a more extensive sea-ice, and smaller coastal polynyas are expected to result in a lower energy depositional environment compared to during interglacials. During glacials, sediments at the core site were most likely deposited by turbidity currents.
- It is suggested that core PS56/029-1 include 39 MIS.

The huge channel/levee structures in the RLS seems like a potential archive for thorough paleoenvironmental reconstructions including important changes linked to climate-relevant processes in the East Antarctica.

Appendix

ALLEY, R. & MACAYEAL, D. 1994. Ice-rafted debris associated with binge/purge oscillations of the Laurentide Ice Sheet. *Paleoceanography and Paleoclimatology,* 9**,** 503-511.

ANDERSON, J. B. 1999. *Antarctic marine geology*, Cambridge University Press.

ANDERSON, J. B., CONWAY, H., BART, P. J., WITUS, A. E., GREENWOOD, S. L., MCKAY, R. M., HALL, B. L., ACKERT, R. P., LICHT, K. & JAKOBSSON, M. 2014. Ross Sea paleo-ice sheet drainage and deglacial history during and since the LGM. *Quaternary Science Reviews,* 100**,** 31-54.

ANDERSON, J. B., SHIPP, S. S., LOWE, A. L., WELLNER, J. S. & MOSOLA, A. B. 2002. The Antarctic Ice Sheet during the Last Glacial Maximum and its subsequent retreat history: a review. *Quaternary Science Reviews,* 21**,** 49-70.

ANDERSON, J. B., WRIGHT, R. & ANDREWS, B. 1986. Weddell Fan and associated abyssal plain, Antarctica: Morphology, sediment processes, and factors influencing sediment supply. *Geo-marine letters,* 6**,** 121-129.

AOKI, S. 2003. Seasonal and spatial variations of iceberg drift off Dronning Maud Land, Antarctica, detected by satellite scatterometers. *Journal of oceanography,* 59**,** 629-635.

ARNDT, J. E., SCHENKE, H. W., JAKOBSSON, M., NITSCHE, F. O., BUYS, G., GOLEBY, B., REBESCO, M., BOHOYO, F., HONG, J. & BLACK, J. 2013. The International Bathymetric Chart of the Southern Ocean (IBCSO) Version 1.0—A new bathymetric compilation covering circum-Antarctic waters. *Geophysical Research Letters,* 40**,** 3111-3117.

ARRIGO, K. R. & VAN DIJKEN, G. L. 2003. Phytoplankton dynamics within 37 Antarctic coastal polynya systems. *Journal of Geophysical Research: Oceans,* 108.

ARRIGO, K. R., VAN DIJKEN, G. L., AINLEY, D. G., FAHNESTOCK, M. A. & MARKUS, T. 2002. Ecological impact of a large Antarctic iceberg. *Geophysical Research Letters,* 29**,** 8-1-8-4.

ARRIGO, K. R., WORTHEN, D., SCHNELL, A. & LIZOTTE, M. P. 1998. Primary production in Southern Ocean waters. *Journal of Geophysical Research: Oceans,* 103**,** 15587-15600.

AZAMARA. 2018. *Paradise frozen: ten incredible Antarctica facts and photos* [Online]. Available: https://www.azamaraclubcruises.com/no/blog/paradise-frozen-ten-incredible-antarctica-facts-and-photos [Accessed November 11th 2018].

BAHR, A., LAMY, F., ARZ, H., KUHLMANN, H. & WEFER, G. 2005. Late glacial to Holocene climate and sedimentation history in the NW Black Sea. *Marine Geology,* 214**,** 309-322.

BAMBER, J., GOMEZ-DANS, J. & GRIGGS, J. 2009. A new 1 km digital elevation model of the Antarctic derived from combined satellite radar and laser data–Part 1: Data and methods. *The Cryosphere,* 3**,** 101-111.

BARKER, P. & THOMAS, E. 2004. Origin, signature and palaeoclimatic influence of the Antarctic Circumpolar Current. *Earth-Science Reviews,* 66**,** 143-162.

BARNES, P. W. & LIEN, R. 1988. Icebergs rework shelf sediments to 500 m off Antarctica. *Geology,* 16**,** 1130-1133.

BASSETT, S., MILNE, G., BENTLEY, M. & HUYBRECHTS, P. 2007. Modelling Antarctic sea-level data to explore the possibility of a dominant Antarctic contribution to meltwater pulse IA. *Quaternary Science Reviews,* 26**,** 2113-2127.

BATCHELOR, C. L. & DOWDESWELL, J. A. 2015. Ice-sheet grounding-zone wedges (GZWs) on high-latitude continental margins. *Marine Geology,* 363**,** 65-92.

BEIERLE, B. D., LAMOUREUX, S. F., COCKBURN, J. M. & SPOONER, I. 2002. A new method for visualizing sediment particle size distributions. *Journal of Paleolimnology,* 27**,** 279-283.

BELDERSON, R., KENYON, N. & WILSON, J. 1973. Iceberg plough marks in the northeast Atlantic. *Palaeogeography, Palaeoclimatology, Palaeoecology,* 13**,** 215-224.

BENTLEY, M. J. 1999. Volume of Antarctic ice at the Last Glacial Maximum, and its impact on global sea level change. *Quaternary Science Reviews,* 18**,** 1569-1595.

BENTLEY, M. J. & ANDERSON, J. B. 1998. Glacial and marine geological evidence for the ice sheet configuration in the Weddell Sea–Antarctic Peninsula region during the Last Glacial Maximum. *Antarctic Science,* 10**,** 309-325.
BENTLEY, M. J., COFAIGH, C. Ó., ANDERSON, J. B., CONWAY, H., DAVIES, B., GRAHAM, A. G., HILLENBRAND, C.-D., HODGSON, D. A., JAMIESON, S. S. & LARTER, R. D. 2014. A community-based geological reconstruction of Antarctic Ice Sheet deglaciation since the Last Glacial Maximum. *Quaternary Science Reviews,* 100**,** 1-9.
BENTLEY, M. J., FOGWILL, C. J., LE BROCQ, A. M., HUBBARD, A. L., SUGDEN, D. E., DUNAI, T. J. & FREEMAN, S. P. 2010. Deglacial history of the West Antarctic Ice Sheet in the Weddell Sea embayment: Constraints on past ice volume change. *Geology,* 38**,** 411-414.
BLOTT, S. J. & PYE, K. 2001. GRADISTAT: a grain size distribution and statistics package for the analysis of unconsolidated sediments. *Earth surface processes and Landforms,* 26**,** 1237-1248.
BOHATY, S. M., ZACHOS, J. C. & DELANEY, M. L. 2012. Foraminiferal Mg/Ca evidence for southern ocean cooling across the eocene–oligocene transition. *Earth and Planetary Science Letters,* 317**,** 251-261.
BOUMA, A. 1964. Turbidites. *Developments in sedimentology*. Elsevier.
BRADLEY, R. 2014. *Paleoclimatology Reconstructing Climates of the Quaternary* Academic Press.
BÖNING, C. W., DISPERT, A., VISBECK, M., RINTOUL, S. & SCHWARZKOPF, F. U. 2008. The response of the Antarctic Circumpolar Current to recent climate change. *Nature Geoscience,* 1**,** 864.
CABURLOTTO, A., LUCCHI, R., DE SANTIS, L., MACRÌ, P. & TOLOTTI, R. 2010. Sedimentary processes on the Wilkes Land continental rise reflect changes in glacial dynamic and bottom water flow. *International Journal of Earth Sciences,* 99**,** 909-926.
CADIGAN, R. A. 1961. Geologic interpretation of grain-size distribution measurements of Colorado Plateau sedimentary rocks. *The Journal of Geology,* 69**,** 121-144.
CARTER, L., MCCAVE, I. & WILLIAMS, M. J. 2008. Circulation and water masses of the Southern Ocean: a review. *Developments in earth and environmental sciences,* 8**,** 85-114.
CENTRAL INTELLIGENCE AGENCY. 2018. *The World Factbook: Southern Ocean* [Online]. Washington, DC. Available: https://www.cia.gov/library/publications/the-world-factbook/geos/oo.html [Accessed October 10th, 2018].
CLARK, C. D. 1993. Mega-scale glacial lineations and cross-cutting ice-flow landforms. *Earth surface processes and landforms,* 18**,** 1-29.
COFAIGH, C. Ó., DAVIES, B. J., LIVINGSTONE, S. J., SMITH, J. A., JOHNSON, J. S., HOCKING, E. P., HODGSON, D. A., ANDERSON, J. B., BENTLEY, M. J. & CANALS, M. 2014. Reconstruction of ice-sheet changes in the Antarctic Peninsula since the Last Glacial Maximum. *Quaternary Science Reviews,* 100**,** 87-110.
COFAIGH, C. O., DOWDESWELL, J. A. & PUDSEY, C. J. 2001. Late Quaternary iceberg rafting along the Antarctic Peninsula continental rise and in the Weddell and Scotia Seas. *Quaternary Research,* 56**,** 308-321.
COFAIGH, C. Ó., TAYLOR, J., DOWDESWELL, J. A. & PUDSEY, C. J. 2003. Palaeo-ice streams, trough mouth fans and high-latitude continental slope sedimentation. *Boreas,* 32**,** 37-55.
COOK, A., FOX, A., VAUGHAN, D. & FERRIGNO, J. 2005. Retreating glacier fronts on the Antarctic Peninsula over the past half-century. *Science,* 308**,** 541-544.
COSSU, R., WELLS, M. G. & WÅHLIN, A. 2010. Influence of the Coriolis force on the velocity structure of gravity currents in straight submarine channel systems. *Journal of Geophysical Research: Oceans,* 115.
COXALL, H. K., WILSON, P. A., PALIKE, H., LEAR, C. H. & BACKMAN, J. 2005. Rapid stepwise onset of Antarctic glaciation and deeper calcite compensation in the Pacific Ocean. *Nature,* 433**,** 53.
CRAWFORD, K., KUHN, G. & HAMBREY, M. J. 1996. Changes in the character of glaciomarine sedimentation in the southwestern Weddell Sea, Antarctica: evidence from the core PS1423-2. *Annals of glaciology,* 22**,** 200-204.
CUNNINGHAM, S. A. 2005. Southern ocean circulation. *Archives of natural history,* 32**,** 265-280.

DAVIES, B. 2014. *Changes to Circumpolar Deep Water* [Online]. AntarcticGlaciers.org. Available: http://www.antarcticglaciers.org/glaciers-and-climate/ice-ocean-interactions/changes-circumpolar-deep-water/ [Accessed October 10th, 2018].
DAVIES, B. 2017. *The Global Last Glacial Maximum* [Online]. AntarcticGlaciers.org. Available: http://www.antarcticglaciers.org/2017/06/global-last-glacial-maximum/ [Accessed October 4th. 2018].
DE SANTIS, L., BRANCOLINI, G. & DONDA, F. 2003. Seismo-stratigraphic analysis of the Wilkes Land continental margin (East Antarctica): influence of glacially driven processes on the Cenozoic deposition. *Deep Sea Research Part II: Topical Studies in Oceanography,* 50**,** 1563-1594.
DECONTO, R. M. & POLLARD, D. 2003. Rapid Cenozoic glaciation of Antarctica induced by declining atmospheric CO2. *Nature,* 421**,** 245-249.
DECONTO, R. M. & POLLARD, D. 2016a. Contribution of Antarctica to past and future sea-level rise. *Nature,* 531**,** 591.
DECONTO, R. M. & POLLARD, D. 2016b. Contribution of Antarctica to past and future sea-level rise. *Nature,* 531**,** 591-597.
DENTON, G. H. & HUGHES, T. J. 2002. Reconstructing the Antarctic ice sheet at the Last Glacial Maximum. *Quaternary Science Reviews,* 21**,** 193-202.
DINNIMAN, M. S., KLINCK, J. M. & SMITH JR, W. O. 2011. A model study of Circumpolar Deep Water on the West Antarctic Peninsula and Ross Sea continental shelves. *Deep Sea Research Part II: Topical Studies in Oceanography,* 58**,** 1508-1523.
DOWDESWELL, J., OTTESEN, D., EVANS, J., COFAIGH, C. & ANDERSON, J. 2008. Submarine glacial landforms and rates of ice-stream collapse. *Geology,* 36**,** 819-822.
DOWDESWELL, J. A. 2009. Ice-Rafted Debris (IRD). *In:* GORNITZ, V. (ed.) *Encyclopedia of Paleoclimatology and Ancient Environments.* Dordrecht: Springer Netherlands.
DROXLER, A. W. & SCHLAGER, W. 1985. Glacial versus interglacial sedimentation rates and turbidite frequency in the Bahamas. *Geology,* 13**,** 799-802.
EC, W. 2009. Aspects of sediment movement on steep delta slopes. *Coarse-grained deltas,* 27**,** 29.
ELVERHØI, A. 1981. Evidence for a late Wisconsin glaciation of the Weddell Sea. *Nature,* 293**,** 641-642.
ESCUTIA, C., NELSON, C., ACTON, G., EITTREIM, S., COOPER, A., WARNKE, D. & JARAMILLO, J. 2002. Current controlled deposition on the Wilkes Land continental rise, Antarctica. *Geological Society, London, Memoirs,* 22**,** 373-384.
EVANS, H. B. GRAPE*-A Device For Continuous Determination Of Material Density And Porosity. SPWLA 6th Annual Logging Symposium (Volume II), 1965. Society of Petrophysicists and Well-Log Analysts.
FACEBOOK. 2018. *Queen Maud Land* [Online]. Available: https://www.facebook.com/pages/biz/Queen-Maud-Land-Dronning-Maud-Land-120549631297500/ [Accessed October 24th, 2018].
FAHRBACH, E. 2013. Stormy and icy seas. In D. Walton (Ed.), Antarctica: Global Science from a Frozen Continent (pp. 137-160). *Cambridge: Cambridge University Press*.
FOGWILL, C., BENTLEY, M., SUGDEN, D., KERR, A. & KUBIK, P. 2004. Cosmogenic nuclides 10Be and 26Al imply limited Antarctic Ice Sheet thickening and low erosion in the Shackleton Range for> 1 my. *Geology,* 32**,** 265-268.
FOLDVIK, A. & GAMMELSRØD, T. 1988. Notes on Southern Ocean hydrography, sea-ice and bottom water formation. *Palaeogeography, Palaeoclimatology, Palaeoecology,* 67**,** 3-17.
FOLDVIK, A., GAMMELSRØD, T., ØSTERHUS, S., FAHRBACH, E., ROHARDT, G., SCHRÖDER, M., NICHOLLS, K. W., PADMAN, L. & WOODGATE, R. 2004. Ice shelf water overflow and bottom water formation in the southern Weddell Sea. *Journal of Geophysical Research: Oceans,* 109.
FOLK, R. L. & WARD, W. C. 1957. Brazos River bar [Texas]; a study in the significance of grain size parameters. *Journal of Sedimentary Research,* 27**,** 3-26.
FORWICK, M. 2001. Development of the sedimentary environment in Balsfjord (northern Norway). *Cand. scient. thesis in geology*.

FORWICK, M. 2013. How to use XRF core scanner data acquired with the Avaatech XRF core scanner at the Department of Geology. *University of Tromsø, a short manual compiled by Matthias Forwick*.
FORWICK, M., LABERG, J. S., HASS, H. C. & OSTI, G. 2015. The Kongsfjorden Channel System offshore NW Svalbard: downslope sedimentary processes in a contour-current-dominated setting. *arktos*, 1**,** 17.
FRETWELL, P., PRITCHARD, H. D., VAUGHAN, D. G., BAMBER, J., BARRAND, N., BELL, R., BIANCHI, C., BINGHAM, R., BLANKENSHIP, D. & CASASSA, G. 2013a. Bedmap2: improved ice bed, surface and thickness datasets for Antarctica. *The Cryosphere*, 7.
FRETWELL, P., PRITCHARD, H. D., VAUGHAN, D. G., BAMBER, J., BARRAND, N., BELL, R., BIANCHI, C., BINGHAM, R., BLANKENSHIP, D. & CASASSA, G. 2013b. Bedmap2: improved ice bed, surface and thickness datasets for Antarctica.
FRIEDMAN, G. M., SANDERS, J. E. & KOPASKA-MERKEL, D. C. 1992. *Principles of sedimentary deposits: stratigraphy and sedimentology*, Macmillan College.
FUKAMACHI, Y., RINTOUL, S., CHURCH, J., AOKI, S., SOKOLOV, S., ROSENBERG, M. & WAKATSUCHI, M. 2010. Strong export of Antarctic Bottom Water east of the Kerguelen plateau. *Nature Geoscience*, 3**,** 327.
GEOLOGY.COM. 2018. *Map of Antarctica and the Southern Ocean* [Online]. Available: https://geology.com/world/antarctica-satellite-image.shtml [Accessed October 10th, 2018].
GEOTEK. 2000. *Multi-Sensor Core Logger* [Online]. Available: https://cmgds.marine.usgs.gov/publications/of2004-1358/AppendixH/Manual-MSCL(VS032603).pdf [Accessed October 24th, 2018].
GEOTEK. 2016. *Multi-sensor core logging (MSCL) and x-ray radiography core logging sevices* [Online]. Available: https://www.geotek.co.uk/wp-content/uploads/2016/07/Geotek-Core-Logging-Services_3.pdf [Accessed October 24th, 2018].
GEOTEK. 2018. *MSCL-S: Multi-Sensor Core Logger* [Online]. Available: https://www.geotek.co.uk/wp-content/uploads/2017/06/MSCL-S.pdf [Accessed October 24th, 2018].
GILBERT, R. 1990. Rafting in glacimarine environments. *Geological Society, London, Special Publications*, 53**,** 105-120.
GILLETT, N. P. & THOMPSON, D. W. 2003. Simulation of recent Southern Hemisphere climate change. *Science*, 302**,** 273-275.
GOLLEDGE, N. R., FOGWILL, C. J., MACKINTOSH, A. N. & BUCKLEY, K. M. 2012. Dynamics of the last glacial maximum Antarctic ice-sheet and its response to ocean forcing. *Proceedings of the National Academy of Sciences*.
GORDON, A. L. & COMISO, J. C. 1988. Polynyas in the southern ocean. *Scientific American*, 258**,** 90-97.
GPG. 2017. *Seismic Velocity* [Online]. Available: https://gpg.geosci.xyz/content/physical_properties/seismic_velocity_duplicate.html [Accessed October 24th, 2018].
GROBE, H. & MACKENSEN, A. 1992. Late Quaternary climatic cycles as recorded in sediments from the Antarctic continental margin. *The Antarctic paleoenvironment: A perspective on Global Change; Antarctic Research Series*, 56**,** 349-376.
GRUTZNER, J., REBESCO, M., COOPER, A., FORSBERG, C., KRYC, K. & WEFER, G. 2003. Evidence for orbitally controlled size variations of the East Antarctic Ice Sheet during the late Miocene. *Geology*, 31**,** 777-780.
GUNN, D. & BEST, A. 1998. A new automated nondestructive system for high resolution multi-sensor core logging of open sediment cores. *Geo-Marine Letters*, 18**,** 70-77.
HARRIS, P. 2000. Ripple cross-laminated sediments on the East Antarctic Shelf: evidence for episodic bottom water production during the Holocene? *Marine Geology*, 170**,** 317-330.
HASS ET AL., H. in prep. Climate-controlled levee sedimentation processes in the Riiser Larsen Sea (Antarctica) during the late Quaternary.
HASS, H., KUHN, G., MONIEN, P., BRUMSACK, H.-J. & FORWICK, M. 2010. Climate fluctuations during the past two millennia as recorded in sediments from Maxwell Bay, South

Shetland Islands, West Antarctica. *Geological Society, London, Special Publications,* 344**,** 243-260.
HASS, H. C., KLAGES, J. P., KUHN, G. & FORWICK, M. A large channel system in the western the Riiser Larsen Sea, East Antarctica: Paleoceanographic and sedimentary aspects. EGU General Assembly Conference Abstracts, 2016. 5123.
HAUG, G. H., HUGHEN, K. A., SIGMAN, D. M., PETERSON, L. C. & RÖHL, U. 2001. Southward migration of the intertropical convergence zone through the Holocene. *Science,* 293**,** 1304-1308.
HAY, W. W., FLÖGEL, S. & SÖDING, E. 2005. Is the initiation of glaciation on Antarctica related to a change in the structure of the ocean? *Global and Planetary Change,* 45**,** 23-33.
HEIN, A. S., FOGWILL, C. J., SUGDEN, D. E. & XU, S. 2011. Glacial/interglacial ice-stream stability in the Weddell Sea embayment, Antarctica. *Earth and Planetary Science Letters,* 307**,** 211-221.
HEPP, D. A., MÖRZ, T. & GRÜTZNER, J. 2006. Pliocene glacial cyclicity in a deep-sea sediment drift (Antarctic Peninsula Pacific Margin). *Palaeogeography, Palaeoclimatology, Palaeoecology,* 231**,** 181-198.
HESSE, R., KLAUCK, I., KHODABAKHSH, S. & PIPER, D. 1999. Continental slope sedimentation adjacent to an ice margin. III. The upper Labrador Slope. *Marine Geology,* 155**,** 249-276.
HILLENBRAND, C.-D., BENTLEY, M. J., STOLLDORF, T. D., HEIN, A. S., KUHN, G., GRAHAM, A. G., FOGWILL, C. J., KRISTOFFERSEN, Y., SMITH, J. A. & ANDERSON, J. B. 2014. Reconstruction of changes in the Weddell Sea sector of the Antarctic Ice Sheet since the Last Glacial Maximum. *Quaternary Science Reviews,* 100**,** 111-136.
HILLENBRAND, C.-D., KUHN, G. & FREDERICHS, T. 2009. Record of a Mid-Pleistocene depositional anomaly in West Antarctic continental margin sediments: an indicator for ice-sheet collapse? *Quaternary Science Reviews,* 28**,** 1147-1159.
HODGSON, D. A., GRAHAM, A. G., ROBERTS, S. J., BENTLEY, M. J., COFAIGH, C. Ó., VERLEYEN, E., VYVERMAN, W., JOMELLI, V., FAVIER, V. & BRUNSTEIN, D. 2014. Terrestrial and submarine evidence for the extent and timing of the Last Glacial Maximum and the onset of deglaciation on the maritime-Antarctic and sub-Antarctic islands. *Quaternary Science Reviews,* 100**,** 137-158.
HONJO, S., MANGANINI, S. J. & COLE, J. J. 1982. Sedimentation of biogenic matter in the deep ocean. *Deep Sea Research Part A. Oceanographic Research Papers,* 29**,** 609-625.
HOWE, J. A., SHIMMIELD, T. M. & DIAZ, R. 2004. Deep-water sedimentary environments of the northwestern Weddell Sea and South Sandwich Islands, Antarctica. *Deep Sea Research Part II: Topical Studies in Oceanography,* 51**,** 1489-1514.
HUYBRECHTS, P. 1990. The Antarctic ice sheet during the last glacial-interglacial cycle: a three-dimensional experiment. *Annals of Glaciology,* 14**,** 115-119.
INGÓLFSSON, Ó. 2004. Quaternary glacial and climate history of Antarctica. *Developments in Quaternary Sciences.* Elsevier.
INGÓLFSSON, Ó., HJORT, C., BERKMAN, P. A., BJÖRCK, S., COLHOUN, E., GOODWIN, I. D., HALL, B., HIRAKAWA, K., MELLES, M. & MÖLLER, P. 1998. Antarctic glacial history since the Last Glacial Maximum: an overview of the record on land. *Antarctic science,* 10**,** 326-344.
ISHIKAWA, T., UKITA, J., OHSHIMA, K. I., WAKATSUCHI, M., YAMANOUCHI, T. & ONO, N. 1996. Coastal polynyas off East Queen Maud Land observed from NOAA AVHRR data. *Journal of Oceanography,* 52**,** 389-398.
JESSEN, S. P. & RASMUSSEN, T. L. 2015. Sortable silt cycles in Svalbard slope sediments 74–0 ka. *Journal of Quaternary Science,* 30**,** 743-753.
JESSEN, S. P., RASMUSSEN, T. L., NIELSEN, T. & SOLHEIM, A. 2010. A new Late Weichselian and Holocene marine chronology for the western Svalbard slope 30,000–0 cal years BP. *Quaternary Science Reviews,* 29**,** 1301-1312.
JOGHUHIN, I. A., B RICHARD. 2011. Stability of the West Antarctica ice sheet in a warming world. *Nature Geoscience* 4**,** 506-513.
JONES, S., JAGO, C., BALE, A., CHAPMAN, D., HOWLAND, R. & JACKSON, J. 1998. Aggregation and resuspension of suspended particulate matter at a seasonally stratified site in

the southern North Sea: physical and biological controls. *Continental Shelf Research,* 18**,** 1283-1309.
JOUGHIN, I., BAMBER, J. L., SCAMBOS, T., TULACZYK, S., FAHNESTOCK, M. & MACAYEAL, D. R. 2006. Integrating satellite observations with modelling: basal shear stress of the Filcher-Ronne ice streams, Antarctica. *Philosophical Transactions of the Royal Society of London A: Mathematical, Physical and Engineering Sciences,* 364**,** 1795-1814.
KEANY, J., LEDBETTER, M., WATKINS, N. & HUANG, T.-C. 1976. Diachronous deposition of ice-rafted debris in sub-Antarctic deep-sea sediments. *Geological Society of America Bulletin,* 87**,** 873-882.
KENNISH, M. J. 2000. *Practical handbook of marine science*, crc press.
KLAGES, J. P. 2010. *Sedimentological investigation of a channel/levee complex in the Riiser Larsen Sea, East Antarctica: A late Quaternary paleoenvironmental record.* Christian-Albrechts-Universität zu Kiel.
KNIES, J., KLEIBER, H.-P., MATTHIESSEN, J., MÜLLER, C. & NOWACZYK, N. 2001. Marine ice-rafted debris records constrain maximum extent of Saalian and Weichselian ice-sheets along the northern Eurasian margin. *Global and Planetary Change,* 31**,** 45-64.
KUHN, G. & DIEKMANN, B. 2002. Late Quaternary variability of ocean circulation in the southeastern South Atlantic inferred from the terrigenous sediment record of a drift deposit in the southern Cape Basin (ODP Site 1089). *Palaeogeography, Palaeoclimatology, Palaeoecology,* 182**,** 287-303.
KUHN, G., MELLES, M., EHRMANN, W. U., HAMBREY, M. J. & SCHMIEDL, G. 1993. Character of clasts in glaciomarine sediments as an indicator of transport and depositional processes, Weddell and Lazarev Seas, Antarctica. *Journal of Sedimentary Research,* 63**,** 477-487.
KUVAAS, B. & KRISTOFFERSEN, Y. 1991. The Crary Fan: a trough-mouth fan on the Weddell Sea continental margin, Antarctica. *Marine Geology,* 97**,** 345-362.
KUVAAS, B., KRISTOFFERSEN, Y., LEITCHENKOV, G., GUSEVA, J. & GANDJUKHIN, V. 2004. Seismic expression of glaciomarine deposits in the eastern Riiser Larsen Sea, Antarctica. *Marine Geology,* 207**,** 1-15.
KUVAAS, B. & LEITCHENKOV, G. 1992. Glaciomarine turbidite and current controlled deposits in Prydz Bay, Antarctica. *Marine Geology,* 108**,** 365-381.
LARTER, R. D., ANDERSON, J. B., GRAHAM, A. G., GOHL, K., HILLENBRAND, C.-D., JAKOBSSON, M., JOHNSON, J. S., KUHN, G., NITSCHE, F. O. & SMITH, J. A. 2014. Reconstruction of changes in the Amundsen Sea and Bellingshausen Sea sector of the West Antarctic ice sheet since the last glacial maximum. *Quaternary Science Reviews,* 100**,** 55-86.
LARTER, R. D., GRAHAM, A. G., HILLENBRAND, C.-D., SMITH, J. A. & GALES, J. A. 2012. Late Quaternary grounded ice extent in the Filchner Trough, Weddell Sea, Antarctica: new marine geophysical evidence. *Quaternary Science Reviews,* 53**,** 111-122.
LAWVER, L. A. G., LISA M. COFFIN MILLARD F. 1992. The developement of paleoseaways around Antarctica *Antarctic research series* 56**,** 7-30.
LE BROCQ, A., BENTLEY, M., HUBBARD, A., FOGWILL, C., SUGDEN, D. & WHITEHOUSE, P. 2011. Reconstructing the Last Glacial Maximum ice sheet in the Weddell Sea embayment, Antarctica, using numerical modelling constrained by field evidence. *Quaternary Science Reviews,* 30**,** 2422-2432.
LEITCHENKOV, G., GUSEVA, J., GANDYUKHIN, V., GRIKUROV, G., KRISTOFFERSEN, Y., SAND, M., GOLYNSKY, A. & ALESHKOVA, N. 2008. Crustal structure and tectonic provinces of the Riiser-Larsen Sea area (East Antarctica): results of geophysical studies. *Marine Geophysical Researches,* 29**,** 135-158.
LIEN, R., SOLHEIM, A., ELVERHØI, A. & ROKOENGEN, K. 1989. Iceberg scouring and sea bed morphology on the eastern Weddell Sea shelf, Antarctica. *Polar Research,* 7**,** 43-57.
LIVINGSTONE, S. J., COFAIGH, C. Ó., STOKES, C. R., HILLENBRAND, C.-D., VIELI, A. & JAMIESON, S. S. 2012. Antarctic palaeo-ice streams. *Earth-Science Reviews,* 111**,** 90-128.
LUCCHI, R., REBESCO, M., CAMERLENGHI, A., BUSETTI, M., TOMADIN, L., VILLA, G., PERSICO, D., MORIGI, C., BONCI, M. & GIORGETTI, G. 2002. Mid-late Pleistocene

glacimarine sedimentary processes of a high-latitude, deep-sea sediment drift (Antarctic Peninsula Pacific margin). *Marine Geology,* 189**,** 343-370.
LYTHE, M. B. & VAUGHAN, D. G. 2001. BEDMAP: A new ice thickness and subglacial topographic model of Antarctica. *Journal of Geophysical Research: Solid Earth,* 106**,** 11335-11351.
MACKINTOSH, A., GOLLEDGE, N., DOMACK, E., DUNBAR, R., LEVENTER, A., WHITE, D., POLLARD, D., DECONTO, R., FINK, D. & ZWARTZ, D. 2011. Retreat of the East Antarctic ice sheet during the last glacial termination. *Nature Geoscience,* 4**,** 195-202.
MACKINTOSH, A. N., VERLEYEN, E., O'BRIEN, P. E., WHITE, D. A., JONES, R. S., MCKAY, R., DUNBAR, R., GORE, D. B., FINK, D. & POST, A. L. 2014. Retreat history of the East Antarctic Ice Sheet since the last glacial maximum. *Quaternary Science Reviews,* 100**,** 10-30.
MALDONADO, A., BARNOLAS, A., BOHOYO, F., ESCUTIA, C., GALINDO-ZALDÍVAR, J., HERNÁNDEZ-MOLINA, J., JABALOY, A., LOBO, F. J., NELSON, C. H. & RODRÍGUEZ-FERNÁNDEZ, J. 2005. Miocene to recent contourite drifts development in the northern Weddell Sea (Antarctica). *Global and Planetary Change,* 45**,** 99-129.
MARKS, K. & TIKKU, A. 2001. Cretaceous reconstructions of East Antarctica, Africa and Madagascar. *Earth and Planetary Science Letters,* 186**,** 479-495.
MASSOM, R., HARRIS, P., MICHAEL, K. J. & POTTER, M. 1998. The distribution and formative processes of latent-heat polynyas in East Antarctica. *Annals of Glaciology,* 27**,** 420-426.
MASSOM, R., HILL, K., LYTLE, V., WORBY, A., PAGET, M. & ALLISON, I. 2001. Effects of regional fast-ice and iceberg distributions on the behaviour of the Mertz Glacier polynya, East Antarctica. *Annals of Glaciology,* 33**,** 391-398.
MATSUOKA, K., HINDMARSH, R. C., MOHOLDT, G., BENTLEY, M. J., PRITCHARD, H. D., BROWN, J., CONWAY, H., DREWS, R., DURAND, G. & GOLDBERG, D. 2015. Antarctic ice rises and rumples: Their properties and significance for ice-sheet dynamics and evolution. *Earth-science reviews,* 150**,** 724-745.
MCCAVE, I. 2008. Size sorting during transport and deposition of fine sediments: sortable silt and flow speed. *Developments in Sedimentology,* 60**,** 121-142.
MCCAVE, I. & HALL, I. R. 2006. Size sorting in marine muds: Processes, pitfalls, and prospects for paleoflow-speed proxies. *Geochemistry, Geophysics, Geosystems,* 7.
MCCAVE, I., MANIGHETTI, B. & ROBINSON, S. 1995. Sortable silt and fine sediment size/composition slicing: parameters for palaeocurrent speed and palaeoceanography. *Paleoceanography,* 10**,** 593-610.
MCCAVE, I. & TUCHOLKE, B. 1986. Deep current-controlled sedimentation in the western North Atlantic. *The Geology of North America,* 1000**,** 451-468.
MCGINNIS, J. P. & HAYES, D. E. 1995. The Roles of Downslope and Along-Slope Depositional Processes: Southern Antarctic Peninsula Continental Rise. *Geology and seismic stratigraphy of the Antarctic margin***,** 141-156.
MELLES, M. & KUHN, G. 1993. Sub-bottom profiling and sedimentological studies in the southern Weddell Sea, Antarctica: evidence for large-scale erosional/depositional processes. *Deep Sea Research Part I: Oceanographic Research Papers,* 40**,** 739-760.
MEMBERS, E. C., AUGUSTIN, L., BARBANTE, C., BARNES, P. R. F., MARC BARNOLA, J., BIGLER, M., CASTELLANO, E., CATTANI, O., CHAPPELLAZ, J., DAHL-JENSEN, D., DELMONTE, B., DREYFUS, G., DURAND, G., FALOURD, S., FISCHER, H., FLÜCKIGER, J., HANSSON, M. E., HUYBRECHTS, P., JUGIE, G., JOHNSEN, S. J., JOUZEL, J., KAUFMANN, P., KIPFSTUHL, J., LAMBERT, F., LIPENKOV, V. Y., LITTOT, G. C., LONGINELLI, A., LORRAIN, R., MAGGI, V., MASSON-DELMOTTE, V., MILLER, H., MULVANEY, R., OERLEMANS, J., OERTER, H., OROMBELLI, G., PARRENIN, F., PEEL, D. A., PETIT, J.-R., RAYNAUD, D., RITZ, C., RUTH, U., SCHWANDER, J., SIEGENTHALER, U., SOUCHEZ, R., STAUFFER, B., PEDER STEFFENSEN, J., STENNI, B., STOCKER, T. F., TABACCO, I. E., UDISTI, R., VAN DE WAL, R. S. W., VAN DEN BROEKE, M., WEISS, J., WILHELMS, F., WINTHER, J.-G., WOLFF, E. W. & ZUCCHELLI, M. 2004. Eight glacial cycles from an Antarctic ice core. *Nature,* 429**,** 623.

MICHELS, K. H., ROGENHAGEN, J. & KUHN, G. 2001. Recognition of contour-current influence in mixed contourite-turbidite sequences of the western Weddell Sea, Antarctica. *Marine Geophysical Researches,* 22**,** 465-485.
MIENERT, J., THIEDE, J., KENYON, N. & HOLLENDER, F. J. 1993. Polar continental margins: studies off East Greenland. *Eos, Transactions American Geophysical Union,* 74**,** 225-236.
MIX, A. C., RUGH, W., PISIAS, N. G. & VEIRS, S. 1992. Color reflectance spectroscopy: A tool for rapid characterization of deep-sea sediments.
MOROS, M., KUIJPERS, A., SNOWBALL, I., LASSEN, S., BÄCKSTRÖM, D., GINGELE, F. & MCMANUS, J. 2002. Were glacial iceberg surges in the North Atlantic triggered by climatic warming? *Marine Geology,* 192**,** 393-417.
MOSHER, D. C., PIPER, D. J., CAMPBELL, D. C. & JENNER, K. A. 2004. Near-surface geology and sediment-failure geohazards of the central Scotian Slope. *AAPG bulletin,* 88**,** 703-723.
MOSHER, T. 2007. *Magnetic Resonance Imaging in Osteoarthritis* [Online]. Available: https://www.sciencedirect.com/topics/medicine-and-dentistry/magnetic-susceptibilityarwegtfg [Accessed October 24th, 2018].
MULVANEY, R., ALEMANY, O. & POSSENTI, P. 2007. The Berkner Island (Antarctica) ice-core drilling project. *Annals of glaciology,* 47**,** 115-124.
MYERS, R. A. & PIPER, D. J. 1988. Seismic stratigraphy of late Cenozoic sediments in the northern Labrador Sea: a history of bottom circulation and glaciation. *Canadian Journal of Earth Sciences,* 25**,** 2059-2074.
NATIONAL RESEARCH COUNCIL. 2011. *Future Science Opportunities in Antarctica and the Southern Ocean, 2 Fundamental Questions of Global Change* [Online]. Available: https://www.nap.edu/read/13169/chapter/4 [Accessed October 17th, 2018].
NATIONAL SNOW & ICE DATA CENTER. 2018a. *Arctic vs. Antarctic* [Online]. Available: https://nsidc.org/cryosphere/seaice/characteristics/difference.html [Accessed October 9th, 2018].
NATIONAL SNOW & ICE DATA CENTER. 2018b. *Sea Ice Features : Polynyas* [Online]. Available: https://nsidc.org/cryosphere/seaice/characteristics/polynyas.html [Accessed October 9th, 2018].
NATIONAL SNOW & ICE DATA CENTER. 2018c. *SOTC: Sea Ice* [Online]. Available: https://nsidc.org/cryosphere/sotc/sea_ice.html [Accessed October 9th, 2018].
NAVARRETE, S. A., WIETERS, E. A., BROITMAN, B. R. & CASTILLA, J. C. 2005. Scales of benthic–pelagic coupling and the intensity of species interactions: from recruitment limitation to top-down control. *Proceedings of the National Academy of Sciences,* 102**,** 18046-18051.
NEELOV, I., DANILOV, A., KLEPIKOV, A. & MALEK, V. 1998. New diagnostic calculations of the Southern Ocean. *Antarctica,* 34**,** 45-51.
NICHOLLS, K. W., ØSTERHUS, S., MAKINSON, K., GAMMELSRØD, T. & FAHRBACH, E. 2009. Ice-ocean processes over the continental shelf of the southern Weddell Sea, Antarctica: A review. *Reviews of Geophysics,* 47.
NICHOLS, G. 2009. *Sedimentology and stratigraphy*, John Wiley & Sons.
O'BRIEN, P., DE SANTIS, L., HARRIS, P., DOMACK, E. & QUILTY, P. 1999. Ice shelf grounding zone features of western Prydz Bay, Antarctica: sedimentary processes from seismic and sidescan images. *Antarctic Science,* 11**,** 78-91.
OHSHIMA, K. I., FUKAMACHI, Y., WILLIAMS, G. D., NIHASHI, S., ROQUET, F., KITADE, Y., TAMURA, T., HIRANO, D., HERRAIZ-BORREGUERO, L. & FIELD, I. 2013. Antarctic Bottom Water production by intense sea-ice formation in the Cape Darnley polynya. *Nature Geoscience,* 6**,** 235.
OHTA, Y., TØRUDBAKKEN, B. & SHIRAISHI, K. 1990. Geology of Gjelsvikfjella and western Muehlig-Hofmannfjella, Dronning Maud Land, East Antarctica. *Polar Research,* 8**,** 99-126.
OPPENHEIMER, M. 1998. Global warming and the stability of the West Antarctic Ice Sheet. *Nature,* 393**,** 325.
ORSI, A., JOHNSON, G. & BULLISTER, J. 1999. Circulation, mixing, and production of Antarctic Bottom Water. *Progress in Oceanography,* 43**,** 55-109.
ORSI, A. H. 1994. On the extent and frontal structure of the Antarctic circumpolar current.

ORSI, A. H., WHITWORTH III, T. & NOWLIN JR, W. D. 1995. On the meridional extent and fronts of the Antarctic Circumpolar Current. *Deep Sea Research Part I: Oceanographic Research Papers,* 42**,** 641-673.
PARKINSON, C. & CAVALIERI, D. 2012. Antarctic sea ice variability and trends, 1979-2010.
PASSCHIER, S. 2011. Linkages between East Antarctic Ice Sheet extent and Southern Ocean temperatures based on a Pliocene high-resolution record of ice-rafted debris off Prydz Bay, East Antarctica. *Paleoceanography and Paleoclimatology,* 26.
PFUHL, H. A. & MCCAVE, I. N. 2005. Evidence for late Oligocene establishment of the Antarctic Circumpolar Current. *Earth and Planetary Science Letters,* 235**,** 715-728.
PINGREE, K., LURIE, M. & HUGHES, T. 2011. Is the East Antarctic ice sheet stable? *Quaternary Research,* 75**,** 417-429.
PIRRUNG, M., FÜTTERER, D., GROBE, H., MATTHIEßEN, J. & NIESSEN, F. 2002. Magnetic susceptibility and ice-rafted debris in surface sediments of the Nordic Seas: implications for Isotope Stage 3 oscillations. *Geo-Marine Letters,* 22**,** 1-11.
POLLARD, D. & DECONTO, R. M. 2009. Modelling West Antarctic ice sheet growth and collapse through the past five million years. *Nature,* 458**,** 329.
PRESTI, M., DE SANTIS, L., BUSETTI, M. & HARRIS, P. T. 2003. Late Pleistocene and Holocene sedimentation on the George V continental shelf, East Antarctica. *Deep Sea Research Part II: Topical Studies in Oceanography,* 50**,** 1441-1461.
PRITCHARD, H., LIGTENBERG, S., FRICKER, H., VAUGHAN, D., VAN DEN BROEKE, M. & PADMAN, L. 2012. Antarctic ice-sheet loss driven by basal melting of ice shelves. *Nature,* 484**,** 502-505.
PRITCHARD, H. D., ARTHERN, R. J., VAUGHAN, D. G. & EDWARDS, L. A. 2009. Extensive dynamic thinning on the margins of the Greenland and Antarctic ice sheets. *Nature,* 461**,** 971.
PUDSEY, C. 2000. Sedimentation on the continental rise west of the Antarctic Peninsula over the last three glacial cycles. *Marine Geology,* 167**,** 313-338.
PUDSEY, C. J. 1992. Late Quaternary changes in Antarctic Bottom Water velocity inferred from sediment grain size in the northern Weddell Sea. *Marine Geology,* 107**,** 9-33.
PUDSEY, C. J. & CAMERLENGHI, A. 1998. Glacial–interglacial deposition on a sediment drift on the Pacific margin of the Antarctic Peninsula. *Antarctic Science,* 10**,** 286-308.
RASMUSSEN, T. L., THOMSEN, E., ŚLUBOWSKA, M. A., JESSEN, S., SOLHEIM, A. & KOÇ, N. 2007. Paleoceanographic evolution of the SW Svalbard margin (76 N) since 20,000 14 C yr BP. *Quaternary Research,* 67**,** 100-114.
RASMUSSEN, T. L., THOMSEN, E. & VAN WEERING, T. C. 1998. Cyclic sedimentation on the Faeroe Drift 53-10 ka BP related to climatic variations. *Geological Society, London, Special Publications,* 129**,** 255-267.
RASMUSSEN, T. L., THOMSEN, E., VAN WEERING, T. C. & LABEYRIE, L. 1996. Rapid changes in surface and deep water conditions at the Faeroe Margin during the last 58,000 years. *Paleoceanography,* 11**,** 757-771.
REBESCO, M., HERNÁNDEZ-MOLINA, F. J., VAN ROOIJ, D. & WÅHLIN, A. 2014. Contourites and associated sediments controlled by deep-water circulation processes: state-of-the-art and future considerations. *Marine Geology,* 352**,** 111-154.
REBESCO, M., LARTER, R. D., CAMERLENGHI, A. & BARKER, P. F. 1996. Giant sediment drifts on the continental rise west of the Antarctic Peninsula. *Geo-Marine Letters,* 16**,** 65-75.
REBESCO, M., PUDSEY, C., CANALS, M., CAMERLENGHI, A., BARKER, P., ESTRADA, F. & GIORGETTI, A. 2002. Sediment drifts and deep-sea channel systems, Antarctic Peninsula Pacific Margin. *Geological Society, London, Memoirs,* 22**,** 353-371.
REBESCO, M. & STOW, D. 2001. Seismic expression of contourites and related deposits: a preface. *Marine Geophysical Researches,* 22**,** 303-308.
RIGNOT, E., JACOBS, S., MOUGINOT, J. & SCHEUCHL, B. 2013. Ice-shelf melting around Antarctica. *Science,* 341**,** 266-270.
RIGNOT, E., MOUGINOT, J., SCHEUCHL, B. 2011. Ice Flow of the Antarctic Ice Sheet. *Science,* 333**,** 1427-1430.

RIGNOT, E., VELICOGNA, I., VAN DEN BROEKE, M. R., MONAGHAN, A. & LENAERTS, J. T. 2011. Acceleration of the contribution of the Greenland and Antarctic ice sheets to sea level rise. *Geophysical Research Letters,* 38.
RIGNOT, E. B., L JONATHAN. VAN DER BROEKE, MICHIEL R. DAVIS, CURT. LI, YONGHONG. VAN DE BERG, WILLEM J. VAN MEIJGAARD, ERIK. 2008. Recent Antarctic ice mass loss from radar interferometry and regional climate modelling. *Nature Geoscience,* 1**,** 106-110.
RIGNOT, E. C., G. GOGINENI, P. KRABILL, W. RIVERA, A. THOMAS, R. 2004. Accelerated ice discharge from the Antarctic Peninsula following hte collapse of Larsen B ice shelf. *Geophysical Research Letter,* 31**,** 1-4.
RINTOUL, S. 2010. Antarctic circumpolar current. *Ocean Currents: A Derivative of the Encyclopedia of Ocean Sciences,* 196.
ROBINSON, S. G., MASLIN, M. A. & MCCAVE, I. N. 1995. Magnetic susceptibility variations in Upper Pleistocene deep-sea sediments of the NE Atlantic: Implications for ice rafting and paleocirculation at the last glacial maximum. *Paleoceanography,* 10**,** 221-250.
ROBINSON, S. G., SAHOTA, J. T. & OLDFIELD, F. 2000. Early diagenesis in North Atlantic abyssal plain sediments characterized by rock-magnetic and geochemical indices. *Marine Geology,* 163**,** 77-107.
ROSENBERG, M. 2018. *The New Fifth Ocean* [Online]. Available: https://www.thoughtco.com/the-new-fifth-ocean-1435095 [Accessed October 5th, 2018].
ROTHWELL, R. G. & RACK, F. R. 2006. New techniques in sediment core analysis: an introduction. *Geological Society, London, Special Publications,* 267**,** 1-29.
RÜTHER, D. C., WINSBORROW, M., ANDREASSEN, K. & FORWICK, M. 2017. Grounding line proximal sediment characteristics at a marine-based, late-stage ice stream margin. *Journal of Quaternary Science,* 32**,** 463-474.
SAHU, B. K. 1964. Depositional mechanisms from the size analysis of clastic sediments. *Journal of Sedimentary Research,* 34**,** 73-83.
SCAMBOS, T., HULBE, C. & FAHNESTOCK, M. 2003. Climate-induced ice shelf disintegration in the Antarctic peninsula. *Antarctic Peninsula Climate Variability: Historical and Paleoenvironmental Perspectives***,** 79-92.
SCAMBOS, T. A., BOHLANDER, J., SHUMAN, C. U. & SKVARCA, P. 2004. Glacier acceleration and thinning after ice shelf collapse in the Larsen B embayment, Antarctica. *Geophysical Research Letters,* 31.
SCHRÖDER, M. & FAHRBACH, E. 1999. On the structure and the transport of the eastern Weddell Gyre. *Deep Sea Research Part II: Topical Studies in Oceanography,* 46**,** 501-527.
SCRIBD. 2018. *Particle Size Analyzers Cilas 1180 Machine Details* [Online]. Available: https://www.scribd.com/document/356833891/Particle-Size-Analyzers-Cilas-1180-Machine-Details [Accessed October 24th, 2018].
SEGERS, R. 2014. *the Coriolis effect* [Online]. Available: http://expeditieaarde.blogspot.com/2014/06/the-coriolis-effect.html [Accessed November 6th, 2018].
SHACKLETON, N. 1967. Oxygen isotope analyses and Pleistocene temperatures re-assessed. *Nature,* 215**,** 15.
SHACKLETON, N. J., SÁNCHEZ-GOÑI, M. F., PAILLER, D. & LANCELOT, Y. 2003. Marine isotope substage 5e and the Eemian interglacial. *Global and Planetary change,* 36**,** 151-155.
SHANMUGAM, G. 1997. The Bouma sequence and the turbidite mind set. *Earth-Science Reviews,* 42**,** 201-229.
SHANMUGAM, G. 2000. 50 years of the turbidite paradigm (1950s—1990s): deep-water processes and facies models—a critical perspective. *Marine and petroleum Geology,* 17**,** 285-342.
SHANMUGAM, G. 2006. *Deep-water processes and facies models: Implications for sandstone petroleum reservoirs,* Elsevier.
SHEPHERD, A., IVINS, E. R., GERUO, A., BARLETTA, V. R., BENTLEY, M. J., BETTADPUR, S., BRIGGS, K. H., BROMWICH, D. H., FORSBERG, R. & GALIN, N. 2012. A reconciled estimate of ice-sheet mass balance. *Science,* 338**,** 1183-1189.

SHINDELL, D. T. & SCHMIDT, G. A. 2004. Southern Hemisphere climate response to ozone changes and greenhouse gas increases. *Geophysical Research Letters,* 31.
SIGMOND, M. & FYFE, J. 2010. Has the ozone hole contributed to increased Antarctic sea ice extent? *Geophysical Research Letters,* 37.
SMITH, J. A., HILLENBRAND, C.-D., PUDSEY, C. J., ALLEN, C. S. & GRAHAM, A. G. 2010. The presence of polynyas in the Weddell Sea during the Last Glacial Period with implications for the reconstruction of sea-ice limits and ice sheet history. *Earth and Planetary Science Letters,* 296**,** 287-298.
SOLLI, K., KUVAAS, B., KRISTOFFERSEN, Y., LEITCHENKOV, G., GUSEVA, J. & GANDJUKHIN, V. 2007. A seismo-stratigraphic analysis of glaciomarine deposits in the eastern Riiser-Larsen Sea (Antarctica). *Marine Geophysical Researches,* 28**,** 43-57.
SOLLI, K., KUVAAS, B., KRISTOFFERSEN, Y., LEITCHENKOV, G., GUSEVA, J. & GANDJUKHIN, V. 2008. The Cosmonaut Sea Wedge. *Marine Geophysical Researches,* 29**,** 51-69.
STOKER, M., EVANS, D. & CRAMP, A. Geological processes on continental margins: sedimentation, mass-wasting and stability. 1998. Geological Society of London.
STOW, D. A. Deep-water contourite systems: modern drifts and ancient series, seismic and sedimentary characteristics. 2002. Geological Society of London.
STOW, D. A., FAUGÈRES, J.-C., HOWE, J. A., PUDSEY, C. J. & VIANA, A. R. 2002. Bottom currents, contourites and deep-sea sediment drifts: current state-of-the-art. *Geological Society, London, Memoirs,* 22**,** 7-20.
STOW, D. A. & MAYALL, M. 2000. Deep-water sedimentary systems: new models for the 21st century. *Marine and Petroleum Geology,* 17**,** 125-135.
STOW, D. A. & SHANMUGAM, G. 1980. Sequence of structures in fine-grained turbidites: comparison of recent deep-sea and ancient flysch sediments. *Sedimentary Geology,* 25**,** 23-42.
SUN, D., BLOEMENDAL, J., REA, D., VANDENBERGHE, J., JIANG, F., AN, Z. & SU, R. 2002. Grain-size distribution function of polymodal sediments in hydraulic and aeolian environments, and numerical partitioning of the sedimentary components. *Sedimentary Geology,* 152**,** 263-277.
SWITHINBANK, C., MCCLAIN, P. & LITTLE, P. 1977. Drift tracks of Antarctic icebergs. *Polar Record,* 18**,** 495-501.
THIEDE, J. & OERTER, H. 2002. Die Expedition ANTARKTIS XVII/2 des Forschungsschiffes POLARSTERN 2000= The expedition ANTARKTIS XVII/2 of the research vessel POLARSTERN in 2000. *Berichte zur Polar-und Meeresforschung (Reports on Polar and Marine Research),* 404.
TJALLINGII, R., RÖHL, U., KÖLLING, M. & BICKERT, T. 2007. Influence of the water content on X-ray fluorescence core-scanning measurements in soft marine sediments. *Geochemistry, Geophysics, Geosystems,* 8.
TURNER, J. & OVERLAND, J. 2009. Contrasting climate change in the two polar regions. *Polar Research,* 28**,** 146-164.
UIT THE ARCTIC UNIVERSITY OF NORWAY. 2018a. *X-Ray instrument* [Online]. Available: https://uit.no/om/enhet/artikkel?p_document_id=390469&p_dimension_id=88137&men=28927 [Accessed October 11th, 2018].
UIT THE ARCTIC UNIVERSITY OF NORWAY. 2018b. *XRF core scanner container lab* [Online]. Available: https://uit.no/om/enhet/artikkel?men=28713&p_document_id=389557&p_dimension_id=88137 [Accessed October 24th, 2018].
USGS SCIENCE FOR A CHANGING WORLD. 2017. *GALLERY OF COMMON SEDIMENT SAMPLING DEVICES* [Online]. Available: https://cmgds.marine.usgs.gov/publications/of2005-1001/htmldocs/corers.htm [Accessed October 11th, 2018].
VAN DER VEEN, C. 1997. Backstress: what it is and how it affects glacier flow. *Byrd Polar Research Center Report No. 15***,** 173-180.

VANDERAVEROET, P., AVERBUCH, O., DECONINCK, J.-F. & CHAMLEY, H. 1999. A record of glacial/interglacial alternations in Pleistocene sediments off New Jersey expressed by clay mineral, grain-size and magnetic susceptibility data. *Marine Geology,* 159**,** 79-92.

VAUGHAN, D. & DOAKE, C. 1996. Recent atmospheric warming and retreat of ice shelves on the Antarctic Peninsula. *Nature,* 379**,** 328-331.

VAUGHAN, D. G. & SPOUGE, J. R. 2002. Risk estimation of collapse of the West Antarctic Ice Sheet. *Climatic Change,* 52**,** 65-91.

VEROSUB, K. L., FINE, P., SINGER, M. J. & TENPAS, J. 1993. Pedogenesis and paleoclimate: Interpretation of the magnetic susceptibility record of Chinese loess-paleosol sequences. *Geology,* 21**,** 1011-1014.

VON BODUNGEN, B., ANTIA, A., BAUERFEIND, E., HAUPT, O., KOEVE, W., MACHADO, E., PEEKEN, I., PEINERT, R., REITMEIER, S. & THOMSEN, C. 1995. Pelagic processes and vertical flux of particles: an overview of a long-term comparative study in the Norwegian Sea and Greenland Sea. *Geologische Rundschau,* 84**,** 11-27.

VORREN, T. 2003. Subaquatic landsystems: continental margins. *Glacial Landsystems. Arnold Publishers, London,* 289**,** 312.

VORREN, T. O. & LABERG, J. S. 1997. Trough mouth fans—Palaeoclimate and ice-sheet monitors. *Quaternary Science Reviews,* 16**,** 865-881.

WEBER, M. E., NIESSEN, F., KUHN, G. & WIEDICKE, M. 1997. Calibration and application of marine sedimentary physical properties using a multi-sensor core logger. *Marine Geology,* 136**,** 151-172.

WELLNER, J., HEROY, D. & ANDERSON, J. 2006. The death mask of the Antarctic ice sheet: comparison of glacial geomorphic features across the continental shelf. *Geomorphology,* 75**,** 157-171.

WHITE, D. A., FINK, D. & GORE, D. B. 2011. Cosmogenic nuclide evidence for enhanced sensitivity of an East Antarctic ice stream to change during the last deglaciation. *Geology,* 39**,** 23-26.

WHITEHOUSE, P. L., BENTLEY, M. J. & LE BROCQ, A. M. 2012. A deglacial model for Antarctica: geological constraints and glaciological modelling as a basis for a new model of Antarctic glacial isostatic adjustment. *Quaternary Science Reviews,* 32**,** 1-24.

WHITWORTH, T., ORSI, A., KIM, S. J., NOWLIN, W. & LOCARNINI, R. 1998. Water masses and mixing near the Antarctic Slope Front. *Ocean, ice, and atmosphere: interactions at the Antarctic continental margin***,** 1-27.

ZACHOS, J. C., QUINN, T. M. & SALAMY, K. A. 1996. High-resolution (104 years) deep-sea foraminiferal stable isotope records of the Eocene-Oligocene climate transition. *Paleoceanography,* 11**,** 251-266.

ZHANG, J. 2007. Increasing Antarctic sea ice under warming atmospheric and oceanic conditions. *Journal of Climate,* 20**,** 2515-2529.